THE CROSSFLOW MICROFILTRATION OF CONCENTRATED TITANIA DISPERSIONS

by
Justin Quinton Marchant

Doctoral Thesis

Submitted in partial fulfilment of the requirements for the award of

Doctor of Philosophy of Loughborough University

1999

ACKNOWLEDGEMENTS

ABSTRACT

This work is the subject of an EPSRC-Tioxide Industrial CASE Award, the principal area of study being factors affecting the achievable steady state permeate flux during the crossflow microfiltration of concentrated titania dispersions. The performance of this continuous thickening process is of particular interest to Tioxide as a potential alternative to current batch filtration processes, which delay the manufacturing process.

The titania suspension was characterised using particle size analysis, Zeta potential measurements (as a function of pH), and viscosity measurements (as a function of dispersion pH, solids concentration and applied shear rate). The rheological characterisation demonstrated the presence of a yield stress, shear-thinning behaviour, and thixotropic behaviour, all of which increased with solids concentration and as the pH approached the iso-electric point (pH 4).

Crossflow filtration experiments determined a maximum achievable feed suspension concentration of 48% volume solids, and investigated the effects of process parameters (transmembrane pressure, crossflow velocity, feed solids concentration, and suspension pH) on the steady state permeate flux. Increases in crossflow velocity and transmembrane pressure resulted in improved permeate fluxes, whilst increasing the feed solids concentration served to reduce permeate flux, and dampen the beneficial effects of other parameters. Flocculated suspensions gave rise to higher steady state permeate fluxes at low solids concentrations, but the increased suspension viscosities presented problems at higher solids concentrations.

A model has been developed using rheological properties of the feed suspension and cake to predict a filter cake thickness and achievable permeate flux at steady state, for a given set of process parameters. This enables the model to be applied to any system where the required empirical data is known. The simplicity of the model however results in some disparity between experimental values and theoretical predictions, and therefore requires further work.

CONTENTS

INTRODUCTION

The objective of this research was to investigate crossflow microfiltration as an alternative to the existing dewatering processes used by Tioxide plc. in the manufacture of titanium dioxide.

Titanium dioxide (TiO_2) occurs naturally as rutile, anatase and brookite, of which the latter is rare and of no commercial interest. Rutile is the most stable form of titania, and the orientation of atoms in its structure result in a more densely packed crystal than anatase, thus giving it a higher density and refractive index[1]. Pure titanium dioxide is a non volatile, insoluble, colourless solid in massive state, but absorbs almost no incident light in the visible region of the spectrum when finely divided, and thus appears white. Additionally, its high refractive index gives the pigment a far greater opacity, and more than twice the tinting strength of any other common white pigment[1].

The use of titania is thus widespread where it is desirable to impart whiteness or brightness to a product, for example in paints, plastics, papers, fibres, and vitreous enamels. Rutile also absorbs UV light and this, combined with its stability, enables the production of paints and other polymeric materials with exceptional weather resistance. High purity grades of titania are also used in pharmaceuticals and cosmetics[1].

The effective particle size of the pigment must be optimised to give the desired degree of light scattering for its specified use, and this is obtained by manufacturing an appropriate pigment crystal size and dispersing it sufficiently. The pigment size is controlled during the precipitation and calcination stages of the manufacturing process, while coating the surface of the crystals can control the ease of dispersion.

Titanium dioxide is manufactured commercially via the 'sulphate process' and, more recently, the 'chloride process'. Both processes use a series of chemical reactions to

produce the TiO_2 from different ores, after which various separation, calcination, drying, coating and milling process are used to create the final product.

Crossflow microfiltration is a potential alternative to some of the current filtration processes, particularly batch processes, which slow down the rate of manufacture. Crossflow filtration could offer continuous operation, the ability to reduce the concentration of salts in suspension via diafiltration, and reduced heating costs during calcination, as a result of more efficient water removal.

The primary objectives of an experimental study were therefore to find the maximum achievable solids concentration during crossflow filtration, and to seek the optimum conditions for permeate removal.

The achievable solids concentration was measured by filtering a titanium dioxide suspension in crossflow whilst removing permeate from the system. The feed suspension thus increased in concentration continuously, and the permeate flux continued to decline until a limit was reached and the filter tube blocked. The alternative method of operation was to return permeate to the feed tank, thus maintaining the concentration of the feed suspension, in which case the permeate flux declined to a steady state level. The effect of the various process operating conditions (transmembrane pressure, crossflow velocity, feed suspension solids concentration, and feed suspension pH) on the level of steady state permeate flux was observed by varying each parameter individually whilst maintaining all others constant. This enabled the effect of each parameter to be evaluated, pointing to conditions for optimum permeate removal.

So that the acquired experimental data would be of use to Tioxide in comparing the productivity, cost and efficiency of current and investigated processes, it was necessary to simulate the operating conditions of a typical TiO_2 process stream in the crossflow filtration experiments performed here. The primary requisite for this comparability was that the titania dispersions should have a Malvern mean particle size of <0.32µm, preferably 0.30µm.

It was thus necessary to develop a process and methodology that would reliably and repeatably ensure the dispersion of rutile powder (supplied by Tioxide for this project) to the desired mean particle size.

The results of the filtration experiments were used to aid the development of a predictive model for steady state permeate flux in crossflow filtration. This incorporated expressions for the operating parameters during filtration, as well as characteristics of the suspension being filtered and the filter cake. A characterisation of the rutile suspensions was therefore undertaken, the results of which also aided in the evaluation of dispersion techniques.

The effect of pH on Zeta potential and particle size was observed across the pH range, and (of specific use to the modelling), a large number of rheological experiments were carried out to evaluate the effects of pH, shear rate and feed suspension solids concentration on the viscosity of the rutile suspensions.

This data was used to predict steady state permeate fluxes via the developed model, and the theoretical values were compared with experimentally measured values.

The results of the dispersion, characterisation, and filtration experiments have been analysed and discussed, as have the results of the modelling work. The findings have then been summarised with some concluding remarks and recommendations for further work.

The experimental work presented in this study has also formed the basis of two published papers concerning the rheological study[2] and the filtration work[3] respectively.

The first paper[2] investigates the effects of pH and temperature on the rheology and stability of aqueous rutile dispersions. The dispersions are shown to exhibit shear-thinning behaviour over the range of shear rates investigated, and this conforms to the Herschel-Bulkley or Casson type rheological models. The dispersion was also

observed to be extremely sensitive to changes in pH, whereby the viscosity increased by as much as an order of magnitude with pH variation at constant volume fraction. Changes in the dispersion temperature indicated that the relative contribution of Brownian motion and shear flow to viscosity is dependent on the extent of flocculation within the dispersion.

The second paper[3] investigates the results of the crossflow filtration work; considering the effects of variation in crossflow velocity, feed solids concentration and transmembrane pressure on permeate flux. Additionally, flux decline curves for crossflow filtration experiments are modelled using dead-end filtration theory to model the initial transient flux decline and a steady state model, based on the Kozeny-Carman equation and Darcy's law, for longer times. The shear thinning behaviour of the dispersions is accounted for by fitting rheological data to a Herschel-Bulkley type model and the resulting fluxes are shown to be in good agreement with experimentally measured values.

CHAPTER ONE

LITERATURE SURVEY

1.1 SOLID-LIQUID SEPARATION

The technique used to separate suspended solids from a liquid depends largely on the size of the solid particles concerned. Suspensions rarely contain particles of uniform shape and size however, and are thus often characterised by a representative dimension or mean size.

Methods of solid liquid separation can be broadly confined to three particle size ranges[4]: those greater than 100μm, those between 10 and 100μm and those less than 10μm.

Particles greater than 100μm are generally removed by screening, where a suspension is passed through vibrating sieves with progressively smaller apertures until all the particles are eventually removed from the system.

Particles between 10 and 100μm can be removed from suspension via a number of different methods. Dead-end filtration for example uses pressure to drive the liquid through a ceramic or polymeric filter, the pores in the filter being too small to permit the passage of the solid particles. Alternatively, particles may be concentrated in a settling tank or thickener, which relies on the particles falling out of suspension under gravity. Clear liquid is taken from the top of the vessel and the concentrated suspension is removed from the bottom. The rate of sedimentation can be increased using an electrolyte to floc the particles. Another option is a cyclone, which rapidly increases the velocity of a suspension, while all but those particles small enough to keep up with the general flow are removed.

For particles less than 10μm, the masses are so small that the force of gravity must be increased a number of times (for example in a centrifuge) before particles will

5

'fall' out of suspension. Most particles of this size are therefore removed via dead-end filtration (down to 0.1μm) or crossflow filtration (10 to 0.001μm)[4].

Dead-end filtration is essentially a batch process, where liquid passes through the filter medium while particles form a cake of solids on the filter surface. The resulting increase in resistance to filtrate flow necessitates a steady increase in pressure for the duration of the process until no more liquid can be (economically) removed. The filter cake must then be removed before the next batch can be processed.

Crossflow filtration uses shear stress, applied by the crossflowing feed suspension, to limit the growth of filter cake, thus a constant transmembrane pressure drop can be maintained and the experiment run virtually continuously as both 'solid' and liquid products are removed simultaneously. The flux of filtrate steadily declines to a steady state value but can often be 'rejuvenated' by periodic cleaning (backflushing) of the filter. This is essentially a process for concentrating suspensions, but is also used for removing fine particulates in clarification and purification processes. Unlike dead-end filtration, it does not result in significant cake growth and it can not be used to classify particles.

1.2 COLLOID SCIENCE

1.2.1 Definition of a Colloid

Colloid science is concerned with the behaviour of matter that has one dimension in the size range one nanometre to one micron[5] Titanium dioxide particles can therefore be defined as colloidal[1], although in close proximity the individual particles are likely to bond and form structures with mean particle sizes outside this range. If these structures are easily destroyed by the application of stresses and reform once the stress is removed, they are termed flocs (loose, thermodynamically metastable structures). If however, the particles cluster tightly and can not be separated in a rheological experiment, they are termed aggregates[6].

1.2.2 Particle Sizing

Particle sizing apparatus generally relies on principles of sedimentation or light diffraction to determine the distribution of particle sizes within a suspension, this being calculated using an algorithm which accounts for factors like the nature of the material. The different methods of measurement and analysis used by the various apparatus invariably results in different analyses for samples of the same suspension, and a true determination of particle size can therefore only be made by physically measuring a sample of suspension using high magnification equipment such as a scanning electron microscope. However, where the relative particle size distribution is important, such as ensuring the homogeneity of a suspension after dispersion, or constancy of particle size distribution in a process production stream, a sizing apparatus that provides repeatable results is sufficient.

1.2.3 Colloids in Suspension

A colloidal dispersion is distinguished from a particulate suspension in that the

7

particles are sufficiently small for the mild mixing produced by ambient thermal fluctuations and/or Brownian motion to keep them uniformly dispersed in the continuous medium[7]. The dispersion may be described as dilute (having negligible inter-particle interaction) or concentrated (having strong inter-particle interaction)[5].

Metal oxide particles dispersed in an aqueous solution will acquire a surface coating of chemically bonded hydroxyl groups through the dissociative adsorption of water molecules[8]. This layer of counter-ions and the remaining co-ions distributed diffusely in the solution neutralise the particle surface charge[9]. The surface hydroxyl groups are amphoteric and their degree of ionisation/ protonation depends on the dispersion pH, consequently the sign and magnitude of a particles surface charge is also a function of pH^{8-12}.

The layers of counter and co-ions around the particle make up the double electrical layer, which is represented by the Stern model[12] (Figure 1.1).
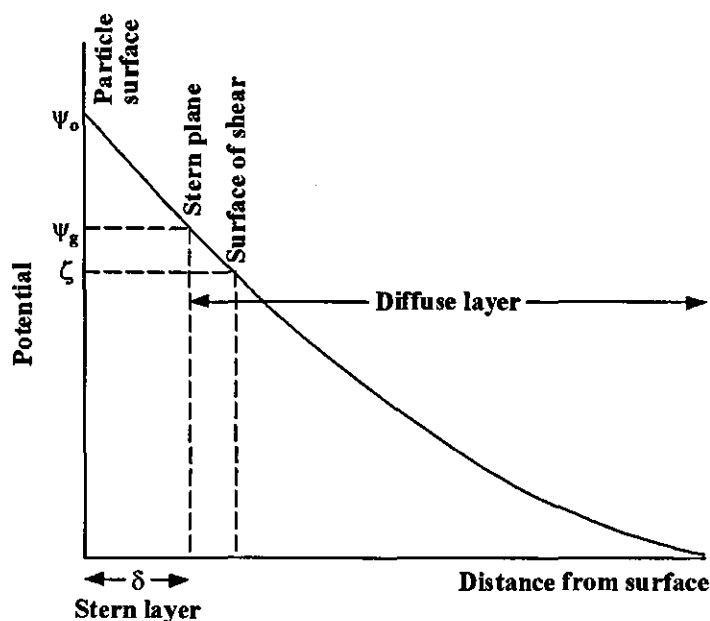
Figure 1.1 Sterns double electrical layer model

1.2.4 Electrical Double Layer Model

The Stern model demonstrates the decay in electropotential (relative to the bulk solution) from a maximum at the particle surface (ψ_o) to zero in the diffuse layer[12]. The strongly adsorbed counter-ions form the 'Stern layer' which extends approximately one hydrated ion radius (δ) from the particle surface[9]. The limit of the Stern layer defines the boundary between the two components of the electrical double layer and is known as the Stern plane. The electropotential at the Stern plane is the Stern potential (ψ_δ).

1.2.5 Electrical Triple Layer Model

This differs from the double layer model in that the ions adsorbed on the particle surface are comprised of specifically complexed ions (chemisorbed) which rest within an "inner sphere" (the inner Helmholz plane), and non-specifically complexed ions which are physically adsorbed and sit within a secondary sphere (the outer Helmholz plane)[7]. The outer Helmholz plane can be identified with the Stern plane[13] and like the Stern model, the uncomplexed, hydrated ions approach no further than this limit, but remain distributed randomly in the diffuse layer.

In aqueous solutions, simple organic cations are more strongly hydrated than anions and therefore have a larger hydration radius; thus anions are more specifically adsorbed.

1.2.6 Zeta Potential

When particles in a colloidal dispersion move, a thin layer of liquid surrounding each particle moves with it such that the hydrodynamic boundary between moving body and stationary liquid is actually a liquid-liquid interface within the solution. The electropotential at this plane is termed the Zeta potential and by identifying the

slipping plane with the Stern plane[14], this can be approximated to the Stern potential. Zeta potential is the only directly measurable potential associated with a particle in suspension, it gives an indication of the degree of inter-particle repulsion and thus the overall stability of the suspension.

Zeta potential is measured by means of electrophoresis, where a potential is applied to a suspension and the resulting movement of particles within the suspension measured (the electrophoretic mobility being independent of particle concentration[15]).

Instruments such as the Malvern Zetamaster use a laser, focussed through a thin walled tube onto a suspension of moving particles, to provide light scatter. An automated system observes the scattered light and, from frequency shift measurements, can determine the sign of the potential and magnitude of the mobility. The Zeta potential is calculated from the acquired mobility data using the Huckel, Smoluchowski, or Henry equation, or a numerical solution[9].

1.2.7 Particle-Particle Interactions

The principal particle-particle interactions affecting the behaviour of colloids in an aqueous suspension[12,16] are the attractive London-van der Waals forces (from permanent or induced dipoles), and repulsive forces resulting from electric double layer interaction or steric hindrance[7]. Forces exerted by dipole-dipole interaction and the double layer are electrostatic, while steric forces are imparted by macromolecules that are adsorbed onto the particle surface and prevent the approach of other particles as a result of their size. The potential energy of attraction is usually expressed using the Hamaker constant[17].

10

1.2.8 Dispersion Stabilisation (DVLO Theory)

DLVO theory considers the interplay of van der Waals forces and the repulsive/ attractive forces associated with charged particles in the classical theory of lyophobic dispersion flocculation[13] (steric repulsion is less well defined in this work). It is named after two pairs of authors who worked simultaneously on the subject, Deryaguin & Landau[18] and Verwey & Overbeek[19].

A dispersion can be considered stabilised if the repulsive forces between particles are greater than the attractive forces to the extent that the existing energy barrier is much greater than the thermal energy of the particles. The potential energies of electrostatic attraction and repulsion between two identical spheres are considered additive and the total potential energy can be plotted against particle separation on a 'DVLO' curve[19] (Figure 1.2).
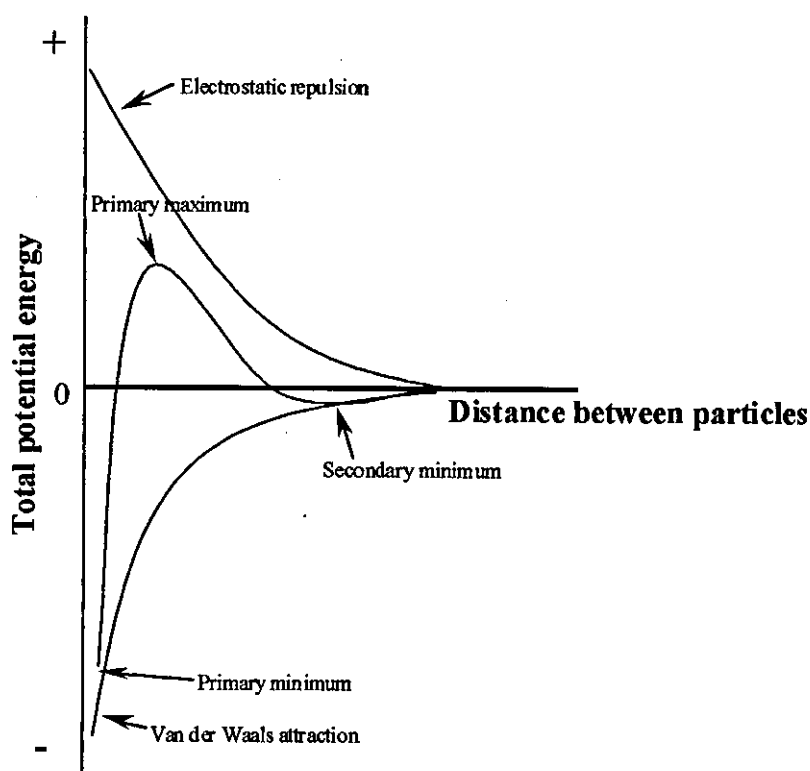
Figure 1.2 DVLO curve

The thermal energy of particles in the secondary minimum (Figure 1.2) is significantly lower than the potential energy of the primary maximum thus at this point the dispersion is stable. If the solids volume concentration is high enough the particles may flocculate, but interparticle interactions force the system to the configuration of least potential energy, so a well defined interparticle distance results[20]. Agglomeration is energetically unfavourable and is accomplished only by reducing the potential energy of the primary maximum (i.e. the interparticle electrostatic repulsive force), sufficiently for particles to ascend it from the secondary minimum and reach the primary minimum. This could be achieved by altering the dispersion pH to reduce the thickness of the electrical double layer, and Figure 1.3 demonstrates the influence of electrolyte concentration on the total potential energy of interaction[21].
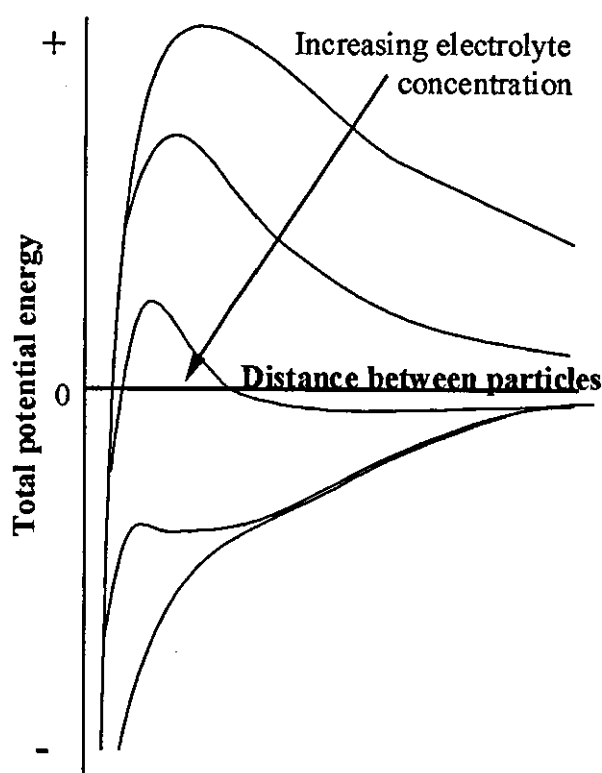
Figure 1.3 The effect of electrolyte concentration on the potential energy of interaction between particles

12

Van der Waals forces oppose the deformation of stable structures by particle separation, however under applied shear the separation of the particles will increase thus increasing the potential energy of the system. This concept is used to explain high viscosities, shear thinning and thixotropy[20].

1.2.9 The Effect of pH on Dispersion Stabilisation

As explained in Section **1.2.3**, the sign and magnitude of particle surface charge is dependent on the pH of the dispersion, and as a result, the thickness of the electrical double layer is also a sensitive function of ionic strength[22]. For a 1:1 electrolyte in water at 25°C;

$$1/\kappa \sim 0.3/c^{1/2} \qquad (1.1)$$

Where c is the molar concentration and $1/\kappa$ is the Debye length in nm (normally used to characterise double layer thickness). If the layer thickness exceeds the range of van der Waals attractions (at low molar concentration) the particles remain dispersed, however as concentration increases and the layer thickness diminishes, the particles tend to agglomerate.

The suspension pH is changed by the addition of an acid or alkali, and at a particular pH the particle surface charge is zero and this is termed the PZC (point of zero charge). The PZC is characteristic of the material and defines the acid/base nature of the surface. At pH values above the PZC, the particles are positive and for pH values less than the PZC the particles are negative. The PZC should not be confused with the IEP (iso-electric point) which is determined from Zeta potential measurements and corresponds to zero charge at the plane of shear[13]. The IEP of a particular TiO_2 suspension will depend on additives to the dispersion (surfactants), and impurities introduced in the titania manufacturing process.

1.2.10 Dispersing Powders in Liquids

To successfully disperse a powder in a liquid three stages must take place[13], and these may occur individually or simultaneously.

i. Surface wetting

    Placing a quantity of powder on top of the liquid medium, the liquid must penetrate the fine capillaries between particles and replace the solid-air interface with a solid-liquid interface.

ii. Mechanical disruption

    Mechanical energy, often using a high shear mixer, is imparted to the solid-liquid mixture to break down agglomerates and ensure a homogeneous distribution of particles.

iii. Stabilisation

    Conditions are established to minimise the flocculation of dispersed particles, for example the adsorption of ions or molecules to the solid-liquid interface. These modify the attraction potential of particles through the introduction of electrostatic repulsion or prevent close approach by steric hindrance.

1.2.11 The Effect of Additives on the Dispersion Process

An additive that adsorbs onto the surface of particles in suspension can change the properties of surface wetting, adhesion, agglomeration and stabilisation in a colloidal dispersion[10,11].

In aqueous dispersions the adsorbent is generally an amphipathic macromolecule, adsorbed from solution in the liquid phase at the solid-liquid interface[13]. The nature of the solubilising group allows classification of the adsorbent as anionic, cationic or non-ionic, and the greater the number of counter-ions available, the greater the

degree of adsorption. Since the dissociation of surfactant molecules is pH dependent, the degree of adsorption is also a function of dispersion pH.

An additive can aid the initial wetting of dry particles by reducing the solid-liquid interfacial tension and therefore the associated contact angle[8,13]. The capillary action of the liquid is able to displace vapour from even finer inter-particle gaps of dry agglomerates, thus promoting a greater degree of dispersion.

To produce a kinetically stable dispersion for experimentation, the interparticle repulsive forces must be stronger and longer range than the attractive forces[8]. An adsorbed layer of macromolecules on the particle surface can improve dispersion stability by either increasing the repulsive electrostatic force between particles, by providing entropic stabilisation[13] (steric hindrance), or through a combination of the two. The common feature is that they separate particles to such a degree that the van der Waals attractive forces are not able to dominate.

With reference to Figure 1.2, the effect of the adsorbent is to increase the potential energy required to overcome the primary maximum, thus particle aggregation within the dispersion is energetically unfavourable.

1.3 SUSPENSION RHEOLOGY

A fluid will offer resistance to flow when a shear stress is applied to it, the degree of which is determined by measuring the resulting rate of shear in the fluid. If the ratio of applied shear stress (τ) to shear rate ($\dot{\gamma}$) is constant then the fluid conforms to equation 1.2 and is defined as a Newtonian fluid[23] with a coefficient of viscosity μ.

$$\mu = \frac{\tau}{\dot{\gamma}} \qquad (1.2)$$

Suspending particles in the same fluid will result in an increased viscosity over that of the fluid alone, the extent of which will depend on the degree of particle-particle and fluid-particle interactions within the suspension. These are dependent on characteristics such as the suspension solids concentration, dispersion pH, mean particle size and shape, and adsorbed molecules[23], and sometimes also the shear induced fluid flow of the suspension.

Where the shear induced flow does affect particle-particle interactions, a departure from Newtonian behaviour is observed, and the suspension may appear to thin (become less viscous) or thicken (become more viscous) with increases in the applied shear stress (Figure 1.4). In these cases, the suspension exhibits uniform flow but the ratio $\tau/\dot{\gamma}$ is not constant, thus the fluid is said to be non-Newtonian and a shear rate specific, 'apparent viscosity' (μ_a) is often used.

These and other rheological phenomena resulting from interactions between the continuous and discontinuous phases are common in high concentration colloidal dispersions[13,20]. Those most commonly associated with titania dispersions are briefly described below with particular reference to particle-particle interactions.

16
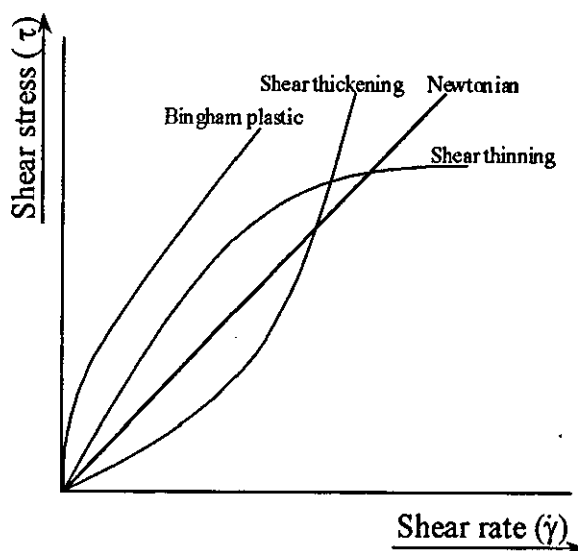
Figure 1.4 The response of Newtonian, Bingham plastic, pseudo-plastic (shear thinning) and dilatant (shear thickening) fluids to an applied shearing stress.

1.3.1 Suspensions Exhibiting a Yield stress

High concentration colloidal dispersions often exhibit plastic behaviour, i.e. distorting elastically and having a yield stress which must be overcome in order for the suspension to flow[13,20]. Bingham[24] suggested that the resistance to flow at low shear rates is a result of weakly bonded particles touching each other in a flocculated array, and in this respect the suspension exhibits properties typical of a solid. The flocs must therefore be broken up before the suspension will flow, and this is achieved by increasing the applied shear stress until sufficient inter-particle bonds have been broken. As the suspension solids concentration is increased, the particles become closer in proximity and the degree of inter-particle bonding increases thus, the yield stress will also increase.

If, having exceeded the yield stress the flow behaviour is effectively Newtonian, then the material is termed a Bingham plastic (Figure 1.4).

17

1.3.2 Shear Thinning Behaviour (Pseudoplasticity)

Where there is an apparent decrease in viscosity with increasing shear rate, the suspension is described as pseudo-plastic or shear thinning[13]. Aqueous suspensions of titanium dioxide exhibit distinct shear thinning characteristics, which become more exaggerated with increasing solids fraction[25]. Like the yield stress, this can also be interpreted in terms of weak inter-particle bonding, which is broken down under shear[13].

In the absence of shear, the titania flocs are said to form rods or chains which curl into spheres however, as the applied shear stress is increased, these straighten out and align themselves with streamlines in the suspension, thus reducing their resistance to flow[13,26].

Light scattering techniques have been used to examine the change in dispersion structure with shear rate[27], and are said to confirm the above theory, having observed crystalline, layered, string-like and amorphous structures.

1.3.3 Thixotropy

This term describes the time dependent behaviour of shear thinning fluids where the loosely bonded structure existing within the dispersion, having been destroyed by shear, does not reform immediately. As the shear rate is reduced, the transition of particles from shear induced alignment back to a loosely bonded structure is subject to a time delay[13]. The apparent viscosity at a particular shear rate while shear rate is being reduced, is therefore lower than was experienced for the same shear rate as shear rate was being increased. Plotting shear rate against shear stress for this process will result in the formation of a 'hysteresis loop' for a thixotropic fluid (Figure 1.5).

18
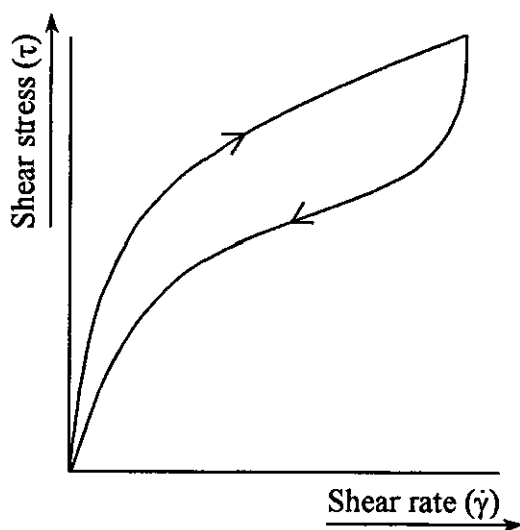
Figure 1.5 Stress-strain curve for a thixotropic fluid

1.3.4 The Effect of Brownian and Hydrodynamic Forces on Rheology

The presence of a yield stress can also be explained by the dominance of Brownian motion over the shear induced hydrodynamic forces within the dispersion at low shear rates.

Shear induced rheological phenomena such as the presence of a yield stress and shear thinning are a result of flocculation in colloidal dispersions, and can be explained by the relative strengths of Brownian motion and shear induced hydrodynamic forces, which favour and oppose flocculation respectively. The effects of Brownian motion and shear induced forces on a dispersion depend on the dispersion temperature, concentration and particle size, where the effects of Brownian motion are negligible for particles with larger than colloidal dimensions[20,28].

At low shear rates, the randomising effect of Brownian motion is dominant[20], and there is a balance between the acting thermal movement and viscous resistance within the dispersion. As the shear rate is increased, hydrodynamic effects begin to

dominate and particles are aligned in opposition to the randomising effect of Brownian motion, thus offering a lower resistance to flow[29]. This is evident from the superimposition of Brownian motion and shear giving translational (Pe_t) and rotational (Pe_r) Peclet numbers[20];

$$Pe_t = \frac{R^2 \dot{\gamma}}{D_t} \qquad (1.3)$$

$$Pe_r = \frac{\dot{\gamma}}{D_r} \qquad (1.4)$$

where D_t and D_r are translational and rotational diffusion constants, expressed by;

$$D_t = kT/6\pi\mu_o R \qquad (1.5)$$

$$\text{and} \quad D_r = kT/8\pi\mu_o R^3 \qquad (1.6)$$

respectively, $\dot{\gamma}$ is the shear rate, R the radius of a spherical particle, k is the Boltzmann constant, T is absolute temperature and μ_o is the viscosity of the suspending medium.

With reference to shear thinning behaviour, at very low shear rates the Peclet numbers are low and diffusion dominates, preventing any alignment of particles with respect to the shear plane. A Newtonian plateau is then sometimes seen at low shear rates where Brownian motion restores equilibrium in the suspension microstructure faster than it is perturbed by shear[27]. As the applied shear stress increases further, so the hydrodynamic forces increase, dominating the Brownian motion and increasing the degree of order in the dispersion, thus non-Newtonian shear thinning behaviour prevails.

1.4 MICROFILTRATION THEORY

1.4.1 Particle Deposition

Particles being removed from a suspension by the dead-end filtration process flow perpendicular to and towards a filter medium, the pores of which may be small enough to retain the particles, but large enough to permit a reasonable flux of liquid through them. The transmembrane pressure provides the driving force for permeation and thus the convection of particles to the filter surface (the rate of particle deposition being dependent on both the magnitude of the transmembrane pressure and the solids concentration in the feed stream). The retained solids accumulate on the filter surface forming a cake through which the rest of the suspension must then pass. This is termed the 'dynamic membrane' and itself provides an improved solids retention (and therefore filtrate quality) but at the cost of a decline in the filtrate flux (at constant transmembrane pressure), eventually to an unacceptably low level. The process must then be stopped, and the filter cake removed from the filter before it is repeated.

1.4.2 Blocking Filtration Laws

Particulate blocking mechanisms describe the ways in which particles may be deposited at or in the pores of a filter to affect its performance. Hermia[30] adapted these models to simulate membrane fouling during the dead-end filtration of a constant feed concentration suspension, and developed equations to relate permeate flux decline to the process suspension properties.

The blocking mechanisms are:

Complete blocking, where every particle that lands on the membrane surface blocks an entire pore (Figure 1.6a).

21

Standard blocking, where particles are deposited on the internal walls of pores, reducing the cross sectional area available for fluid flow and thus the flux of filtrate through the medium (Figure 1.6b).
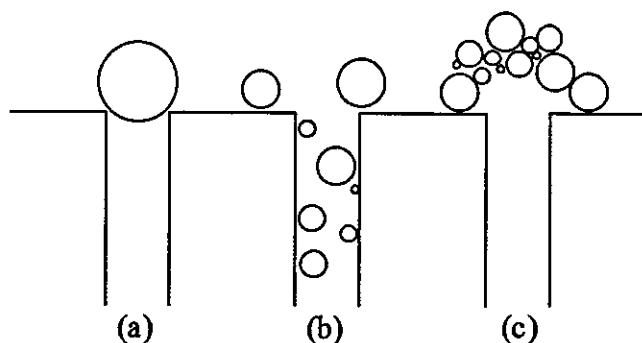
Figure 1.6   Particulate blocking mechanisms.

Cake filtration, where the particles form a permeable layer on the membrane surface. This results in a reduced flux of suspension to the membrane, but leaves the resistance of the filter medium itself unchanged (Figure 1.6c).

Finally, intermediate blocking, where the rate of blocking lies between those expected for cake or standard.

Permeate flux decline data can be used to test for the presence of these mechanisms by fitting it to the following equations for complete, standard, cake and intermediate blocking respectively (equations 1.7 To 1.10)

$$-\ln\left(\frac{J}{J_0}\right) = K_b t + E \tag{1.7}$$

$$\frac{t}{V} = \frac{K_d}{2} t + \frac{1}{J_0} \tag{1.8}$$

$$\frac{t}{V} = \frac{K_k}{2}V + \frac{1}{J_0}$$ (1.9)

$$\frac{1}{J} = K_i t + \frac{1}{J_0}$$ (1.10)

Where J is the permeate flux at time t, J_0 is the clean water flux, V is the volume of permeate collected at time t, and K_b, K_d, K_k, K_i and E are constants.

Equations 1.7 To 1.10 take the form $y = mx + c$, thus the plotted data should take on a linear relationship if the mechanism is present. Most microfiltration processes cannot be described by one blocking mechanism alone, but a combination of the laws can give a fairly accurate description of the particle deposition processes taking place.

1.4.3 Crossflow Microfiltration and the Onset of Steady State

The objective of crossflow microfiltration is to reduce the extent of particle deposition during filtration by feeding the process stream tangentially to the filter surface. In theory, the combination of a low permeate velocity and the high shear stress exerted at the filter surface by the high velocity feed stream prevents any particle deposition, thus no decline in permeate flux is experienced. This is true for low pressure crossflow filtration, where the permeate flux is below the 'critical flux'[31]. In most practical applications however, the shear stress is not large enough to prevent some particle deposition on the membrane surface and this, as in dead-end filtration, will result in permeate flux decline (Figure 1.7).

Unlike dead-end filtration however, the shear stress parallel to the filter surface promotes mechanisms that oppose the convective flow of particles to the cake[32-34], and these arrest the flux decline. Where the feed suspension is maintained at

23

constant solids concentration, this results in a steady state permeate flux (Figure 1.8).
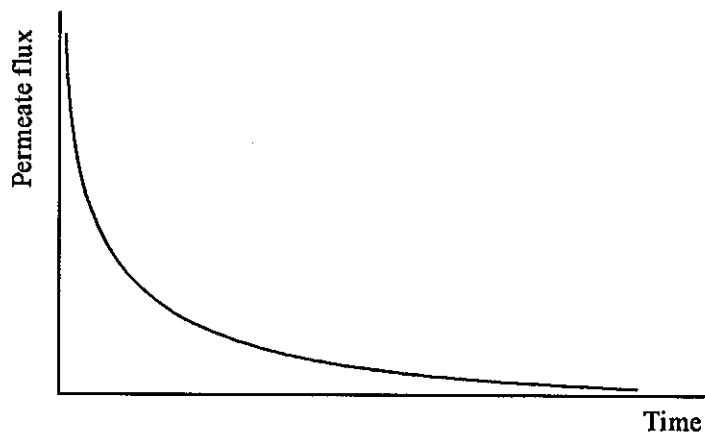
Figure 1.7 Typical flux decline curve for dead-end filtration
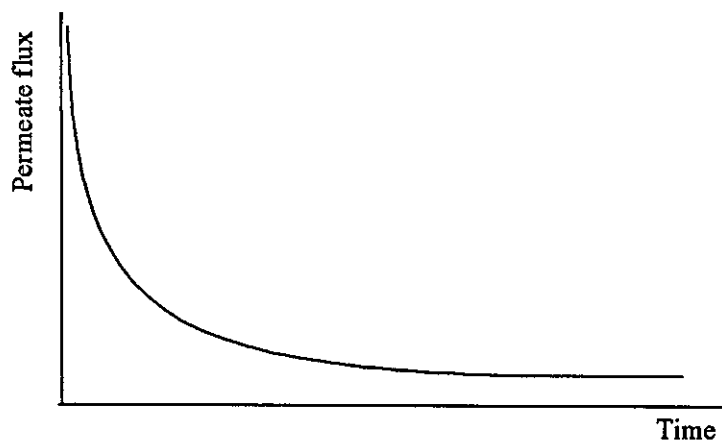
Figure 1.8 Typical flux decline curve for crossflow filtration

24

During filtration, the mechanisms opposing particle accumulation on the filter are enhanced by the increasing cake thickness, which reduces the filter channel cross sectional area, thus providing increased crossflow velocity (and therefore shear stress) at constant volumetric flow rate. The mechanisms of particle deposition and removal interact and counteract, slowing the rate of cake growth and permeate flux decline until a steady state is eventually reached where both cake thickness and permeate flux remain constant.
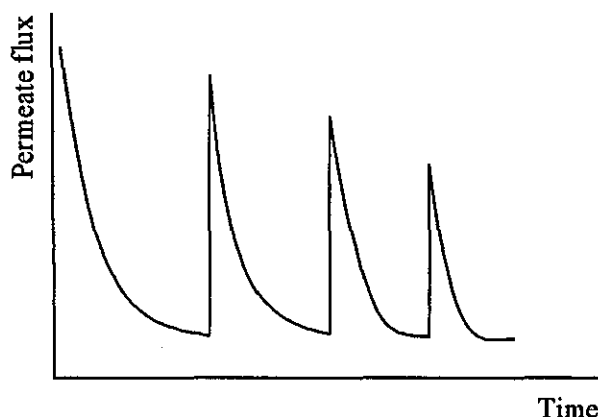
Figure 1.9 Flux decline curve with permeate flux partially recovered through periodic back flushing

The steady state permeate flux is considered a pseudo steady state value[35], as over a much longer time scale, consolidation of the filter cake may see it decline further. Should the filtrate flux fall to an unacceptably low level, the cake can be removed by back flushing in an attempt to regain the initial level (Figure 1.9).

1.4.4 Adaptations of Classical Cake Filtration Theory

Work by Davis[36], Redkar and Davis[37] and Datta and Gaddis[38] has observed that the cake build up and associated flux decline in the initial stages of crossflow microfiltration is independent of shear rate and can be approximated by dead-end

filtration theory. This is termed the region of transient flux decline and can be modelled using Darcy's law, which states that the average velocity of permeate, as measured over the whole area of the filter bed, is proportional to the driving pressure across it, and inversely proportional to the bed thickness. For flow through two porous media in series (the filter cake and the membrane), this is expressed by equation 1.11[37].

$$J(t) = \frac{\Delta P_{TM}}{\mu_o \left(R_m + R_c \delta_c(t) \right)}$$ (1.11)

Where $J(t)$ is the time dependent permeate flux, μ_o the viscosity of the suspending medium, R_m is the membrane resistance, R_c is the specific cake resistance and $\delta_c(t)$ is the time dependent filter cake thickness.

The membrane resistance (R_m) is determined using the permeate flux measured through the unfouled membrane (J_o), also known as the clean water flux. This is calculated by taking the limit of equation 1.7 where $t=0$, (thus $\delta_c=0$) and rearranging for R_m[37];

$$R_m = \frac{\Delta P_{TM}}{\mu_o J_o}$$ (1.12)

The specific cake resistance (R_c) can be estimated using the Blake-Kozeny correlation for laminar flow through an incompressible packed bed of monodisperse spheres[33,37].

$$R_c = \frac{150 \phi_c^2}{(2a)^2 (1 - \phi_c)^3}$$ (1.13)

Where ϕ_c is the volume fraction of solids in the cake layer and a is the mean particle radius.

Equation 1.11 was developed for flat sheet membranes and will hold for cylindrical filters provided that the cake layer is thin relative to the tube radius. For cylindrical filters with thick cake layers, a curvature correction factor is required due to the reduced area available for filtration as cake thickness increases. Correcting equation 1.11 gives equation 1.14[37]

$$J(t) = \frac{\Delta P_{TM}}{\mu_o \left(R_m + R_c H_o \ln \left[\frac{H_o}{(H_o - \delta_c(t))} \right] \right)}$$ (1.14)

where H_o is the filter tube radius.

Equations 1.11 and 1.14 for dead-end filtration, will produce flux decline curves that tend to zero with increasing time as the filter cake continues to grow (Figure 1.7). In order to successfully model the flux decline in crossflow filtration (with constant feed solids concentration), it is thus necessary to modify Darcy's law to predict the onset of steady state. This requires determination of the mechanisms by which particles are removed from or are prevented from being deposited on the filter cake, and is the subject of considerable work in the literature[32-34,36,39-57].

The mechanisms used to describe the process of particle removal in crossflow filtration fall into two main categories. Back transport mechanisms, which remove particles laterally from the filter cake into the bulk suspension, and pure convection, in which the flow of particles to the filter surface is balanced by a longitudinal migration of particles along the surface of the filter, or filter cake.

Sections **1.4.5** to **1.4.10** consider these mechanisms and the models based on them briefly, and a comprehensive treatment of the principal crossflow filtration models can be found in work by Chaudhury[54] and Belfort *et al.*[58].

1.4.5 Particle Removal for Ultrafiltration Models (Film Theory)

The Gel Polarisation Film Model attempts to describe the crossflow ultrafiltration of macrosolutes in suspension, where ultrafiltration implies particle removal by membranes with pore sizes in the range 0.001μ to 0.1μ[59] (moderate to high molecular weight solutes and colloids). The back transport mechanism is the result of matter attempting to diffuse from the high concentration filter deposit to the lower concentration bulk solution.

Figures 1.10a and 1.10b show the stages of gel polarisation at the filter surface, with the macrosolute concentration gradually increasing to saturation before the solute begins to precipitate.
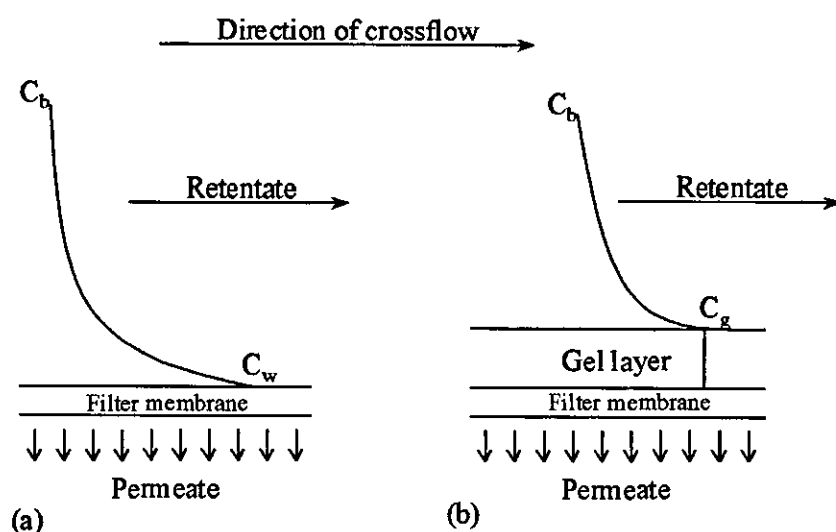
Figure 1.10 Gel polarisation in crossflow ultrafiltration

As the clean membrane is fouled by the flux of solute to its surface, the solute concentration at the membrane wall (C_w) gradually increases (Figure 1.10a). The accumulation of solute may eventually reach saturation point, or 'gel concentration' (C_g), and the solute will begin to precipitate (Figure 1.10b), with further solute deposition and precipitation serving simply to 'thicken the gel layer'. The gel

28

concentration is characteristic of the solute and depends primarily on the size, shape and degree of hydration/solvation of the solute particles in suspension.

The gel layer (dynamic membrane) and the filter membrane can be considered as one composite body[59,60], with the filter membrane acting as a porous, low resistance support for the gel layer which is a thin, high resistance barrier. The much improved retention characteristics of this composite membrane results in a higher quality filtrate but at the cost of a lower level of permeate flux.

The increase in concentration between the bulk solution and the membrane wall is termed 'Concentration Polarisation'[52,60], the extent of which depends on the solute flux to the filter surface and the rate of solute back diffusion to the bulk solution. The ratio of solute in bulk suspension (C_b) to solute at the membrane wall is called the polarisation modulus (C_w/C_b), and is used to calculate values of permeate flux using the following model:

Blatt et al.[59] give the film model equation;

$$J = K_s \ln \frac{C_w}{C_b} \qquad (1.15)$$

Where J is the permeate flux, K_s is the solute back diffusion mass transfer coefficient (calculated using the Stokes Einstein equation), and C_w is usually taken as the gel concentration. This implies that the level of permeate flux can be increased by improving the mass transfer coefficient (e.g. by raising temperature or increasing suspension mixing), or increasing the polarisation modulus (e.g. by reducing the feed suspension concentration or increasing the transmembrane pressure drop). Rautenbach and Schock[40] found that when applied to high molecular weight solutions, the calculated permeate fluxes were somewhat lower than those determined experimentally. In a few cases, the discrepancy was reduced by considering the concentration dependent properties of mass transfer, though the concluding recommendation was that Brownian back diffusion itself was not

29

sufficient and that additional transport mechanisms should be considered. The equation could not be successfully applied to crossflow microfiltration, having under predicted experimental fluxes by a factor of ten.

The conventional film-theory model (above) assumes that the membrane surface is homogeneously permeable and the steady state flux is independent of membrane properties. It assumes that the filtrate flux is dependent on the properties of the dynamic membrane alone and is therefore a function of C_g, C_b, and the solute mass transfer coefficient K_s. Fane[60] introduced an effective free area correction factor (X_e) to account for the non-homogeneity of membrane surfaces and their effect on flux, where X_e is defined as 'the area in the plane of the membrane surface through which the majority of the solvent passes'. He concluded that "the gel polarisation model appears to have physical limitations but still remains convenient from a practical point of view".

1.4.6 Particle Removal Mechanisms for Crossflow Microfiltration

Early Crossflow Microfiltration models were based on the principles of the gel-polarisation model for ultrafiltration and used the Stokes-Einstein equation[61] to predict diffusion coefficients. The filtrate fluxes calculated using this model were however, up to two orders of magnitude below those observed experimentally[59,61]. Green and Belfort[45] called this the 'flux paradox' for colloidal suspensions, but Wakeman and Tarleton[62] point out that this is not a flux paradox so much as the model does not adequately portray the phenomena occurring at and close to the membrane surface. Romero and Davis[33] state that the effect of Brownian back diffusion on larger than sub-micron particles is negligible compared to the permeate drag forces and as such cannot be used alone to account for the back flux of particles. Subsequent models for microfiltration therefore attempt to remedy the discrepancy between theoretical and experimental results using different mechanisms for particle removal. These include back transport mechanisms such as shear-induced diffusion[32,33,42,43,63] and inertial lift[34,45] (lateral migration), and

30

surface transport mechanisms (longitudinal migration) as used in pure convection models[41,64].

1.4.7 Shear Enhanced Hydrodynamic Diffusion

This model supports the theory that diffusion is the primary mechanism for the back flux of particles from the membrane surface, but considers the diffusion to be shear induced rather than Brownian[32,43]. The theory suggests that a crossflowing suspension with sufficient shear, will cause particles at the cake layer/bulk suspension interface to move over each other, expanding the upper portion of the cake and effectively re-suspending the particles, thus allowing them to flow. (This theory is not supported by the visualisation studies of Mackley and Sherman[44] or Wakeman[65], neither of which detected any expansion or re-suspension). The re-suspended particles will move as a result of two different particle interactions[42,43]. Firstly, the particles may rotate, entraining the fluid around them and causing it to circulate, exerting a drag force on neighbouring particles. Secondly, particles flowing with the suspension travel along different streamlines, resulting in small displacements as they pass each other and move out of each other's way. The surface roughness of the particles means that these small displacements are irreversible and result in a net lateral migration (Arp and Mason[66]). This effect is enhanced in the presence of concentrated suspensions (where a greater number of multiparticle interactions result), and by the existence of a concentration gradient across the flow channel. The migration of particles in this way is typical of a random walk process.

Some work has been done, aimed at determining the shear induced diffusion coefficient for this process; initially by Eckstein *et al.*[43] who placed a marked particle in Couette flow and observed its lateral movement across the channel in successive circuits of the Couette cylinder. The authors believed their results to be only a factor of two out.

Leighton and Acrivos[42] however, argued that the error was far greater, especially at higher concentrations. They performed a similar study but instead, recorded the time taken to complete successive circuits of the Couette, effectively measuring the circumferential (longitudinal) distance travelled by the particle. These measurements were analysed using a data reduction procedure which gave diffusion coefficients greater than those reported by Eckstein et al.[43]. They were also found to increase with volume fraction of solids. Despite being reported by the authors as being approximately correct, these results were lower than the effective diffusion coefficients calculated by Leighton and Acrivos[46] which treated particle movement as a result of both self diffusion and random drift (as a result of concentration gradients).

Zydney and Colton[67] used the shear enhanced diffusion coefficients calculated by Eckstein et al.[43] in place of Stokes-Einstein diffusivities to develop the concentration polarisation model for crossflow microfiltration. This fitted the experimental data with greater accuracy than previous models, but comparing the permeate flux velocity with calculated values of inertial lift velocity revealed that the inertial lift force was much less than the permeate flux and could not therefore account for the total back flux of particles. This discrepancy also disputes Green and Belfort's model[45] for lateral migration which proposes that a stagnant cake layer accumulates on the membrane until the inertial lift velocity becomes equal to the permeate velocity, after which no more particles would be deposited.

1.4.8 The Inertial Lift Model

Lokjine et al.[41] state that "the parabolic velocity field existing within the tube flow of a suspension generates a pressure difference across the diameter of a particle flowing in that suspension". This results in a lateral migration of the particle known as 'inertial lift'. The lift force generated is related directly to the particle diameter, thus for typical crossflow microfiltration systems, the inertial lift velocity of these very small particles is much less than the opposing permeate velocity[32]. This

suggests that particles could continue to be deposited until the channel becomes completely blocked although in practice this does not occur.

Studies by Davis and Leighton[32], Altena and Belfort[34] and Wakeman[65] conclude that the inertial lift force (which supplements the Brownian back diffusion) contributes little to the overall back flux of particles and is unlikely to play a major role in the modelling of crossflow microfiltration systems.

1.4.9 Pure Convection Models

Pure convection models[41,64] ignore the 'negligible' effects of shear induced diffusion and inertial lift, and suggestions that particles cease to be deposited on the filter at steady state. It relies on the principle that a particle will start 'rolling' along a filter surface when the drag force exerted on the particle parallel to the membrane, is greater than the pressure force perpendicular to the membrane[39,68]. The drag force parallel to the membrane in this case is provided by the crossflowing bulk suspension, and by this method, the rate of particle deposition is balanced throughout steady state filtration by the shear induced transport of some/all of the filter cake along the length of the filter[41,32,64].

Visualisation studies by Wakeman[65] confirm the existence of this mechanism, although they suggest that it is only the particle layers at the filter cake-bulk suspension interface that tend to move in this manner. In this case, the filter cake is considered to be comprised of a loosely packed upper layer, flowing over a densely packed stagnant lower layer, with the flow rate of the relative particle layers dependent on the rheology of the filter cake.

1.4.10 Semi-Empirical Models

Mikhlin *et al.*[69] developed a semi-empirical model that estimates the resistance of cake formations by assuming that the rate of permeate flux decline is proportional

to the rate of particle accumulation at the membrane surface. This accounts for both the deposition and removal of particles from the membrane surface and was shown by Tarleton[70] to give reasonably good agreement with experimental data. It is however, necessary to measure the flux decline before the model can be used and cannot therefore be used predictively.

Zhenovatyi[47] used a semi-empirical correlation to relate flux decline to the process conditions of a suspension in crossflow where no filter cake is formed. Unfortunately, the application of the model was limited to the filter and filtration conditions used by Zhenovatyi, and comparing derived results with experimental results showed a poor agreement[70].

1.5 VISUALISATION STUDIES

The models for the crossflow microfiltration process present different theories for the mechanisms of particle deposition and removal from a membrane surface, none of which would seem to be remarkably accurate in predicting filtrate fluxes under 'typical' process conditions.

In both cases clarification is necessary, and this can only be done through direct observation of the cake formation process. Mackley and Sherman[44] filmed cake formation (crossflow velocity of 0.25 ms^{-1} and transmembrane pressure drop of 5 kPa) using a video camera at 50 frames/second with 15x magnification. This recorded cake thicknesses in the range 1 to 4mm but limited the lower observable particle size to approximately 125-180μm, well above those generally associated with microfiltration. Hodgson *et al.*[71] photographed suspensions with median particle sizes of 7μm and 20μm, using a light microscope fitted with SLR camera. The photographs were taken from beneath the (transparent) membrane looking up through it, such that no deposition, removal, or determination of cake thickness could be directly observed. They 'observed' however, (contrary to other findings[44,65,72]) that the cakes formed were of the order 1 particle layer thick. Wandelt *et al.*[72] used non-intrusive NMR imaging with resolution 10-20μm to observe the deposition of bentonite particles (median size 0.7μm) in hollow fibre membranes. The imager was aligned such that the cake could be observed developing, and recorded thicknesses of between 30 and 120μm. Although the bulk cake growth could be observed, single particles could not be resolved, and examination of graphical data presented in the paper pointed to the system not having reached equilibrium.

Visualisation studies by Wakeman[65] recorded the movement of particles (mean sizes 0.5-25μm) in suspension (0.1-1.8% volume fraction) at the filter surface for a range of crossflow velocities (1-4ms^{-1}) and pressures (69-276 kNm^{-2}), typical of those used in industry. Cake formation and particle movements could be seen through the toughened glass walls of the filter cell, and were recorded by a high

speed (400 frames/second), high magnification video camera. The camera was positioned to see almost horizontally across the cake layer, at right angles to the bulk flow, and focused close to the centre axis of the membrane so as not to measure wall effects. The permeate flux was monitored for the duration of each experiment in order to obtain simultaneously, observed and measured evidence of particle motion and fouling layer development.

The studies confirmed that the initial rapid flux decline is due to a very high initial particle deposition rate. This is a result of the particles travelling along streamlines which (due to the high interstitial flux of liquid through the clean membrane) have a large velocity component, normal to the bulk flow of suspension, towards the membrane. The high deposition rate leads to a reduced filtrate flux and therefore lower normal velocity component, resulting in a lower deposition rate. This continues until, after a long time, the filtrate flux becomes very low (as does the normal velocity component) and few particles are deposited. Wakeman's studies[65] also showed that few particles rebounded from the cake surface in the pseudo steady state, most rolling along the cake surface after impacting. Some fixed particles on the bed surface were seen to re-mobilise (as a result of the shear) and roll along the bed surface for a number of particle diameters before coming to rest again. Traversing the length of the membrane revealed the cake layer to be approximately uniform in thickness along 90% of its length, the two ends being slightly thinner (about $^3/_4$ thickness). This would suggest that the permeate flux through the filter is fairly uniform and independent of distance along the filter.

Varying the crossflow velocity had different effects on suspensions of different mean particle size. The suspension of larger (25μm) particles formed cakes of increased resistance at higher crossflow velocities resulting in lower permeate fluxes. Although the cake became thinner, it was composed of a disproportionally high percentage of the finer particles from the feed suspension, forming a thinner but more densely packed cake. This was not observed to be a result of hydrodynamic diffusion preferentially removing larger particles from the cake[73]. Instead, the larger particles entering the filter cell appeared to have greater

momentum, making them less susceptible to the drag force towards the filter surface, enabling them to pass straight through the filter cell (Section **1.6.4.2.1**). In any case, only particles entering the cell within 10 particle diameters of the membrane were seen to be deposited on the filter.

Increasing the crossflow velocity of the smaller mean particle size suspension (2.6μm) resulted in an improved filtrate flux. The increase shear thinned the cake layer, reducing its resistance to flow but had little effect on its composition.

The visualisation also revealed that the mechanisms for particle removal from the cake layer are different for different particle size suspensions. The uppermost 3 layers of a cake layer of large particles are seen to form an uneven surface into which particles from the free stream jump in and out of. The smaller particles however are seen to form an immobile layer with an erratically moving (and therefore densely packed) upper layer. Close up studies revealed a 1 deep particle layer rolling continuously, in and out of the dips, along the surface of the membrane.

Increasing the transmembrane pressure drop generally consolidates the cake layer and drives more particles towards the membrane, with the resulting increase in resistance almost completely nullifying any prospective improvement in flux. Suspensions of anatase however, showed an increase in flux with pressure, possibly due to the erratic mode of deposition which results in the particles jostling for position, and forming such a densely packed bed initially that there can be little further consolidation.

1.6 EXPERIMENTAL STUDIES

The experimental studies consider the effects on the filtration process of varying process and system parameters. These can be characteristics of the particles, suspension or membrane (e.g. mean particle size, concentration or pore size), or a change in the process operating conditions (e.g. crossflow velocity or transmembrane pressure drop). Work by Wakeman and Tarleton[62,74-76] reported the results of a great number of experiments carried out under controlled conditions practically applicable to those used in industry. Process parameters were changed systematically, allowing the effect on filtration of each specific parameter to be monitored individually. Consequently, this work provides a comprehensive set of analysed results and has proved to be the primary source of information for this chapter.

1.6.1 The Effect of Particle Characteristics on Filtration

1.6.1.1 Particle Size

Smaller particles are more likely to penetrate the pores of a membrane and foul it internally, increasing its resistance and therefore lowering the flux of filtrate through it.

They may also form a thinner, more densely packed cake than would be formed by an equivalent suspension of larger particles, thus resulting in a higher resistance dynamic membrane that further contributes to reducing filtrate flux. In general then, where all other parameters remain constant, the smaller the mean particle size of a system, the more rapidly its filtrate flux will decline and the lower its filtrate flux will be at steady state (Figure 1.11).
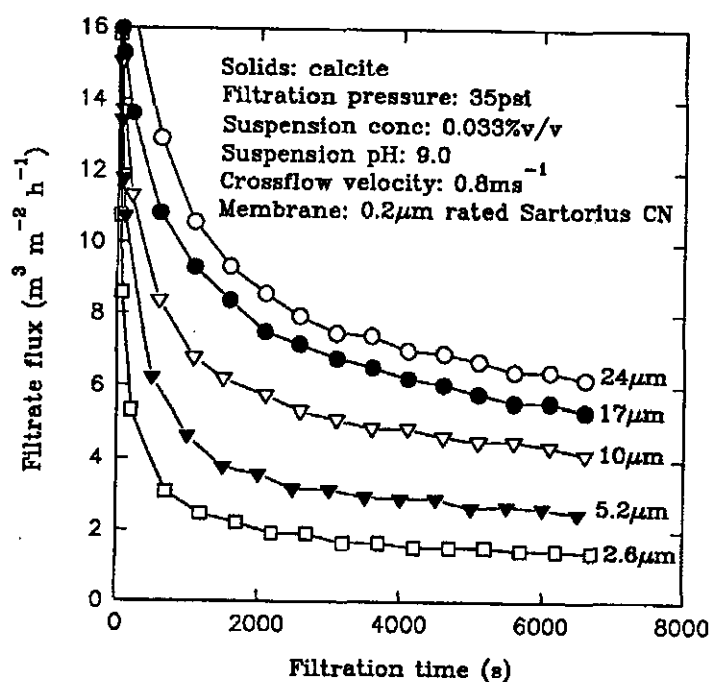
Figure 1.11 The effect of particle size on flux decline for calcite suspensions[74].

1.6.1.2 Particle Size Distribution

Suspensions are most often characterised by a 'mean particle size' with sometimes the smallest and largest 10% particle sizes quoted. The distribution of particle sizes can also be represented graphically as in Figure 1.12. The mean particle size is a good general guide for a comparison of studies, but may be misleading when predicting the performance of a filtration process.

For example, a wide particle size distribution feed suspension, characterised by a mean particle size, is likely to form a higher resistance cake than would be expected from a bed comprised uniquely of the mean size particles (i.e. a lower than expected filtrate flux would be observed). The reason for this being that smaller particles rest between the interstices of larger particles in the filter cake, thus reducing the available free volume through which liquid can permeate (Figure 1.13). This effect is pronounced at lower crossflow velocities, while higher crossflow velocities

encourage the preferential deposition of fines (Section **1.6.4.2.1**) which again result in the formation of a cake with a higher than expected resistance.
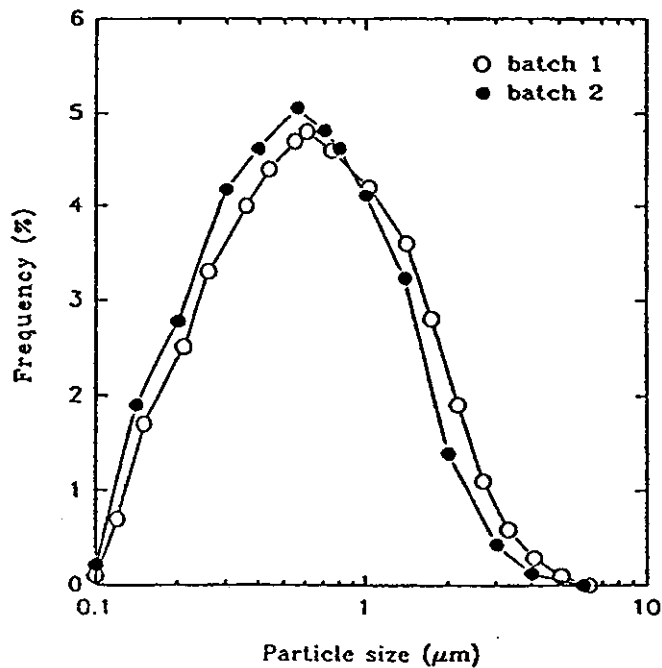
Figure 1.12 Particle size distribution curves for two calcite grinds[62].
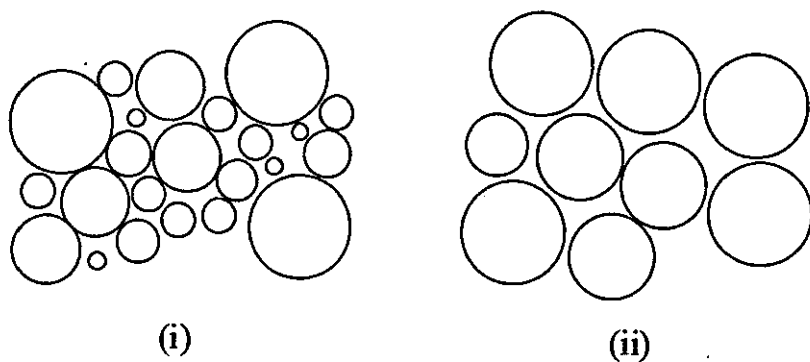
Figure 1.13 Particle packing in filter cakes with (i) a wide size distribution, and (ii) a narrow size distribution.

Wakeman and Tarleton[62] demonstrated the dominant influence of particle fines in microfiltration by adding very small quantities of anatase (mean size 0.5μm) to suspensions of calcite (mean size 24.3μm) and observing significant drops in the level of steady state permeate flux.

Anomalous results such as these demonstrate that, contrary to what Section **1.6.1.1** may suggest, a mean particle size alone can not be relied on to predict the resistance of a filter cake, particularly at higher crossflow velocities (Figure 1.14). As a result, Tarleton and Wakeman[74] recommended that feed suspensions should be classified by a particle diameter more representative of their potential fouling capability, i.e. one that is smaller than the mean particle size.
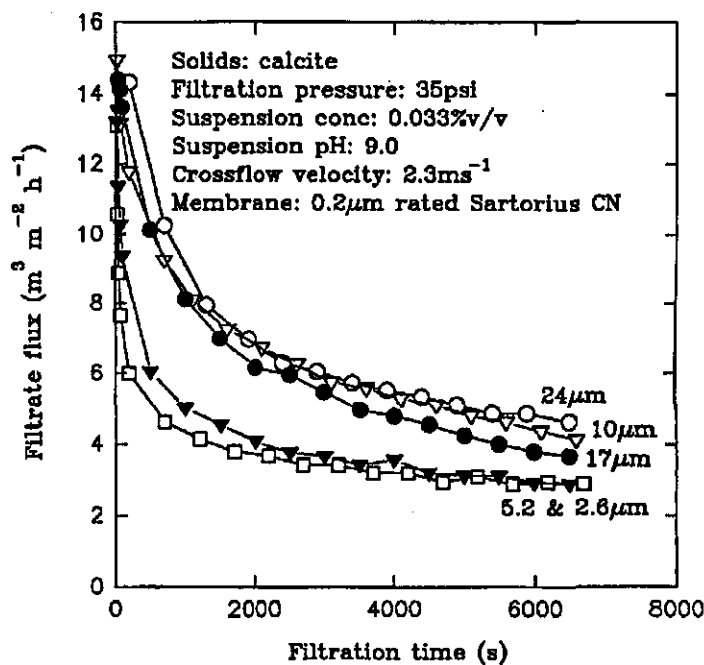
Figure 1.14 The effect of the preferential deposition of fines at higher crossflow velocities on a range of suspensions with different particle mean sizes and size distributions[74].

41

1.6.1.3 Particle Shape

Quantifying the effects of different particle shapes on filtration performance is difficult for a number of reasons. Fundamentally, the nature of the different solids governs their shape, making it virtually impossible to reproduce in another material. Even mild comparisons between different shapes of similar size are difficult to make, as a representative particle size can not be easily identified. Finally, without a universally accepted method of particle shape classification, any predictions that could be made are less easily applied to other systems.

Some particle systems however, have a definite effect on filtration performance. For example, china clay particles (the shape of which is described as 'flat platelets'[62]) orientate themselves parallel to the membrane surface, to form a high resistance cake layer. Compared to spherical particles, the inter-particle contact area is much greater, reducing the interstitial volume of space through which liquid can flow.
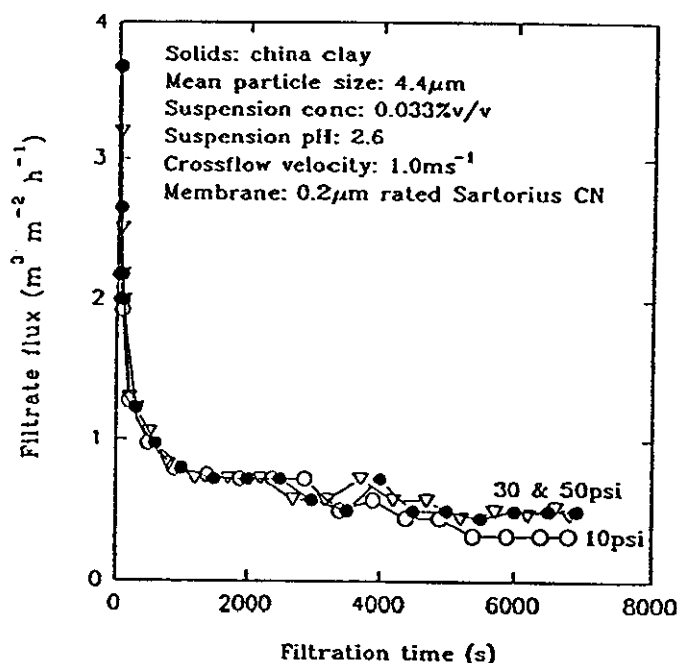
Figure 1.15 The effect of transmembrane pressure on crossflow filtration of china clay suspensions[62]

Figures 1.15 and 1.16 exemplify the effect of tight packing china clay particles. The 4.4μm china clay platelets pack so tightly, that under similar operating conditions, the associated flux decline rate and steady state flux are comparable to the much smaller 0.5μm anatase particles.
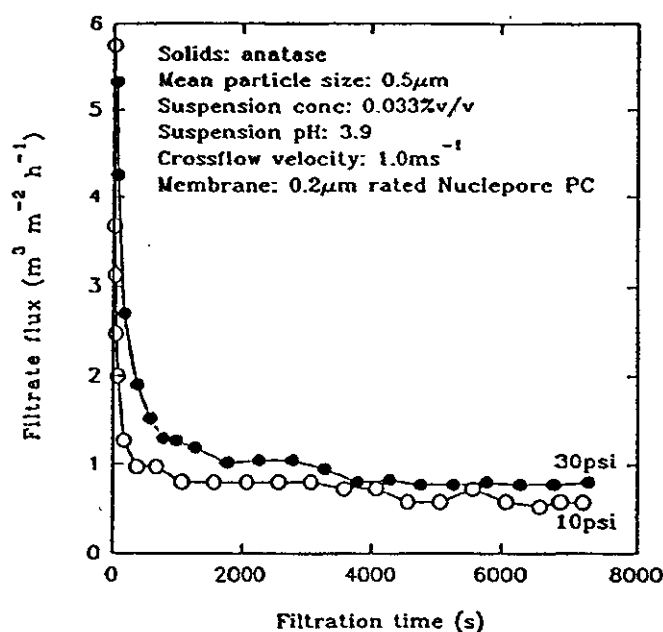
Figure 1.16 The effect of transmembrane pressure on crossflow filtration of anatase suspensions[62]

The china clay platelets pack so tightly, that neither increases in suspension concentration or transmembrane pressure drop affected the permeate flux, i.e. there was no room for consolidation of the cake layer. The influence of this particular shape can therefore be demonstrated, but it can not be easily predicted.

1.6.2 The Effect of Suspension Characteristics on Filtration

1.6.2.1 Solids Concentration

Feed suspensions containing a high percentage of solids by volume produce a greater flux of particles to the filter than would a low solids concentration suspension. This results in a more rapid establishment of the cake layer and with it the steady state filtrate flux, which is often at a lower level than would be experienced with a lower concentration suspension (Figure 1.17).
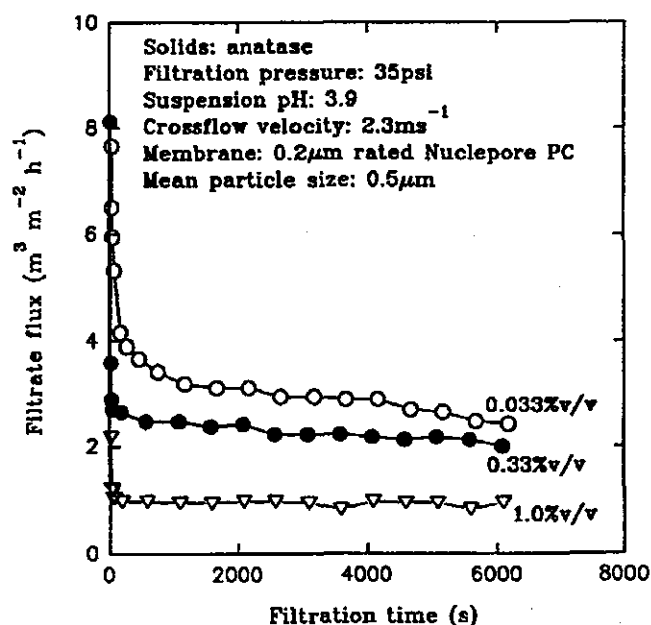
Figure 1.17 The effect of anatase feed solids concentration on flux decline[75].

The higher solids concentration feed streams show a preference for particles bridging membrane pores while more dilute streams exhibit a more significant degree of pore plugging[45]. This results in a reduced resistance to permeate flow by the membrane, but an increased resistance to flow by the filter cake. Thus at steady

state, the membrane merely provides a support for the filter cake/dynamic membrane, which itself provides the controlling resistance to permeate flow.

Comparing flux decline rates for different solids concentration suspensions of china clay reveals that while they are initially different, they become similar for longer filtration times (Figure 1.18). This appears to be an effect of the particle shape and packing, which provides a disproportionately high resistance to permeate flow at low feed solids concentrations (compared with anatase), but that does not reduce further as the feed solids concentration is increased 60 fold.
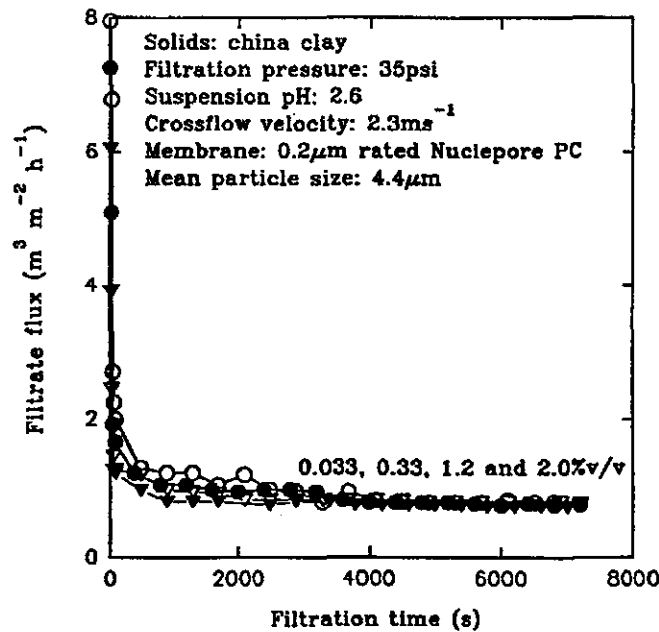
Figure 1.18 Different concentration suspensions of china clay tend to the same steady state flux[75].

1.6.2.2 Suspension pH

The effect on filtration of changing the pH of a suspension depends on the size and Zeta potential (Section 1.2.6) of the particles within it. For example, calcite has a large median size and a low Zeta potential, so the effect on inter-particle interactions is negligible, and hydrodynamic forces dominate the formation of the cake layer. A suspension of anatase however (small median size particles with

relatively high Zeta potential) is affected significantly by the increased surface charge, especially at higher concentrations. The resulting very small, highly dispersed particles will tend to block pore throats, and form a high resistance cake layer (Section **1.4.2**).
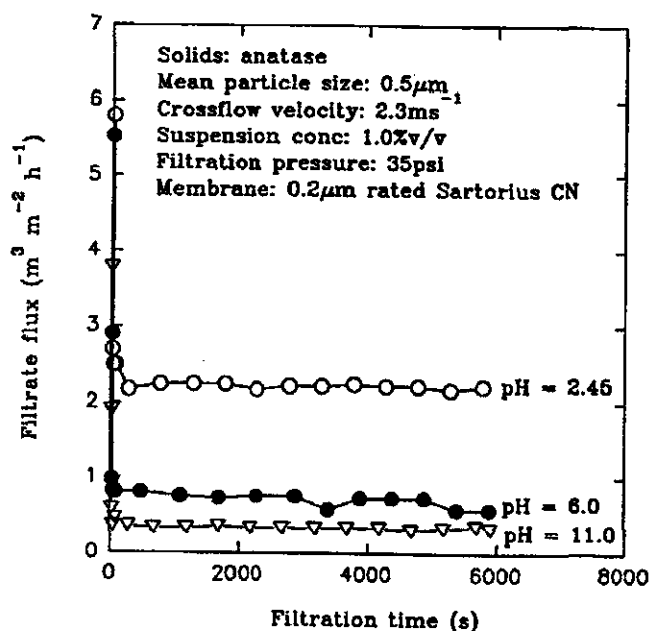
Figure 1.19 The effect of pH on flux decline for anatase suspensions (IEP is approx. pH 2.45)[75].

Experimental results suggest that suspension pH should be adjusted to encourage a low surface charge, thus attaining the largest size particles possible. This will result in reduced membrane fouling and a lower resistance filter cake.

1.6.3 The Effect of Membrane Characteristics on Filtration

Polymeric microfiltration membranes are characterised by pore size and distribution, topography (pore shape), membrane cross section, clean water flux/permeability, and contact angle.

The criteria for membrane rating varies from manufacturer to manufacturer, whereby two different membranes with the same pore size rating may exhibit radically different mean pore sizes and pore size distributions. Wakeman and Tarleton[62] and Tarleton and Wakeman[76] have compared different membranes with similar (manufacturer stated) pore size ratings and show that they gave different flux performances although the filtrate quality seemed unaffected. There was no evidence to suggest that the different fluxes resulted from adsorption, the different membrane materials or membrane/particle surface charge effects, so it would appear, primarily, to be due to the mechanical interaction of particles and membrane at the membrane surface (the cake formation mechanisms).
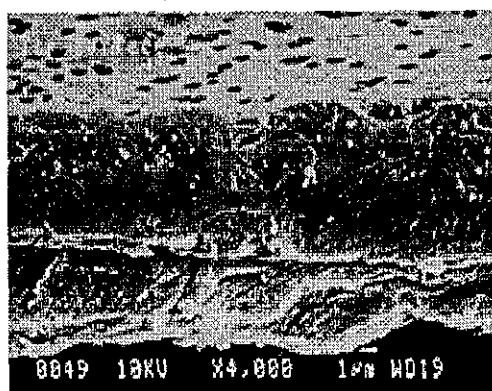
Figure 1.20 The cross section through a 1μm rated Nuclepore PC (polycarbonate) membrane[74]

1.6.3.1 Membrane Morphology

Polymeric membranes for use in crossflow microfiltration processes exist in various forms, largely a result of the different manufacturing processes used. Nuclepore PC (polycarbonate) membranes, for example, offer a flat surface containing a random pattern of cylindrical pores of uniform diameter (Figure 1.21). These are produced by firing radiation nuclei at a thin, hydrophilic, polycarbonate film to produce consistent, highly defined pore sizes[77].
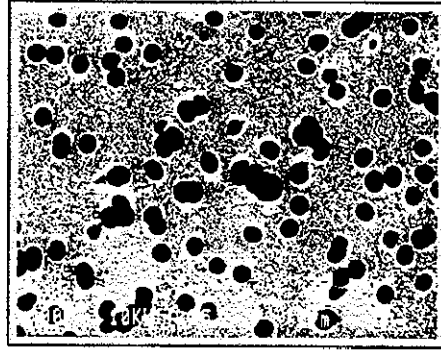
Figure 1.21 The topography of a 1μm rated Nuclepore PC membrane[62]
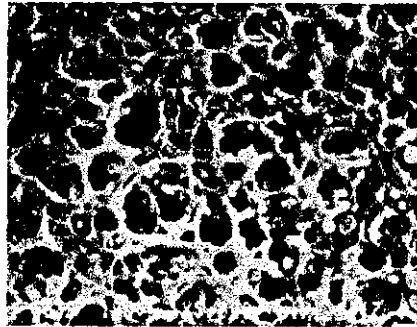
Figure 1.22 The topography of a 1.2μm rated Sartorius CN membrane[74]

Alternatively, Sartorius CN (cellulose nitrate) membranes are formed via a wet casting process, which results in a homogenous, matrix of interconnected pores or tortuous structure (Figure 1.22).

Hydrophobic membranes affect the initial stages of filtrate flux decline, the initial wetting of the membrane resulting in an increase in flux from zero to a maximum value, followed by the typical flux decline curve.

1.6.3.2 Pore Size

The effect of varying the membrane pore size on a filtration process will depend on the size distribution of particles in the feed suspension, as it is the overlap of particle and pore sizes that determine the most likely fouling mechanisms. Where the largest pore sizes are smaller than the smallest particle sizes, membrane fouling (penetration of the pores) is negligible and the filtration flux is determined by the resistance of the cake layer. Wakeman and Tarleton[62] have shown that for a given feed suspension, the rate of permeate flux decline and steady state permeate flux values are virtually independent of pore size as long as the pores are smaller than the particles, but not so small as to restrict permeate flow. Slightly increasing the pore size makes the membrane more susceptible to fouling by the smaller particles in the feed suspension. These become trapped in the pore throats, reducing the available area for permeate to flow through, thus decreasing the filtrate flux. Where the pore sizes are much larger than the particles, there is an improvement in the steady state level of flux but at the cost of the filtrate quality.

Logically, the larger mean pore size membranes, and those with a wide pore size distribution are more likely to be internally fouled by finer particles in the suspension feed. This effect is however reduced in the case of higher concentration suspensions, where the increased flux of particles to the membrane promotes pore bridging and thicker cakes. In these cases, the permeate flux decline and steady state is dependent more on the cake layer resistance with the membrane itself acting only as a support.

1.6.3.3 Asymmetric Membranes

Asymmetric membranes such as the Domnick Hunter Asypor (Figure 1.23) attempt to combine the benefits of a small pore size membrane (high retention coefficient) with a large pore size membrane (lower pressure drop), by presenting a surface of relatively small pore entrances to the feed suspension, whilst providing a relatively

large volume of pores for the exiting permeate. Some of the pores may block, but the good lateral connectivity between them helps maintain a high flow rate of permeate.
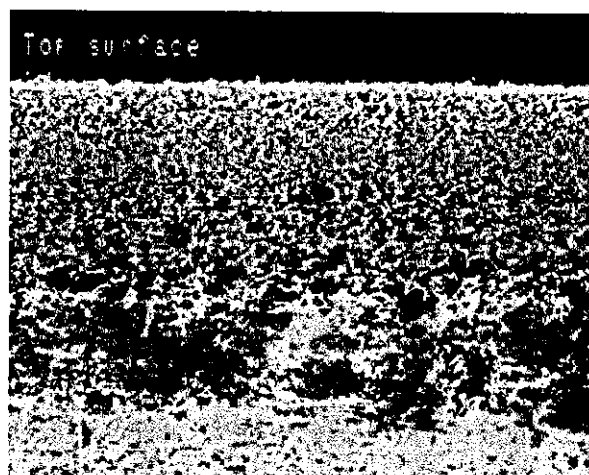
Figure 1.23 The cross section through an 0.8μm rated Domnick Hunter Asypor membrane[76]

1.6.3.4 Membrane Surface Charge

Tarleton and Wakeman[76] demonstrated that membrane surface charge has a negligible effect on the fouling rate of particulate feeds, incurring changes in flux so small that they could be attributed to other factors such as the membrane structure. Molecular/ionic components however, can be absorbed at the membrane surface, making the degree of fouling more sensitive to changes in surface charge.

1.6.4 The Effect of Process Parameters on Filtration

1.6.4.1 Transmembrane Pressure

This is the difference between the pressure in the feed suspension and that in the permeate, with quoted values often averaged along the length of the filter.

Increasing the transmembrane pressure encourages consolidation of the filter cake and additional particle deposition, the result being a higher resistance cake layer that can, to some extent, offset the potential improvements in permeate flux. Experiments by Tarleton and Wakeman[75] using suspensions of anatase, calcite and china clay reveal that the increase in cake resistance is largely dependent on the nature of the particles and their respective packing mechanisms.
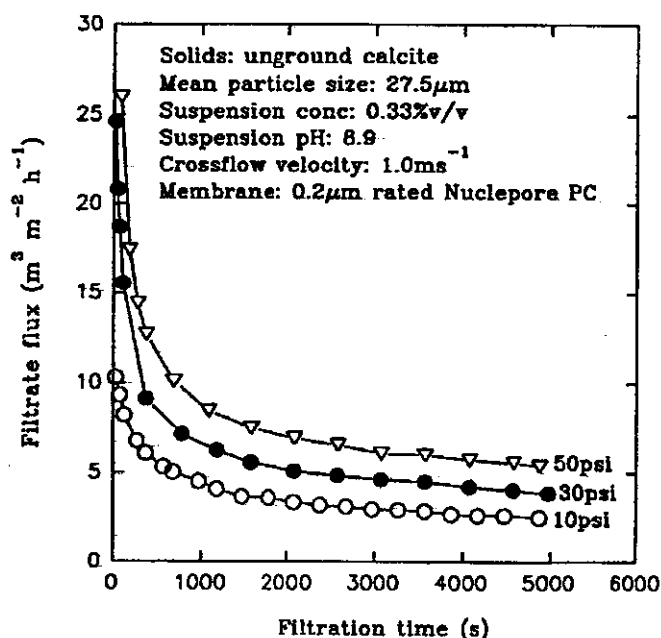
Figure 1.24 The effect of transmembrane pressure on permeate flux[75]

51

As a result of their shape (which lends itself well to compaction under pressure) china clay suspensions (Figure 1.15) demonstrated virtually no improvement in steady state flux with increasing transmembrane pressure. Permeate flux decline curves for 2.7μm calcite suspensions (Figure 1.24) and flocculated 0.5μm anatase suspensions (Figure 1.16) however, show a significant increase in steady state flux with increasing transmembrane pressure, although the gain in flux seems to be reduced for successive pressure increases.

1.6.4.2 Crossflow Velocity

Raising the crossflow velocity of the feed suspension increases the shear stress parallel to the membrane surface and thus generally leads to a thinning of the cake layer[65]. The associated reduction in cake resistance results in an increased steady state permeate flux.
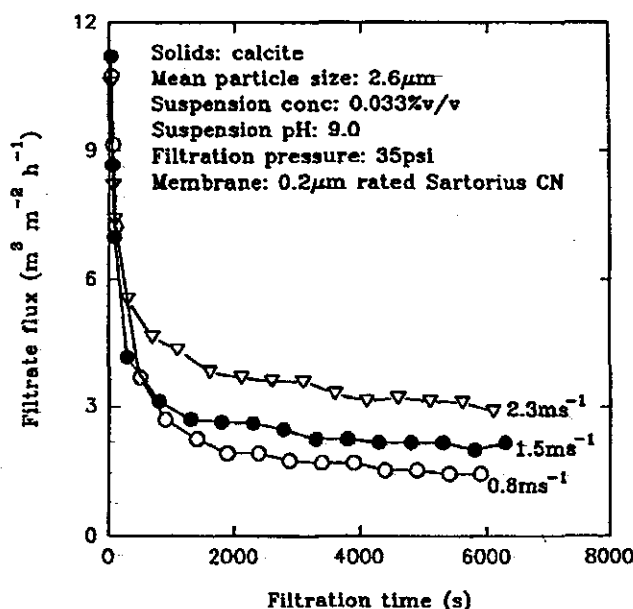
Figure 1.25 The effect of crossflow velocity on the filtrate flux of ground calcite suspensions[75]

There are some exceptions to this trend however, for example where a wide particle size distribution suspension is being filtered (Section **1.6.1.2**) and the increased crossflow velocity promotes the preferential deposition of fines. This results in the formation of a thinner but more densely packed filter cake, which will, if its specific resistance is high enough, lead to a reduction in steady state permeate flux as crossflow velocity is increased (Figure 1.27).
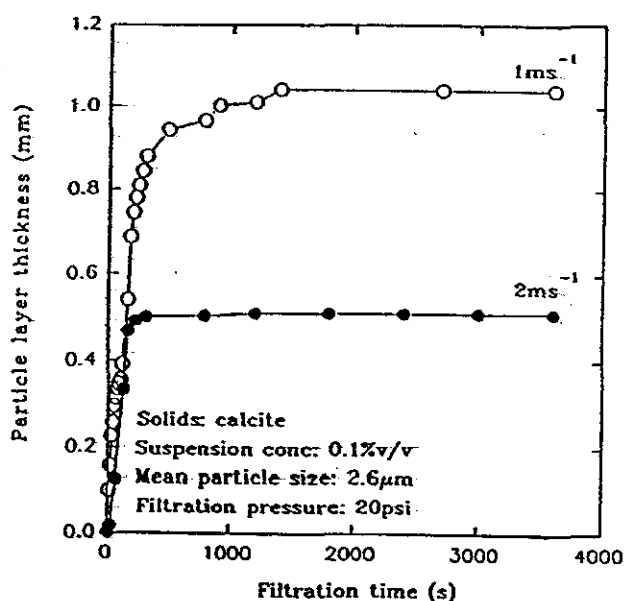
Figure 1.26 The effect of crossflow velocity on cake layer thickness[62]

1.6.4.2.1 The Preferential Deposition of Fines

The preferential deposition of finer particles in crossflow filtration can be explained by considering the momentum of the particles entering the filter cell. Larger particles with greater momentum will tend to continue in a straight line through the cell whereas smaller particles with less inertia are more readily dragged off their streamlines, following the flux of suspension to the membrane surface (Figure

53

1.28). This hypothesis is confirmed by visualisation studies of cake formation in crossflow microfiltration[65].
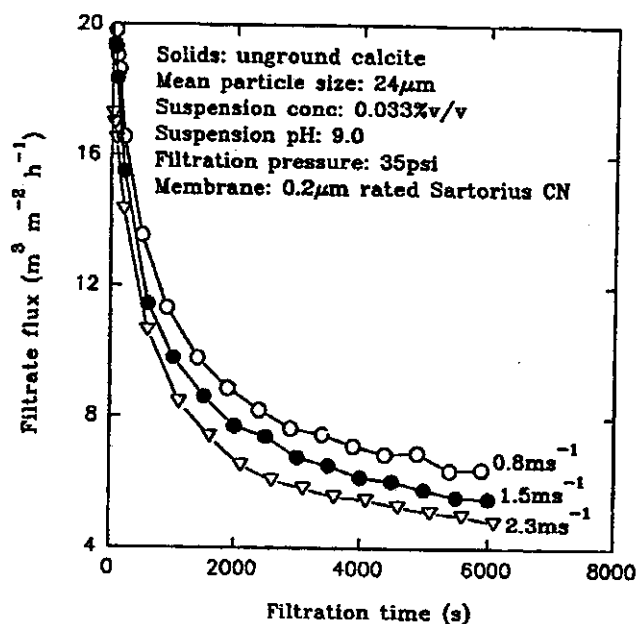
Figure 1.27 The effect of crossflow velocity on a wide size distribution suspension of calcite[75]

1.6.4.3 Temperature

Lokjine *et al.*[41] note the effect of temperature on the crossflow filtration of cell suspensions. They found that increasing the suspension temperature reduced the viscosity of the continuous phase, resulting in a greater filtrate flux through the membrane.
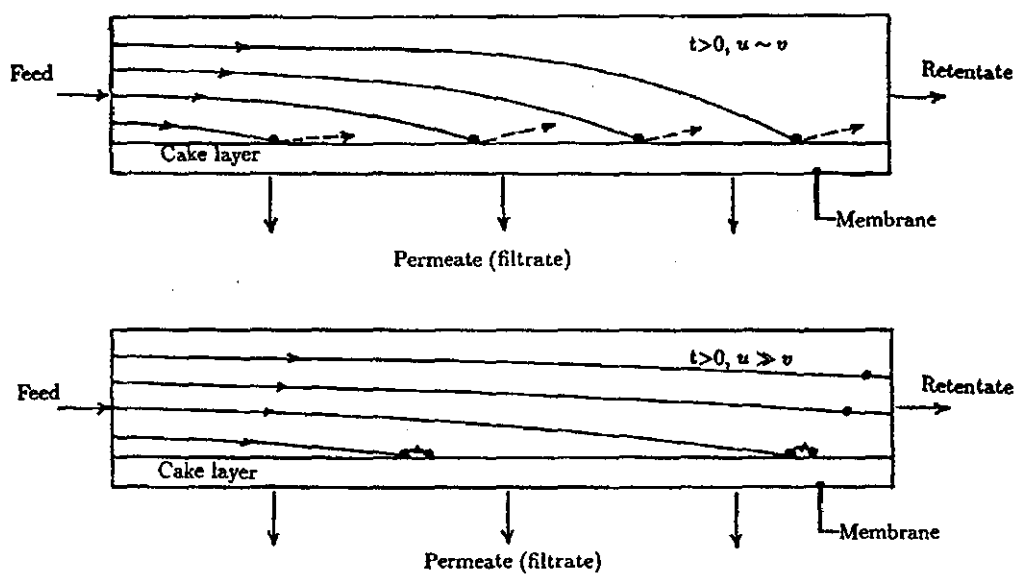
$$v = FiltrateFlux\left(\frac{cm^3/s}{cm^2}\right)$$

$$u = CrossflowVelocity(cm/s)$$

Figure 1.28 Particle flow through a crossflow filtration cell[65]

1.7 PUBLISHED WORK IN RELATION TO TITANIA SUSPENSIONS

Titanium dioxide exists as small particles with a high surface charge, either in the form of rutile crystals (0.17-0.24μm) or the marginally smaller anatase crystals (0.14-0.17μm)[1]. As with other systems of small highly charged particles, the surface chemistry and environmental conditions can significantly effect the behaviour of titanium dioxide in suspension.

Titania being representative of a number of similar particle systems, Wakeman and Tarleton[62] used anatase to study the effects of different process operating conditions during crossflow filtration. These studies include the characterisation of the particles as well as the effects of changing process parameters (such as crossflow velocity, transmembrane pressure drop, suspension concentration, and suspension pH) on permeate flux decline.

1.7.1 Particle Characterisation

Particle size distribution analysis[62] gave the anatase in aqueous suspension a particle mean size of approximately 0.55μm, which is much larger than the crystal sizes quoted above (from the Tioxide literature[1]). Electron microscopy revealed that the anatase crystals were not fully dispersed in water, and that the particle size measured was in fact that of an agglomeration of much smaller particles.

The high surface charge of anatase makes it very sensitive to changes in pH, and measurements of Zeta potential across the pH range (Figure 1.29) showed the IEP to lie around pH 3.9, with a peak surface charge around pH 9.0. This suggests that an anatase suspension will remain well dispersed around pH 9.0, gradually agglomerating as the pH is reduced to the IEP.
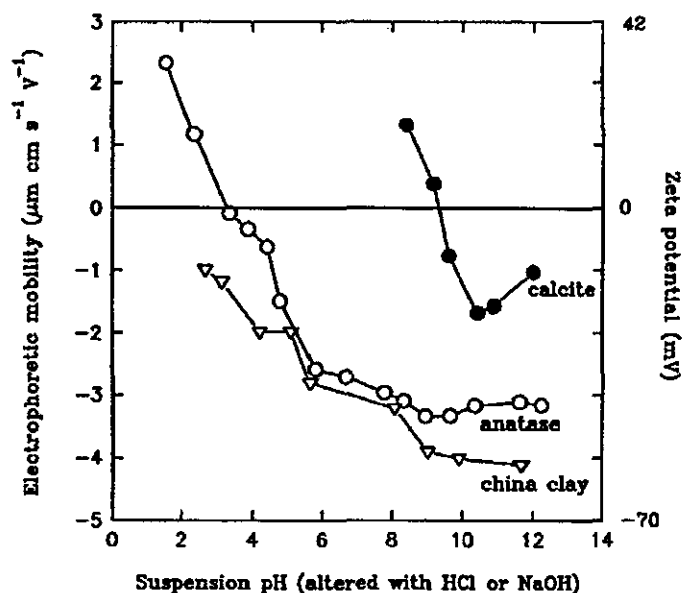
Figure 1.29 Zeta potential vs. pH for suspensions of anatase, calcite and china clay[75]

1.7.2 Effect of Process Parameters on Filtration of Titania Suspensions

1.7.2.1 Transmembrane Pressure Drop (10-50psi).

There were differences in the response of high and low pH suspensions to increasing transmembrane pressure[62,75]. At the IEP (pH 3.9), particles agglomerated and thus formed higher voidage cakes when packed, which gave a slight improvement in filtrate flux at higher pressures (Figure 1.16). At pH 9.0 however (Figure 1.30), the well dispersed particles exhibit a much reduced flux at 10psi (compared with the suspension at the IEP), and a flux approaching zero for pressures greater than this. This is due, in part, to a more significant percentage of fines penetrating and fouling the membrane pores at this pH, although at higher pressures the filter cake appears to pack very tightly. This was confirmed by dead-end filtration tests[62], which showed that cakes composed of well dispersed anatase particles were more compressible than those of agglomerated particles.
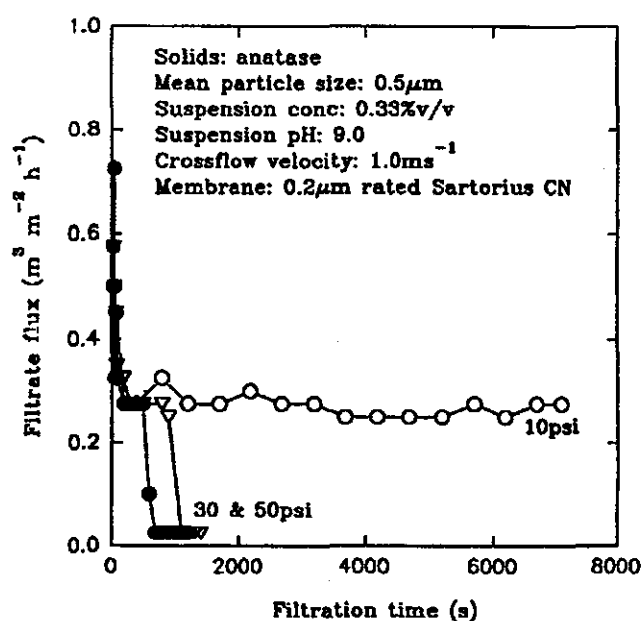
Figure 1.30 The effect of transmembrane pressure on well dispersed anatase suspensions[75]

1.7.2.2 Crossflow Velocity (0.8-2.3ms^{-1})

Raising the velocity of the crossflowing suspension led to a general increase in the level of steady state filtrate flux, although the improvement was greatly reduced for the well dispersed suspension (Figures 1.31 and 1.32).

The well dispersed, smaller, particles are more likely to foul the membrane and will form a more densely packed cake than particles in an equivalent suspension at the IEP. The increased shear stress does not aid the removal of particles from the membrane pores, and has a reduced effect on the rate of particle removal from a tightly packed cake. Thus, raising the crossflow velocity in this case leads to relatively smaller improvements in filtrate flux.
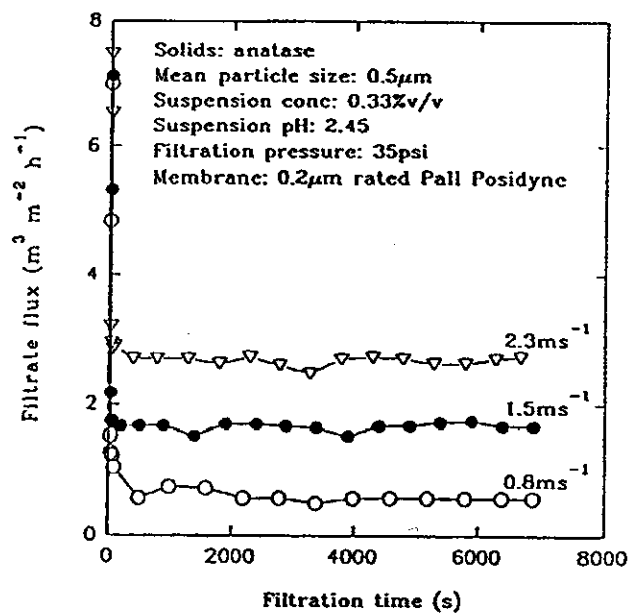
Figure 1.31 The effect of crossflow velocity on agglomerated anatase suspensions[62]
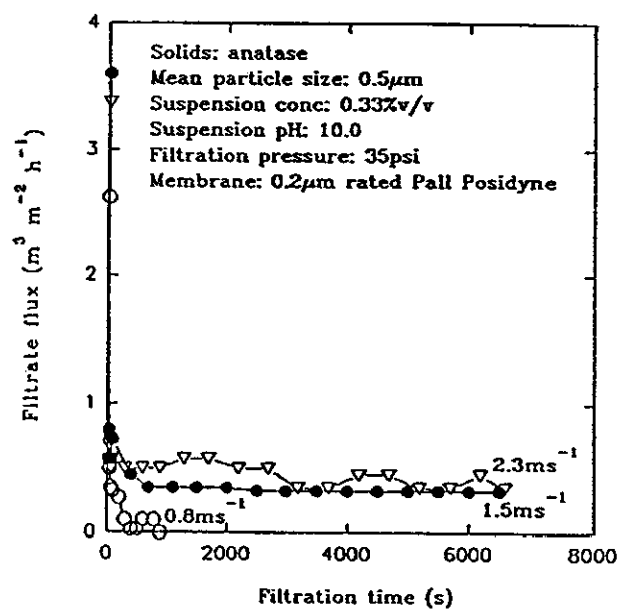
Figure 1.32 The effect of crossflow velocity on well dispersed anatase suspensions[62]

1.7.2.3 Suspension Solids Concentration (0.033-1.0% $^v/_v$ solids)

Raising the suspension solids concentration (and therefore the flux of particles to the membrane surface) results in a more rapid establishment of the steady state flux and at a reduced level (Figure 1.17). The higher concentration also means that particles are in closer proximity, and the effects of particle-particle interactions will be more evident (rheological effects for example).

1.7.3 Filter Cake Formation

Visualisation studies by Wakeman[65] used a high magnification, high speed video camera to observe filter cake formation during the crossflow filtration of an anatase suspension (Section 1.5). While the particles closest to the membrane remained immobile, those in contact with the flow of bulk suspension rolled along the top of the cake, jostling for position before eventually depositing themselves comfortably within the cake layer. This mode of deposition results in a very densely packed bed, such that increases in the transmembrane pressure drop do little to consolidate it further.

1.7.4 Filter Cake Composition

Baker *et al.*[73] investigated the specific cake resistance and composition of filter cakes formed during the crossflow filtration of anatase suspensions and compared them to those obtained from an equivalent dead-end filtration process. Preliminary experiments compared the specific cake resistance of cakes formed under steady state crossflow filtration after 5, 15, 30, 45 and 60 minutes. At the nominated time, the equipment was stopped, the filter module isolated and drained, and the deposited cake removed by backflushing the filter with permeate. The collected cake was dried and weighed, and each experiment was repeated up to five times to

improve the accuracy of results. The specific resistance (α) was calculated using Carman's equation[78].

$$\alpha = \frac{180(1-\varepsilon)}{\rho_p d_p^2 \varepsilon^3}$$

(1.16)

Where ρ_p is the particle density, d_p the particle diameter, and ε the cake voidage. The feed suspension had a particle mean size of 3.2μm, and in each case was filtered with an average transmembrane pressure drop of 80kPa, crossflow velocity of 3.0ms^{-1} and a temperature of 28°C.

As expected, the increasing cake mass resulted in a decline in the permeate flux. The specific cake resistance however, remained constant, starting only to increase as the permeate flux reached (pseudo) steady state (i.e. the flux continued to decline but at a much lower rate). Analysis of the cake compositions at steady state revealed that the continued decline was due to a collection of fines within the cake, increasing the specific cake resistance.

The second set of experiments examined the effects of transmembrane pressure drop and crossflow velocity on the specific resistance and composition of a filter cake formed in 30 minutes crossflow filtration of an anatase suspension (mean particle size 1.5μm).

Plotting the specific cake resistance against transmembrane pressure drop (Figure 1.33) revealed that:

1. The cake formed in the crossflow filter had a specific cake resistance at least twice that of the cake formed under the same pressure in a dead-end filter.
2. A minimum specific cake resistance existed at about 85kPa.

Cake composition analysis showed that a cake formed with a transmembrane pressure drop of about 85kPa also had the minimum fines content.

The authors[73] define this as the critical pressure which apparently divides a fine line between two mechanisms, both of which lead to the preferential deposition of fines. At lower pressures, the convective flux of material to the filter surface is said to be too low for larger particles to overcome their lateral migration back into the bulk stream. Thus, the fines content of the cake (and therefore specific cake resistance) increases with decreasing pressure, while at higher pressures, the high flux of particles to the filter surface means a greater scope for fines capture in the filter cake. Thus, the specific cake resistance also increases for pressures above the critical pressure. Data in Figure 1.33 shows that this theory is based on a fairly narrow range of conditions, thus the existence of a critical pressure with minimum specific cake resistance can not be confirmed from this data alone.
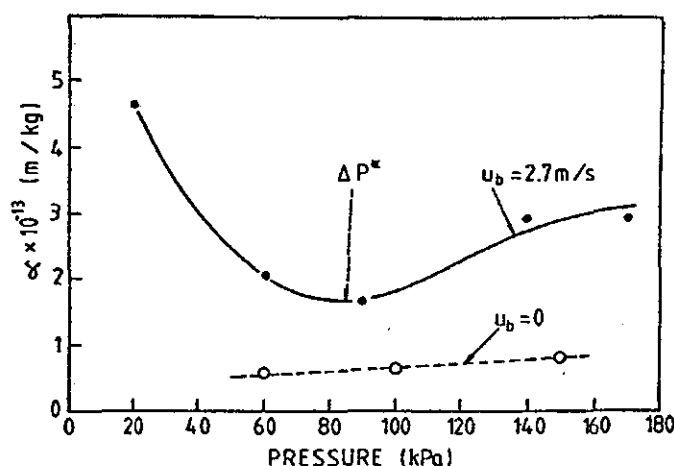
Figure 1.33 The effect of pressure on specific cake resistance for cakes formed in 30 minutes on a crossflow filter ($U_b=2.7ms^{-1}$), and a dead-end filter ($U_b=0ms^{-1}$). (U_b=The crossflow velocity of the suspension)[73]

Increases in the crossflow velocity (0 to $5ms^{-1}$) resulted in an improved filtrate flux and a corresponding decrease in cake mass. The authors explain the thinning of the cake layer using the lateral migration model to account for the removal of the larger

particles within it, (although it is acknowledged that this could also be a result of scouring/erosion). The increased fines content of cakes formed at higher crossflow velocities result in a significant increase in the specific cake resistance such that, at 3.6ms^{-1}, it is four times that of the equivalent dead-end filtration cake. The increased specific resistance is also likely to be a result of the manner in which the filter cake is deposited, as described in Section **1.7.3** above.

The results of this study generally corroborate the findings of visualisation studies[58] and experimental studies by Wakeman and Tarleton[62], i.e.:

That the filtrate flux decreases with time until it reaches a 'pseudo steady state' where, as a result of continued fines deposition, the flux continues to decrease but at a much slower rate.

That increasing the crossflow velocity leads to a higher filtrate flux and a thinner more densely packed cake.

CHAPTER TWO

EQUIPMENT AND EXPERIMENTAL METHODS

The two main areas of experimental study in this work have been a series of crossflow filtration experiments using suspensions of titanium dioxide, and a characterisation of these same suspensions.

The principal objective of the filtration experiments was to examine the effects of process parameters on the permeate flux at steady state, and this was achieved by varying, and observing the effects of each parameter individually whilst maintaining all others constant. It was thus essential to have control over all variables, and to this end all the titania used in this study was manufactured by Tioxide in a single batch. This minimised any deviation due to surface chemistry effects, which may have been of concern had particles in the feed suspensions been the product of a variety of coating procedures.

The titania (rutile) powder was supplied in 25kg bags, and dispersed on site to a mean particle size of 0.32μm (measured on the Malvern Mastersizer). This provided the flexibility to make up the desired quantity of suspension, at the chosen solids concentration, whenever necessary. It was however, critical that the specified particle mean size be obtained, and that the dispersion process be repeatable, to ensure that the feed material for each experiment was characteristically similar.

The characterisation study of the rutile used in these experiments included measurements of particle size distribution and Zeta potential as a function of pH, and viscosity measurements as a function of pH, solids concentration and shear rate.

This chapter describes the apparatus used in the dispersion, characterisation, and filtration studies outlined above. The function, operation and, where relevant, calibration and cleaning procedures have been explained with reference to the titania suspensions used in this study.

2.1 SUSPENSION CHARACTERISATION

2.1.1 Use of Ultra Pure Water

Ultra pure water was used to produce the titania dispersions, to dilute feed suspensions in the crossflow microfiltration rig, and for the preparation of samples for characterisation. The water was obtained from a Millipore MilliRX20 water purification system which produces water low in ionic, organic (>100NMWL), bacterial and particulate contaminants (typically >99% rejection), and with conductivity below $10\mu s$[79].

Potable water is pumped to a reverse osmosis (RO) membrane, which removes the bulk of contaminants, and then on to an electro de-ionisation module which reduces the ionic content. Pre-treatments protect the RO cartridge from attack by particles, free chlorine and mineral scale. A 250 litre tank stores the cleaned water, which is pumped on demand to a tap.

2.1.2 Particle Size Measurements

A Malvern MS20 Mastersizer was used to measure the particle size distribution in the titania suspensions. Particle size was used in the characterisation study to determine the effects of surface charge on flocculation/agglomeration, and also to measure the degree of dispersion achieved by the methods used in Section **2.2**. Throughout the filtration experiments, particle size measurements were used to ensure that the feed suspensions had been adequately dispersed, and to observe any changes in suspension mean particle size during filtration.

Samples are measured by firing a laser at a dilute suspension of particles, and focussing the resulting scatter of light onto a sensor (Figure 2.1). The degree of light scattering is dependent on the particle size distribution, and the light scattering characteristics of the material being sampled. Operation of the Mastersizer is via a

computer, which also stores and analyses the data provided by the light sensor. Repeated measurements are taken rapidly, and the computer calculates the particle size distribution, via an algorithm that incorporates a presentation factor to account for the scattering characteristics of the material. The lens and focal length are selected to be appropriate to the size of particles in the suspension, and the presentation factor is obtained from the Mastersizer instruction manual[80].
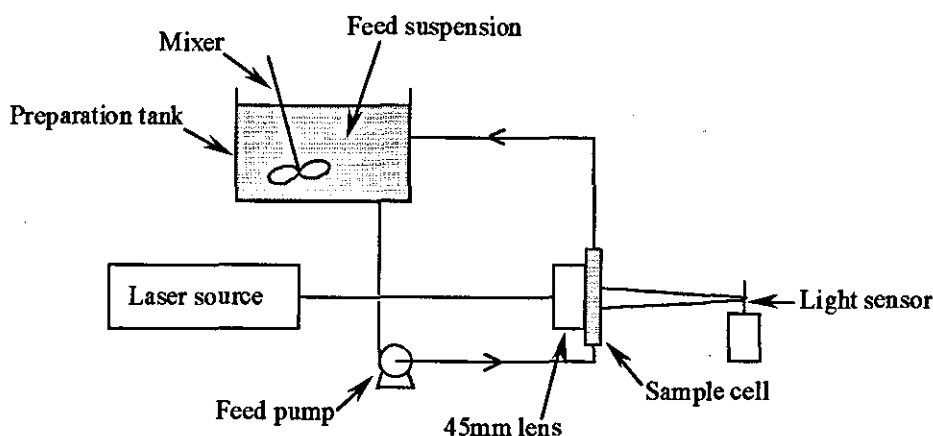
Figure 2.1 Schematic of the Malvern Mastersizer

The Mastersizer was used with a 45mm lens and a presentation factor of 2209 (as used by Tioxide). The preparation tank was fed with Millipore de-ionised water, and results were plotted as a volume distribution curve with particle size on a log scale (0.1 to 100μm).

Before introducing any suspension to the preparation tank a background reading was taken. Having set the stirrer speed to 80% and pump speed to 60%, a small sample of suspension was added to the preparation tank using a disposable pipette. The sample concentration was monitored by the computer, and suspension was added until the loading (concentration of particles) in the preparation tank was sufficient to

register 'ideal'. A sample was then measured and the preparation tank flushed and rinsed ready for the next reading.

When sizing particles at the extremes of the pH range, where dilution in the preparation tank may have had some effect on the particle size distribution, the pH of the water in the preparation tank was altered to that of the suspension prior to adding the sample.

2.1.3 Zeta Potential Measurements

The Zeta potential was measured for different pH suspensions as part of the characterisation study, and the data plotted to indicate the tendency of particles to agglomerate at a given pH.

The Malvern Zetamaster measures the electrophoretic mobility of particles in a suspension, using a laser and light sensor to detect charged particles moving through an applied electric field. The speed with which the particles move is related to their surface charge, which is in turn related to the Zeta potential (Section 1.2.6). The Zetamaster was computer controlled, fitted with a Mettler DL21 auto titrator (filled with 0.1 molar hydrochloric acid and 0.1 molar sodium hydroxide), and a 250ml glass flask for the feed suspension. Half a litre of cloudy, calgon dispersed titania suspension was made, 250ml for the acid side measurements, and 250ml for the base side.

Having filled the feed vessel, the range of pH to be covered and the number of samples required was specified to the computer. The auto titrator then adjusted the pH of the feed suspension accordingly, and removed samples for measurement of Zeta potential. Both the pH and Zeta potential were recorded automatically on the computer. Once completed, a new 250ml sample was placed in the feed vessel and the other side of the pH range examined.

2.1.4 Measurement of Suspension pH

Suspension pH was measured with a Griffin model 80 pH meter (Griffin & George Ltd. G.B) with a plastic bodied, gel filled, combination electrode The meter was calibrated using buffer solutions of pH4, pH7 and pH9.2. The probe was rinsed with ·Millipore de-ionised water between readings and stored in a pH 7 buffer solution.

When measuring a large volume of concentrated titania suspension, the sample was first mixed with a steel stirring rod to ensure that the measurement was representative of the suspension as a whole. After measurements, the probe was placed in an ultrasonic bath to remove traces of titania before rinsing and replacing it in storage.

2.1.5 Rheological Measurements

Rheological measurements were made using a Carrimed CS100K controlled stress rheometer with both concentric cylinder (Figure 2.3) and cone and plate (Figure 2.4) configurations. It was connected to a water supply for the Peltier temperature control unit, and an air supply at 40psi to feed the air bearing and pneumatic ram. A computer, supporting Carrimed software, controlled the application of shear rate to the suspension and monitored the resulting shear stress.

The upper part of the configuration (Perspex cup or stainless steel cone) was linked to a variable torque motor (0-10000 mPa) by a rotating shaft, mounted on an air bearing. The base plate remained stationary and was sited on a pneumatic ram, which could be lowered and raised to facilitate placement of the suspension into the configuration. The base plate took on the role of the plate in the cone and plate configuration, and it contained the Peltier temperature control system, which regulated the temperature of the suspension resting on the plate.
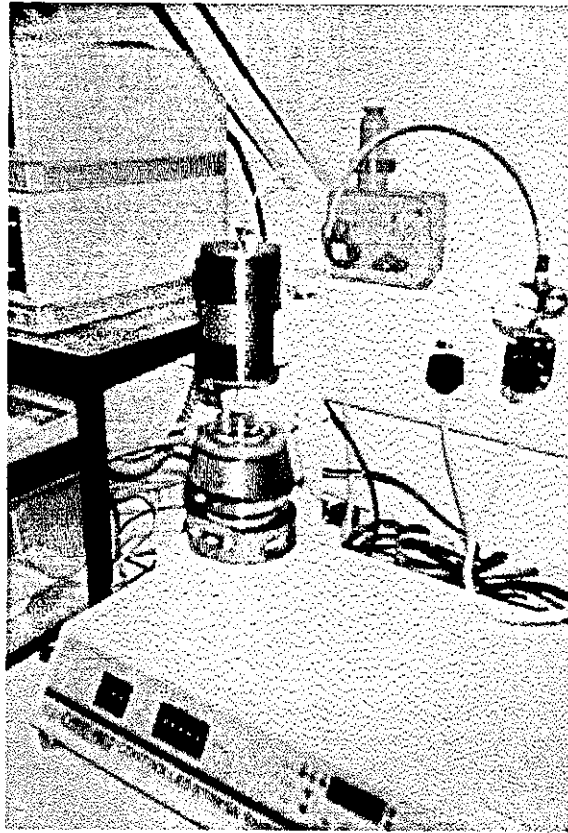
Figure 2.2 Photo of the Carrimed controlled stress rheometer with concentric cylinder configuration
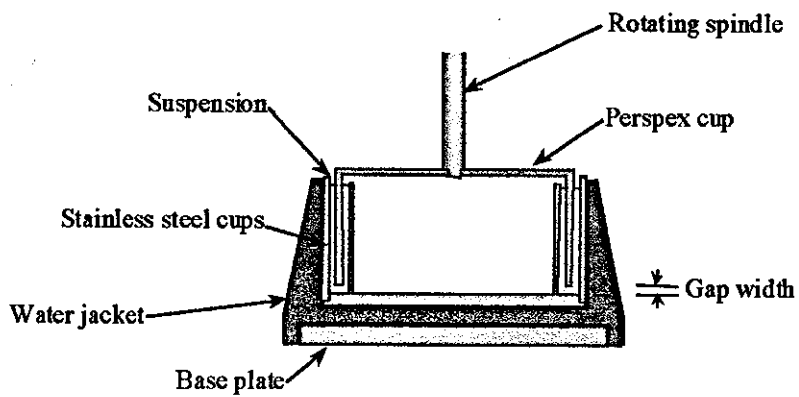
Figure 2.3 Concentric cylinder arrangement

69

The stainless steel cups of the concentric cylinder configuration were seated in a water jacket that fixed to the rheometer base plate. The jacket was attached to a water bath, which maintained the temperature of the suspension in the concentric cylinder configuration.
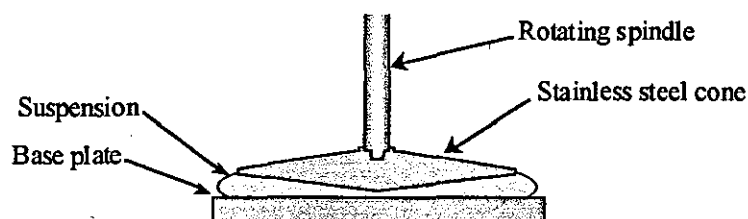
Figure 2.4 Cone and plate arrangement

Once the configuration had been fitted to the rheometer, the pneumatic ram was raised and an appropriate gap set between the lower and upper parts of the configuration[81]. The pneumatic ram was then lowered and an appropriate volume of suspension placed into the configuration using a disposable pipette[81] (or a syringe for higher concentration suspensions). Values for the maximum applied torque, experimental duration, and factors to account for the configuration were then entered into the software. Finally, the ram was raised and the suspension temperature allowed to stabilise before starting rheological measurements. Once sufficient readings had been taken from a given sample of suspension, the apparatus was dismantled and the configuration cleaned, with Millipore de-ionised water, and dried before being re-fitted and reset for a new sample.

During rheological measurements, torque was applied to the system and the change in strain was observed as the shear rate was increased for 1 minute, held at a maximum for 1 minute and decreased again over 1 minute to zero. The first reading taken with each sample was used to determine the maximum shear stress that could be induced in the sample within the operating limits of the apparatus. This enabled

data to be obtained over the widest range of shear rates possible in the further readings. Shear rate and shear stress data for each experiment was collected and stored on disc along with the experimental details. Analysis was then performed using the Carrimed software to fit an appropriate rheological model to the suspension.

2.1.6 Suspension Homogenisation

An Ultra Turrax T25 homogeniser (Janke & Kunkel, IKA Labortechnik), with 25mm dispersing tool (IKA S 25N – 25F) was used at 8000rpm for 10 minutes to homogenise up to 900ml of suspension at a time. The suspension was placed in a plastic beaker, sized to fully cover the homogeniser rotor, and subsequently clamped in place. The homogenisation was aided by stirring manually to ensure that no large agglomerations existed, and that the whole batch had passed through the homogeniser. The homogenised suspension was then placed into a clean vessel and covered with Clingfilm to minimise water loss through evaporation.
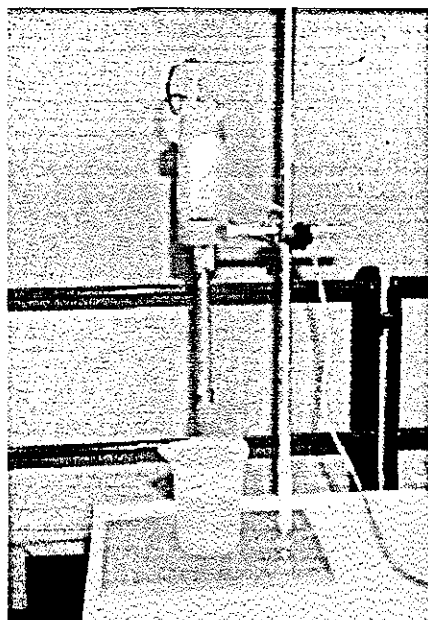
Figure 2.5 Photo of the Ultra Turrax T25 homogeniser

2.2 METHODS OF DISPERSION

The rutile powder was dispersed in water, and processed until it was representative of the Tioxide manufacturing process stream. This was judged to have been successful if the powder had been dispersed to a Malvern mean particle size of 0.32µm or less.

It was also necessary that the feed suspension for each experiment be dispersed to a similar standard for the experimental results to be comparable, thus a reliable dispersion process was required.

This Section details the dispersion methods investigated in an effort to achieve a Malvern mean size of 0.32µm, and a comparison of the results are presented in Section **3.1.1**.

2.2.1 Dispersion in De-ionised Water

This was performed in the preparation tank of the Malvern Mastersizer (Section **2.1.2**), where having taken a background reading and set the pump and stirrer speeds, small quantities of titania powder were added to the preparation tank using a spatula. The pump and stirrer provided a small degree of mixing, distributing the titania throughout the volume of water, and once the sample loading lay in the ideal zone, a measurement of particle size distribution was taken.

2.2.2 Dispersion by Ultrasound

The ultrasound facility in the Malvern Mastersizer preparation tank was used in an attempt to further disperse a small quantity of rutile. The procedure was similar to that of Section **2.2.1** except that ultrasound was applied to the titania suspension in the preparation tank before measuring the particle size distribution.

2.2.3 Effect of pH on Mean Particle Size

One litre samples of dilute titania suspension were pH adjusted using either dilute sodium hydroxide or dilute hydrochloric acid, and their particle size distributions measured.

A feedstock of suspension concentrate was made by mixing 0.6g of titania with 150ml of de-ionised water in a beaker, using a spatula. A 5ml sample of this was removed using a micropipette and added to 1250ml water to produce a suspension of 0.0003% volume solids, the pH of which was then measured and altered as required. The particle sizing procedure differed from that described in Section **2.1.2**, in that once the background reading had been taken, the Mastersizer preparation tank was drained of its contents, and replaced by approximately one litre of the pH adjusted suspension. The pump and stirrer were then restarted and the particle size measured as normal.

The process was repeated to measure the particle size of samples across the pH range by making up new batches of suspension from the feedstock concentrate, and adjusting the pH accordingly.

2.2.4 Dispersion Using a Ball Mill

A ball mill was used to impart shear energy to the agglomerates in suspension, and break them down by a process of attrition. A one-litre porcelain jar was filled with 1kg of 9mm grinding balls, 500ml clean water and 100g of titania (approximately 4.5% volume solids suspension). The jar was rotated at 96rpm and samples of suspension removed at intervals covering three hours. For each sample the stopwatch and the mill were stopped simultaneously. The jar was removed and agitated to settle the balls, and a 2ml sample was taken with a pipette and placed in a small glass container. The jar was then resealed and placed back on the mill to start

running while the particle size distribution of the sample was analysed in the Mastersizer.

2.2.5 Dispersion Using a Surfactant

Mono-isopropanolamine (MIPA) and sodium hexametaphosphate (Calgon) surface active agents were added to titania suspensions, the quantity of dispersant added being based on the weight of titania in suspension (0.3% for MIPA and 0.15% for Calgon). The Calgon was supplied as a powder and was dissolved in Millipore water prior to use. A Calgon solution of 0.27g/ml was produced, and the volume of water used to make up the titania suspension was corrected for the volume of Calgon solution used.

Having calculated the relevant quantities of titania, dispersant, and clean water required, the dispersant was added to the water in a beaker using a micropipette, and the titania stirred into the water-dispersant mix with a spatula. When using MIPA, the appropriate safety precautions were taken (transferring the MIPA to the water in a fume cupboard, wearing protective clothing).

2.3 SUSPENSION PREPARATION

An investigation of the dispersion techniques above (Section **3.1.1**) resulted in the following method for preparing dispersed titania suspensions, with a mean particle size ≤0.32μm, for both the characterisation and filtration experiments. The suspensions were manufactured at 50% volume solids and approximately pH 9.5 in order to achieve the required degree of dispersion. The concentration and pH were subsequently altered as required for each particular experiment.

2.3.1 Dispersion Procedure

The titania powder was dispersed at 50% volume solids in a solution of calgon dispersant (0.27g/ml) and Millipore water (corrected for the volume of calgon solution used). The dispersant solution was added to the water in a mixing vessel (plastic beaker or bucket), following which the titania was added incrementally, continuously mixing it into the suspension with a large stainless steel stirring rod to ensure that no large agglomerations of particles were present. The titania powder was weighed out (in batches) into a 2-litre beaker using a Sartorius, type 1403 balance. Once all the powder has been added and stirred in, the pH of the suspension was increased to approximately 9.5 to reduce the suspension viscosity before homogenisation.

The particle size distribution of the homogenised suspension was checked (using the Malvern Mastersizer) to ensure that the required mean size had been obtained. The dispersed suspension was relatively stable and could be stored overnight (covered with Clingfilm) without detrimental effect to the particle size distribution. Subsequent dilution of the suspension to the desired concentration (using Millipore water) had no effect on the particle mean size.

2.3.2 Determination of Suspension Concentration

The volume fraction of solids in suspension is determined using the following equation (from Appendix I):

$$\phi_b = \frac{\left(\rho_{suspension} - \rho_{water}\right)}{\left(\rho_{TiO_2} - \rho_{water}\right)} \qquad (2.1)$$

where ϕ_b is the volume fraction of solids in suspension, ρ_{TiO_2} is the density of rutile (4260kg/m^3), ρ_{water} is the density of water and $\rho_{suspension}$ is the density of the suspension, which is obtained by weighing a known volume (measured into a volumetric flask) on a top pan balance.

2.4 DESCRIPTION OF THE CROSSFLOW FILTRATION APPARATUS
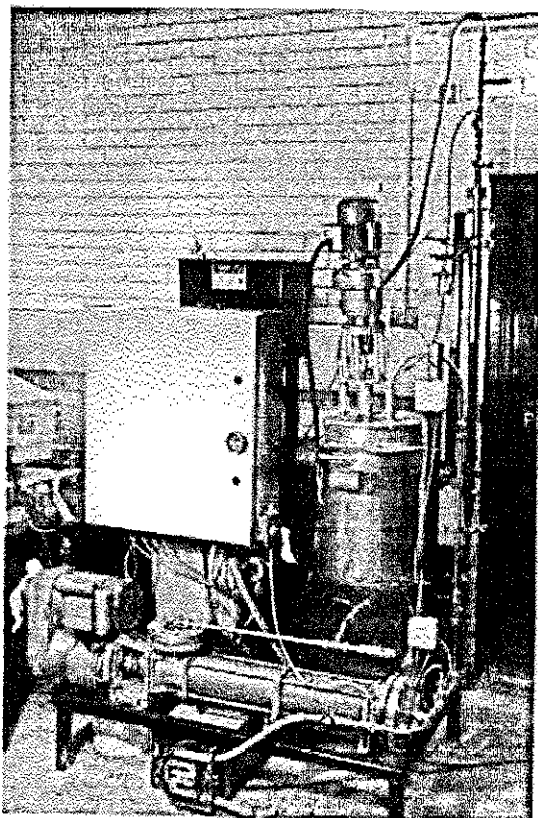
Figure 2.6 A photograph of the crossflow filtration rig

2.4.1 The Crossflow Filtration Rig

A schematic of the rig used for the crossflow microfiltration experiments is shown in Figure 2.7. The suspension was fed to the filter by a variable speed Mono pump, allowing a range of crossflow velocities to be examined. Pressure transducers at either end of the filter module measured the trans-module pressure, which was controlled by full flow ball valves. Temperature was monitored by thermocouples, computer controlled, and maintained by a hot water jacket around the feed tank An automatic data logging system recorded transmembrane pressure, temperature and

77

pump speed while permeate flux measurements were taken manually. The rig was operated both at constant concentration, by returning permeate to the feed tank, and in concentrating mode, by removing permeate from the system. A minimum inventory of approximately 14 litres is required to run the rig and prevent cavitation.

2.4.2 The Crossflow Rig Control Panel

The main functions of the rig were operated via a 386 personal computer with software written in visual basic. The screen display (Figure 2.8) incorporated:

i.   A control panel with on/off switches for the Mono pump, mixer, heating elements, and heating loop pump. (The control loop was automatically activated when the heating elements are switched on).

ii.   Output readings for temperatures, pressures and Mono pump speed. (This data was logged to a file at user defined intervals).

iii. Slider controls for fixing the temperature control loop set point, transmembrane pressure monitor set point, and the interval at which on screen data was logged.

2.4.3 The Filter Element

The titania suspensions were filtered by an asymmetric, $0.1\mu m$ rated, 16mm internal diameter, silicon carbide filter tube. The fine silicon carbide (SiC) filter surface is deposited on the inner face of a sintered SiC support tube (0.9m long and 25mm outside diameter), which will withstand transmembrane pressures up to 10 bar. The filter tube ends are sealed and supported in a stainless steel module by a rubber O-ring at each end. The module was attached vertically to the crossflow rig via flanges at either end, which were clamped to flanges on the rig and sealed with plastic gaskets.

78

P Pressure transducer — · — Information from PC

T Thermocouple — - - - Information to PC

Retentate return

Bypass loop

Feed tank

Water jacket

Hot water supply

Heaters

Stirrer

Priming loop

Filter module

Permeate

Drain

Pressure switch

Personal computer
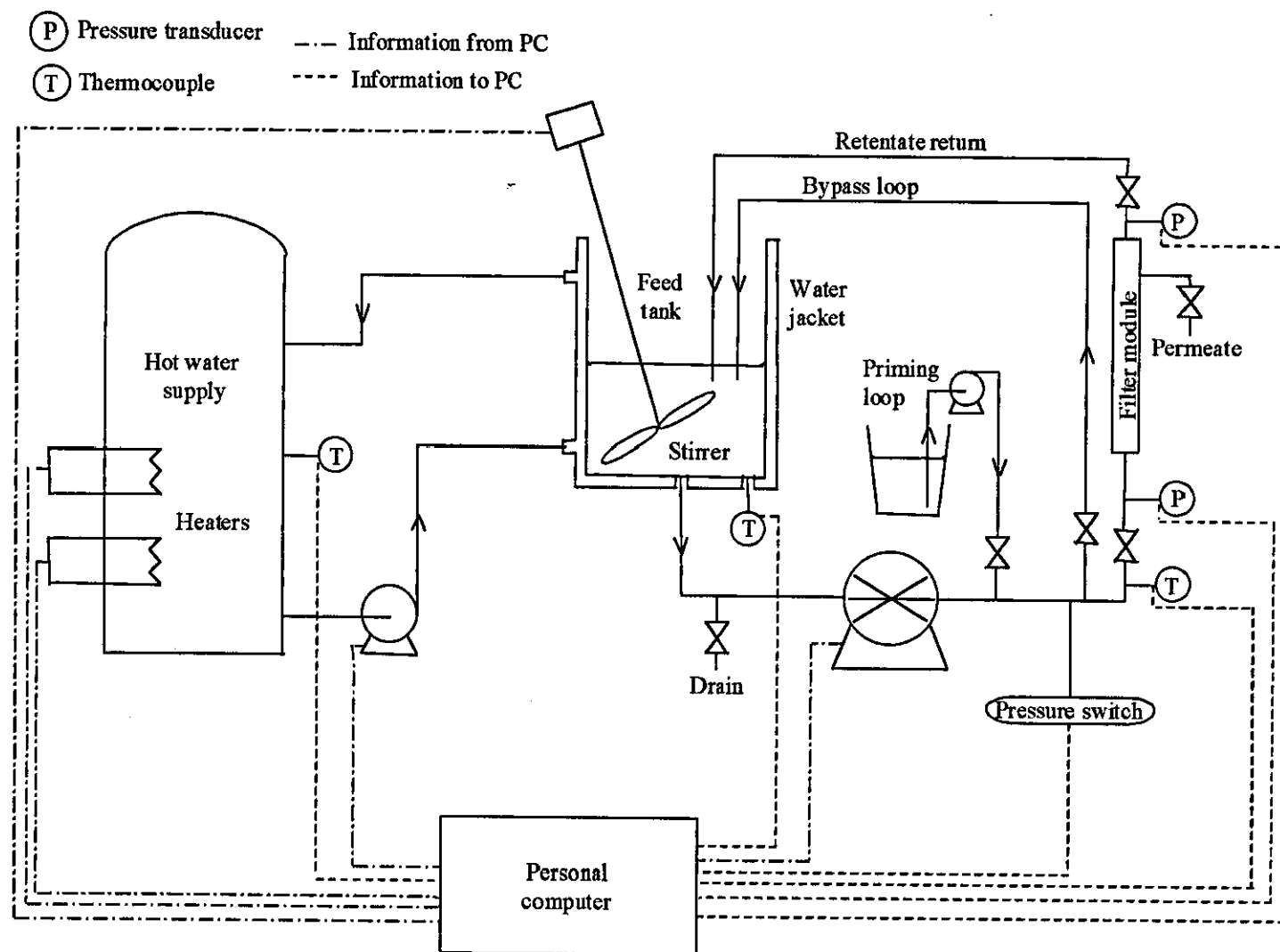
Figure 2.7 A schematic of the crossflow microfiltration rig

79

Figure 2.8 The filtration rig on screen display and control panel

80
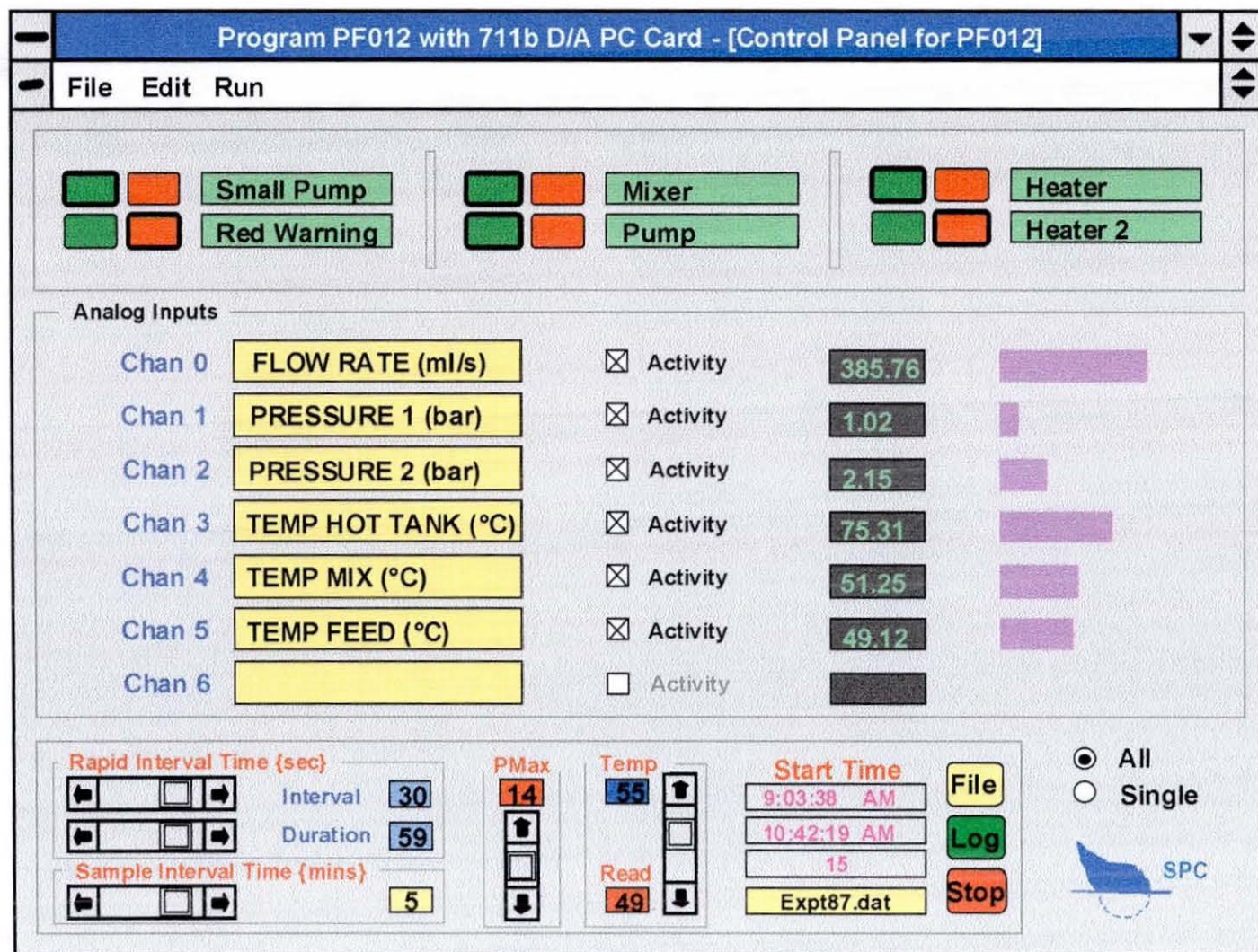
The suspension flowed through the centre of the filter tube, and permeate was removed from the top of the filter module via an exit valve near the top. The filter was maintained wet, with water filling both retentate and permeate sides whenever the unit was isolated. Crossflow velocities of 1 to 4 ms^{-1} through the unfouled 16mm diameter tube correspond to shear rates of 500 to $2500s^{-1}$ respectively, which was the range of shear rates covered by the Carrimed CS100K constant stress rheometer.

2.4.4 The Feed Pump

The viscous and abrasive nature of the titania suspensions limited the choice of pump and eliminated most forms of on line volumetric flow measurement. For this reason, a manually controlled, variable speed, positive displacement Mono pump (model number SB051AC1A8/V) was selected for the experimental rig. The single stage, stainless steel Mono pump utilised a rubber nitrile stator, suitable for suspensions of pH in the range 3 to 10, and temperatures up to and over 50°C. It was capable of delivering approximately $2m^3$/hour of suspension. .

2.4.5 Fittings

The ½ inch diameter pipework, fittings, and full flow ball valves were stainless steel, as was the 35 litre feed tank which had a lid and a built in water jacket. Retentate was returned to the feed tank via 20mm diameter, terylene mesh reinforced PVC tubing, which passed through the lid of the rig into the feed suspension. Permeate was returned to the feed suspension via a length of 9.5mm polypropylene tubing.

2.4.6 The Stirrer

The feed tank was fitted with a stainless steel, disc mounted pitch blade turbine (six 10cm blades pitched at 45°). This was attached to a 12mm stainless steel shaft, which passed through the feed tank lid to a high torque electric motor. This rotated the mixer at 60rpm to maintain the homogeneity of the suspension.

2.4.7 The Priming Loop

The priming loop was used to fill the empty rig with water or suspension. A Watson-Marlow 6035S, 0-165rpm peristaltic pump forced liquid upwards through the Monopump and pipework into the feed tank, thus displacing all air in the system. Approximately 5 litres of liquid were required to fill the void and rise into the feed tank.

2.4.8 Pressure Control

A pair of Farnell MM10013 pressure transducers (0-100psig) monitored the pressure at either end of the filter module, and from these measurements, the transmembrane pressure and pressure drop along the filter length were deduced. The transmembrane pressure was calculated using equation 2.2, where the pressure in the permeate line ($P_{permeate}$) was assumed to be atmospheric.

$$P_{transmembrane} = \frac{P_{outlet} + P_{inlet}}{2} - P_{permeate} \qquad (2.2)$$

The PC calculated the transmembrane pressure and activated red and green lights on the rig to indicate whether this was greater or smaller (respectively) than the user defined set point. A slow and progressive closure of the module exit valve from fully open, until the red light just came on (with time allowed for the PC to take its

readings), gave a good first approximation. Observing the data recorded by the logger indicated whether any fine tuning was necessary.

The pump outlet was fitted with a pressure switch that would cut power to the rig if a blockage in the system caused pressure to exceed 5.3bar.

2.4.9 Temperature Control

Two 3kW heating elements heated an insulated storage tank from which water was pumped around the suspension feed tank hot water jacket. RS PT100 thermocouples measured the process feed temperature, which was maintained automatically, according to the user defined temperature set point, by turning the heating elements on and off as required.

2.4.10 Measurement of Permeate Flux

Permeate exited near the top of the filter module through an arrangement of two valves, one allowing permeate to flow back into the feed tank and the other to a sample point. Permeate flux measurements were taken by diverting permeate to the sample point, then using a measuring cylinder and stopwatch to measure its flow rate manually. This was done by allowing the collected permeate to reach a pre-determined mark on the measuring cylinder, noting a start time, then after a pre determined time closing the permeate flux exit valve. Allowing the permeate to flow for a period of time before measuring the flux helped minimise errors that may otherwise have occurred as a result of air held up in the permeate sample line. The average permeate flux was then calculated using the volume collected in the allotted time.

2.5 FILTRATION APPARATUS CALIBRATION

The calibration of output signals from the rig, which were monitored and stored by the PC, all follow the same basic principles. The monitoring devices, when activated, produce analogue electronic signals that are converted to digital and sent to the PC for interpretation by the software. By applying a series of known input values to the device over its operating range, the output signal it produces can be logged and plotted against the corresponding input value. Superimposing a best-fit line over this data gives a calibration curve, which allows any signal from the device to be transformed into an actual "reading".

2.5.1 Pump Calibration

Calibration was effected by setting a pump speed (rpm) and measuring the associated volumetric flow rate of water through the filter with a 2 litre measuring cylinder and stopwatch. The measured volumetric flow rate was plotted as a function of pump speed and the equation of the resulting line (Appendix II) used to calculate an on-screen value of volumetric flow rate as the pump speed was adjusted manually.

The extreme temperature, pH and abrasive nature of the feed suspensions led to erosion of the rubber nitrile stator and as a result the pump required frequent re-calibration. The stator was replaced twice during the course of experiments, as was the pump gland. Wear on the stator had a varying degree of effect on pumping efficiency, depending on the concentration of the feed suspension. As a result, the on screen calibration was used as a rough guide, with the actual volumetric flow rate through the filter for each experiment being checked manually once steady state had been reached.

2.5.2 Pressure Transducer Calibration

A known pressure was applied to each pressure transducer using a compressed air line and pressure calibrator. The resulting digital output signal was plotted against the input pressure and a calibration curve produced (Appendix II). This was used in the software to convert the output signal to a real pressure value on the PC screen.

2.5.3 Temperature Transducer Calibration

Temperatures between approximately 0°C and 100°C were obtained by allowing ice to melt in a beaker, then heating the resulting water on a hot plate. Temperatures were measured using a thermometer then logged and plotted against the corresponding digital output from the thermocouple. This was repeated for each thermocouple to give the Figures in Appendix II, which were subsequently input into the software to provide on-screen readouts of the various process temperatures.

2.5.4 Filter Tube Calibration

Two similar filter tubes were used in the experimental programme; the first one having cracked as a result of a design fault. The clean water permeate flux through a new filter tube was measured at constant volumetric flow rate over a range of transmembrane pressures using the clean water rig (Section 2.6.4). Plotting this data allowed determination of the clean water flux for any given transmembrane pressure (Appendix II).

2.6 PREPARATION PROCEDURES FOR FILTRATION EXPERIMENTS

2.6.1 Feed Suspension Preparation

Titania suspensions were prepared at 50% volume solids (Section **2.3**), and diluted to the desired experimental feed concentration, with Millipore water, in the filtration rig. The volume of suspension prepared for each experiment was dependent on the feed concentration required, and these values are tabulated below with the corresponding volumes of water (Tables 2.1 to 2.3).

2.6.1.1 Experimental Series A

Series A was comprised of experiments performed both in concentrating mode, and at constant concentration. The first three experiments were performed in concentrating mode, by removing permeate from the system, and covered feed suspension concentrations of 2-6, 6-18, and 18-50% volume solids.

Table 2.1 Experimental series A, feed suspension compositions for concentrating experiments

Feed solids volume concentration (%)	Suspension volume (litres)	Water volume (litres)
2 to 6	1.7	42
6 to 18	4.8	34
18 to 50	14	25

Table 2.2 Experimental series A, feed compositions for constant concentration experiments

Feed solids volume concentration (%)	Suspension volume (litres)	Water volume (litres)
15	4.5	10.5
25	7	7
35	14	6

Series A experiments were performed at constant concentration, by returning the permeate to the feed tank.

2.6.1.2 Experimental Series B

Experiments in series B were performed using similar concentration feed suspensions to those in the series A concentrating experiments. The feed suspension pH was however, adjusted to approximately 4.0 prior to filtration.

2.6.1.3 Experimental Series C

All experiments in series C were run to steady state at constant feed concentration, by returning the permeate to the feed tank. In each case, two experiments were run consecutively to conserve time and materials. Once the first experiment had reached steady state, the feed concentration was altered (using Millipore water or 50% volume solids suspension as described below), the filter cleaned, and the second experiment commenced. Experimental series C was run on a five day schedule as follows;

Day one	First experiment at 40%, dilute to 33% for second
Day two	Prepare feed for experiment at 26%
Day three	First experiment at 26%, dilute to 19% for second, prepare feed for 5% and 12%
Day four	First experiment at 5%, concentrate to 12% for second
Day five	Prepare feed for experiment at 40%

The volumes of suspension and water required for the first experiments, and the subsequent dilution/concentration for the second experiments, are given in Table 2.3.

Table 2.3 Experimental series C, feed suspension compositions

Starting volumes for first experiment			Second experiment	
50% volume solids suspension (litres)	Millipore water (litres)	Feed concentration (% volume solids)	Addition to first experiment (litres)	Feed concentration (% volume solids)
1.6	12.7	5.5	2.4 (suspension)	12
7.4	6.8	26	5.15 (water)	19
11.5	2.86	40	2.8 (water)	33

2.6.2 Crossflow Rig Preparation

Having prepared the appropriate volume of titania suspension, the filtration apparatus was switched on, and the 3kW heating elements activated to heat up the hot water feed tank. Temperature and pressure set points were entered into the software, as was a data logging interval and a data storage filename. This would store pressure, temperature and feed rate data at the defined logging interval, while a stopwatch, measuring cylinder, and data sheet were used to measure and record the permeate flux.

With the rig cleaned (Section **2.8**) and containing 14 litres of Millipore water, the Mono pump was started, an approximate transmembrane pressure set (Section **2.4.8**), and a volumetric flow rate set (by adjusting the Mono pump speed). The filter module was then isolated (full of water), simultaneously switching the flow to the bypass loop before adding the make-up suspension (Section **2.6.3**).

The heating circuit pump was switched on to feed hot water through the water jacket, and the feed suspension was simultaneously mixed and brought up to the desired feed temperature by circulating it through the bypass loop. The filter clean water flux was then measured using the clean water rig (Section **2.6.4**).

Finally, a sample of the feed suspension was removed to check its pH, concentration and the mean particle size. Where necessary, the pH was adjusted by addition of sodium hydroxide/ hydrochloric acid.

2.6.3 Addition of Titania Suspension to the Crossflow Rig

The Mono pump was stopped and water removed from or added to the rig (via the drain valve) such that the amount remaining would dilute the 50% volume solids suspension to the desired feed concentration (Section **2.6.1**). The feed tank turbine was switched on, and the bulk of the suspension poured in with the water in the feed tank. The Mono pump was then restarted and the suspension pumped through the bypass loop to mix it, meanwhile any residual suspension in the containers was removed to the feed tank using a spatula. Some water (typically 500ml) was often removed from the water make up volume to rinse the titania suspension containers, thus ensuring that the minimum of slurry was lost in the make up procedure.

This procedure was modified for experimental series C where the starting feed suspension of 40% volume solids was used. Only 2.8 litres of make up water was required, which was less than the five litres required to prime the system (Section **2.4.7**). The rig was therefore drained completely and the priming loop used to fill it with a dilute suspension (approximately 25% volume solids) comprising the 2.8 litres of Millipore water and approximately 3 litres of the 50% suspension. The rest of the suspension was then added to the feed tank as in the other experiments.

2.6.4 Clean Water Flux Measurements

The two filter tubes, used in the filtration study, became progressively blocked with titania over the duration of the experimental programme. These particles could not be successfully removed from the filter pores by forward or backflushing, and resulted in a decline in the filter tube permeability until the clean water permeate flux, at a given pressure, reduced to approximately 30% that of the new filter tube. Although the effect of this on the steady state permeate flux was negligible (Appendix II) it may have had some bearing on the initial stages of filtration, and it was thus necessary to measure the clean water flux before each experiment.
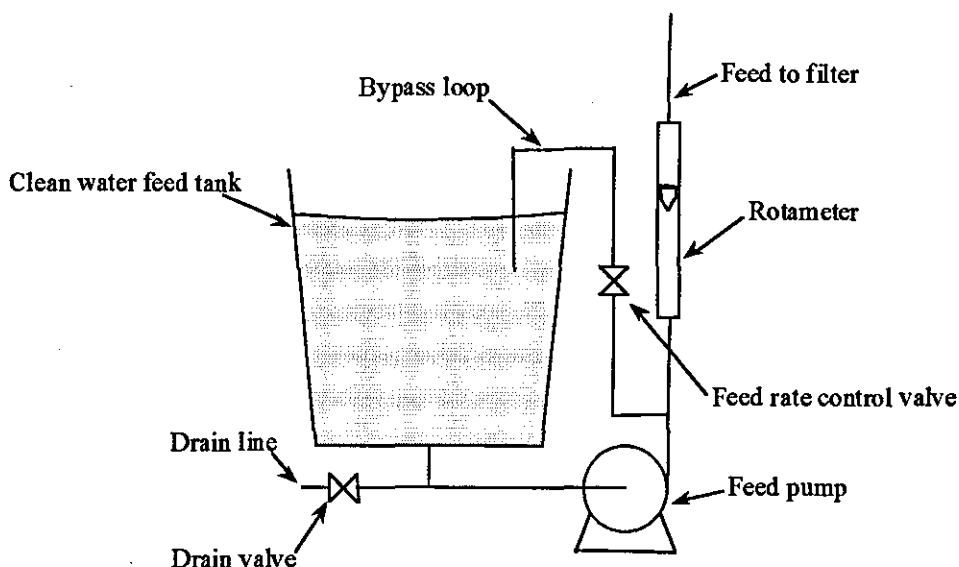
Figure 2.9 A schematic of the clean water rig

The clean water rig (Figure 2.9) was used to supply titania free water for the clean water flux measurements. A Beresford PV42 centrifugal pump (180Watt, 2800rpm) supplied Millipore water from a 25 gallon feed tank, through a flowmeter, directly to the inlet of the filter module (to which it was clamped). The retentate water passed through the filter to drain. The post filter-module valve and clean water rig feed rate valve were used to achieve the desired flow rate and transmembrane pressure. This was monitored using the post-module pressure transducer alone and an estimated value of static head in the filter. Once all measurements had been taken, the filter module was reconnected, and refilled with Millipore water by backflushing (Feeding via the permeate line).

Measurements with the clean water rig were made at a constant feed volumetric flow rate of $0.17m^3/h$. The pressure produced by the clean water rig pump was not sufficient to reach experimental transmembrane pressures, so the clean water flux through the fouled filter was calculated as a percentage of that through the new filter at the same transmembrane pressure. This percentage was then used with the clean filter calibration curve (Appendix II) to estimate the clean water flux at the experimental transmembrane pressure, thus giving the clean water flux prior to each experiment.

2.7 CROSSFLOW FILTRATION EXPERIMENTAL METHOD

Having prepared the experiment (Section **2.6**), the PC auto-logging system was initiated and the flow of suspension switched from the bypass loop through the filter. The transmembrane pressure was then set manually (Section **2.4.8**), and the permeate flux measured (Section **2.4.10**), and recorded. Permeate flux measurements were taken in quick succession during the initial stages of filtration, where flux decline was rapid, becoming less frequent as the experiment progressed. The transmembrane pressure was monitored using the auto-logged data and indicator lights, and maintained manually (Section **2.4.8**).

Where permeate was removed from the system (increasing the feed concentration), it was not possible to reach a steady state, and the experiment was terminated when either the volume remaining in the rig had been reduced to 14 litres (minimum inventory) or the filter tube choked (full of solid). Experiments run at constant feed concentration (returning permeate to the feed tank) were terminated when the system reached a steady state. This was defined, in these experiments, by consistent measurements of permeate flux over a period of at least an hour.

At the end of the experiment, the volumetric flow rate of suspension through the filter was checked manually by diverting the retentate flow into a 2 litre measuring cylinder and using a stopwatch to measure the flow rate. A sample of the suspension was also removed to check pH, concentration, and mean particle size at the end of the experiment.

For experimental series A and B, and the second of two consecutive experiments in series C, the auto-logging system, heating elements and heating loop pump would now have been switched off and the cleaning regime initiated (Section **2.8.1**). Where this marked the end of the first experiment in a series C run however, the relevant amount of Millipore water or 50% volume solids suspension would now have been added to the feed tank according to the operating procedures specific to experimental set C (Section **2.7.1**).

2.7.1 Operating Procedure Specific to Experimental Series C

At the end of the first experiment, a volume of water or suspension was added to the feed suspension as described in Section **2.6.1.3**.

Following dilution with Millipore water, the filter was cleaned (Section **2.8.2.2**) and the clean water flux measured (Section **2.6.4**) before commencing the second experiment in a similar manner to the first (Section **2.7**).

Where suspension was added however (increasing the titania concentration), no filter cleaning was required, as justified by the results of the series A experiments (Section **3.3.1**). In this case, the post filter module valve was opened briefly and the permeate line closed, using the resulting increase in shear stress to remove the bulk of the existing cake. The flow was then diverted to the bypass loop, while the fresh suspension was added and mixed, before returning it through the filter and starting the second experiment.

2.8 FILTRATION APPARATUS CLEANING REGIMES

2.8.1 Crossflow Rig Cleaning Regime

It was necessary to clean the filtration apparatus thoroughly after each experiment to prevent a build up of titania. Titania deposits (particularly dried) would have proven difficult to remove and may have contributed to excessive wear, specifically of the Monopump. The filter was maintained wet at all times and, for long periods of rest, was left containing some dispersant as well.

2.8.1.1 Emptying

At the termination of an experiment, the permeate line was closed, the module exit valve opened and the Mono pump speed increased to aid removal of cake from the filter surface. After a few minutes, the speed was decreased again and the pump stopped. The suspension was then removed from the rig, firstly from the feed tank, via the drain valve, then from the rest of the system through the pump sump plug. The used feed suspension was stored in high density, polypropylene waste drums where it was allowed to sediment and concentrate.

2.8.1.2 Flushing

Having replaced the pump sump plug, the priming loop (Section 2.4.7) was used to pump 14 litres of tap water into the rig. This was pumped around the system at high flow rate to flush titania from the filter tube, pipework, and pump. Two to three flushes (depending on the experimental feed concentration), combined with hand cleaning the inside of the feed tank were required to remove all significant traces of titania in the system, and a small addition of dispersant such as Decon 90 often aided this process.

93

2.8.1.3 Rinsing

The rig was rinsed by operating the mono pump at low speed and continuously removing water to drain from the bypass loop outlet whilst adding new water to the feed tank. This was continued until the exiting water was absent of visual traces of titania.

2.8.1.4 Clean Fill

Finally, the system was drained, rinsed, and filled with 14 litres of Millipore water from the priming loop. The filter tube was cleaned (Section **2.8.2.1**) to remove as much titania as possible before the module was reconnected to the rig and isolated full of water. The rig, and PC were then shut down.

2.8.2 Filter Tube Cleaning Regimes

2.8.2.1 Standard Filter Tube Cleaning Regime

The module was unclamped from the rig and attached to the clean water rig (Section **2.6.4**), where it was flushed with Millipore water until visible traces of titania were negligible. The tube was then backflushed with Millipore water (fed through the permeate line) to remove further deposits from the tube surface, before forward flushing again, this cycle being repeated until all visible traces of titania ceased to be present in the flow exiting the filter tube.

2.8.2.2 Filter Tube Cleaning Regime Specific to Experimental Series C

Once the appropriate volume of Millipore water or 50% solids suspension had been added to the feed suspension (Section **2.7.1**), the permeate line valve was closed and the module exit valve opened to allow a purely parallel flow of suspension across

the filter, thus increasing the shear stress at the cake surface and removing the bulk of it. The filter module was then isolated and the bulk flow of suspension re-routed through the bypass loop. The module was unclamped from the rig (collecting its contents in a plastic beaker to be poured back into the feed tank) and attached to the clean water rig, where it was flushed with Millipore water until visible traces of titania were negligible. The tube was then backflushed with Millipore water (feeding it through the permeate line) to remove further deposits from the tube surface, before forward flushing again, this cycle being repeated until all visible traces of titania ceased to be present in the flow exiting the filter tube.

Having cleaned the filter, its clean water flux was measured (Section **2.6.4**) and the module re-connected to the filter rig.

CHAPTER THREE

RESULTS AND DISCUSSION

3.1 DISCUSSION OF RESULTS IN RELATION TO SURFACE CHEMISTRY

3.1.1 Dispersion techniques

As outlined in the introduction, it was necessary to disperse the titania powder to a "Malvern" mean particle size of $0.32\mu m$ or less. A series of dispersion techniques were experimented with in order to achieve this including mechanical separation, using ultrasound, a ball mill and a high speed mixer, the use of surface active agents, changes in ionic strength of the continuous medium, and combinations of techniques.

Initially an essentially unaided process was tried, whereby a small quantity of titania powder was added to double distilled water in the Malvern Mastersizer preparation tank. The pump and mixer components of the Mastersizer imparted some mechanical energy to the system and a Malvern mean size of approximately $4.3\mu m$ was obtained. To reduce this to the target size of $0.32\mu m$ required either an increase in the mechanical energy to physically break the inter-particle bonds, or that the attractive energy be reduced chemically.

Additional energy was supplied to the system using the ultrasound facility in the Mastersizer preparation tank (prepared in Section **2.2.2**) at 100% for two minutes. This reduced the Malvern mean size from $4.3\mu m$ to $0.65\mu m$, however no further reduction was obtained by increasing the duration of the ultrasound and the sample was prone to re-agglomeration when left standing. Similar results were observed by Liddell and Boger[11], who also found that sonication helped to break up large lumps or granules within the suspension, but that this was usually achieved within the first 30 to 60 seconds of sonicating, after which there was little further improvement.

A ball mill was then used (Section **2.2.4**) to disperse a 4.5% volume solids titania-water suspension, and this led to a reduction in the mean particle size from 4.4μm to 3.8μm in the first six minutes, then down to 3.3μm after one hour following which no discernible change in size was noted.

Mono-isopropanolamine (MIPA) dispersant was recommended by Tioxide, and this was used at 0.3% based on the weight of titania in suspension (Section **2.2.5**). A 0.1% volume solids titania suspension was prepared and the mean particle size reduced to 0.65μm. There was also an increase in the natural pH of the suspension from pH 5.7 to pH 6.1 and, unlike the samples reduced to 0.65μm using ultrasound, this suspension appeared to remain dispersed and stable. There was no tendency to agglomerate or settle and no residue appeared to be left in the glass beakers or on the lenses of the Mastersizer.

Neither the application of ultrasound to the MIPA dispersed suspension or an increase in MIPA concentration succeeded in reducing the particle size of this low solids concentration dispersion any further. Repeating the ball mill experiment with a MIPA dispersed suspension, however, reduced the mean particle size from 0.68μm to 0.62μm after four hours, but this was still too large.

A MIPA dispersed suspension was prepared at 40% volume solids, and this succeeded in reducing the mean particle size to 0.60μm. Further increasing the volume solids concentration to 50% resulted in a dispersion of pH 10.3, and an improvement in the mean particle size to 0.38μm. Sonicating the 50% volume solids, MIPA dispersed suspension with an ultrasonic probe failed to improve this result, instead the particles migrated to the probe surface where they appeared to concentrate. The application of high shear however (using a Moulinex food mixer at 10000rpm for 3 minutes), successfully reduced the particle size distribution further, to a mean size of 0.30μm. A laboratory bench top mixer (2200rpm) was unable to reduce the size distribution as successfully as the Moulinex and, as a result of the concentrated suspension viscosity, was not capable of maintaining a high speed for extended periods.

It is evident from these results that mechanical energy alone is not sufficient to disperse the titania particles in water. A surface-active agent is required and serves two functions. Firstly, it reduces the solid-liquid interfacial tension so that the wetting process itself becomes more efficient. This is evident from the significantly smaller mean particle size achieved through the use of MIPA, even without mechanical agitation. Secondly, the dispersion becomes more stable, i.e. less prone to agglomeration, which is the result of increased inter-particle repulsion forces. These may be electrostatic, steric or a combination of the two.

Table 3.1 Summary of results for the rutile dispersion experiments

Dispersion process	Result	Comments
Disperse in Mastersizer tank	4.3μm	
Ultrasound for 2mins @100%	0.65μm	Tendency to re-agglomerate
Ball mill 4.5% v/v solids	3.3μm	No improvement after 1 hour
MIPA disperse 0.1% v/v suspension	0.69μm	Dispersion maintained
Ball mill MIPA dispersed suspension	0.62μm	After 4 hours
MIPA dispersed 40% v/v suspension	0.60μm	Dispersion maintained
MIPA dispersed 50% v/v suspension	0.38μm	Dispersion maintained
Mix MIPA dispersed 50% v/v suspension at 10000rpm for 3 minutes	0.30μm	Dispersion maintained

The fact that a high volume fraction of solids is required to achieve the desired degree of dispersion suggests that the mechanics of particle separation is effected primarily by inter-particle repulsive forces, and that aggregates must be forced into close proximity before these forces are able to break them up. Having achieved this degree of dispersion, the suspension can be diluted without any detrimental effect to the mean particle size, and dried particles were observed to spontaneously re-disperse upon addition of water, suggesting that the dominant repulsive force is steric hindrance[20].

In conclusion, the titania powder must be dispersed in water at 50% solids by volume, using a suitable surface active agent in order to achieve the desired mean particle size. High shear mixing/ homogenisation is then required to ensure a narrow particle size distribution.

All subsequent experiments were performed using a different supply of rutile (different coating), for which sodium hexametaphosphate proved a marginally better dispersant. The same dispersion procedure was employed (Section **2.3**) although the dispersion pH was adjusted to 9.5 with NaOH, prior to homogenisation, to reduce the suspension viscosity.

3.1.2 Measurements of Zeta Potential

The Zeta potential and mean particle size of a calgon dispersed titania suspension were measured as a function of dispersion pH, the results of which are plotted in Figure 3.1.

The greatest surface charge (-64.5mV) occurs at pH 11.5 and the iso-electric point (zero charge) is at pH 4.24. Zeta potential remains approximately constant at -50mV between pH 7 and pH 10.5, and associated particle size measurements show that the material forms a stable well dispersed suspension in this region with a mean particle size of approximately 0.35μm. Zero Zeta potential implies that there are no inter-particle repulsive forces, thus the van der Waals attractive forces dominate, resulting in the flocculation of particles. This is verified by the corresponding increase in particle size as the dispersion moves from a stable, well dispersed state towards the IEP where the mean particle size is approximately 1.6μm

As pH decreases further the Zeta potential becomes positive and increases in magnitude, however despite this apparent increase in inter-particle repulsive forces the mean particle size continues to rise rapidly. The increase in ionic strength appears to have brought about a reduction in the primary maximum (Section **1.2.8**),
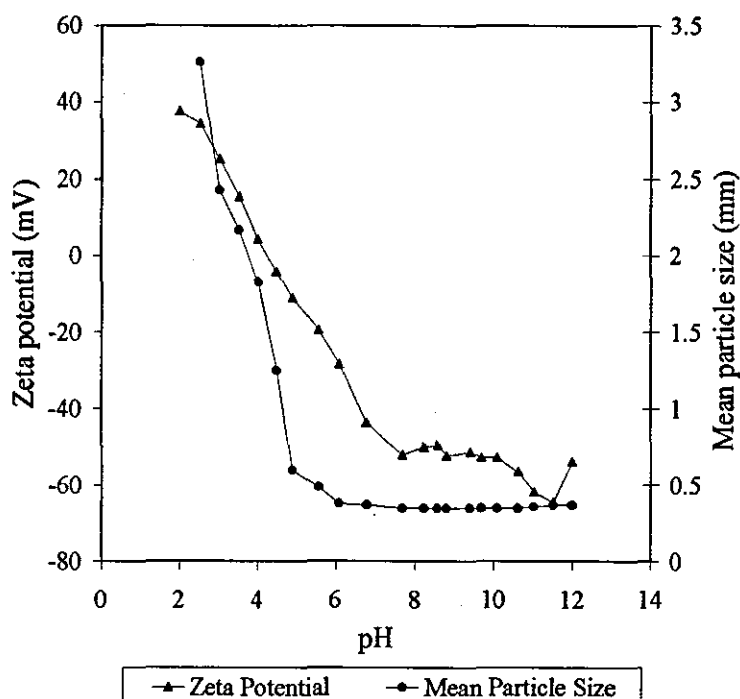
Figure 3.1 Zeta potential and mean particle size vs. pH for calgon dispersed rutile

i.e. a thinning of the electrical double layer (Section **1.2.4**). As a result, particles are able to approach each other more closely and aggregate, hence a larger mean particle size. If particles move past the primary maximum to the energetically very stable position of the primary minimum, a large rise in the potential energy of repulsion of the system is required to re-disperse the particles. The continuing increase in particle size as pH is reduced below the IEP suggests that this energy is not provided sufficiently by the corresponding increase in particle surface charge.

3.2 DISCUSSION OF EXPERIMENTAL RESULTS IN RELATION TO RHEOLOGICAL EXPERIMENTS

Calgon dispersed rutile suspensions were prepared as described in Section 2.3 and diluted to obtain solids concentrations of 2, 5, 10, 20, 30 and 40% by volume. The dispersion viscosity at each concentration was then measured as a function of applied shear rate, dispersion pH and temperature within the operating limits of the Carrimed controlled stress rheometer. Where possible, concentrated solutions of sodium hydroxide and hydrochloric acid were used to alter the pH so as to minimise dilution of the suspension.

Concentric cylinders were used for the majority of experiments. However, at 50% volume solids concentration the suspension viscosity was so great that the resistance provided by the concentric cylinders prevented any flow at all and the cone and plate set up was the only viable option. A limited number of experiments were thus carried out using this configuration.

3.2.1 Rheological Characterisation of Titania Dispersions

Figure 3.2 is a typical shear stress-shear rate curve, produced by the Carrimed rheometer for a calgon dispersed titania suspension.

The initial increase in shear stress with no corresponding increase in shear rate demonstrates the presence of a yield stress which must be overcome before the suspension is able to flow, a property typically exhibited by a Bingham plastic.

Further increases in shear rate, however, resulted in a reduction in the apparent viscosity (particularly at higher solids concentrations), so the dispersion also exhibited characteristics of shear thinning or pseudoplasticity. Establishing a maximum shear rate and maintaining it for a period before reducing it again to zero,

101

revealed a hysteresis loop[2] where the apparent viscosity was lower for decreasing shear rates than at the equivalent increasing shear rate.
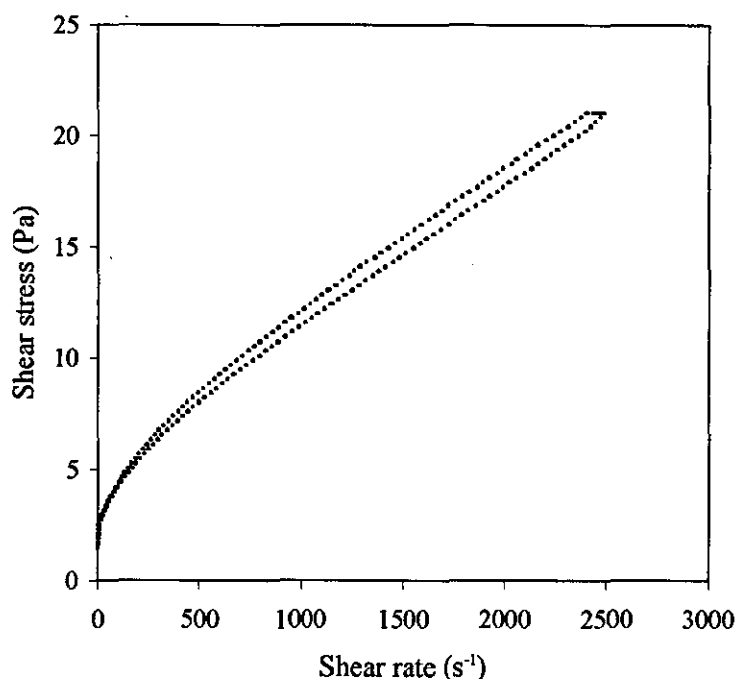
Figure 3.2 Calgon dispersed titania, 30% volume solids, pH 5.61, 20°C

The Calgon dispersed titania suspensions are thus characterised by a yield stress, a degree of shear thinning behaviour, and a degree of time dependency[2], what could be defined as thixotropic-plastic flow.

These properties can be explained in terms of the structure of particles within the dispersion, which form weakly bonded flocs that are easily broken down under shear. The randomising thermal movement of the dispersed particles results in rapid breaking and reformation of these weak bonds, thus at low shear where Brownian motion dominates, the weakly bonded structure within the suspension is maintained. As shear is increased, hydrodynamic forces tend to prevail over random movement

and the structure of the suspension is destroyed, allowing it to flow and hence exhibiting a yield point. Further increases in shear tend to promote alignment of the particles and flocs in such a manner as to alleviate the viscous stress and, hence, to reduce the viscosity[2]. This is apparent in the shear thinning behaviour. The thixotropic behaviour implies that the reformation of inter-particle bonds and the resulting restructuring of the dispersion is not spontaneous upon the reduction of shear. The time delay in restructuring results in an apparently less viscous dispersion for decreasing shear than would be found for increasing shear rates.

No attempt has been made in this work to measure the degree of thixotropy or the parameters that characterise it.

3.2.2 Results of Rheological Experiments

Linear interpolation of the shear rate - shear stress data recorded by the Carrimed allows an apparent viscosity to be calculated for a suspension of specific concentration, pH, shear rate and temperature. To account for the thixotropic nature of the dispersion, the average apparent viscosity of the increasing and decreasing shear curves was calculated. Viscosities were plotted as a function of the controlling parameters such that their effects could be individually assessed (Appendix IX).

3.2.2.1 Effect of Suspension Solids Concentration on Viscosity

Figure 3.3 demonstrates the effect of increasing volume solids concentration on the viscosity of calgon dispersed titania suspensions at pH 10 between shear rates of $500s^{-1}$ and $2500s^{-1}$. Below a concentration of 8% volume solids there is a relatively small increase in viscosity with solids concentration and the coincidence of data for different shear rates implies that there is no shear thinning effect. This suggests that the solids in suspension are too widely separated to have a formal structure and

consequently do not have a dominant effect on the rheological characteristics of the suspension.
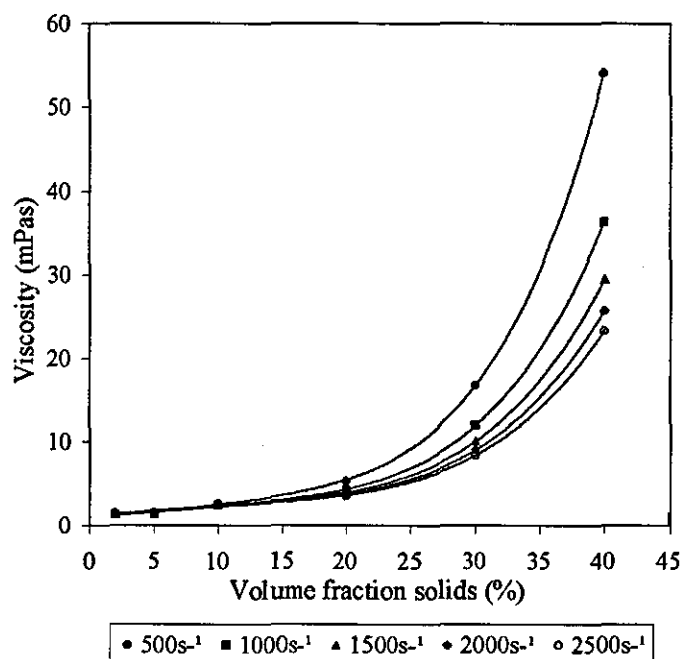
Figure 3.3 Viscosity vs. solids concentration and shear rate for a pH 10 dispersion, (Data fitted with 4th order polynomials)

As the solids concentration is increased however, there is a corresponding rise in the suspension viscosity which, across the range of shear rates, can be fitted with a fourth order polynomial (as in Figure 3.3). This, combined with the increasing difference between the viscosity-concentration curves for increasing shear rates, implies that as the particles come into closer proximity they tend to form a loosely bound structure which increases the apparent viscosity of the suspension. The yield stress, degree of shear thinning and thixotropic behaviour are all increased as the dispersion solids concentration increases[2].

3.2.2.2 Effect of pH on Viscosity

The effect of pH on suspension viscosity is shown in Figures 3.4 to 3.9. Considering the 10% volume solids suspension (Figure 3.6), there appears to be a stable region between pH 5 and pH 12 where the change in viscosity is negligible regardless of the applied shear rate. As the pH drops below pH 5 however, there is a rapid increase in viscosity (up to an order of magnitude), peaking at pH 3.4 before declining slightly again. Viscosity also increases past pH 12 and in both cases this results in an enhancement of the shear thinning effect.

The transition from low to high viscosity as the ionic strength of the dispersion increases is characteristic of all Figures 3.4 to 3.9. However, as the dispersed solids concentration increases the stable region becomes narrower, shear rate has a greater effect and there is an increase in the overall viscosity[2]. The range of pH over which suspension viscosity can be measured is also reduced with increasing solids volume fraction, the yield stress being too great for the Carrimed to overcome.
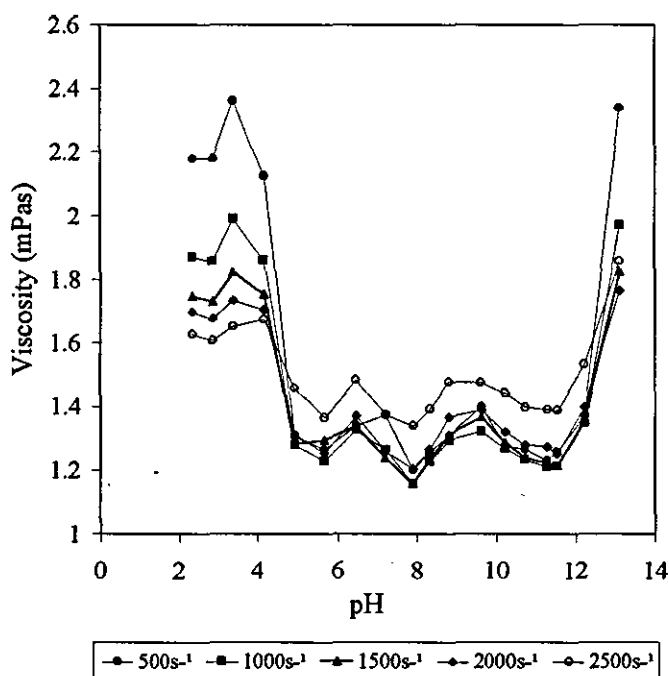
Figure 3.4   Viscosity vs. pH and shear rate, 2% volume solids
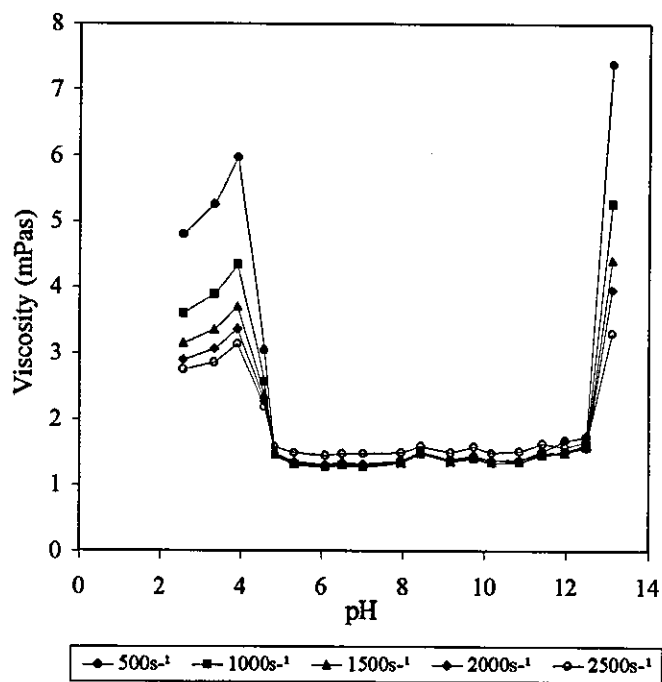
Figure 3.5   Viscosity vs. pH and shear rate, 5% volume solids
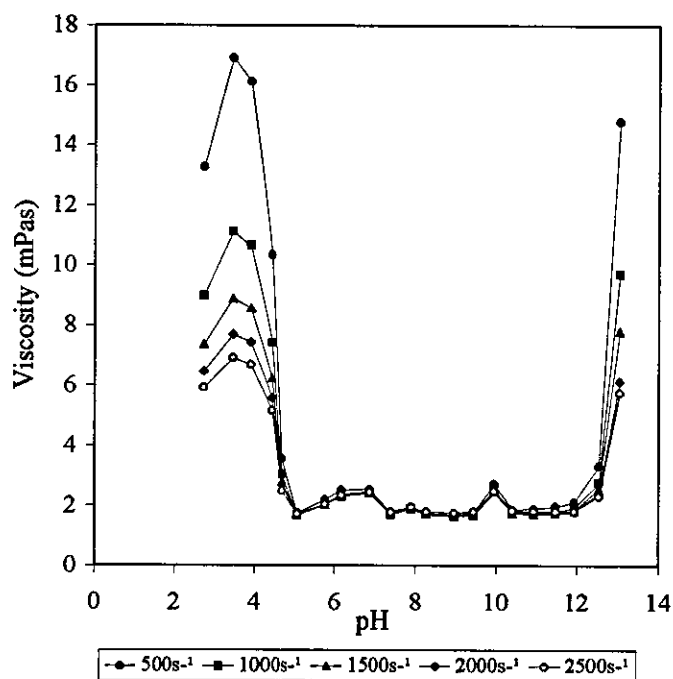
Figure 3.6   Viscosity vs. pH and shear rate, 10% volume solids

106
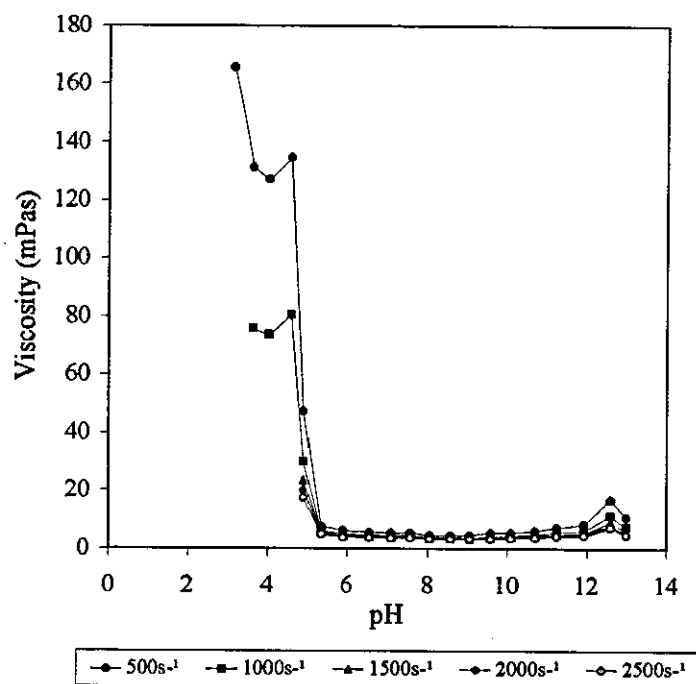
Figure 3.7   Viscosity vs. pH and shear rate, 20% volume solids
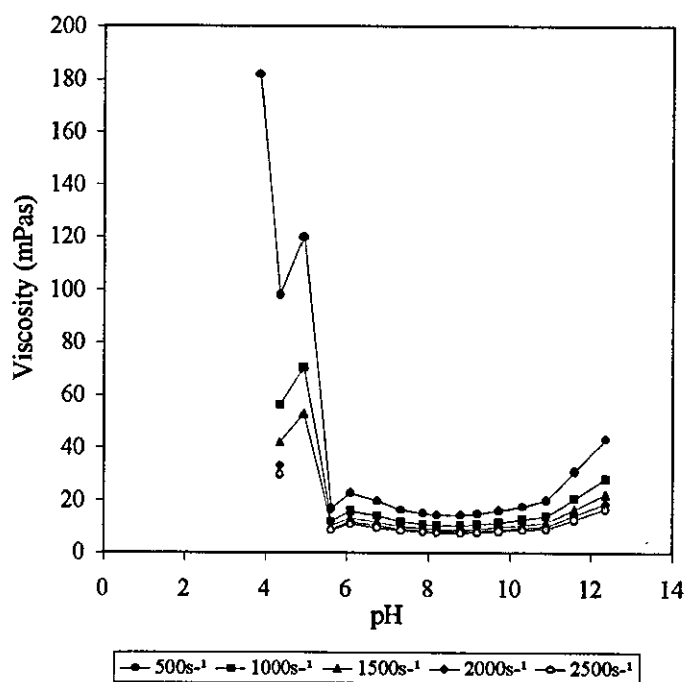
Figure 3.8   Viscosity vs. pH and shear rate, 30% volume solids
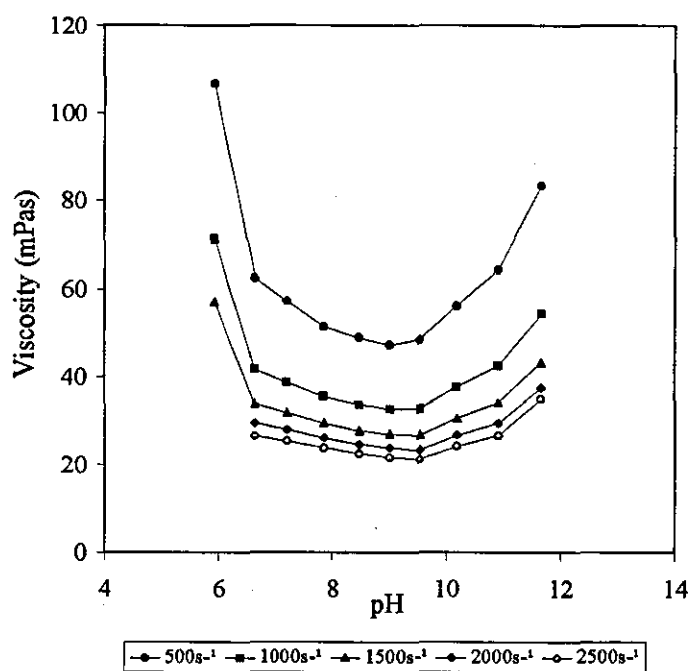
Figure 3.9   Viscosity vs. pH and shear rate, 40% volume solids

If Figure 3.6 is considered with respect to the Zeta potential data (Figure 3.1), the region of rheological stability (pH 5 to pH 12) corresponds with a large negative Zeta potential and the rise to a maximum viscosity with the iso-electric point[2] (confirmed by Liddell and Boger[11]). The increases in viscosity with dispersion ionic strength can be associated with a reduction in the thickness of the electrical double layer[22]. The consequential reduction in inter-particle repulsive forces allows particles to approach more closely and flocculate, thus the van der Waals attractions dominate and produce a cohesive suspension more resistant to flow[2].

3.2.2.3 Effect of Shear Rate on Viscosity

The shear thinning effect can be described in terms of shear induced hydrodynamic forces, which dominate Brownian motion and bring a degree of order to the suspension. Under shear, the particles or flocs are 'aligned' with streamlines, so as to

reduce their resistance to flow, consequently the apparent viscosity decreases with increasing shear rate[2].

Figures 3.3 to 3.9 all demonstrate the effect of shear rate on the viscosity of titania suspensions. It is evident from these that the degree of shear thinning exhibited is dependent on the pH and volume solids concentration of the suspension under examination[2], i.e. the degree of structure and inter-particle bonding present.

As solids concentration is increased (Figure 3.3), particles are forced into closer proximity and van der Waals forces become more significant. Likewise, an increase in ionic strength, leading to a reduction in the electrical double layer thickness, will also increase the significance of van der Waals forces. More strongly bonded particles will provide an increased resistance to flow, hence a higher yield stress is obtained. However, as the inter-particle bonds are destroyed by shear and the particles aligned, the reduction in viscosity becomes progressively easier, hence the shear thinning behaviour.

3.2.2.4 Effect of Temperature on Viscosity

Figure 3.10 shows that like other parameters, the effect of temperature on suspension viscosity becomes more evident as the suspension volume solids concentration is increased[2]. Unlike other parameters however, this effect is comparatively small and accounts for a drop of only 3mPas in 30K for a 30% volume solids suspension at pH 9 and a shear rate of 1000s[-1]. The effect at 10% volume solids is negligible

Changes in dispersion temperature affect the viscosity of the water in the suspension, and water tables[82] suggest a decrease in the water viscosity from 1.002 to 0.544 mPas as the temperature is increased from 293 to 323K. A rise in suspension temperature will also increase the value of diffusion coefficients for the translational and rotational movement of particles in suspension (Section **1.3.4**).

This, combined with the reduction in water viscosity, results in a halving of the Peclet number for a given shear rate as T is increased from 293 to 323K. (Calculated from the ratios of T/μ_o at the given temperatures (equations 1.5 and 1.6));

$$\frac{293/\mu_{o_{293}}}{323/\mu_{o_{323}}} = \frac{293/1.002 \times 10^{-3}}{323/0.544 \times 10^{-3}} = \frac{292415.1697}{593750} = 0.492 \qquad (3.1)$$
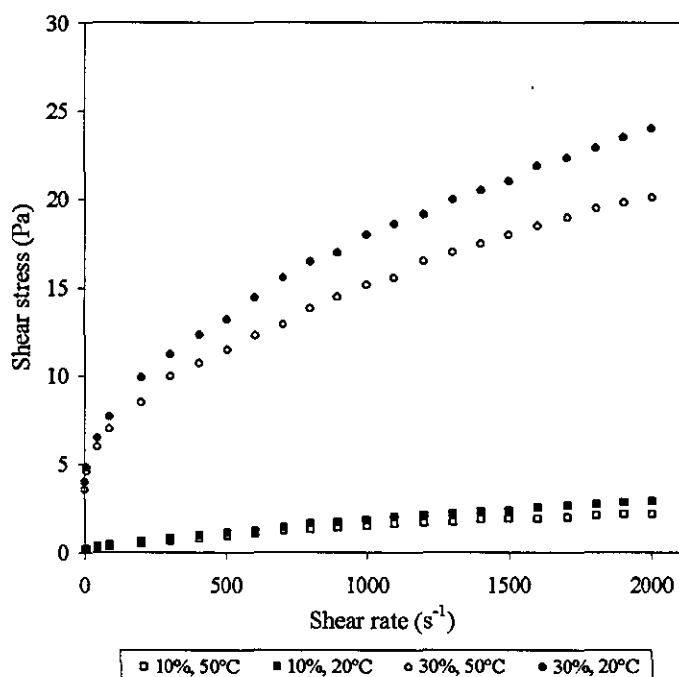
Figure 3.10 The effect of temperature on the viscosity of 10 and 30% volume solids calgon dispersed titania suspensions at pH 9

This implies that as the temperature of the system is increased, diffusive forces (Brownian motion) will dominate shear induced hydrodynamic forces to a greater extent, providing more resistance to the alignment of particles with streamlines[2].

The resulting yield stresses will be higher, the degree of shear thinning will be lower and the suspension should therefore be more viscous at a given shear rate. However, the experimental results observe a lowering of the shear stress and increased shear thinning which imply the existence of an additional mechanism. This could be a change in the state of ionic dissociation within the aqueous solution, affecting the strength of the particle electrical double layer. Increasing inter-particle repulsion could result in the observed changes in suspension rheology with temperature. These changes are, however, still very small over this range of temperatures.

3.2.3 Rheological Models

Rheological models were fitted to the experimental results using the Carrimed curve-fitting program. The two best fitting models are the Herschel Bulkley and Casson models[2], with the Casson model providing a more consistent fit with the data. The models are formally expressed by:

Herschel-Bulkley
$$\tau_w = \tau_y - \eta_1 \dot{\gamma}^n \qquad (3.2)$$

Casson
$$\tau_w = \left(\sqrt{\tau_y} + \sqrt{K}\sqrt{\dot{\gamma}}\right)^2 \qquad (3.3)$$

Where τ_w is the wall shear stress, τ_y is the yield stress, $\dot{\gamma}$ is the shear rate, n is the flow behaviour index, η_1 is the plastic viscosity or consistency coefficient for the herschel Bulkley model, and K is the consistency coefficient for the Casson model.

An apparent viscosity (μ_a) can be calculated using

$$\mu_a = \frac{\tau_w}{\dot{\gamma}} \qquad (3.4)$$

111

Constants for the Casson model were evaluated as a function of dispersion concentration, at pH 9.5, with a view to incorporating rheological behaviour into a predictive mathematical model for crossflow microfiltration using the Casson fit (Appendix VII). (The majority of crossflow experiments having been run at pH 9.5).

Consistency coefficient and yield stress data for calgon dispersed rutile at pH 9.5 was plotted as a functions of solids concentration (Figures 3.11 and 3.12).
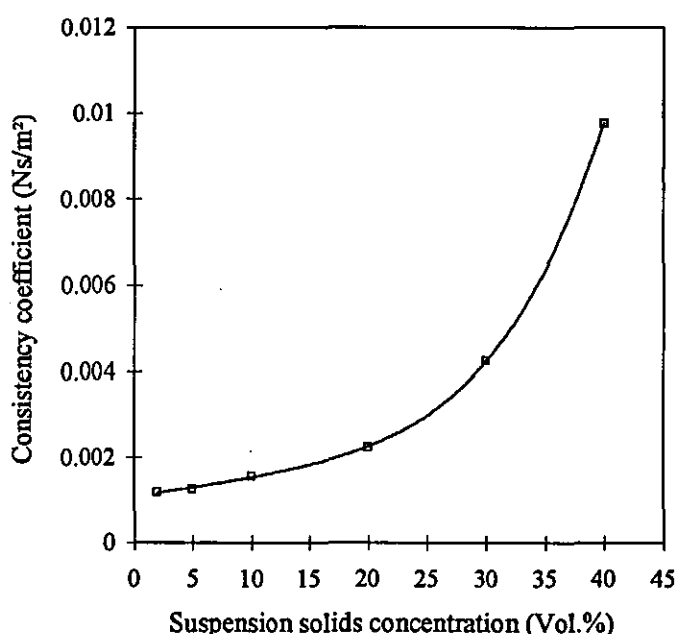
Figure 3.11 Casson consistency coefficient vs. solids concentration for calgon dispersed rutile at pH 9.5, data fitted with 4th order polynomial

The following fourth order polynomial gave a good fit to the consistency coefficient data:

Casson consistency coefficient

$$K = 5e\text{-}9C_s^4 - 2e\text{-}7C_s^3 + 3e\text{-}6C_s^2 + 3e\text{-}5C_s + 0.0011 \ (\text{Ns/m}^2)$$
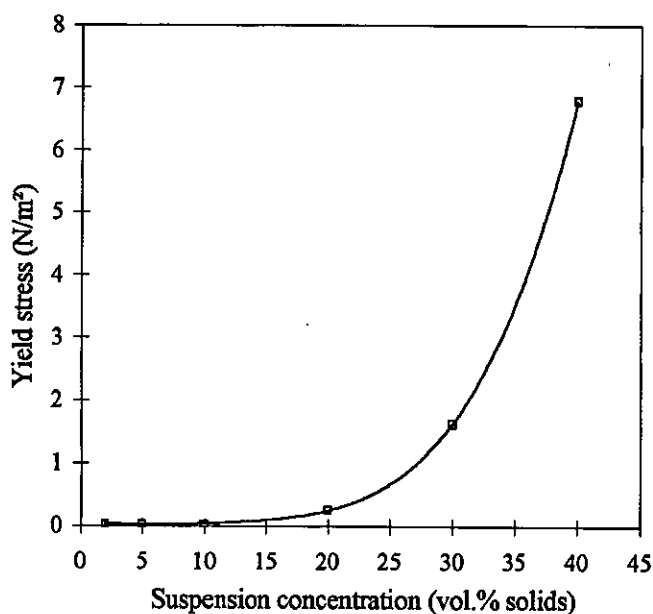
Figure 3.12 Casson yield stress vs. solids concentration for calgon dispersed rutile at pH 9.5, data fitted with 4th order polynomial

The following fourth order polynomial gave a good fit to the yield stress data:
Casson yield stress

$$\tau_y = 7e\text{-}6C_s^4 - 0.0003C_s^3 + 0.0042C_s^2 - 0.0255C_s + 0.0686 \ (N/m^2)$$

Where C_s is the percentage volume of solids in suspension.

Incorporating these polynomials into the Casson equation would yield the wall shear stress and therefore the apparent viscosity for any given solids concentration and shear rate at pH 9.5.

3.3 DISCUSSION OF EXPERIMENTAL RESULTS IN RELATION TO CROSSFLOW FILTRATION EXPERIMENTS

This investigation considered the effects of crossflow velocity, transmembrane pressure, suspension concentration, and suspension pH on the steady state permeate flux and achievable solids concentration during the crossflow microfiltration of calgon dispersed titania suspensions. The effect of each parameter in isolation was examined by observing its effect on steady state permeate flux over a range of values while maintaining all other variables constant. Calculations of crossflow velocity and permeate flux are based on the clean filter internal diameter.

Table 3.2 Process parameters studied in filtration experiments and their ranges

Parameter	Minimum value	Maximum value
Crossflow velocity (superficial)	0.33ms^{-1}	1.52 ms^{-1}
Transmembrane pressure	0.5 bar	2 bar
Suspension concentration	2% volume solids	48% volume solids
Suspension pH	pH 4	pH 9.5

Three sets of crossflow filtration experiments were performed in total; experimental sets A, B, and C. Experimental sets A and B were performed predominantly in concentrating mode where permeate was removed from the system until either the inventory was reduced to 14 litres or the filter tube choked with solids. Experiments in set C were performed at constant concentration by returning permeate to the feed tank, the experiments being run until a steady state permeate flux had been established.

3.3.1 Experimental set A

All experiments in set A were performed using well dispersed suspensions (pH 9.5) with a mean particle size of ≤0.32μm (Section **2.6.1.1**). Initial experiments, conducted in concentrating mode, did not reach a steady state as the volume fraction

114

of solids in the feed was constantly being reduced. Measurements of steady state permeate flux were therefore recorded as a function of the feed solids concentration. It was perceived however, that the relatively high solids concentrations being used in these experiments would result in the rapid establishment of a pseudo-steady state permeate flux. I.e., after the initial rapid flux decline where the clean filter is fouled, further measurements of permeate flux as a function of concentration could be considered equivalent to a steady state flux.

The first three experiments in series A recorded the change in permeate flux as the feed volume solids concentration was increased, by removal of permeate, from 2% to 50% (in three stages). Three further experiments were then performed at constant concentrations (15, 25 and 35% volume solids, by returning permeate to the feed) and the steady state permeate flux measurements compared to those obtained at the same solids concentrations in concentrating mode.

Table 3.3 Results for comparison of permeate flux data obtained at steady state with those obtained in concentrating mode.

Volume solids in feed (%)	13.9	24.5	32.8
Steady state permeate flux ($lh^{-1}m^{-2}$)	19.2	7.8	4.6
Permeate flux, concentrating feed ($lh^{-1}m^{-2}$)	17.9	8.1	4.6

This shows that the permeate flux data obtained by concentrating the suspension correlates well with that obtained at steady state while filtering a suspension at constant concentration.

Figure 3.13 is a plot of compiled data from the first three experiments, where feed suspensions were concentrated from 2% to 6%, 6% to 18%, and 18% to 50% volume solids. This shows the increase in suspension concentration and the corresponding decline in permeate flux with time.

It is evident that while the data collected in the latter experiments (6 to 18% and 18 to 50%) follows a steady trend, there is a tendency to decline to a much lower flux when starting at 2% solids. This could be the result of a different fouling regime at lower feed solids concentrations, where a lower flux of particles to the filter surface results in less pore bridging, a slower rate of cake build up, and therefore a greater degree of pore penetration. In this event, the resulting reduction in filter tube permeability would seem to be the primary factor in determining the achievable steady state permeate flux.
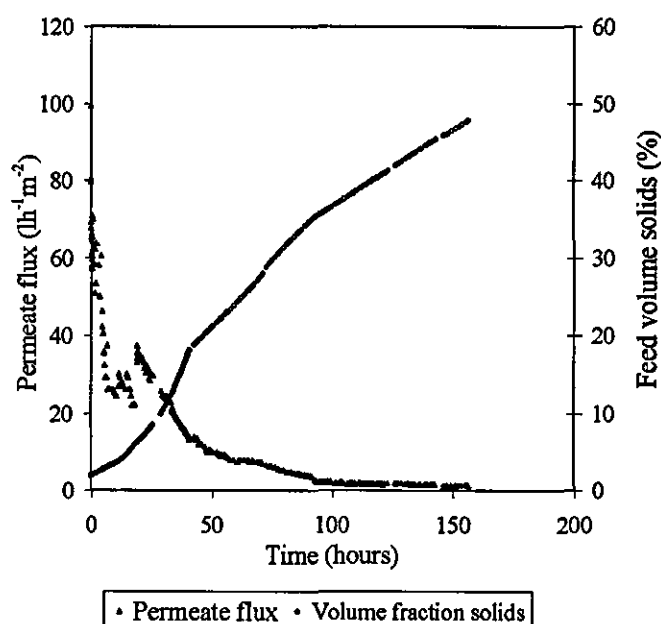
Figure 3.13 Compiled data from experiments A1r, A2 and A6r. Suspensions filtered at 1bar, 2ms^{-1}, pH 9.5 and 50°C

At higher feed concentrations however, the filter would act simply as a support for the filter cake, which would itself provide the main barrier to particles, and control the permeate flux.

116

This theory may be tested by applying the blocking filtration models developed by Hermia[30] to permeate flux decline data acquired in the series A experiments (Appendix III).

Appendix V shows that dead-end theory gives a good prediction of the initial flux decline in crossflow filtration, and the increase in suspension solids concentration during this period will be relatively small. The blocking models (derived for constant feed solids concentration suspensions in dead-end filtration) may therefore provide some indication of the type of fouling present during the initial stages of these experiments.

Figure 3.14 is typical of the poor fit obtained when fitting the data examined to the complete and intermediate blocking filtration models.
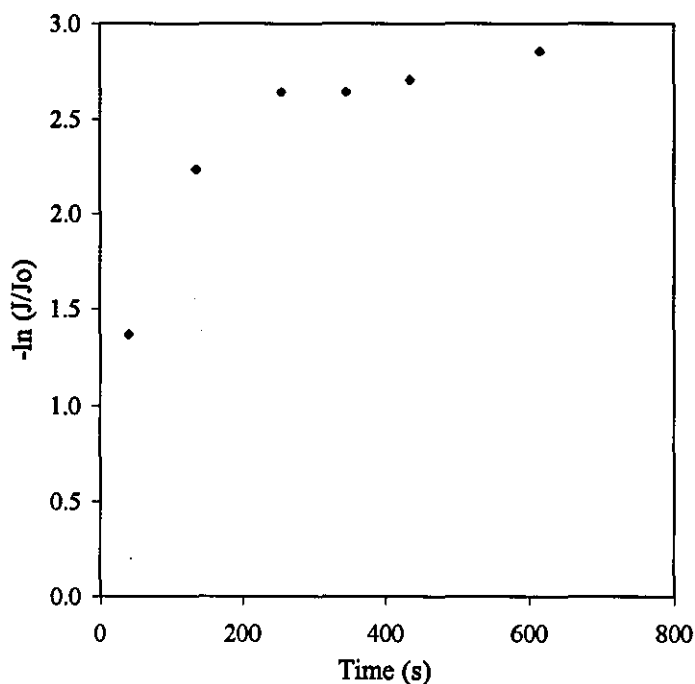
Figure 3.14 Complete blocking model fit to experiment starting at 6% volume solids

117

In comparison, the cake and standard filtration models give relatively linear relationships, with a good fit to their respective best-fit lines (Figures 3.15 to 3.18). The results of these plots are however inconclusive, as neither model appears to dominate the initial stages of filtration in either experiment.

Standard blocking is known to have affected the filter, as the membrane clean water flux was observed to drop after successive experiments (eventually reaching a steady level). There is also evidence of cake formation, provided by the choking of the filter tube when the feed suspension concentration reached approximately 48% (a sample of cake was removed from the filter suggesting a cake concentration of 59.5% volume solids). It is therefore evident that while both types of fouling are definitely present, the application of Hermia's[30] blocking filtration laws (if they are indeed applicable to these circumstances) to the flux decline data concerned does not favour one over the other.
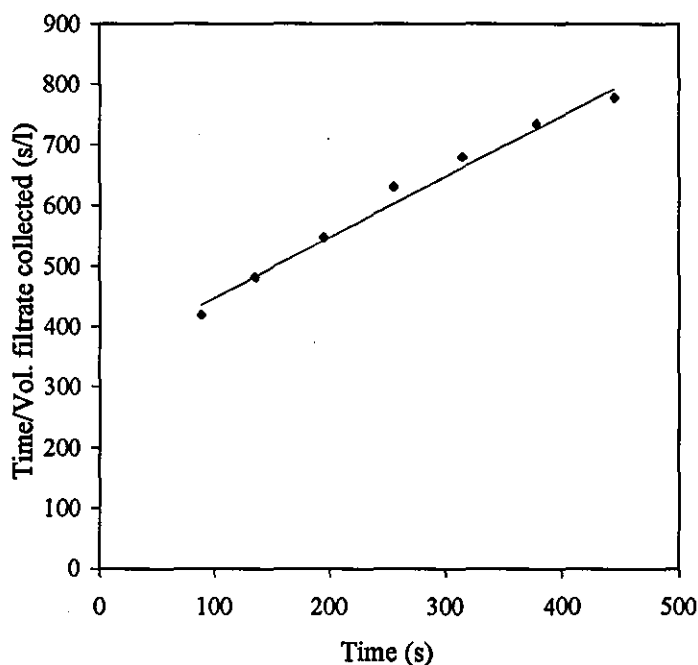
Figure 3.15 Standard blocking model fit to experiment starting at 2% volume solids
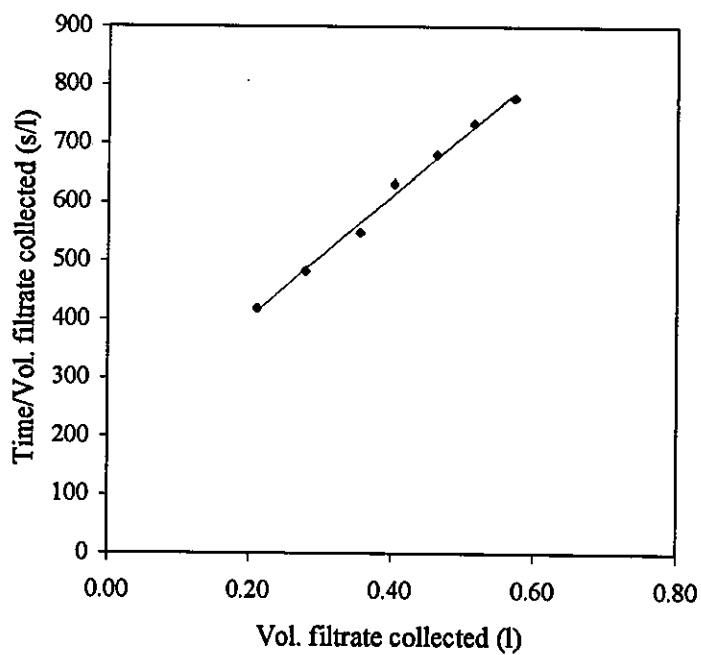
Figure 3.16 Cake filtration model fit to experiment starting at 2% volume solids
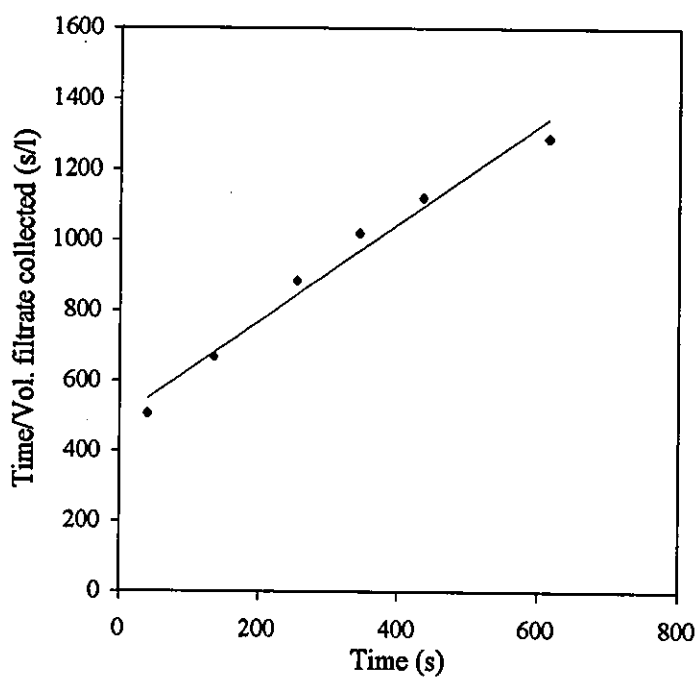
Figure 3.17 Standard blocking model fit to experiment starting at 6% volume solids

119
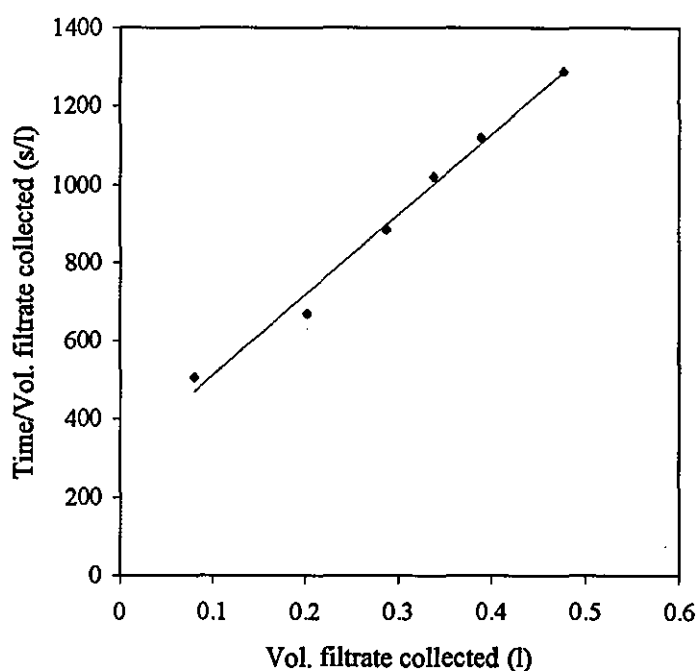
Figure 3.18 Cake filtration model fit to experiment starting at 6% volume solids

The series A results show therefore, that where a high volume solids feed suspension is used the steady state permeate flux is reached relatively quickly, and that by removing permeate to concentrate the feed suspension, a comprehensive set of pseudo steady state permeate flux data can be obtained for a wide range of feed solids concentrations. Due to the volume of liquid that must be removed at a very low permeate flux however, this method takes an extremely long time to complete (see abscissa of Figure 3.13). It is also evident that both standard blocking and cake filtration are present during the initial stages of flux decline, although neither regime has been proven to dominate.

3.3.2 Experimental set B

The concentrating experiments in set A were repeated in set B but using a flocculated suspension in order to examine the effects of particle size on permeate flux. The suspension pH was reduced to pH 4.0, which is around the IEP of the suspension (Figure 3.1). This gave a mean particle size of approximately 4μm, which is more than 10 times larger than the dispersed mean particle size.
Figure 3.19 shows the compiled flux decline curve for two experiments as permeate was removed and the feed solids concentration increased from 2 to 6% and 6 to 14% volume solids respectively.

Above feed concentrations of 14% volume solids, problems were experienced with foaming in the feed tank such that the rig could not be operated past this point. Comparing the data at pH 4.0 with that obtained at pH 9.5 (Figure 3.20), it is evident that the achievable permeate flux is much greater when filtering a flocculated system than a dispersed system, particularly at low feed concentrations. This results in a much faster rate of feed suspension concentration, and less than five hours were required to reach 14% volume solids compared with almost 40 hours for the dispersed system.

These results show that a flocculated suspension will give a higher steady state permeate flux than the equivalent dispersed suspension filtered at constant concentration. This is confirmed in results obtained by Tarleton and Wakeman[75] during the crossflow filtration of 1% volume solids concentration anatase suspensions at pH 2.45, pH 6.0 and pH 11.0 (Figure 1.17). A Zeta potential curve reveals the IEP for the anatase suspension (Figure 1.29) to be around pH 4, with a well flocculated suspension obtained at pH 2.45, and relatively well dispersed suspensions at pH 11.0 and pH 6.0.

The higher levels of permeate flux obtained using the flocculated suspensions can be attributed to the particle-pore size ratio, which was increased by an order of magnitude in the case of the dispersed and flocculated rutile suspensions.
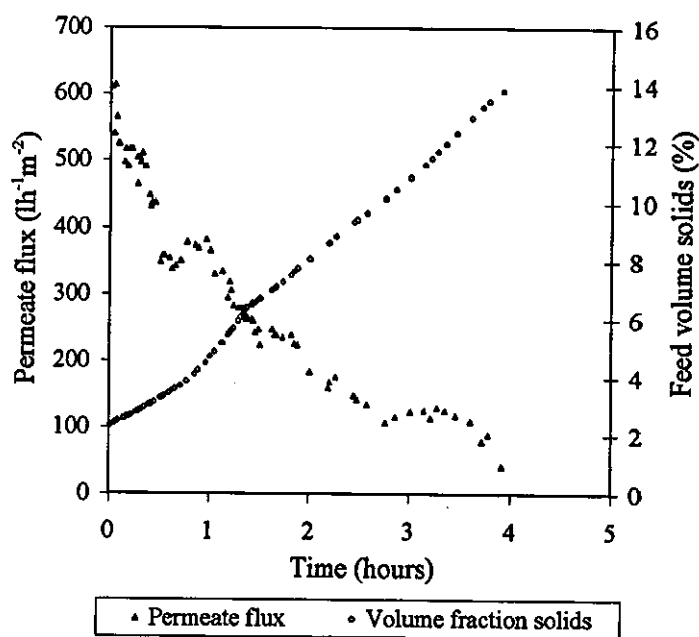
Figure 3.19 Compiled data from experiments B2 and B3. Suspensions filtered at 1bar, 2ms^{-1}, pH4 and 50°C
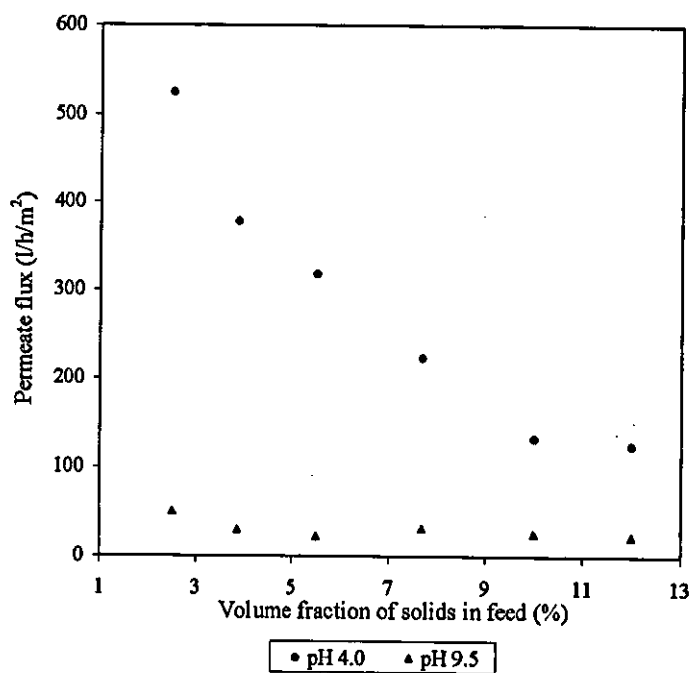
Figure 3.20 Permeate flux vs. feed solids concentration for flocculated and well dispersed suspensions

122

The particle size distribution within the flocculated suspension much reduces the probability of particles penetrating the 0.1μm filter pores, thus minimising any non-reversible, internal fouling of the microfilter. A further consequence of this is that there is no region of lower than expected permeate flux at low feed concentrations as was experienced with the dispersed suspension.

Additionally, the filter cake formed by the flocculated particles will have a much higher porosity than a cake formed by particles in a dispersed system under similar conditions. This will provide less resistance to permeate flow, hence much higher permeate fluxes are realised for flocculated suspensions than dispersed suspensions at similar feed concentrations.

This effect does however appear to become less pronounced as the feed solids concentration increases, and the flux-concentration curve for the flocculated system is seen to rapidly approach that of the dispersed system. This could be a result of inter-particle attraction, which (as is evident from Figures 3.3 to 3.9) increases rapidly as the suspension pH approaches the IEP, and as the suspension solids concentration is raised. Increasing the ionic strength results in a thinning of the electrical double layer and a reduction of the inter-particle repulsive forces, thus particles tend to aggregate. A further result of this is an increase in the solid-liquid interfacial tension such that water cannot penetrate the finer capillaries of aggregated particles. As the suspension feed concentration increases, these aggregates become larger, trapping water within their structures that can not easily be separated from the aggregates. It therefore becomes more difficult to remove water from the system and the permeate flux decreases much more rapidly than is experienced in a dispersed system.

3.3.3 Experimental Set C

Experiments in set C were performed using a well dispersed suspension, and run to steady state where the permeate flux was recorded as a function of suspension

concentration, crossflow velocity and transmembrane pressure. This method was chosen for the bulk of the crossflow filtration data acquisition as it was less time intensive and the shorter duration of experiments resulted in less deterioration of the pump stator than was experienced during the concentrating experiments of experimental sets A and B. The effects of variation in process parameters on permeate flux were observed for feed concentrations of 5, 12, 19, 25, 33 and 40% volume solids, transmembrane pressures between 0.5 and 2 bar, and crossflow velocities between 0.3 and 1.5ms^{-1} (calculated from experimentally measured volumetric flow rates, based on the clean filter diameter).

3.3.3.1 Effect of Process Parameters on Permeate Flux Decline

Figure 3.21 is a plot of four flux decline curves from experimental set C. These exhibit similar characteristics such as a large drop in permeate flux over the first 5 to 10 minutes, an approximate steady state after about 30 minutes, and a verifiable steady state after about 3 hours. It is however, evident from these curves, as noted by Mikulasek et al.[3], that the rate of flux decline from the start of the experiment to steady state is significantly dependent on the existing process parameters.

Increasing the feed solids concentration from 12% to 40% volume solids, results in a faster rate of flux decline, to a lower level, while doubling transmembrane pressure, at constant concentration, from 1 to 2 bar has little effect on the initial rate of flux decline but slows down more rapidly in intermediate stages. Increasing the crossflow velocity at constant concentration again has little effect on the initial stages of flux decline but results in a higher steady state value.

These results suggest that the primary factor controlling the initial stages of flux decline is the feed suspension solids concentration[3]. Higher concentrations will have a higher flux of particles to the membrane surface, thus the rate of decline will be faster (as shown in Figure 3.21). Transmembrane pressure and crossflow

velocity have no discernible effect until after the first few minutes of filtration when the disparity between curves of constant concentration becomes more apparent.
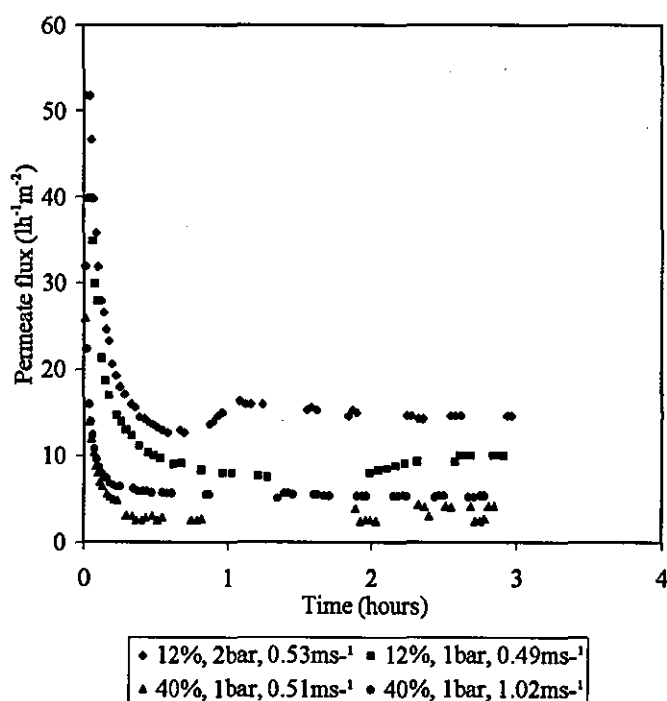
Figure 3.21 Effect of process parameters on flux decline at pH 9.5, 50°C

A number of the experiments, predominantly those at 2 bar transmembrane pressure and with feed volume solids concentrations of 19% or less, produced flux decline curves exhibiting what appear to be a pronounced damped oscillation (Figure 3.22). The permeate flux falls from the clean water flux to a minimum (often lower than the ultimate steady state flux) before rising again and finally declining to its steady state value. This phenomenon is not apparent in the flux decline curves of dead-end filtration experiments or crossflow filtration experiments cited in the literature (Section 1.6), suggesting that it is linked to both the mechanisms responsible for the realisation of steady state (Section 1.4), and the solids concentration of the feed stream.

125
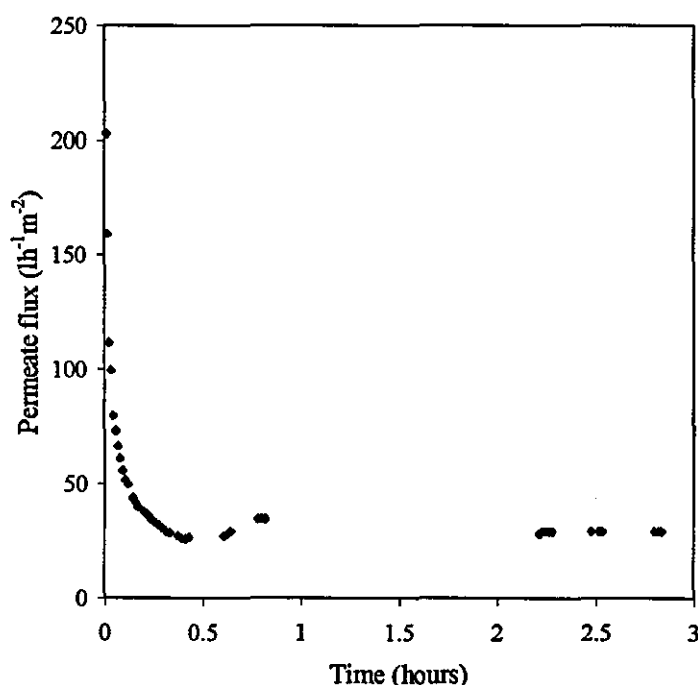
Figure 3.22 Permeate flux decline for a 5.5% volume solids suspension at 2bar, $0.75ms^{-1}$, pH 9.5 and 50°C

The driving forces for particle deposition and removal do not appear to interact progressively in these cases, instead the flux decline curves suggests an increase in cake thickness until a 'critical' wall shear stress is reached at which point there is an active removal of resistance to permeate flow. This could be a complete removal of the upper layers of the cake, or their fluidisation and mobilisation (in the form of a flowing cake layer with a lower solids concentration than the fixed cake) as the wall shear stress lifts and removes particles from the cake. The rise in permeate flux is then followed by a smooth decline to steady state as is normally experienced.

The fact that these oscillations occur predominantly in experiments conducted at 2 bar transmembrane pressure is significant. Experimental results suggest that these filter cakes are compressible (Section **3.3.3.2.2**), thus at higher transmembrane pressures a more compact cake may be formed from which particles cannot be so

easily removed at low shear rates. This could allow the filter cake to continue building up until the open flow diameter constricts to such a point that the critical wall shear stress described above is reached

At feed concentrations above 19% volume solids, the increased suspension viscosity and high initial rate of particle deposition may result in the presence of higher shear stresses from the outset of the experiment. These will be more effective at limiting cake growth from the early stages, thus a critical point may never be reached. Alternatively, the feed volumetric flow rate may be so low that the shear stress is unable to reach the critical point, even as the tube diameter is reduced, thus a lower than expected steady state permeate flux is obtained.
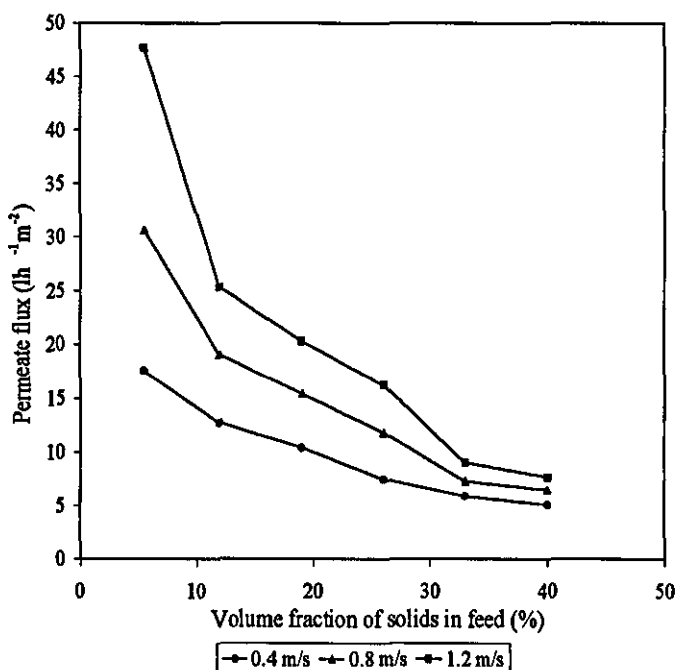
Figure 3.23 Permeate flux vs. suspension solids concentration at 2bar, pH 9.5, 50°C

This second theory is reinforced by the crossflow filtration results for experimental set C at 2 bar (Figure 3.23), which show a disproportionately high permeate flux at low feed solids concentrations and high crossflow velocity. These higher than expected fluxes have been largely obtained from experiments that exhibited these oscillating flux decline curves

This suggests that where the feed volumetric flow rate is sufficient, but transmembrane pressure is high, the mechanisms of particle removal have a reduced effect until the wall shear stress reaches a critical value after which the removal of particles from the well packed cake becomes possible.

3.3.3.2 Effects of Process Parameters on Steady State Permeate Flux

The effects of feed solids concentration, transmembrane pressure and crossflow velocity can be seen in Figures 3.23, 3.24, and 3.28 to 3.30 (see also Appendix IV). Figures 3.23, 3.24 and 3.30 demonstrate the effect of feed solids concentration and superficial crossflow velocity at fixed transmembrane pressures while Figures 3.28 and 3.29 demonstrate the effect of solids concentration and transmembrane pressure at fixed superficial crossflow velocities.

3.3.3.2.1 Feed Suspension Solids Concentration

Figure 3.24 shows clearly the decline in achievable steady state permeate flux with increasing feed solids concentration[3] where all other parameters are held constant. This is consistent with data available in the literature (Section 1.6.2.1) and a logical result of the higher flux of particles to the filter cake/surface[3]. Visualisation studies by Wakeman[65] show that higher feed solids concentrations result in thicker steady state filter cake deposits, thus the resistance to permeate flow increases and consequently reductions are observed in the steady state permeate flux.

128
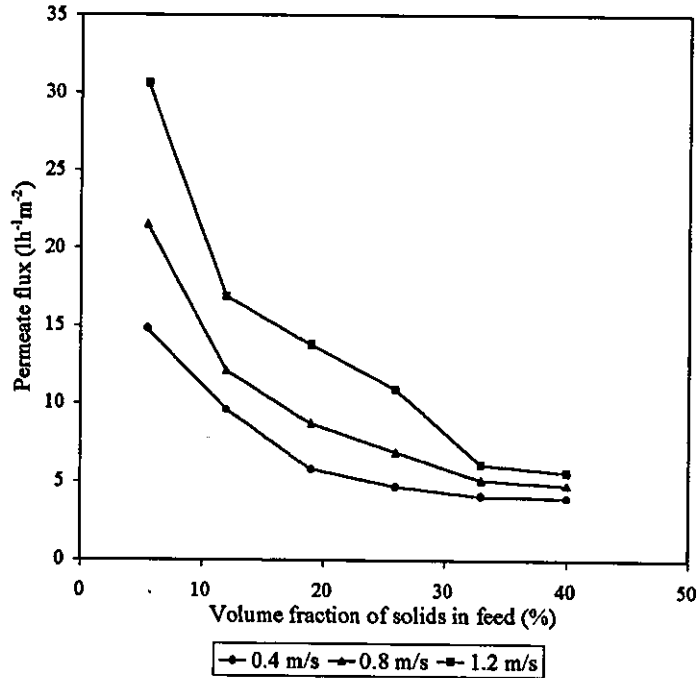
Figure 3.24 Permeate flux vs. suspension solids concentration at 1bar, pH 9.5, 50°C

Assuming a constant value for the specific cake resistance, the modified Darcys law equation (equation 1.14) can be used to determine a relationship between steady state filter cake thickness and feed solids concentration for the data in Figure 3.24 (Appendix IV).

$$ J_{ss} = \frac{\Delta P_{TM}}{\mu_p \left(R_m + R_c H_o \ln\left[\dfrac{H_o}{H_o - \delta_{css}} \right] \right)} \tag{1.10} $$

δ_{css} is the steady state cake thickness and J_{ss} is the steady state permeate flux (calculated using the clean filter diameter).

129

Figure 3.25 reveals this relationship to be approximately linear (for the data at a superficial crossflow velocity of 0.8ms^{-1}), and suggests an increase in cake thickness to approximately 5.5mm at a feed volume solids fraction of 40%.
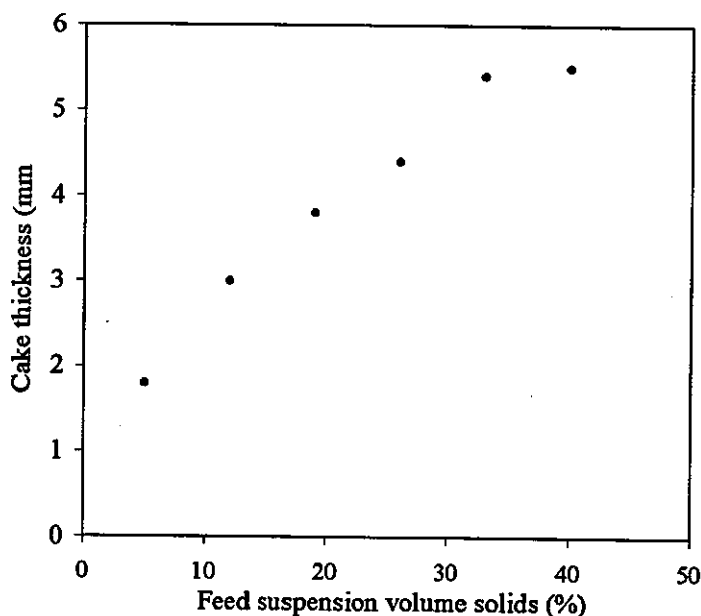
Figure 3.25 Cake thickness vs. feed solids fraction, calculated using equation 1.14 and steady state permeate fluxes from fig 3.24 at 0.8ms^{-1}

The consequence of these thick cakes is a reduced diameter open to flow and therefore, at constant feed volumetric flow rate, an increased crossflow velocity. Calculating crossflow velocities from the values of cake thickness in Figure 3.25 (Appendix IV) suggests an increase in crossflow velocity to over 8ms^{-1} at 40% volume solids (Figure 3.26).

Thus, although a higher solids concentration feed suspension will result in an increased flux of particles to the filter surface, the increased cake thickness has implications for the wall shear stress and therefore the mechanisms, which limit cake development in crossflow filtration.
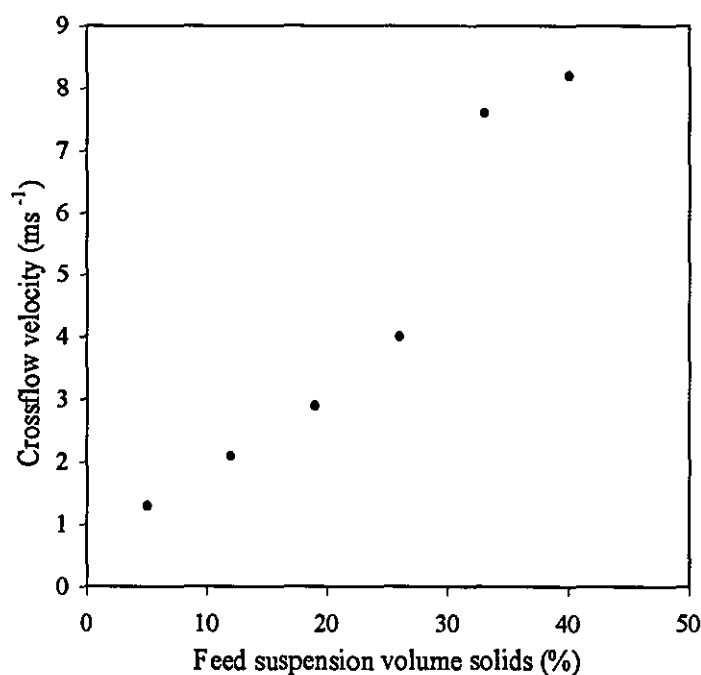
Figure 3.26 Crossflow velocity vs. feed solids fraction, based on data taken from Figure 3.24

As successive particles attempt to deposit themselves on the filter surface, thus reducing the diameter open to flow (d_f), the shear rate ($\dot{\gamma}$) increases according to equation 3.5 for Newtonian suspensions (where Q is the feed volumetric flow rate).

$$\dot{\gamma} = \frac{32Q}{\pi d_f^3} \qquad (3.5)$$

The shear rate can be related to wall shear stress using the Casson equation (equation 3.3), and this shows that at constant feed volumetric flow rate, any reduction in the open flow diameter results in a disproportionate increase in shear stress.

Additionally, an increase in the feed solids concentration also results in increased values of yield stress (Figure 3.12) and consistency coefficient (Figure 3.11), and

substituting these values into the Casson model reveals a disproportionate increase in wall shear stress with feed solids fraction over a range of shear rates (Figure 3.27).
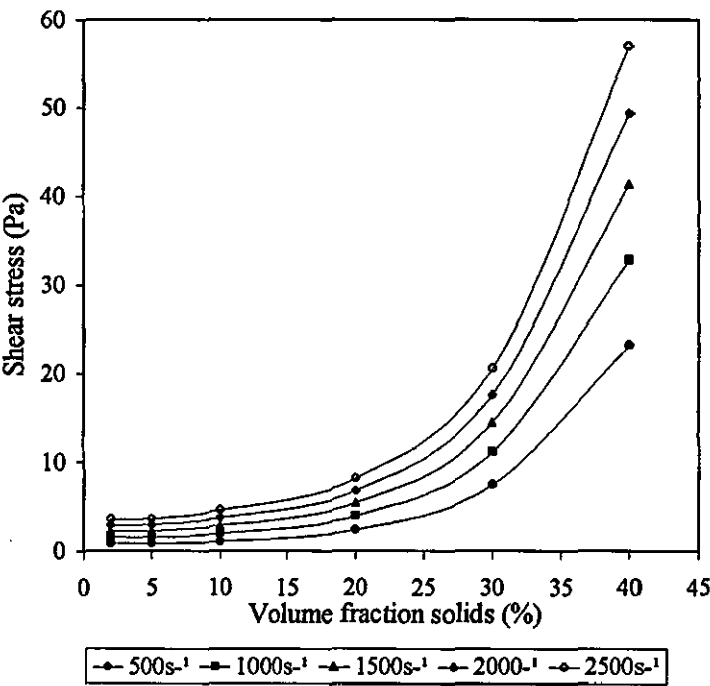
Figure 3.27 Effect of feed solids conc. on wall shear stress (Appendix IV.3)

The potential for increasing cake thickness at higher feed solids concentrations is therefore limited by the simultaneous and disproportionately large increases in wall shear stress. The rate of increase in cake thickness, and consequential reduction in steady state permeate flux, is thus reduced with increasing feed solids concentration, as in Figure 3.24.

The effects of pH, crossflow velocity and transmembrane pressure on permeate flux are all more pronounced at low concentrations and have reduced effects at higher concentrations[3].

3.3.3.2.2 Transmembrane Pressure

Figure 3.28 shows the effect of transmembrane pressure on permeate flux as it is increased between 0.5 bar and 2 bar.
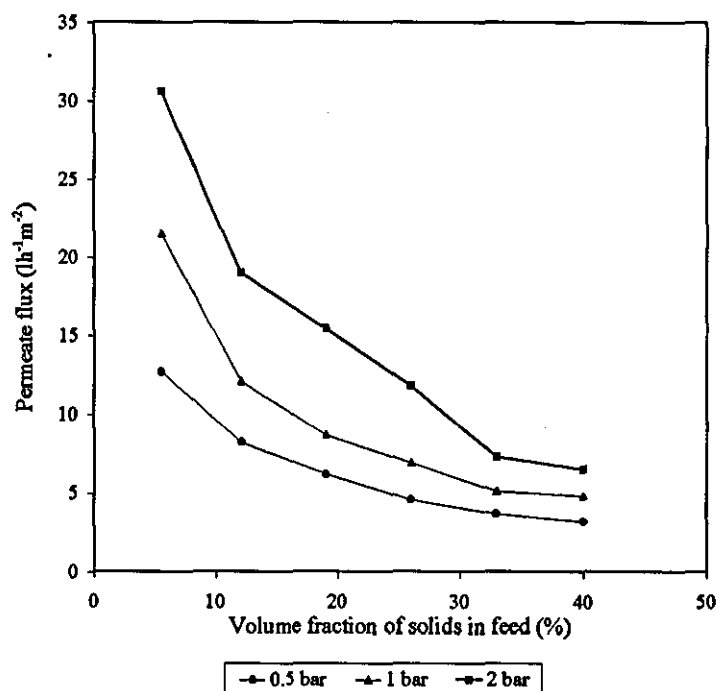
Figure 3.28 Permeate flux vs. suspension solids concentration at 0.8ms^{-1}, pH9.5 and 50°C

Again, the effect of solids concentration is evident, and the improvements in flux obtained at higher transmembrane pressures are progressively reduced as the feed solids fraction increases[3].

The principal effect of increased transmembrane pressure in crossflow filtration is to increase the flux of suspension to the filter surface. The expected increase in permeate flux as a result of this is offset to a degree by the associated increase in the flux of particles to the filter surface, the resulting thicker filter cake increasing the resistance to permeate flow. The increased transmembrane pressure may also

compress the filter cake, thus reducing its porosity and further increasing the cake resistance. Consequently, the overall effect of increasing transmembrane pressure on a crossflow system depends on the composition and compressibility of the filter cake.

Figure 3.29 (like 3.28) shows that each increase in transmembrane pressure results in a non-proportional increase in permeate flux.
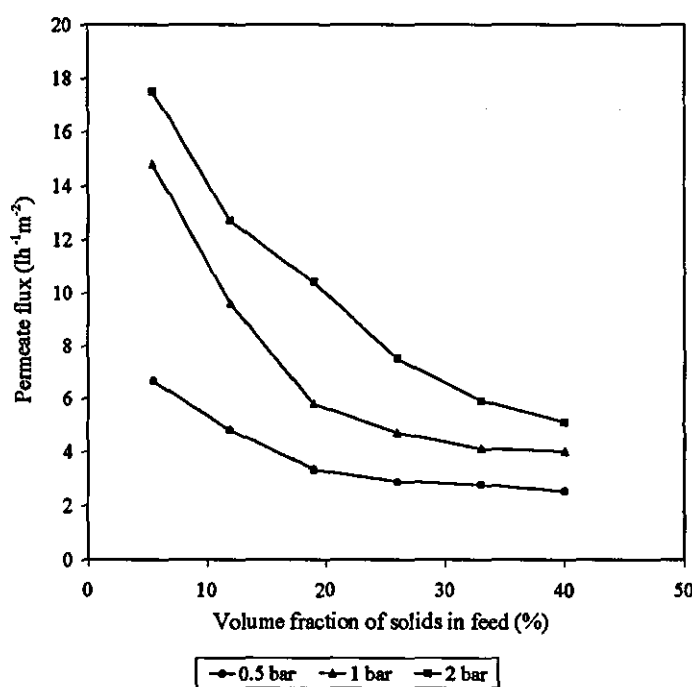
Figure 3.29 Permeate flux vs. suspension solids concentration at $0.4ms^{-1}$, pH9.5, 50°C

This is a result of either cake compression, increasing cake thickness or, more likely, a combination of the two mechanisms.

Tarleton and Wakeman[75] obtained similar results for the crossflow filtration of calcite suspensions at transmembrane pressures of 10, 30, and 50psi (Figure 1.24). The progressively smaller improvements in steady state permeate flux for each successive increase in transmembrane pressure demonstrates the possibility that at

higher transmembrane pressures the increased flux of particles and degree of cake compressibility may nullify any advantages that might otherwise have been obtained.

The mean particle size of the calcite suspension (2.7μm) is significantly larger than that of the rutile suspensions used in this study (0.3μm), so further work by Tarleton and Wakeman[75] which concerned the crossflow filtration of anatase (0.5μm) would be expected to provide closer fitting results to those obtained for rutile. However, despite the similarity in their particle/pore size ratios (0.5/0.2 for anatase and 0.3/0.1 for rutile), the anatase system exhibited extreme reductions in the steady state permeate flux at transmembrane pressures above 10psi (Figure 1.30).

Tarleton and Wakeman[75] explained this reduction in flux as a consequence of denser particle packing at higher transmembrane pressures, and this theory is supported by dead-end filtration tests[62] and cake composition analysis in which Baker *et al.*[73] found that anatase filter cakes formed at increased transmembrane pressures had a higher fines content (Figure 1.33).

It is possible that raising the transmembrane pressure could increase the degree and severity of pore blocking in the initial stages of filtration. The high solids concentration feed suspensions used in this study however, are likely to result in pore bridging almost instantly so that although the degree of initial pore penetration may rise marginally with transmembrane pressure, the faster rate of particle deposition traps fines at an earlier stage, thus preventing excessive pore plugging. Further to this, the deposit formed while filtering the higher solids concentration feed will be so great at steady state that in comparison the resistance provided by the membrane itself is negligible.

3.3.3.2.3 Superficial Crossflow Velocity

Figure 3.30 demonstrates the effect of crossflow velocity on steady state permeate fluxes over a range of feed suspension concentrations and transmembrane pressures.
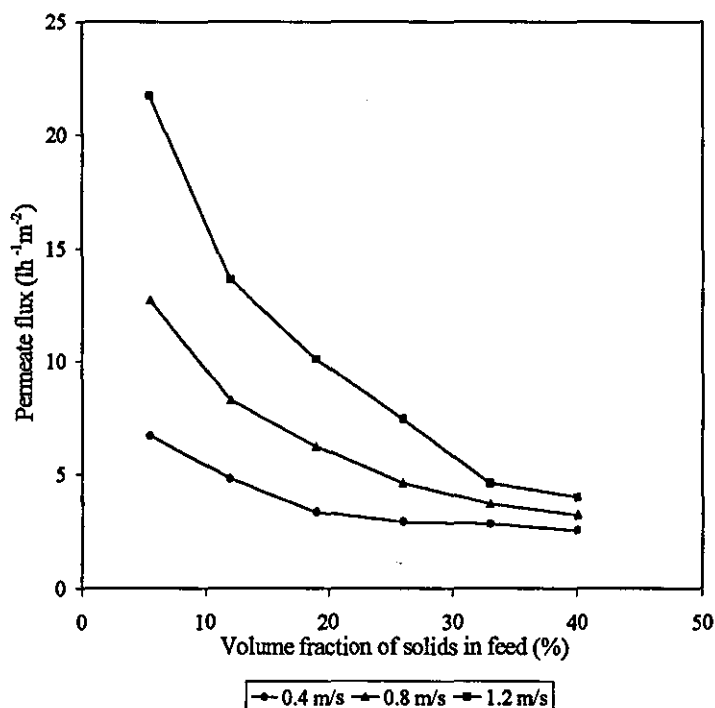
Figure 3.30 Permeate flux vs. suspension solids concentration at 0.5bar, pH 9.5 and 50°C

It is evident from these results that, when holding all other process parameters constant, an increase in the crossflow velocity will lead to an improvement in steady state permeate flux.

The values of crossflow velocity referred to in this work are calculated from the experimentally determined feed volumetric flow rates and based on the clean filter diameter (16mm), i.e. no corrections are made for the reduction in diameter

resulting from cake build up. These values can therefore be regarded as "feed velocities" or "superficial crossflow velocities".

The effect of raising crossflow velocity is to increase the shear stress parallel to the filter/cake surface, and as such it is the parameter that limits the rate of particle deposition in crossflow filtration and is therefore ultimately responsible for the onset of steady state[3].

The most likely mechanism of particle removal, and the one observed in visualisation studies[44,65] is described by pure convection models (Section **1.4.9**) which balance the deposition rate of particles with the longitudinal movement of all or part of the cake layer. Leonard and Vassilief[64] suggest that the filter deposit is comprised of a densely packed, stagnant cake on the membrane surface and a less dense mobile layer at the cake-suspension interface induced by the shear stress of the crossflowing stream. Smaller particles entering the filter cell are drawn to the flowing layer where they roll along the cake surface to the filter cell exit[65]. Larger particles with sufficient momentum however will remain on their streamlines, thus the crossflow filtration of a wide particle size distribution suspension results in the preferential deposition of fines in the filter cake and this effect is enhanced with increasing crossflow velocity[65]. This, combined with the agitation of particles in the mobile layer results in a well consolidated filter cake with a higher than expected specific resistance (based on the mean particle size of the suspension), that increases with crossflow velocity[3].

The filtration of unground calcite suspensions[62] (Figure 1.27) is a typical example of the preferential·deposition of fines from suspensions exhibiting a wide particle size distribution (mean particle size 24μm). In this case the specific cake resistance increases to the extent that it outweighs the benefit of any cake thinning, and the steady state permeate flux actually decreases with increasing crossflow velocity.
The results for rutile fit more closely with those obtained for anatase suspensions[62] (Figure 1.31) exhibiting significant increases in permeate flux with rising crossflow velocity. This suggests a reduced resistance to permeate flow in the form of cake

thinning and also that there is negligible change in cake composition. This fits the hypothesis that smaller mean particle size suspensions with narrow size distributions consolidate well in crossflow filtration, thus resisting increases in specific cake resistance with crossflow velocity (Figure 1.26).

Without employing the use of visualisation techniques, it is impossible to determine the exact depth and distribution of filter cake thickness formed in any one of these experiments. It would however be possible to approximate a cake thickness (assuming uniform thickness along the tube length) by substituting non-porous tubes of known internal diameter in place of the filter tube[83]. The pressure drop over the tube length could be measured and plotted as a function of feed flow rate and tube diameter, thus enabling a value for the open flow diameter to be determined for any crossflow experiment at steady state where the feed volumetric flow rate and associated tube length pressure drop were known.

CHAPTER FOUR

MODELLING CROSSFLOW FILTRATION

The ability to predict steady state permeate fluxes in crossflow filtration, without the need for prior experiments, would be a valuable tool in the design of crossflow filtration equipment. It was thus desirable to develop a model that, by incorporating expressions for the operating conditions, filter cake packing characteristics, and feed suspension rheology, could be applied to range of process operating conditions and feed suspensions.

Preliminary work in this study considered the application of dead-end filtration models to crossflow filtration, comparing the fit of theoretical flux decline curves with those obtained experimentally. An existing crossflow filtration model was then used to aid prediction of steady state filter cake thicknesses, and this led to the development of a new model for predicting steady state permeate flux.

4.1 DEAD-END FILTRATION MODELS FOR FLUX DECLINE

The application of dead-end filtration theory to crossflow filtration was evaluated by comparing flux decline curves obtained in the experimental study, with theoretical curves for dead-end filtration under similar process conditions. The theoretical flux decline curves were produced using equation 4.1, which was derived for constant pressure, dead-end filtration processes with incompressible membranes and cakes[37].

$$J(t) = \frac{J_o}{\left(1 + \dfrac{t}{\tau_c}\right)^{1/2}} \qquad (4.1)$$

139

The clean water flux (J_o) was determined experimentally (for the crossflow experiments), t is the time after the commencement of filtration, and τ_c is a time constant determined using equation 4.2[37].

$$\tau_c = \frac{R_m (\phi_c - \phi_b)}{2 J_o R_c \phi_b} \tag{4.2}$$

The membrane resistance (R_m) was evaluated using Darcys law (equation 4.3), and the specific cake resistance (R_c) using the Blake-Kozeny equation (4.4)[33,37]. The volume fraction of solids in the cake layer (ϕ_c), permeate viscosity (μ_p) and mean radius of the particles in suspension (a) were obtained experimentally, and the volume fraction of solids in the bulk feed (ϕ_b), and experimental transmembrane pressure (ΔP_{TM}) were set process conditions.

$$R_m = \frac{\Delta P_{TM}}{\mu_p J_o} \tag{4.3}$$

$$R_c = \frac{150 \phi_c^2}{(2a)^2 (1 - \phi_c)^3} \tag{4.4}$$

Figures 4.1 and 4.2 (see also Appendix V) reveal a good approximation of the theoretical dead-end filtration curves to experimental data in the initial stages of crossflow filtration[3]. For longer filtration times however, the experimental flux levels out while the theoretical flux continues to decline.

The departure from dead-end theory, and the presence of a steady state in crossflow filtration arise as a result of arrested cake growth, which occurs when the rate of particle removal from the filter cake equals the rate of particle deposition, or when the shear stress at the cake surface is high enough to prevent further deposition of particles[3] (Section **1.4.3**).

140

These phenomena are entirely due to the shear stress applied by the crossflowing suspension, and the effect of increasing shear stress (crossflow velocity) on the rate of flux decline and level of steady state flux can be seen by comparing Figure 4.1 with Figure 4.2.
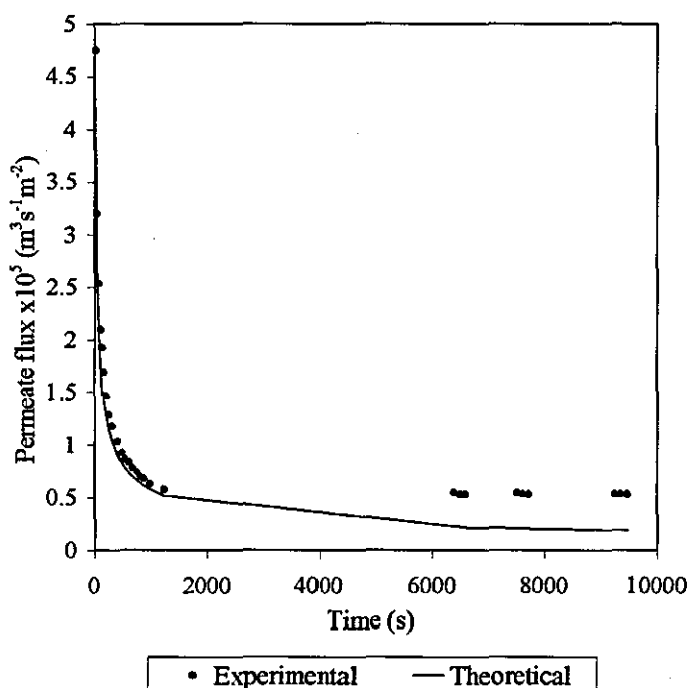
Figure 4.1 Experimental and theoretical permeate flux decline curves, 5.5% volume solids, 1bar, 0.68ms^{-1}, pH9.5, 50°C

The rate of particle deposition is a function of both the transmembrane pressure and the feed suspension solids concentration, while the mechanisms of particle removal, such as shear induced diffusion or inertial lift (Section **1.4.3**), are related to the crossflow velocity. As the filter cake thickness increases, the reduction in tube diameter (at constant volumetric flow rate) results in an increased crossflow velocity and therefore an increased wall shear stress. The mechanisms of particle removal are therefore enhanced with increasing filtration time, whilst the

141

convective flow of particles to the filter cake simultaneously decreases (at constant transmembrane pressure), with the reduction in permeate flux.
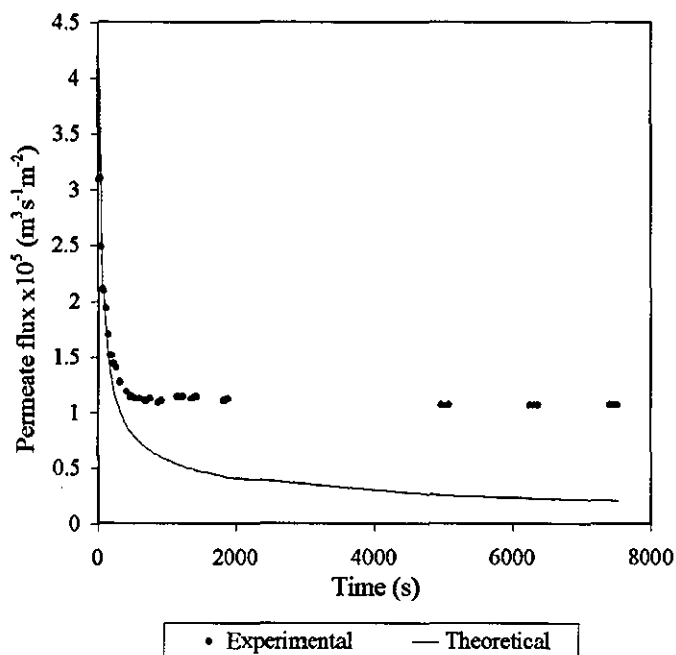
Figure 4.2 Experimental and theoretical permeate flux decline curves, 5.5% volume solids, 1bar, 1.56ms^{-1}, pH9.5, 50°C

If it were possible to model the opposing forces of particle deposition and removal leading to steady state, it might also be possible to predict the arrest in cake growth and thus a steady state cake thickness. Darcy's law could then be used to determine the steady state permeate flux using equation 4.5 (where δ_c is the filter cake thickness).

$$J(t) = \frac{\Delta P_{TM}}{\mu_p (R_m + R_c \delta_c(t))} \qquad (4.5)$$

For filtration through a tubular filter, this equation assumes the formation of a thin cake layer relative to the tube radius, as do the majority of predictive crossflow filtration models[58], such as those based on mechanisms of Brownian diffusion, shear induced diffusion, and inertial lift. The concentrated nature of the suspensions used in this study however, often resulted in a significant thickness of cake relative to the cross section of the filter tube. Steady state cake thicknesses of at least 5mm were removed from the filter, and experiments performed in concentrating mode showed that at 48% feed volume solids concentration the filter tube choked, i.e. the deposit completely filled the tube cross section (Section **3.3.1**).

Equation 4.5 was therefore modified for filtration through a tubular filter with a significant depth of filter cake[37] giving equation 4.6, which incorporates a curvature correction factor to account for the reduced surface area available for filtration. H_o is the clean tube radius.

$$J(t) = \frac{\Delta P_{TM}}{\mu_p \left(R_m + R_c H_o \ln\left[\frac{H_o}{(H_o - \delta_c(t))} \right] \right)} \qquad (4.6)$$

4.2 HOLDICH et al.[84,85] MODEL FOR PREDICTING CAKE THICKNESS

Holdich et al[84,85] and Ismail[86] developed the following steady state, crossflow microfiltration model relating the diameter of a fouled tubular filter that remains open to flow (d_f), to process parameters and physical properties of the cake, permeate and feed suspension.

$$d_f^3 = \frac{k_1 x f \rho_m 4 Q^2 \mu_p}{\pi^2 \Delta P_{TM}} \left[\frac{\ln\left(d_o / d_f\right)}{K_c} + \frac{2R_m}{d_o} \right] \cdot \qquad (4.7)$$

The constant $(k_1 x)$ is determined empirically, f is the fanning friction factor (from the Reed-Metzner correlation for non-Newtonian flow[87]), ρ_m is the feed suspension density, Q is the volumetric flow rate of feed suspension, μ_p is the permeate viscosity, ΔP_{TM} is the transmembrane pressure, d_o is the clean filter tube diameter, R_m is the membrane resistance, and K_c is the filter deposit permeability.

Once a value for the empirical constant $k_1 x$ has been determined for a particular solid-liquid system, equation 4.7 can be solved by iteration to find the diameter open to flow (d_f) and therefore the steady state cake thickness, for that specific system, under any set of process conditions.

The value of $k_1 x$ for a given system is determined by performing crossflow experiments on that system over a range of transmembrane pressures and crossflow velocities. The steady state permeate flux (J_{ss}) is then plotted against wall shear stress (τ_w) for all the experiments, the result of which should reduce to a single correlation[85] of the form;

$$J_{ss} = k_1 x \tau_w + k_0 \qquad (4.8)$$

Thus verifying the work of Blake, Cumming and Streat[48] on which equation 4.7 is based. Equation 4.8 was derived from a force balance on any given particle in a filter cake[48] and gives two empirical constants $k_1 x$ and k_0. For the purpose of equation 4.7, k_0 is assumed to be zero, thus $k_1 x$ can be calculated from knowledge of J_{ss} and τ_w alone. Steady state permeate flow is measured experimentally, while the shear stress at the filter cake surface is calculated from equation 4.9 using the experimentally measured pressure drop along the length of the filter tube (ΔP_L) and the filter tube length (L);

$$\tau_w = \frac{d_f \Delta P_L}{4L} \qquad (4.9)$$

Calculation of τ_w and J_{ss} however, still require knowledge of the diameter open to flow at steady state (d_f), the resolution of which is also the goal of the exercise.

4.2.1 Determination of the Open Flow Diameter by Holdich *et al.*[84,85]

To solve this problem, Holdich *et al.* performed a series of experiments on their crossflow apparatus using non-porous tubes of known internal diameter in place of the filter tubes[83]. The pressure drop over the tube length was measured and plotted as a function of feed flow rate and tube diameter, this enabling a value of d_f to be determined for any crossflow experiment at steady state where the feed volumetric flow rate and the associated tube length pressure drop were known. The shear stress (τ_w) and steady state permeate flux (J_{ss}) could then be calculated, and consequently, the empirical constant $k_1 x$ for a given system. Substituting this into equation 4.7 then allowed the diameter open to flow to be predicted for that particular system under any process conditions.

Holdich *et al.* concluded[84] that the deposit thickness was significant where high solids concentration suspensions were concerned, and that its consideration was essential in any calculation of wall shear stress. It was also stated that any

determination of pressure drop along the length of the filter tube, where the pressure transducers are located a significant distance from the entry and exit points of the tube, must consider the pressure loss resulting from changes in the flow diameter and recirculation zones at the tube exit.

4.2.2 Alternative Method for Determination of the Open Flow Diameter

In the absence of empirical data relating tube diameter, flow rate and tube length pressure drop (as obtained by Holdich *et al.*[83]) it was necessary to estimate an initial value of d_f, in order to calculate τ_w (using equation 4.9) and J_{ss}, and consequently resolve a value for k_1x (Appendix VI).

Assuming that equation 4.8 held true, and that k_o was equal to zero (as in the derivation of 4.7[85]), the correct estimation of d_f would yield the correct value of k_1x for a given system (equation 4.10).

$$k_1 x = \frac{J_{ss}}{\tau_w} = \frac{4LJ_{ss}}{d_f \Delta P_L} \qquad (4.10)$$

Substituting k_1x into equation 4.7 and solving for d_f would reveal the accuracy of the initial estimate of d_f, which could then be corrected and the procedure repeated. By this method, k_1x changes with each iteration of d_f, and when the iteration has been successfully completed, both d_f and k_1x have been determined.

The steady state diameter open to flow (d_f) was determined in this manner for a number of experiments at different feed flow rates and transmembrane pressures, and the resulting values of wall shear stress (calculated using experimentally measured ΔP_L and iteratively determined value of d_f) plotted against steady state permeate flux. This should have reduced to a single calibration (as found by Holdich *et al.*[84,85]) but the result was instead a sporadic array of points (Figure 4.3).

146
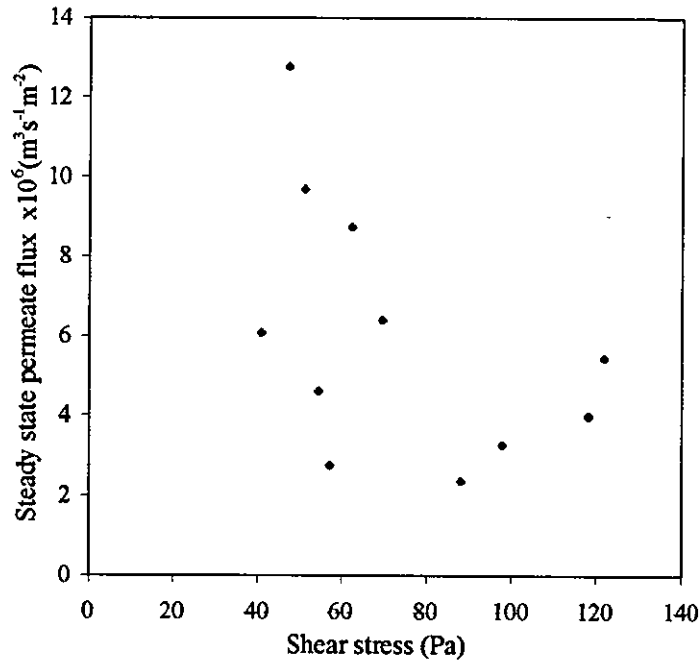
Figure 4.3 Determination of empirical constant k_1x for rutile suspensions in crossflow

4.2.3 Validity of Equation 4.7

Holdich et al.[85] obtained equation 4.7 by rearranging equation 4.11[85] for the diameter open to flow (d_f).

$$\Delta P_{TM} = k_1 x \frac{f}{2} \rho_m \left(\frac{4Q}{\pi d_f^2} \right)^2 \frac{\mu}{2} \left[\frac{d_f}{K_c} \ln\left(\frac{d_o}{d_f} \right) + 2R_m \frac{d_f}{d_o} \right] \qquad (4.11)$$

Equation 4.11 was in turn obtained by substituting equation 4.12 into 4.13[85], and Equation 4.12 is the result of substituting equation 4.14[85], into equation 4.8, assuming the constant k_o equal to zero.

$$\frac{Q_p}{\pi d_f L} = J = k_1 x \frac{f \rho_m}{2} \left(\frac{4Q}{\pi d_f^2} \right)^2 \qquad (4.12)$$

147

$$\Delta P_{TM} = \frac{Q_p}{\pi d_f L} \frac{\mu}{2} \left[\frac{d_f}{K_c} \ln\left(\frac{d_o}{d_f}\right) + 2R_m \frac{d_f}{d_o} \right] \qquad (4.13)$$

$$\tau_w = \frac{f \rho_m}{2} \left(\frac{4Q}{\pi d_f^2} \right)^2 \qquad (4.14)$$

Equation 4.11 thus contains an expression for shear stress at the filter wall from the definition of Fanning friction factor (Equation 4.14).

The empirical constant $k_1 x$ is also determined using an expression for shear stress at the filter wall (Section 4.2.1), although in this case it is calculated using equation 4.9, thus equation 4.11 contains a second expression for wall shear stress.

The iterative equation 4.11[85] developed by Holdich et al. therefore includes two expressions for the shear stress at the filter wall and effectively states that;

$$\Delta P_{TM} = \frac{J}{\tau_{w2}} \tau_{w1} \frac{\mu}{2} \left[\frac{d_f}{K_c} \ln\left(\frac{d_o}{d_f}\right) + 2R_m \frac{d_f}{d_o} \right] \qquad (4.15)$$

where τ_{w1} is expressed by equation 4.14 and τ_{w2} by equation 4.9.

The two values of wall shear stress, although calculated by different means, should be equal, and their division equal to unity. Calculating values of τ_{w1} and τ_{w2} for a number of experiments (Appendix VI, Table VI.2), and comparing the values in Figure 4.4 however, reveal a non-linear relationship with values for the ratio τ_{w1}/τ_{w2} of between 0.57 and 1.83.
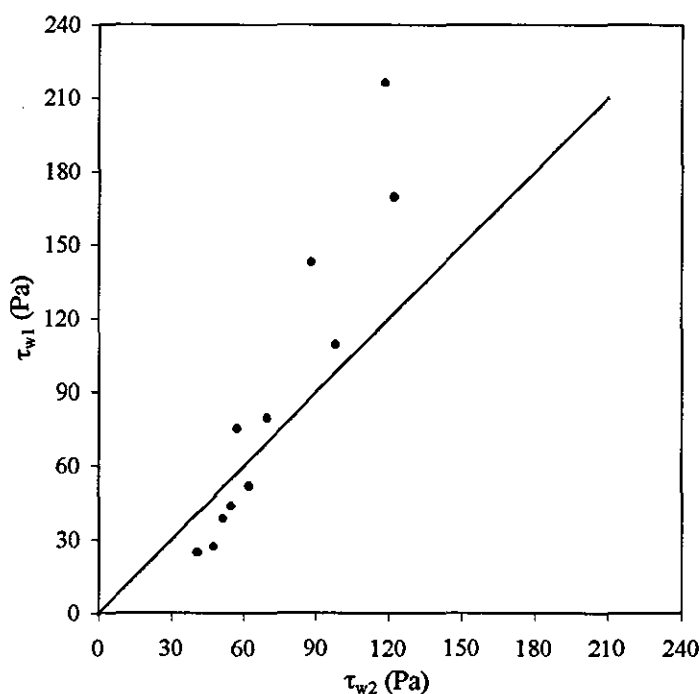
Figure 4.4 Ratio of shear stresses for Holdich *et al.* model. The line is for $\tau_{w1}=\tau_{w2}$. And shows that $\tau_{w1}>\tau_{w2}$ at higher shear rates.

4.2.4 Evaluation of results from the Holdich *et al.*[84,85] model

A number of reasons could account for the inability to obtain a reasonable correlation using this method, the assumption that k_0 is zero being an obvious one. More likely however, is the fact that the Holdich *et al.* model was developed for use with power law fluids. Although the titania suspensions are shear thinning, the curve fitting software supplied with the Carrimed constant stress rheometer suggests that a Casson model gives the best fit to this data. The model outlined above may not therefore, be appropriate for use with this system.

Strictly, the wall stress described by equation 4.9 applies to flow tangential to a solid surface, rather than the porous surfaces used in crossflow filtration. Assuming the relationship between the pressure drop along the length of a tube and the tube

149

diameter (equation 4.9) is valid however, using this in conjunction with the Casson rheological model may be able to provide an indication of the degree of cake formation during the filtration of titania suspensions. This principle forms the basis of the model developed in the following sections.

4.3 THE ANNULUS MODEL FOR PREDICTING CAKE THICKNESS

This model equates the wall shear stress, calculated using tube length pressure drop, to the shear stress in the suspension, calculated using the Casson rheological model. For a given set of process operating conditions, one tube diameter will exist at which the two are equal.

4.3.1 Annulus Model Development

At steady state, it is suggested that particles deposited by the feed suspension will form a dense uniform cake on the wall of the filter tube, while the bulk suspension continues to move in plug flow through the open channel. In line with observations in visualisation studies[65], a small transition region, sometimes described as a flowing cake, will also exist between the bulk flow and the fixed cake. The change in suspension solids concentration from the bulk through the transition region to the fixed cake is accounted for in this model by a series of annuli, which increase in concentration as they approach the filter cake.

Dividing the feed flow of suspension into seven annuli for example (Figure 4.6), the annuli are numbered from 0 (at the centre) to 6 (touching the filter cake), these numbers are then used in subscript to denote properties associated with each annulus. Annulus 0 is assigned an outer diameter (d_0) corresponding to the centre of the tube, thus annulus 1 takes on the form of a cylinder of diameter d_1 and represents the bulk plug flow of suspension at the feed concentration. The outer diameter of the largest annulus (in this case d_6) is equivalent to the diameter open to flow (fouled tube diameter) d_f, and the filter tube diameter is given by d_t.

151
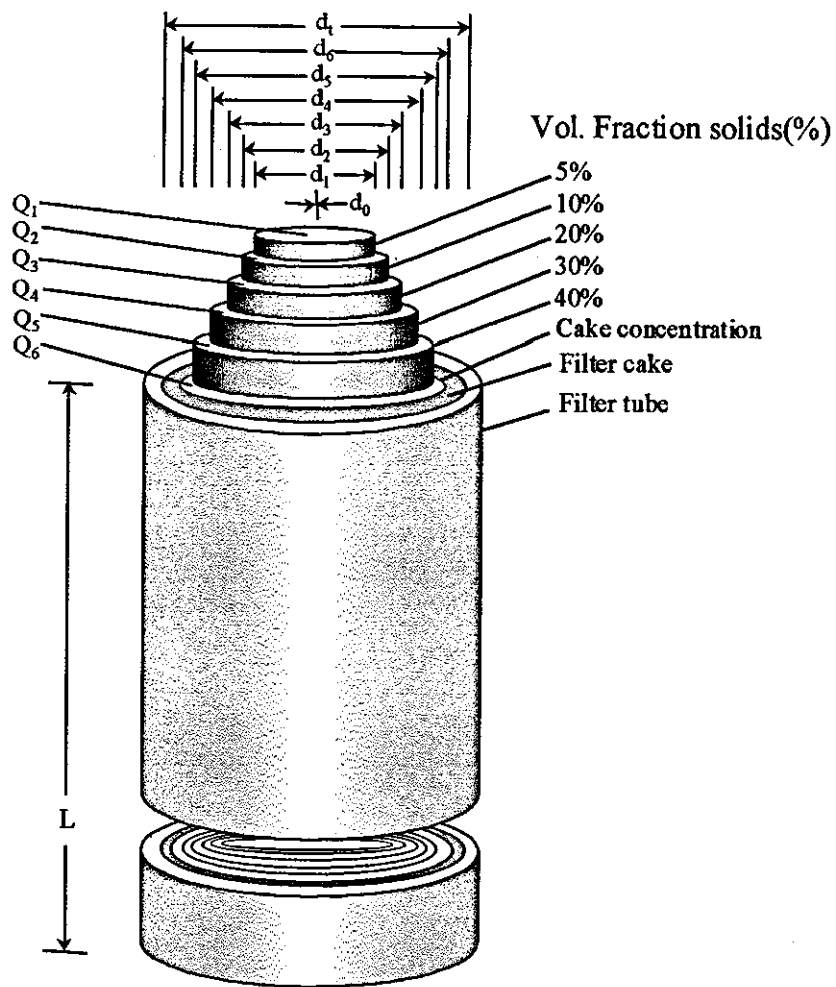
Figure 4.6 A schematic of the suspension flow in seven annuli (0 to 6) through a tubular filter

Considering a single annulus 'n', the following terms can be specified;
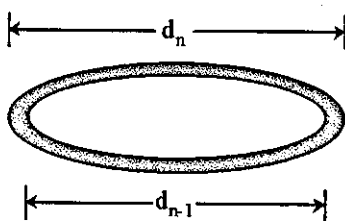
d_n = Annulus outer diameter
d_{n-1} = Annulus inner diameter
Q_n = Volumetric flow rate through annulus
A_n = Cross sectional area of annulus
u_n = Mean suspension velocity through annulus
$\dot{\gamma}_n$ = Shear rate at outer diameter
τ_{wn} = Shear stress at outer diameter
τ_{yn} = Suspension yield stress at outer diameter
K_n = Consistency coefficient at outer diameter

Figure 4.7 Annulus properties

This model has been developed to allow determination of the diameter open to flow at steady state and thus the thickness of filter cake formed. The wall shear stress is determined using;

$$\tau_w = \frac{\Delta P_L d_f}{4L}$$ (4.9)

The filter tube length (L) is known, the diameter open to flow (d_f) is estimated, and the pressure drop along the length of the tube (ΔP_L) can be measured experimentally (taking into account the pressure loss at the filter exit and the distance of the pressure transducers from the ends of the filter). The estimated tube diameter (d_f) will be correct where the appropriate value of shear stress (τ_w) is input to the equation, and this can be obtained from an expression for the rheological properties of the suspension.

For increasing shear rates (ignoring the thixotropic behaviour associated with decreasing shear rate), the titania suspensions used in this study are shear thinning with a yield stress and have been shown to give good correlation with the Casson rheological model.

$$\sqrt{\tau_w} = \sqrt{\tau_y} + \sqrt{K}\sqrt{\dot{\gamma}}$$ (4.18)

Where τ_y is the suspension yield stress, $\dot{\gamma}$ is the shear rate and K is the plastic viscosity or consistency coefficient. The consistency coefficient (K) and yield stress (τ_y) have been determined experimentally for the titania suspension used in this study, and by fitting polynomials to the experimental data these values can be calculated as a function of suspension solids concentration (Appendix VII).

As a first approximation, the shear rate ($\dot{\gamma}$) at a specific diameter (d) can be defined using equation 4.19 for Newtonian fluids,

$$\dot{\gamma} = \frac{8u}{d} \qquad (4.19)$$

where (u) is the average crossflow velocity and can be calculated for a particular annulus 'n' using

$$u_n = \frac{Q_n}{A_n} \qquad (4.20)$$

The cross sectional area of the annulus can be written

$$A_n = \pi\left(\frac{d_n}{2}\right)^2 - \pi\left(\frac{d_{n-1}}{2}\right)^2 = \frac{\pi}{4}\left(d_n^2 - d_{n-1}^2\right) \qquad (4.21)$$

Thus, substituting (4.21) into (4.20) gives

$$u_n = \frac{4Q_n}{\pi\left(d_n^2 - d_{n-1}^2\right)} \qquad (4.22)$$

and substituting (4.22) into (4.19) gives an expression for Newtonian derived shear rate at the outer edge of an annulus.

$$\dot{\gamma}_n = \frac{32Q_n}{\pi d_n\left(d_n^2 - d_{n-1}^2\right)} \qquad (4.23)$$

Substituting equations (4.23) and (4.9) into (4.18) and rearranging for Q_n gives

$$Q_n = \frac{\pi d_n\left(d_n^2 - d_{n-1}^2\right)}{32K_n}\left(\sqrt{\frac{\Delta P_L d_n}{4L}} - \sqrt{\tau_{yn}}\right)^2 \qquad (4.24)$$

where K_n and τ_{yn} are determined from empirical data, ΔP_L was obtained from experimental data and the values of d_n and d_{n-1} are derived as follows.

The outer diameter of each annulus is assigned a solids concentration (C_n) between that of the bulk suspension ($C_b = C_1$) and the cake ($C_c = C_6$), with an equal rise in concentration between each annulus. By then superimposing a parabolic concentration profile across the transition region, and estimating diameters for the bulk feed flow ($d_b = d_1$) and the diameter open to flow ($d_f = d_6$), a diameter (d_n) can be determined for each value of C_n (annulus outer diameter) using;

$$d_n = d_b + \left(d_f - d_b\right)\sqrt{\left(\frac{C_n - C_b}{C_c - C_b}\right)} \qquad (4.25)$$

where C_n is determined by;

$$C_n = C_b + \left(n - 1\right)\left(\frac{C_c - C_b}{A - 1}\right) \qquad (4.26)$$

Where n is the number of the annulus and A is the total number of annuli.

This value of C_n also enables calculation of the consistency coefficient (K) and yield stress (τ_y) for the concentration of suspension in each annulus.

Thus, with knowledge of C_b, C_c, and ΔP_L, estimates of d_b and d_f, and an allotted number of annuli, values of d_n, d_{n-1}, K_n, τ_{yn} and ultimately Q_n can be calculated for each annulus.

4.3.2 Determination of the Fouled Diameter

The correct estimates of diameter are obtained by comparing model-calculated suspension and solid flow rates, with experimentally determined values.

155

Summing Q_n for all the annuli gives a model-calculated retentate flow rate through the fouled filter tube, and the summation $\sum Q_n C_n$ gives a model-calculated solids throughput.

The actual solids throughput at steady state can be calculated using the process feed flow rate and, assuming 100% rejection by the membrane, the feed solids concentration. The estimated diameter (d_f) and the filter tube diameter (d_t) can be used to calculate a cake deposit thickness (δ_c), which may then be used in the modified Darcy's law equation (equation 4.6) with the relevant values of transmembrane pressure, permeate viscosity, membrane resistance, cake resistance, and clean tube diameter (Appendix VII), to calculate a steady state permeate flux. The actual retentate flow rate can then be calculated by subtracting the evaluated permeate flow rate from the process feed flow rate.

When the model-calculated retentate flow rate and solids flow rate balance the experimental measurements, the values of d_b and d_f may be considered correct. The process of estimating these values can be automated and incorporated into a computer program which will iterate to find the best fit.

4.3.3 Annulus Model Integrity

The procedure in Section **4.3.1** has been incorporated into a Pascal computer program, which will calculate a steady state diameter open to flow and a steady state permeate flux for any given experiment in this study (Appendix X). The flow diagram (Figure 4.8) outlines the process by which the diameter is calculated and lists the required input data. The volume fraction of solids in the filter cake must be determined experimentally and a first estimate can be made using a dead-end filtration experiment. Baker et al.[73] however, have shown that cakes formed in crossflow filtration can have four times the specific resistance of equivalent dead-end cakes, so a more rigorous measurement is advisable.

156

The program can be adapted for other filter cell configurations and for any suspension with known rheological characteristics and cake solids concentration.
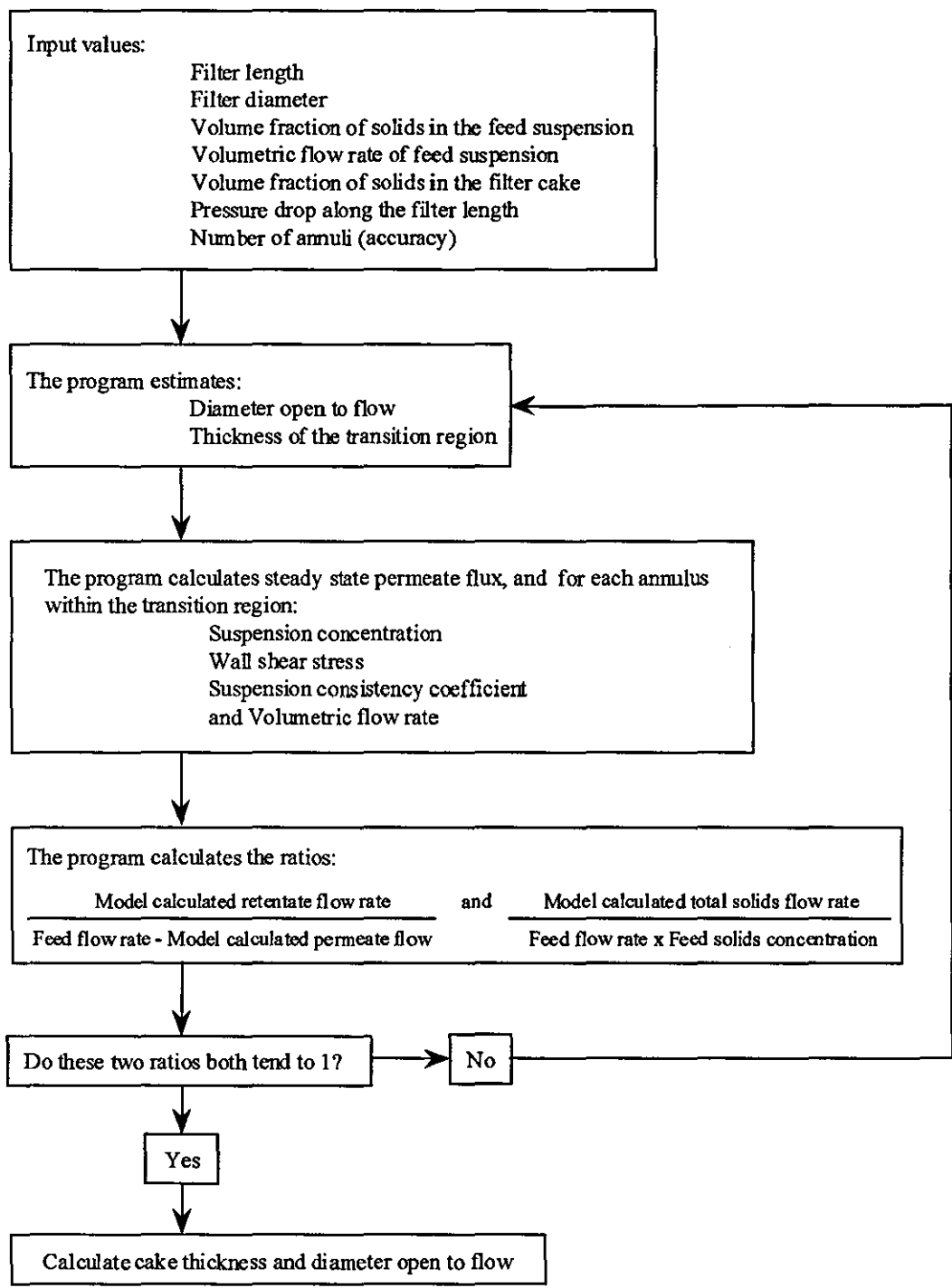
Figure 4.8 Annulus model, computer program flow sheet.

157

4.3.4 A Qualitative Evaluation of Predictions from the Annulus Model

The qualitative performance of the annulus model was determined by substituting process parameters from experiments in set C into the computer program, and calculating an associated theoretical filter cake thickness (Appendix VII). Trends relating cake thickness to superficial crossflow velocity, transmembrane pressure and feed solids concentration could then be compared with the observations of visualisation studies (Section 1.5).

4.3.4.1 Effect of Superficial Crossflow Velocity

Figure 4.9 demonstrates a reduction in the predicted cake thickness with increasing superficial crossflow velocity, and this property has been confirmed by visualisation studies[44,65].
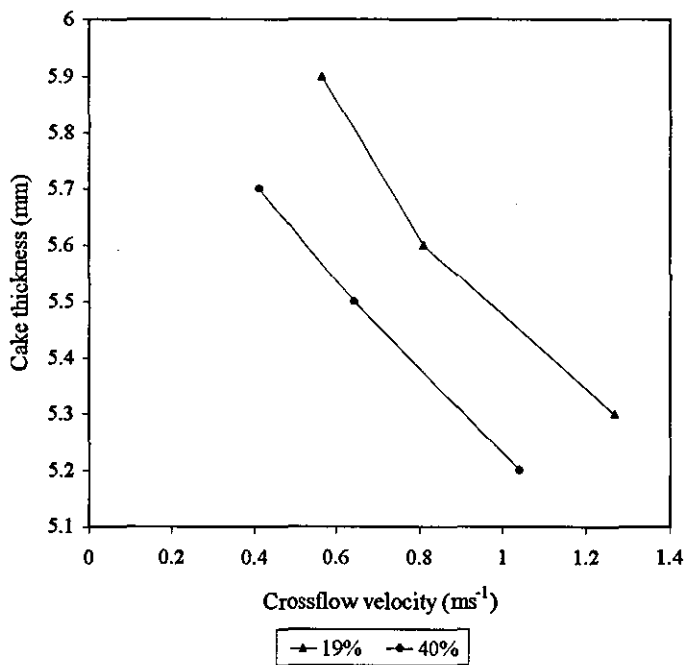
Figure 4.9 The effect of superficial velocity on theoretical cake thickness at 2bar, pH9.5, and 50°C, with feed suspension volume solids fractions of 19% and 40%

158

The reduction in cake thickness is a result of the increased wall shear stress, which arrests cake growth by either removing particles or limiting the rate of deposition. The reduced cake thickness provides less resistance to permeate flow, thus where all other parameters are held constant, an increase in permeate flux is obtained.

4.3.4.2 Effect of Transmembrane Pressure

Increasing the transmembrane pressure (Figure 4.10) resulted in a model predicted increase in cake thickness over the range of feed suspension concentrations considered.
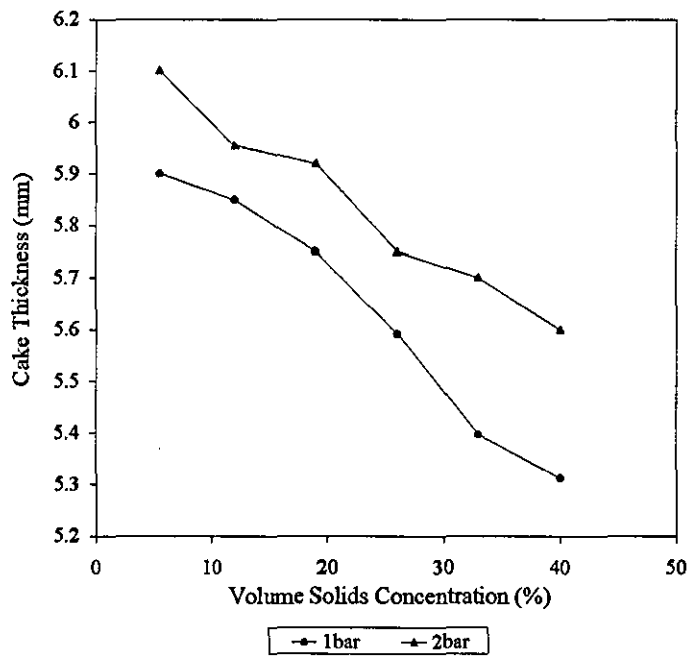
Figure 4.10 The effect of transmembrane pressure on theoretical cake thickness at $0.5ms^{-1}$, pH9.5, 50°C

This again agrees with visualisation studies[44,65], and the theory that a raised pressure will increase the flow of suspension normal to the filter surface, thus increasing the

flux of particles towards it and the flux of permeate through it. The increased shear stress normal to the cake at higher transmembrane pressures results in a greater degree of particle retention and thus a thicker steady state filter cake.

4.3.4.3 Effect of Feed Solids Concentration on Cake Thickness Prediction

Increasing the feed suspension solids concentration at fixed crossflow rate and transmembrane pressure predicted a reduction in steady state cake thickness (Figure 4.10). Experimental results however, show a reduction in permeate flux with increasing feed solids concentration thus, if the model is predicting correctly, there must be an associated rise in the specific cake resistance. Although this is possible, the prediction of a thinning cake is inconsistent with both the visualisation studies[65], which observed cakes of increasing thickness with feed solids concentration, and the experimental results of this work, where the filter tube was observed to choke (become fully blocked with filter cake) when the feed concentration reached approximately 48% volume solids.

4.3.5 A Quantitative Analysis of Predictions from the Annulus Model

A quantitative evaluation of the model predictions was obtained by comparing model predicted values of steady state permeate flux (the specific cake resistance is assumed to be constant for all of the crossflow experiments) with experimental values for a range of crossflow velocities, transmembrane pressures, and feed solids volume concentrations (Figure 4.11). The theoretical fluxes were calculated using the procedure outlined in Section **4.3.2**. The experimental fluxes were calculated using experimental steady state permeate flow rates, and the open area of tube based on the model predicted open flow diameter. I.e., both fluxes are based on the model predicted open area of tube, not the filter tube internal diameter.
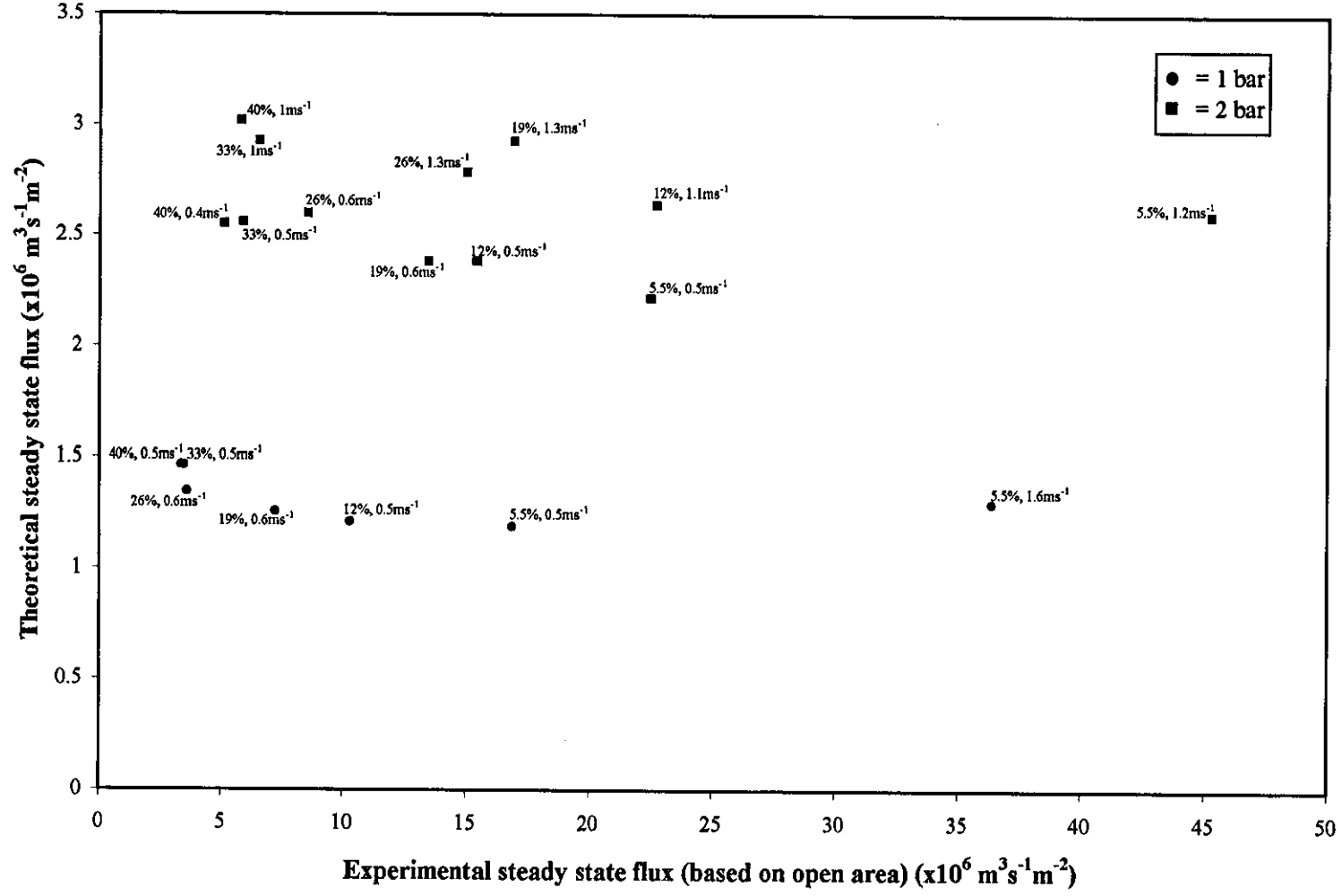
Figure 4.11 Experimental steady state permeate fluxes vs. theoretical fluxes from the annulus model (pH 9.5, 50°C). Both fluxes are based on open area, calculated using model predicted δ_c.

This reveals an inaccurate prediction of experimental steady state flux. The correlation between theoretical and experimental results is better under conditions that favour a thicker cake formation, i.e. relatively high feed solids concentrations and low superficial crossflow velocities. The least accurate predictions of permeate flux occur at the highest crossflow velocities and lowest feed solids concentrations, i.e. the conditions that favour the formation of the thinnest cakes. The transmembrane pressure does not appear to have a significant effect on the degree of accuracy.

4.3.5.1 Corrected values of cake thickness

The predicted fluxes are universally lower than the equivalent experimental values, suggesting that either the predicted values of cake thickness or the specific cake resistance used are too great. Predicted thicknesses were calculated using a cake solids fraction of 0.595 throughout, and are predominantly in the range 5-6mm. Using the same cake solids fraction, experimental permeate flow rates were used with equation 4.6 (Appendix VII.2) to back calculate 'correct' values of cake thickness. These are given in table VII.1 and are plotted against values predicted by the model in figure 4.12.

The 'corrected' values of cake thickness cover a much wider range than those predicted by the annulus model, predominantly between 1 and 5mm. This range seems more appropriate, considering the range of operating conditions used in the filtration experiments.

4.3.5.2 Corrected values of specific cake resistance

Another significant parameter in the calculation of permeate flux is the specific cake resistance, and it is probable that the constant value of R_c, used for all experiments in the modelling calculations, will also have contributed to the

162

discrepancy between predicted and experimental permeate fluxes. The various process conditions employed in the different experiments are likely to promote differing modes of particle deposition, packing and cake consolidation, thus resulting in a range of values for specific cake resistance.
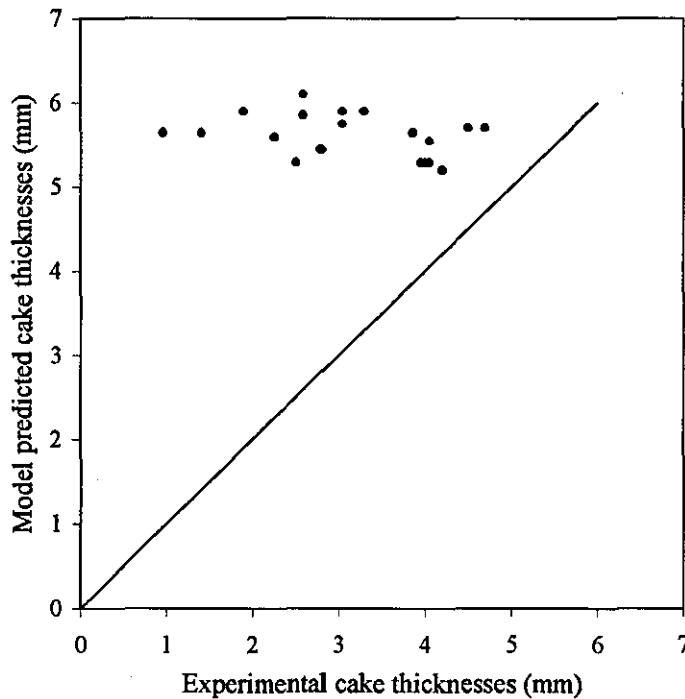
Figure 4.12 Model predicted cake thickness vs experimental predicted cake thickness

To obtain the correct predictions of permeate flux from the cake thicknesses predicted by the annulus model, values of specific cake resistance were re-evaluated using the procedure in Appendix VII.3. These values are plotted against feed solids fraction in figure 4.13 and suggest a steady increase in cake volume solids from 30 to 50%, as the feed volume solids increases from 5.5 to 40%.

These values are lower than measured experimentally, and lower than found by Datta and Gaddis[38] in their analysis of titania cakes formed in crossflow, but not so low as to be considered inconcievable.
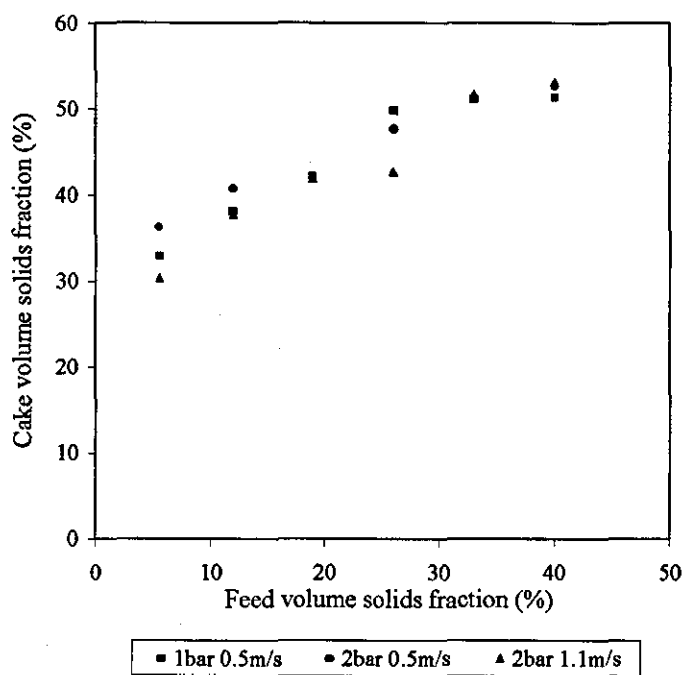
Figure 4.13 Corrected values of cake solids fraction vs feed solids fraction, at given transmembrane pressures and approximate superficial crossflow velocities.

These values suggest that a more rigorous approach to the evaluation of specific cake resistance may significantly improve the accuracy of predicted permeate fluxes.

4.3.6 Refinements to the Annulus Model

The development of the annulus model has been simplified in order to obtain a first estimate of steady state cake thickness and permeate flux. The use of constant

specific cake resistance for all cases within this study is therefore only one of a number of assumptions. In addition, the filter cake thickness and specific resistance is assumed to be uniform over the entire inner surface of the filter tube, suggesting a uniform distribution of transmembrane pressure over the filter surface. This is however, contrary to experimental data, which indicates a pressure drop along the length of the filter tube and therefore a drop in transmembrane pressure. The resulting variations in cake thickness and specific resistance along the length of the filter tube have further consequences for the annulus model, which assumes that the annuli are concentric, and of uniform thickness along their lengths. The model also assumes that each annulus is a discrete entity and does not allow for a movement of particles between them.

With regard to the mathematical development, the equation used to calculate shear stress at the filter tube/annulus wall (equation 4.9) assumes a solid walled tube of constant diameter and has not been modified to account for the porous nature of the filter tube wall. Additionally, the equation used to calculate shear rate (equation 4.19) assumes, contrary to the results of the the rheological study, that the suspension is Newtonian. Equation 4.27 for 'general time independent non-Newtonian fluids'[89], could be used to account for the non-Newtonian behaviour, however this still fails to account for the thixotropic nature of the titania suspensions.

$$\dot{\gamma} = \left(\frac{8u}{d}\right)\left(\frac{3n+1}{4n}\right) \qquad (4.27)$$

u is the velocity at diameter d, and n is the flow behaviour index.

The simplicity of the current model and the assumptions made will therefore have contributed to the poor agreement between theoretical and experimental results.

CHAPTER FIVE

CONCLUSIONS AND RECOMMENDATIONS

5.1 CONCLUSIONS

5.1.1 Suspension Characterisation

Titanium dioxide suspensions have been characterised, observing the effects of pH, solids concentration and shear rate on their behaviour. Behavioural changes were caused largely by flocculation or aggregation within the suspension, resulting from either an increase in the solids concentration, or a reduction in particle surface charge.

Measuring Zeta potential as a function of suspension pH revealed that the calgon dispersed suspensions had an iso-electric point around pH 4.0. The effect of reducing a suspension from a well dispersed state (between pH 8 and pH 11) to the IEP was to induce flocculation, and this had implications for the suspension behaviour in both rheological and filtration experiments.

The flocculated suspensions provided more resistance to shear stress i.e., where all other parameters were held constant, their viscosities increased. Increasing degrees of flocculation also resulted in the presence of a yield stress, shear thinning behaviour, and a degree of thixotropy. These phenomena were further enhanced as the suspension solids concentration was increased, thus increasing the proximity of particles within the suspension.

5.1.2 Crossflow Filtration Experiments

Crossflow filtration experiments were conducted in both concentrating mode, by removing permeate from the system, and at constant concentration, by returning

permeate to the feed tank. Comparing permeate flux measurements for the two modes of operation showed that measurements taken at a specific feed concentration in concentrating mode could approximate those obtained at steady state in an equivalent constant feed solids concentration experiment run to steady state.

In concentrating mode, a maximum feed suspension concentration of 48% volume solids was obtained before the filter tube choked. A sample of filter cake also revealed that the filter cake concentration was approximately 59.5% volume solids.

The results of experiments conducted at constant concentration showed a clear relationship between the process operating conditions and the achievable steady state flux.

5.1.3 Effects of Process Parameters on Permeate Flux in Crossflow Filtration

5.1.3.1 Transmembrane Pressure

Increases in the transmembrane pressure resulted in a non-proportional increase in permeate flux, i.e. either the filter cake was compressible or there may have been increased penetration and blocking of the membrane pores at these higher transmembrane pressures

5.1.3.2 Crossflow Velocity

Increases in the superficial crossflow velocity also resulted in improved permeate fluxes, as the increased wall shear stress presumably limited growth of the filter cake[3]. The reduced cake thickness thus provided less resistance and an improved permeate flux was realised.

5.1.3.3 Suspension Solids Concentration

Increases in the feed suspension solids concentration resulted in higher flux of particles to the filter surface, which helped further the growth of the filter cake. Consequently a reduction in permeate flux was observed. Increasing feed solids concentration was also observed to progressively reduce the improved permeate fluxes realised as a result of increasing crossflow velocities and transmembrane pressures.

5.1.3.4 pH

The larger mean particle sizes found in the flocculated suspensions resulted in the formation of lower resistance filter cakes than produced by well dispersed suspensions during filtration. This, along with the accompanying reduction in pore penetration, resulted in much improved permeate fluxes over well dispersed systems at low feed solids concentrations. At higher feed solids concentrations however, the improvement in flux was much reduced, and the highly viscous nature of the flocculated suspension prevented much filtration above 14% volume solids.

5.1.4 The Annulus Model

The results of the filtration experiments provide a comprehensive guide to the effects of process parameters on achievable steady state permeate flux during the crossflow filtration of titania suspensions. Trends can be seen in the plotted results that demonstrate definite relationships between the operating conditions and filtration performance. However, although the effect of an isolated parameter can be fairly well predicted using these results, the result of multiple parameters interacting simultaneously can be less well quantified.

For this reason, an attempt was made to model cake formation in crossflow filtration using the annulus model, from which a prediction of steady state permeate flux could be obtained.

Qualitatively the annulus model correctly predicted trends of increasing cake thickness with increasing transmembrane pressure and decreasing crossflow velocity. However, it was less successful in predicting the effect of increasing feed solids concentration, contradicting the experimental results of this study and what has been observed in visualisation studies[65] (Section 1.5).

Steady state permeate fluxes were predicted assuming that all cakes were composed of 59.5% solids by volume. Comparing these results to experimental values showed a poor correlation between the two, although the accuracy of predictions improved for operating conditions that favoured the formation of thicker cakes.

An investigation into the effects of specific cake resistance on permeate fluxes predicted using the annulus model, revealed that reasonable changes in the cake solids fraction had significant effects on the resulting permeate fluxes. Fluxes predicted using the annulus model could be 'corrected' to meet experimental fluxes by adjusting cake volume solids fractions within the range 0.25 to 0.53.

5.2 RECOMMENDATIONS FOR FURTHER WORK

5.2.1 Experimental Studies

A comprehensive set of results have been obtained during both the suspension characterisation studies and the crossflow filtration experiments. Further work could however, include the effects of temperature and extend the ranges of the process parameters studied, to see at what point increases in crossflow velocity and transmembrane pressure cease to have a significant improvement on achievable permeate flux. This could be achieved using the current apparatus with either a larger capacity pump, or a smaller diameter filter tube. Different filter configurations might also allow for the filtration of suspensions at the IEP to higher concentrations.

Further modifications to the rig for a more in depth study could include facilities for regular backwashing, and chemical cleaning of the filter elements, as would be required on a full scale pilot plant study.

5.2.2 Modelling Cake Formation in Crossflow Filtration

The results of the modelling highlight the simplicity of the annulus model, however the assumptions made in its development leave room for improvement.

The representation of the system as a series of non-interacting 'sliding pipes' is unrealistic in reality, and tube length pressure drop measurements do not allow for the porous nature of the filter tube. The thixotropic behaviour is also unaccounted for in shear rate calculations, and the assumption of a constant specific cake resistance over the full range of process parameters has a significant effect on the resulting predictions of permeate flux.

In addition to refining the mathematical development of the model, further work should include a comprehensive characterisation of the filter cakes formed in crossflow filtration as a function of crossflow velocity, transmembrane pressure, feed solids concentration and pH.

5.2.3 Industrial Applications

The results of these experimental studies reveal the potential of crossflow filtration for de-watering high solids concentration suspensions in terms of achievable solids concentration and permeate removal rates. An evaluation of crossflow filtration as an economic alternative to existing de-watering processes for high volume solids concentration suspensions however, would require further studies on a larger scale pilot plant to determine optimum operating pressures, crossflow velocities and feed solids concentrations for permeate removal.

The viability of the process on a production scale may then be evaluated by comparing the costs of installation and operation with any savings made through improved permeate removal rates, reduced process downtime, increased achievable solids concentration, implications for waste removal, and reduced evaporation costs in subsequent drying processes.

REFERENCES

1   Tioxide Group Ltd., 1992, Manufacture and general properties of titanium dioxide pigments, TiINFO Systems.

2   Mikulásek, P., Wakeman, R.J., Marchant, J.Q., 1997, The influence of pH and temperature on the rheology and stability of aqueous titanium dioxide dispersions, *Chem. Eng. J.*, **67**: 97-102.

3   Mikulasek, P., Wakeman, R.J., Marchant, J.Q., 1998, Crossflow microfiltration of shear-thinning aqueous titanium dioxide dispersions, *Chemical Engineering Journal*, **69**, 53-61.

4   Michaels, S.L. (Millipore Corp.), 1989, Crossflow microfilters: The ins and outs, *Chemical Engineering*, **96**(1): 84-91.

5   Vincent, B., 1995, The nature of colloids, University of Bristol spring school in colloid science, Course notes.

6   International union of pure and applied chemistry, 1972, Manual on colloid and surface chemistry, Butterworth, New York.

7   Tadros, Th.F., 1980, Physical stability of suspension concentrates, *Adv. Colloid and Interface Science*, **12**: 141-161.

8   Thomson, D.W., 1995, Adsorption at interfaces, controlled aggregation, University of Bristol spring school in colloid science, Course notes.

9   Goodwin, J., 1995, Properties of charged particles in dispersed systems, University of Bristol spring school in colloid science, Course notes.

10   Strauss, H., Heegn, H., and Strientz, I., 1993, Effect of PAA adsorption on the stability and rheology of TiO_2 dispersions, *Chem. Eng. Sci.*, **48** No.2: 323-332.

11   Liddell, P.V. and Boger, D.V., 1994, Influence of processing on the rheology of TiO_2 pigment suspensions, *Ind. Eng. Chem. Res.*, **33**: 2437-2442.

12   Coulson, J.M., and Richardson, J.F., 1991, Particle Technology and Separation Processes, Chemical Engineering Vol. 2, 4th ed., Pergamon Press, Oxford.

13   Parfitt, G.D., 1973, Dispersion of powders in liquids, 2nd ed., with special reference to pigments, Applied Science Publishers Ltd., London.

14   Lyklema, J., 1977, Water at interfaces, a colloid-chemical approach, *Journal of Colloid and Interface Science*, **58** No.2: 242-250.

15   Rao, A.S., 1987, Rheology of aqueous dispersions of alumina, titania and mixture of alumina and titania powders, *J. Dispersion Science and Technology*, **8**: 457-476.

16   Vincent, B., 1995, Stability of colloidal dispersions, (2) Charged systems, University of Bristol spring school in colloid science, Course notes.

17   Hamaker, H.C., 1937, *Physica*, **4**: 1058.

18   Deryaguin, B.V., and Landau, L.D., 1941, *Acta Physiochim, URSS*, **14**: 637.

19   Verwey, E.J.W., and Overbeek, J.Th.G., 1948, Theory of the stability of lyophobic colloids, Elsevier, Amsterdam.

20   Mewis, J., Spaull, A.J.B., 1976, Rheology of concentrated dispersions, *Adv. Colloid and Interface Science*, **6**: 173-200.

21   Vincent, B., 1995, Stability of colloidal dispersions, (1) Charged systems, University of Bristol spring school in colloid science, Course notes.

22   Napper, D.H., 1989, Polymeric stabilisation of colloidal dispersions, Academic press, London.

23   Muller, H.G., 1973, An introduction to food rheology, Heinemann, London.

24   Bingham, E.C., 1922, Fluidity and Plasticity, McGraw Hill, New York.

25   Sato, T., 1996, Effect of particle concentration on physical properties of TiO2 suspensions, *J.Dispersion Science and Technology*, **17**: 83-96.

26   Weber, H.H., 1960, *Deutsche Farb.Zeit.*, **14**: 312.

27   Jones, D.A.R., Leary, B., Boger, D.V., 1991, The rheology of a concentrated colloidal suspension of hard spheres, *J. Colloid Interface Science*, **147**: 479-495.

28   Krieger, I.M., 1963, A dimensional approach to colloid rheology, *Trans. Soc. Rheology*, **7**: 101-109.

29   Krieger, I.M., and Dougherty, T.J., 1959, A mechanism for non-Newtonian flow in suspensions of rigid spheres, *Trans. Soc. Rheology*, **3**: 137-152.

30   Hermia, J., 1982, Constant pressure blocking filtration laws, application to power law non-Newtonian fluids, *Trans I ChemE*, **60**: 183.

31   Field, R.W., Wu, D., Howell, J.A., and Gupta, B.B., 1995, Critical flux concept for microfiltration fouling, *Journal of Membrane Science*, **100**: 259-272.

32   Davis, R.H. and Leighton, D.T., 1987, Shear induced transport of a particle layer along a porous wall, *Chem. Eng. Sci.*, **42(2)**: 275-281.

33   Romero, C.A. and Davis, R.H., 1991, Experimental verification of the shear induced hydrodynamic diffusion model of crossflow microfiltration, *Journal of Membrane Science*, **62**: 249-273.

34   Altena, F.W. and Belfort, G., 1984, Lateral migration of spherical particles in porous flow channels: application to membrane filtration, *Chem.Eng.Sci.*, **39(2)**: 343.

35   Henry, J.D., 1972, Crossflow filtration, in *Recent developments in separation science*, Vol. 2, Ed. Li, N.N., CRC Press, Ohio, 205-255.

36   Davis, R.H., 1993, Modelling of fouling of crossflow microfiltration membranes, Separation and Purification Methods, **21(2)**: 75-126.

37   Redkar, S.G., and Davis, R.H., 1993, Crossflow microfiltration of yeast suspension in tubular filters, *Biotechnol. Progress*, **9**: 625-634.

38   Datta, S. and Gaddis, J.L., 1997, Dynamics and rheology of fouling cakes formed during ultrafiltration, Separation Science and Technology, **32(1-4)**: 327-353.

39   Fischer, E. and Raasch, J., 1986, Model tests of the particle deposition at the filter medium in crossflow filtration, *Proc. 4th World Filtration Congress*, 11.11-11.17, KVIV, Ostend, Belgium.

40   Rautenbach, R. and Schock, G. 1988, Ultrafiltration of macromolecular solutions and crossflow microfiltration of colloidal suspensions, a contribution to permeate flux calculations, *Journal of Membrane Science*, **36**: 231-232.

41   Lokjine, M.H., Field, R.W. and Howell, J.A., 1992, Crossflow microfiltration of cell suspensions, a review of models with emphasis on particle size effects, *Trans IChemE*, **70**, Part C: 149.

42   Leighton, D. and Acrivos, A., 1987, Measurement of shear induced self diffusion in concentrated suspensions of spheres, *Journal of Fluid Mech.*, **177**: 109-131.

43   Eckstein, E.C., Bailey, D.G., and Shapiro, A.H., 1977, Self diffusion of particles in shear flow of a suspension, *Journal of Fluid Mech.*, **79**(1): 191-208.

44   Mackley, M.R. and Sherman, N.E., 1992, Crossflow cake filtration mechanisms and kinetics, *Chem. Eng. Sci.*, **47**: 3067.

45   Green, G. and Belfort, G., 1984, Fouling of ultrafiltration membranes: lateral migration and the particle trajectory model, *Desalination*, **35**: 129.

46   Leighton, D. and Acrivos, A., 1987, The shear induced migration of particles in concentrated suspensions, *Journal of Fluid Mech*, **181**: 415-439.

47   Zhevnovatyi, A.I., 1975, Basic principles of filtration of suspensions in flow without formation of deposits, *J. Applied Chem. USSR*, **48**(2.i): 335.

48   Blake, N.J., Cumming, I.W., and Streat, M., 1992, Prediction of steady state crossflow filtration using a force balance model, *Journal of Membrane Science*, **68**: 205-216.

49   Pirou, E., René, F., and Latrille, E., 1995, Crossflow Microfiltration model based on integration of the mass transport equation, *Journal of membrane Science*, **108**: 57-70.

50   Dharmappa, H.B., Verink, J., Ben Aim, R., Yamamoto, K., and Vigneswaran, S., 1992, A comprehensive model for crossflow filtration incorporating polydispersity of the influent, *Journal of membrane Science*, **65**: 173-185.

51   Lu, W.M., Hwang, K.J., Ju, S.P, and Chen, C.K., 1990, Mechanisms of crossflow filtration of non-Newtonian slurries, *Adv. Filtration sep. technol.*, **1**.

52   Song, L. and Elimelech, M., 1995, Theory of concentration polarisation in crossflow filtration, *J. Chem. Soc., Faraday Trans.*, **91**(19): 3389-3398.

53   Zhang, G.M., 1992, Crossflow microfiltration modelling and mechanical means to prevent membrane fouling, *PhD Thesis*, Loughborough University.

54   Chaudhury, M.S.S.L.T., 1996, Mechanisms of membrane fouling, *PhD Thesis*, Exeter University.

55   Dong-Jang Chang, Feng-Chia Hsu, and Shyh-Jye Huray, 1995, Steady state permeate flux of crossflow microfiltration, *Journal of Membrane Science*, **98**: 97-106.

56   Vassilis, G. and Bengt, H., 1987, Mass transfer in the membrane concentration polarisation layer under turbulent crossflow, I. Critical literature review and adaptation of exsting sherwood correlation to membrane operations, *Journal of Membrane Science,* **30**: 153-170.

57   Romero, C.A. and Davis, R.H., 1988, Global model of crossflow microfiltration based on hydrodynamic particle diffusion, Journal of Membrane Science, **39**: 157-185.

58   Belfort, G., Davis, R.H., and Zydney, A.L., 1994, Review: The behaviour of suspensions and macromolecular solutions in crossflow microfiltration, *Journal of Membrane Science,* **96**: 1-58.

59   Blatt, W.F., Dravid, A., Michaels, A.S., and Nelson, L., 1970, *Membrane science and Technology,* Ed. Flinn, J.E., Plenum Press, New York.

60   Fane, A.G., 1986, Ultrafiltration: Factors influencing flux and rejection, in *Progress in Filtration and Separation* Vol. 4, Ed. R.J. Wakeman, 101-179, Elsevier, Amsterdam.

61   Porter, M.C., 1972, Ultrafiltration of colloidal suspensions, in *Recent Advances in Separation Techniques,* A.I.ChemE. Symposium Series, **68**: 21-30.

62   Wakeman, R.J. and Tarleton, E.S., 1992, Understanding flux decline in microfiltration, Vol.1, Prepared for B.P. International.

63   Zydney, A.L. and Colton, C.K., 1986, A concentration polarisation model for the filtrate flow in crossflow microfiltration of particulate suspensions, *Chem. Engng. Comm.,* **47**: 1-21.

64   Leonard, E.F. and Vassilieff, C.S., 1984, The deposition of rejected matter in membrane separation processes, *Chem. Engng. Comm.,* **30**: 209.

65   Wakeman, R.J., 1994, Visualisation of cake formation in crossflow microfiltration, *Trans. IChemE,* **72**, Part A: 530.

66   Arp, P.A. and Mason, S.G., 1977, The kinetics of flowing dispersions-IX: doublets of rigid spheres, *J. Colloid Interface Sci.,* **61**: 44.

67   Zydney, A.L. and Colton, C.K., 1987, Continuous flow membrane plasmapheresis: Theoretical models for flux and haemolysis prediction, *Trans. Am. Soc. Artif. Int. Organs,* **28**: 408-412.

68   Lu, W.M. and Ju S.C., 1989, selective particle deposition in crossflow filtration, *Sep. Sci. Technol,* **24**: 512-540.

69   Mikhlin, J.A., Weber, M.E., and Turkson, A.K., 1982, Electrically aided axial filtration, *J. Separation Process Techniques*, **3**(1): 16.

70   Tarleton, E.S., 1986, *PhD Thesis*, Exeter University.

71   Hodgson, P.H., Pillay, V.C., and Fane, A.G., 1993, Visual studies of crossflow microfiltration with inorganic membranes: resistance of biomass and particulate cakes, *Proc. 6th World Filtration Congress*, 607-610, The Filtration Society, Nagoya.

72   Wandelt, B., Schnitz, P.H., and Houi, D., 1993, Investigation of transient phenomena in crossflow microfiltration of colloidal suspensions using NMR micro imaging, *Proc. 6th World Filtration Congress*, 601-606, The Filtration Society, Nagoya.

73   Baker, R.J., Fane, A.G., Fell, C.J.D., and Yoo, B.H., 1985, Factors affecting flux in crossflow filtration, *Desalination*, **53**: 81-93.

74   Tarleton, E.S. and Wakeman, R.J., 1993, Understanding flux decline in crossflow microfiltration: Part I-Effects of particle and pore size, *Trans. IChemE*, **71**, PartA: 399.

75   Tarleton, E.S. and Wakeman, R.J., 1994, Understanding flux decline in crossflow microfiltration: Part II-Effects of process parameters, *Trans. IChemE*, **72**, PartA: 431.

76   Tarleton, E.S. and Wakeman, R.J., 1994, Understanding flux decline in crossflow microfiltration: Part III-Effects of membrane morphology, *Trans IChemE*, **72**, PartA: 521.

77   Gregor, E.C., 1988, The state of the art of microfiltration: current and future applications, *Tappi Journal*, April: 123.

78   Carman, P.C., 1938, Fundamental principles of industrial filtration, *Trans. Inst. Chem. Eng.*, **16**: 168.

79   Millipore RX20 User Manual, 1995, Millipore (U.K.) Ltd., England.

80   Mastersizer Manual: IM100, Issue 3, P.4.28, Malvern Instruments Ltd., England

81   Instruction Manual for the Carri-Med Controlled Stress Rheometer, 1985, Carri-Med Ltd., Glebelands Centre, Vincent Lane, Dorking, Surrey RH4 3YX, England.

82   Rogers, G.F.C., and Mayhew, Y.R., 1991, Thermodynamic and Transport Properties of Fluids, 4th Edition, Basil Blackwell Ltd.

83   Holdich, R.G., Private communication.

84   Holdich, R.G., Cumming, I.W., and Ismail, B., 1995, The variation of crossflow filtration rate with wall shear stress and the effect of deposit thickness, *Trans. IchemE*, **73** Part A.

85   Holdich, R.G., Cumming, I.W., Ismail, B., 1996, Crossflow microfiltration for mineral suspension thickening and washing, *Minerals Engineering*, **9** No. 2: 243-257.

86   Ismail, B., 1996, Crossflow microfiltration of concentrated non-Newtonian slurries, *PhD Thesis*, Loughborough University.

87   Metzner, A.B., and Reed, J.C., 1995, Flow of non-Newtonian fluids-correlation of the laminar, transition and turbulent flow regimes, *A.I.Ch.E.J.*, **1**, 434-440.

88   Massey, B.S., 1990, Mechanics of Fluids, 6th Edition, Chapman and Hall Ltd, London.

89   Holland, F.A., 1986, Fluid Flow for Chemical Engineers, Edward Arnold, London

90   Marchant, J.Q., and Wakeman, R.J., 1997, Crossflow microfiltration of concentrated titania suspensions, Proc. IChemE Jubilee Research Event, Nottingham, Vol.2, p.1061

NOMENCLATURE

A	total number of annuli
A_n	cross sectional area of annulus 'n' (m^2)
a	mean particle radius in filter cake (m)
C_b	bulk solution concentration in film model (g ml^{-1})
C_b	bulk suspension solids fraction in annulus model (volume %)
C_c	cake solids fraction in annulus model (volume %)
C_g	gel concentration in film model (g ml^{-1})
C_n	solids fraction at diameter d_n of annulus 'n' (volume %)
C_s	Suspension solids fraction (volume %)
C_w	solute concentration at the membrane wall in film model (g ml^{-1})
c	molar concentration (mol dm^{-3})
D_r	rotational diffusion coefficient (s^{-1})
D_t	translational diffusion coefficient (m^{2}s^{-1})
D	diameter (m)
d_b	diameter occupied by bulk feed suspension in annulus model (m)
d_f	diameter open to flow (m)
d_n	outer diameter of annulus 'n' (m)
d_{n-1}	inner diameter of annulus 'n' (m)
d_o	filter tube internal diameter (m)
d_p	particle diameter (m)
E	complete blocking law constant
f	fanning friction factor
H_o	filter tube radius (m)
J	permeate flux (m^{3}m^{-2}s^{-1})
J_o	clean water permeate flux (m^{3}m^{-2}s^{-1})
J_{ss}	steady state permeate flux (m^{3}m^{-2}s^{-1})
K	Casson consistency coefficient (Pa s)
K_b	Complete blocking filtration law constant (s^{-1})
K_c	filter deposit permeability (m^2)
K_d	Standard blocking law constant (m^{-3})
K_i	Intermediate blocking law constant (m^{-1})
K_k	Cake filtration law constant (sm^{-6})
K_n	Casson consistency coefficient at outer diameter of annulus 'n' (Pa s)
K_s	solute back diffusion mass transfer coefficient in film model (m s^{-1})
k	Boltzmann constant (Nm kelvin^{-1})
k_0	empirical constant in Holdich model (m s^{-1})
$k_1 x$	empirical constant in Holdich model (m^{3}N^{-1}s^{-1})
L	filter tube length (m)
n	flow behaviour index
n	subscript denotes annulus number 'n'
P	pressure (Pa)
ΔP_L	tube length pressure drop (Pa)
ΔP_{TM}	transmembrane pressure (Pa)

Pe_r	rotational peclet number
Pe_t	translational peclet number
Q	feed volumetric flow rate $(m^3 s^{-1})$
Q_n	volumetric flow rate through annulus 'n' $(m^3 s^{-1})$
Q_p	permeate volumetric flow rate $(m^3 s^{-1})$
R	radius of a spherical particle (m)
R_c	specific cake resistance (m^{-2})
R_m	membrane resistance (m^{-1})
Re^*	modified Reynolds number
T	absolute temperature (kelvin)
t	time (s)
u	crossflow velocity (ms^{-1})
u_n	mean suspension velocity through annulus 'n' (ms^{-1})
z	height above an arbitrary plane (m)
α	specific cake resistance $(m\ kg^{-1})$
$\dot{\gamma}$	shear rate (s^{-1})
$\dot{\gamma}_n$	shear rate at outer diameter of annulus 'n' (s^{-1})
δ	hydrated ion radius (Stern layer thickness) (m)
δ_c	filter cake thickness (m)
δ_{css}	steady state cake thickness (m)
ε	cake voidage
ϕ_b	volume fraction of solids in titania suspension
ϕ_c	volume fraction solids in filter cake
ψ_o	electropotential at particle surface (mV)
ψ_g	electropotential at Stern plane (mV)
$1/\kappa$	debye length (nm)
μ	dynamic viscosity (Pa s)
μ_a	apparent viscosity (Pas)
μ_o	viscosity of the suspending medium (Pa s)
μ_p	permeate viscosity (Pa s)
η_l	consistency coefficient for Herschel-Bulkley/ power law model (Pa s)
ρ	density $(kg\ m^{-3})$
ρ_m	feed suspension density $(kg\ m^{-3})$
ρ_p	particle density $(kg\ m^{-3})$
τ	shear stress (Pa)
τ_c	time constant (Pa)
τ_w	wall shear stress (Pa)
τ_{wn}	shear stress at outer diameter of annulus 'n' (Pa)
τ_y	yield stress (Pa)
τ_{yn}	yield stress at outer diameter of annulus 'n' (Pa)
ζ	electropotential at the surface of shear (Zeta potential) (mV)

APPENDIX I

CALCULATION OF TITANIA SUSPENSION VOLUME SOLIDS CONCENTRATION

This follows the development of the equation used to calculate the volume fraction of titanium dioxide particles in suspension. The density of rutile is 4260 kg/m^3 and anatase is 3.84kg/m^3.

Considering a sample of suspension of volume $\quad V_s$ (m^3)

$\qquad\qquad\qquad\qquad$ and mass $\quad M_s$ (kg)

which contains x m^3 of water and y m^3 of titanium dioxide:

$$V_s = x + y \qquad\qquad (I.1)$$

and

$$M_s = \rho_w x + \rho_{TiO_2} y \qquad\qquad (I.2)$$

Rearranging equation I.1 for x, and substituting into equation I.2 gives

$$M_s = \rho_w (V_s - y) + \rho_{TiO_2} y \qquad\qquad (I.3)$$

Rearranging equation I.3 for y gives the volume of titania present (m^3) in the measured volume of suspension;

$$y = \frac{M_s - \rho_w V_s}{\rho_{TiO_2} - \rho_w} \qquad\qquad (I.4)$$

Dividing y by V_s gives the volume fraction of titania present in the suspension (ϕ_b);

$$\phi_b = \frac{1}{V_s}\frac{M_s - \rho_w V_s}{\rho_{TiO_2} - \rho_w} = \frac{M_s/V_s - \rho_w V_s/V_s}{\rho_{TiO_2} - \rho_w} = \frac{\rho_s - \rho_w}{\rho_{TiO_2} - \rho_w} \qquad (I.5)$$

Thus

$$\phi_b = \frac{\left(\rho_{suspension} - \rho_{water}\right)}{\left(\rho_{TiO_2} - \rho_{water}\right)} \qquad (I.6)$$

182

APPENDIX II

CALIBRATION DATA FOR THE FILTRATION RIG

II.1 THE MONO PUMP

II.1.1 Stator Characterisation

Three pump stators were used during the experimental study, each having been progressively eroded by the titania suspensions. The stator supplied with the pump was made of natural rubber, designed to operate at 20°C and within the pH range 5-9. This wore extremely rapidly, due to the excessive conditions outside its operating range, and was replaced (after experimental series A and B) by a rubber nitrile stator, designed for temperatures >50°C and pH within the range 3-10. This lasted considerably longer but was itself replaced with a second nitrile stator once it was no longer capable of producing the required pressures and flowrates.
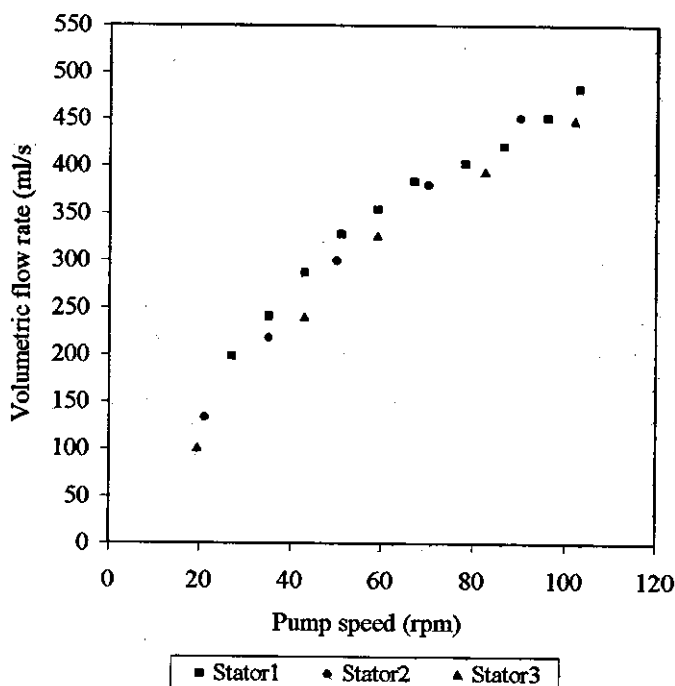
Figure II.1 Mono pump calibration curves for the three stators

The calibration curves for the new stators (Figure II.1) show that they were characteristically similar. The data is not expected to coincide exactly as the pump rotor also underwent some deterioration, which affected the ability of subsequent stators to perform as well as their predecessors.

II.1.2 Pump Calibration

Pump speed was measured using a light sensor, focussed on a notched ring on the pump shaft. The analogue signal from the sensor was converted to a digital reading by the filtration rig PC, and was subsequently plotted against the pump speed, which was measured manually as shown in (Figure II.2).
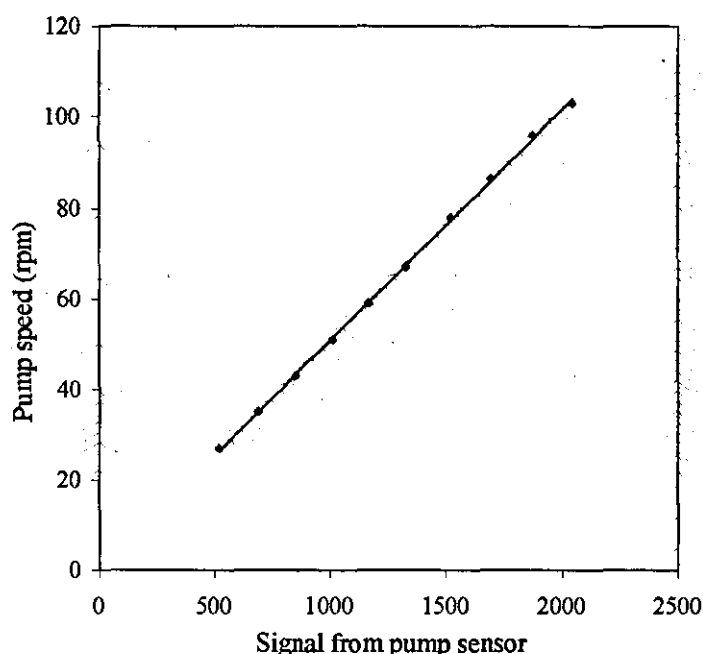
Figure II.2 Pump speed (rpm) as a function of the digital signal from the sensor

The volumetric flow rate through the filter assembly was also measured (using a 2 litre measuring cylinder and stopwatch), and similarly plotted as a function of the signal from the sensor (Figure II.3).
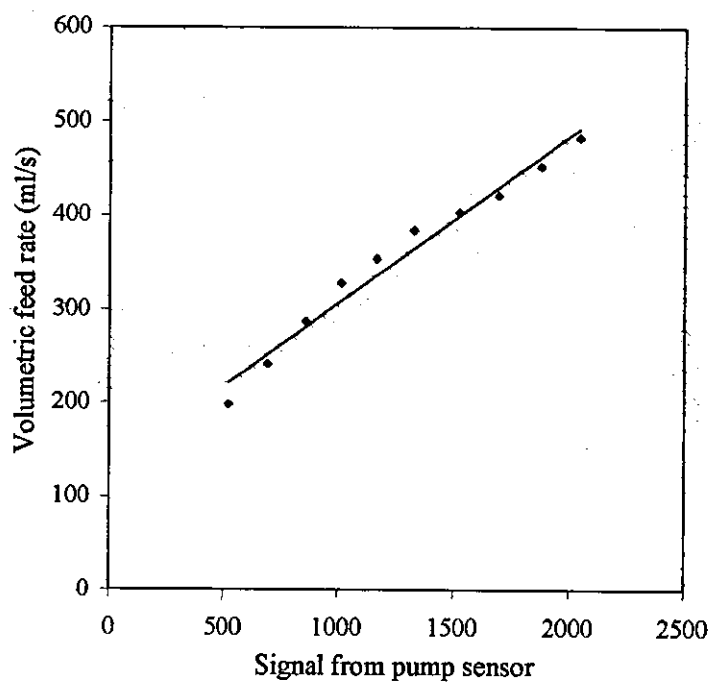
Figure II.3 Volumetric flow rate (ml/s) as a function of the digital signal from the sensor

Equation II.1 was fitted to the data in Figure II.3, and used by the PC as the calibration curve to convert the signal from the sensor into an on screen value for volumetric flow rate.

$$\text{Flow rate (ml/s)} = (0.1777 \times \text{signal}) + 129.46 \qquad \text{(II.1)}$$

II.2   PRESSURE TRANSDUCER CALIBRATION

Pressure transducers were fitted at either end of the filter module, transducer 1 at the exit and transducer 2 at the inlet. Pressure transducers 1 and 2 were calibrated separately, and the data for these is given in Figures II.4 and II.5.
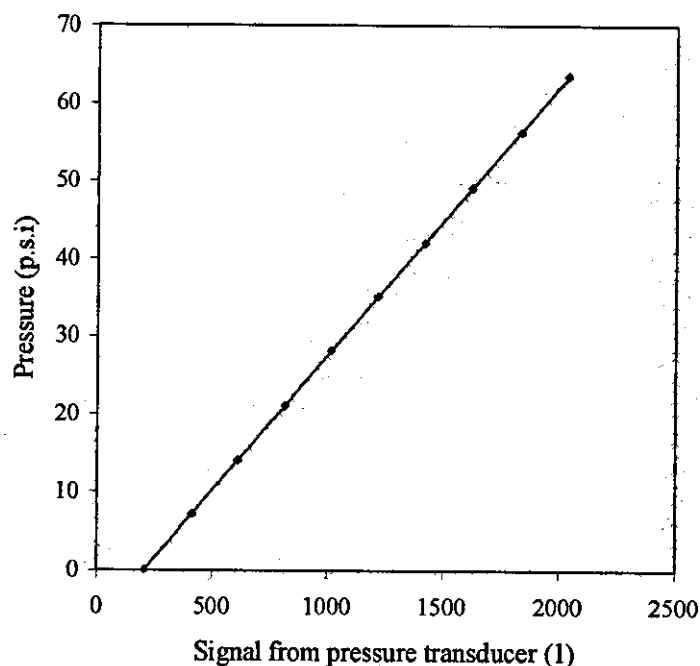
Figure II.4   Calibration for pressure transducer 1

The data from pressure transducer 1 was fitted by equation II.2, and the data from transducer 2 by equation II.3.

$$P_{outlet} \text{ (p.s.i)} = (0.0347 \times \text{signal}) - 7.114 \qquad (II.2)$$

$$P_{inlet} \text{ (p.s.i)} = (0.0346 \times \text{signal}) - 1.3795 \qquad (II.3)$$

186
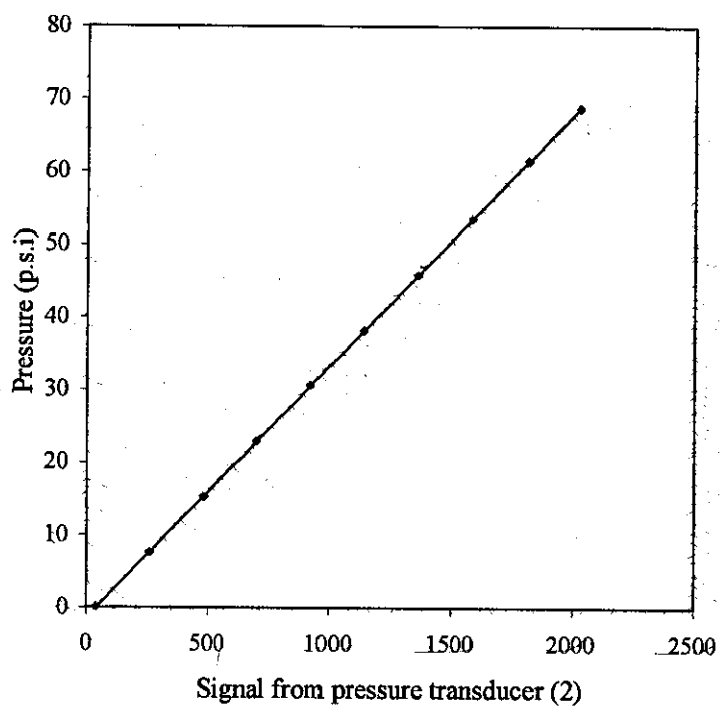
Figure II.5 Calibration for pressure transducer 2

II.3 THERMOCOUPLE CALIBRATION

Thermocouples were used to monitor the temperature in the hot water tank (1), the suspension feed tank (2), and the feed line to the filter (3).
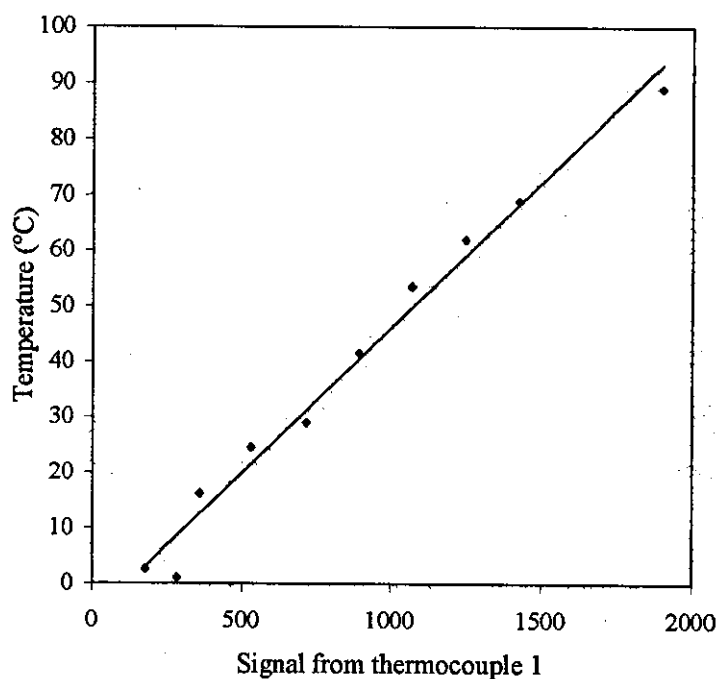
Figure II.6 Calibration data for thermocouple 1. (hot water tank monitor)

Equation fitted to thermocouple 1:

$$T_1 = (0.0525 \text{ x signal}) -6.2934 \qquad \text{(II.4)}$$

Equation fitted to thermocouple 2:

$$T_2 = (0.2317 \text{ x signal}) -1.0586 \qquad \text{(II.5)}$$

Equation fitted to thermocouple 3:

$$T_3 = (0.226 \text{ x signal}) -4.8907 \qquad \text{(II.6)}$$
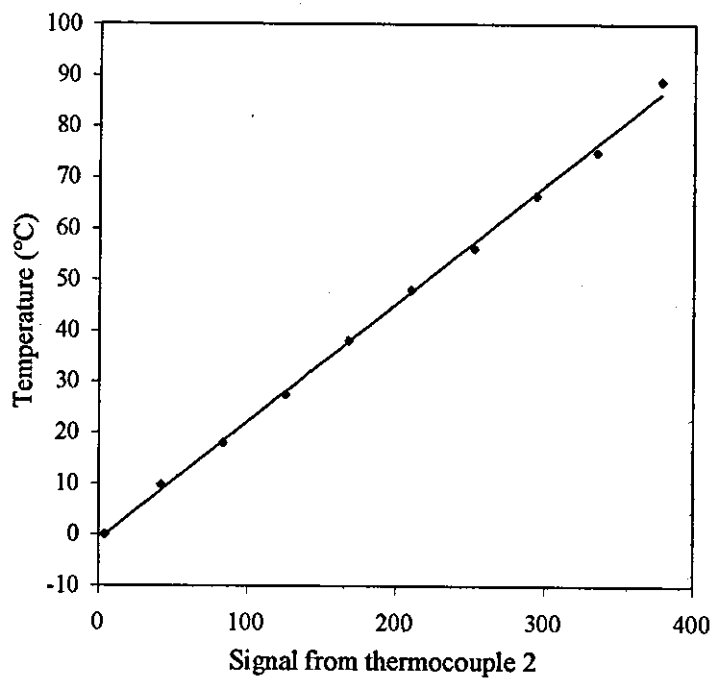
Figure II.7 Calibration data for thermocouple 2. (suspension feed tank monitor)
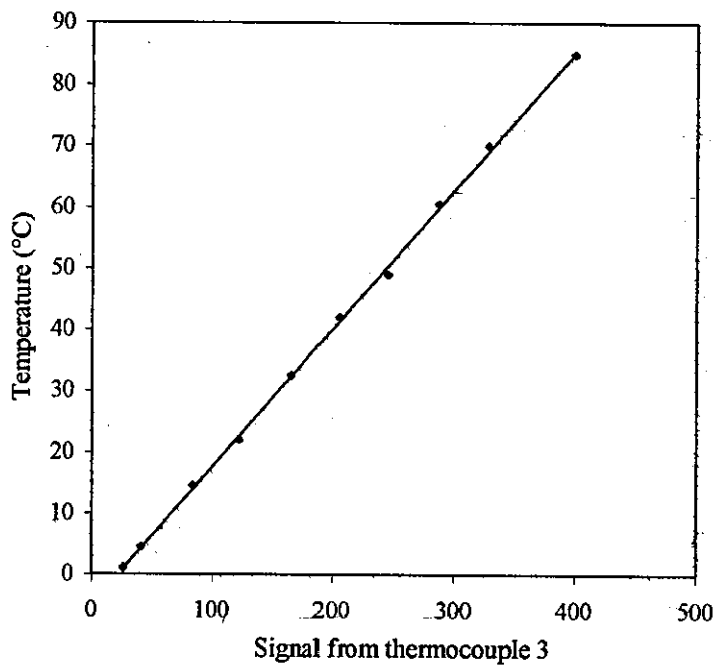
Figure II.8 Calibration data for thermocouple 3. (filter feed line monitor)

189

II.4 FILTER TUBE CALIBRATION

II.4.1 Clean Water Flux Data

Two similar filter tubes were used in the course of the filtration experiments, and the permeate flux of Millipore water through the new (unfouled) membranes was measured as a function of transmembrane pressure. This would enable any non-recoverable losses in filtration performance to be monitored, and establish the degree to which they might affect permeate fluxes at steady state.

The clean water flux through the filters was measured over a small range of transmembrane pressures (limited by the pump available) using the clean water rig (Section 2.6.4), and the data for the two tubes is plotted in Figure II.9.
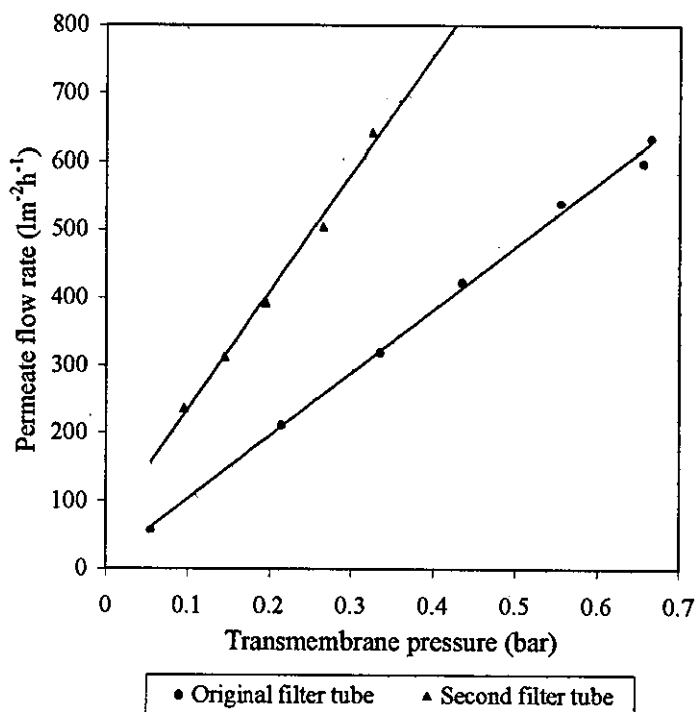
Figure II.9 Clean water flux data for Atech, 16mm i.d., 0.9m long SiC filter tubes

Attaching the clean water rig prevents use of the lower pressure transducer, thus a measurement of static head was used to estimate the entry pressure to the filter (approximately 0.055 bar).

Figure II.9 shows that the filters obey Darcy's law (as would be expected), and that the data can be fitted with the following equations;

$$J = 929.83 \Delta P_{TM} + 10.34 \qquad \text{(II.7)}$$

$$J = 1735.2 \Delta P_{TM} + 61.91 \qquad \text{(II.8)}$$

for the original and second filters respectively, where J is the permeate flux ($lm^{-2}h^{-1}$) and ΔP_{TM} is the transmembrane pressure in bar. The original filter was used for all series A and B experiments, and up to experiment C36, after which the second filter tube was used.

Equations II.7 and II.8 suggest that some permeate flow will be achieved even in the absence of transmembrane pressure. This could result from the fact that the downstream pressure transducer is located approximately 20cm above the filter tube exit, in pipework that is over 3mm smaller than the filter tube in diameter (Figure II.10). I.e., the measured pressure is different to the actual pressure at the filter outlet.

Bernoulli's equation states that for a fluid of constant density (i.e. internal energy remains constant), the sum of the static head, velocity head and gravity head remains constant[88]. This can be applied to the system in Figure II.10, using Equation II.9.

$$\frac{p_1}{\rho g} + \frac{u_1^2}{2g} + z_1 = \frac{p_2}{\rho g} + \frac{u_2^2}{2g} + z_2 \qquad \text{(II.9)}$$

The subscripts 1 and 2 denote positions upstream and downstream respectively. In relation to the current system (Figure II.10), position 1 is just before the filter tube exit, while 2 is at the pressure transducer. At each point, p is the pressure, ρ is the fluid density, g is the force due to gravity, u is the velocity of the stream, and z is the height above an arbitrary plane.

Pipework

Transducer

z_2
p_2
u_2

z_1
p_1
u_1

Filter tube

Flow
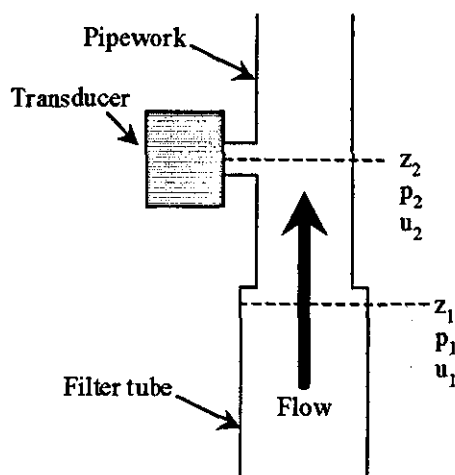
Figure II.10 Diagram showing the reduction in diameter from filter tube to pipework.

Equation II.9 can be rearranged to demonstrate the effect of the contraction, and additional length on the difference in pressure between the filter exit and the pressure transducer (equation II.10).

$$p_1 - p_2 = \rho g(z_2 - z_1) + \frac{\rho}{2}\left(u_2^2 - u_1^2\right) \qquad (\text{II.10})$$

z_2 is greater than z_1, and u_2 is greater than u_1, thus p_1-p_2 is positive, so p_1 (pressure at the filter exit) must be greater than p_2 (pressure measured by the transducer). I.e., the actual transmembrane pressure drop will be greater than suggested by the downstream pressure transducer.

When considering the above, it should be noted that the water flux through the clean filters was more than an order of magnitude larger than the flux through the tiania fouled filters at steady state. It was thus evident that even when non-recoverable fouling had reduced the filters to 40% of their original permeability, the effect of this on experimental steady state permeate fluxes was still negligible.

APPENDIX III

APPLICATION OF BLOCKING FILTRATION LAWS TO EXPERIMENTAL SERIES A RESULTS.

A plot of permeate flux as a function of feed suspension concentration (Figure 3.13) is composed of the results of three experiments, where titania suspensions were concentrated from 2-6%, 6-18%, and 18-50% volume solids respectively. Combining the data on one plot revealed that the transition of results from the 2-6% experiment to the 6-18% experiment is discontinuous. I.e., when starting an experiment at lower feed solids concentrations, there is a tendency to decline to a much lower flux (for a given feed suspension concentration) than if the experiment was started at a higher feed solids concentration.

Appendix V demonstrates that the initial stages of flux decline can be predicted using dead-end filtration theory. It may therefore be possible to apply the blocking filtration laws developed by Hermia[30] (Equations 1.7 to 1.10, Section **1.4.2**) to this data, and ascertain whether the rates of flux decline can be associated with specific blocking mechanisms.

The initial flux decline data from experiments A6r (2-6% volume solids) and A1r (6 to 18% volume solids), and the clean water flux data from Appendix VIII has been applied to all four models. The resulting plots are given in Figures III.1 to III.8 along with 'best fit' lines, obtained using linear regression.

Figure III.1 Standard blocking model fit to experiment starting at 2% volume solids

Figure III.2 Cake filtration model fit to experiment starting at 2% volume solids

195
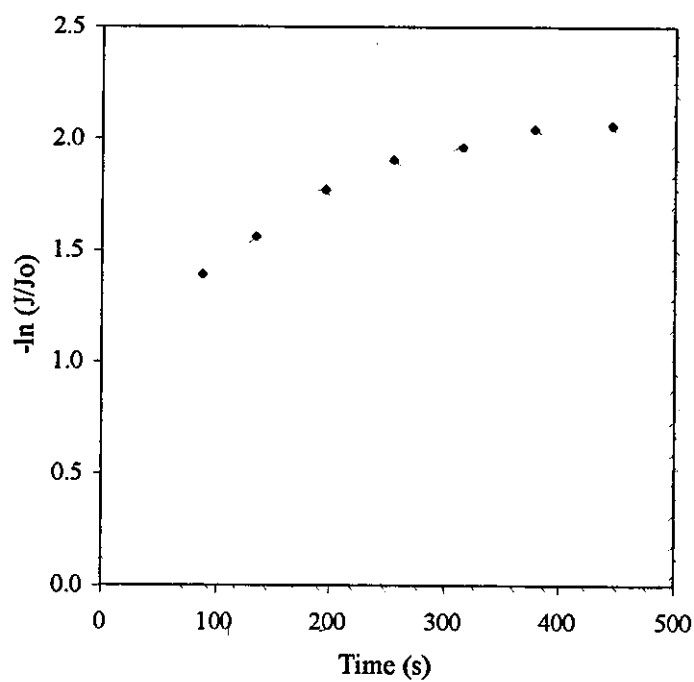
Figure III.3 Complete blocking model fit to experiment starting at 2% volume solids
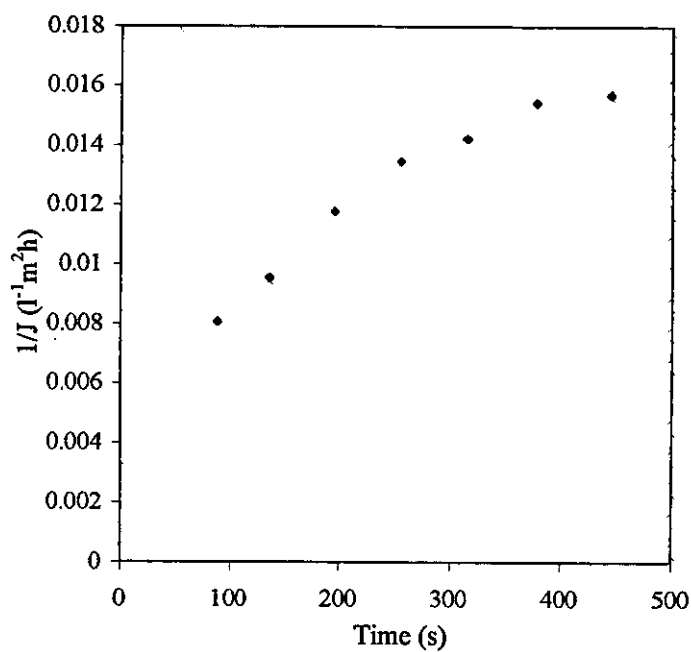
Figure III.4 Intermediate blocking model fit to experiment starting at 2% volume solids
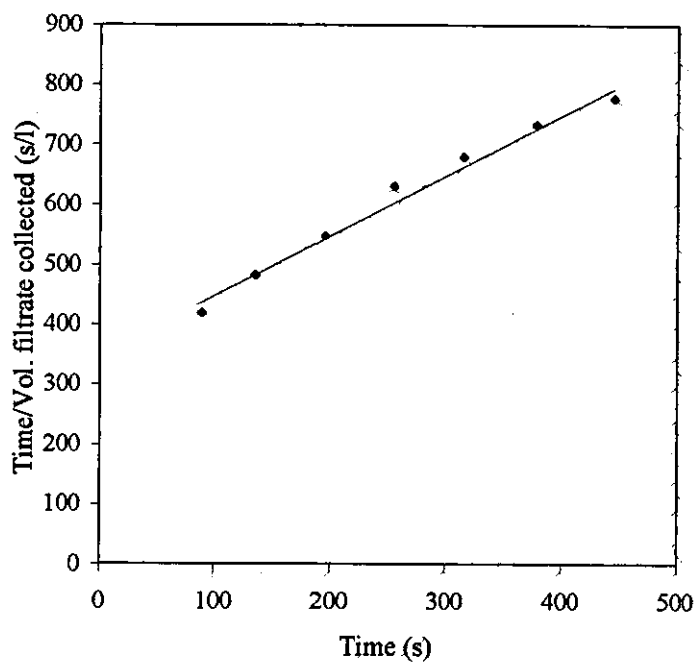
196
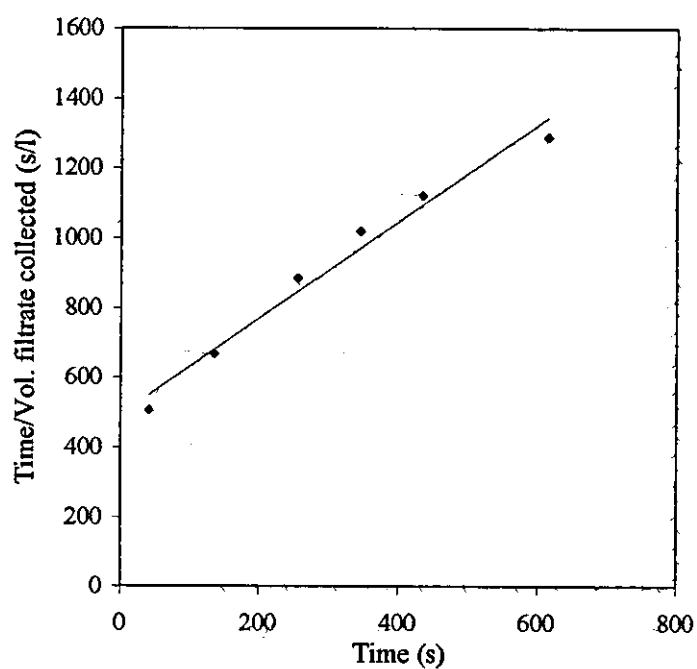
Figure III.5 Standard blocking model fit to experiment starting at 6% volume solids
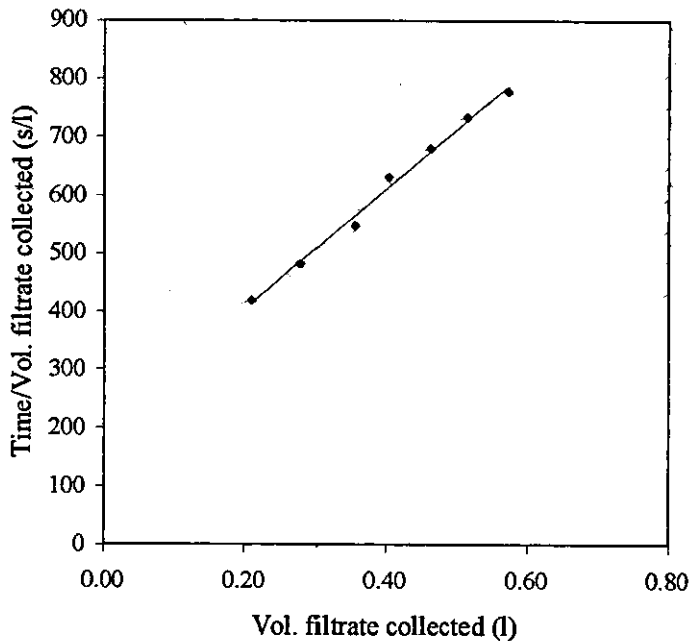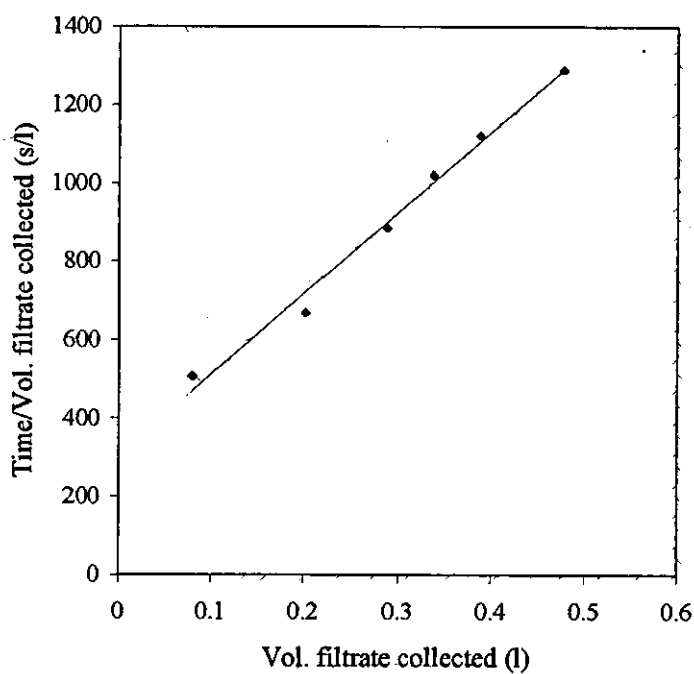

Figure III.6 Cake filtration model fit to experiment starting at 6% volume solids

197
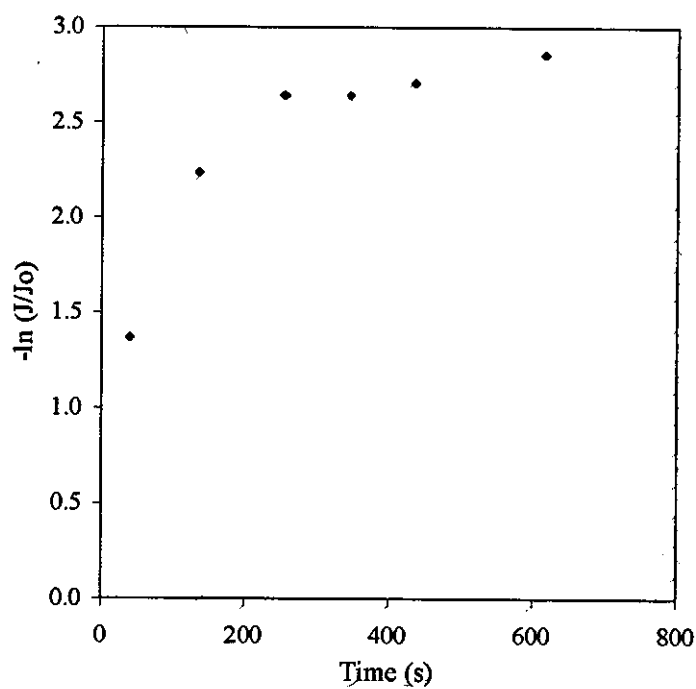
Figure III.7 Complete blocking model fit to experiment starting at 6% volume solids
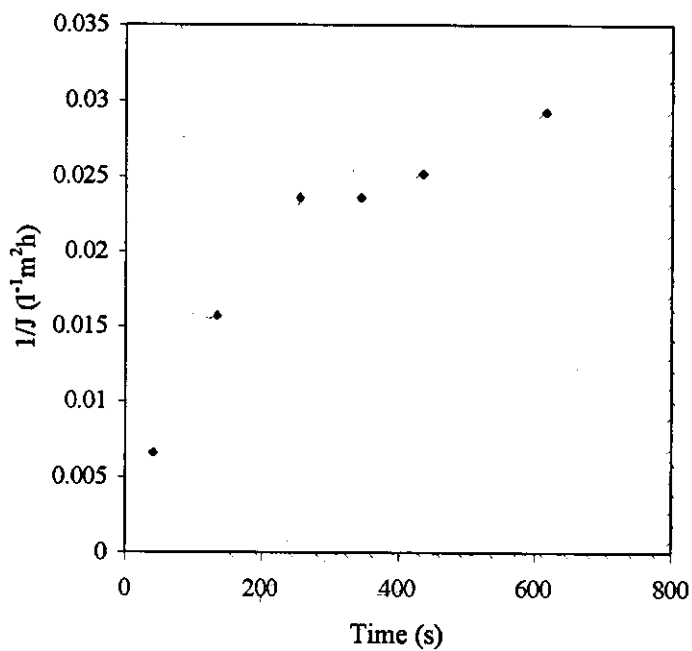
Figure III.8 Intermediate blocking model fit to experiment starting at 6% volume solids

198

APPENDIX IV

EXPERIMENTAL SET C RESULTS

IV.1 Manipulation of Experimental set C results

Experiments in set C gave up steady state permeate flux data as a function of feed solids concentration, transmembrane pressure, and superficial crossflow velocity (where pH and temperature were maintained constant at approximately pH9.5 and 50°C respectively). Feed concentrations of 5.5, 12, 19, 26, 33 and 40% volume solids were filtered at transmembrane pressures of 0.5, 1 and 2 bar, and superficial crossflow velocities between 0.33 and $1.52ms^{-1}$.

Transmembrane pressures could be reliably set up and maintained during filtration, while the superficial crossflow velocity, for various reasons, was more difficult to set up and subsequently liable to change during the course of an experiment. Initial conditions were set up using water in the rig, before the addition of the suspension, and the introduction of solids to the process stream resulted in a change in the volumetric flow rate for a given pump speed. The flow rate then reduced during filtration, as the thickening filter cake increased the resistance to feed flow, thus placing a greater load on the progressively eroding mono pump.

As a consequence it was decided to set an approximate superficial crossflow velocity at the start of each experiment and then, at steady state, measure the actual volumetric flow rate manually.

This problem was not noted initially, and an inability to guarantee the specified crossflow velocities of earlier experiments means that the results used in analysis are comprised primarily of results from experiment C25 onwards.

Figures IV.1, IV.2 and IV.3 show the raw data collected at 0.5, 1 and 2 bar respectively. Steady state permeate flux has been plotted as a function of superficial crossflow velocity and curves fitted to the points of equal solids concentration.
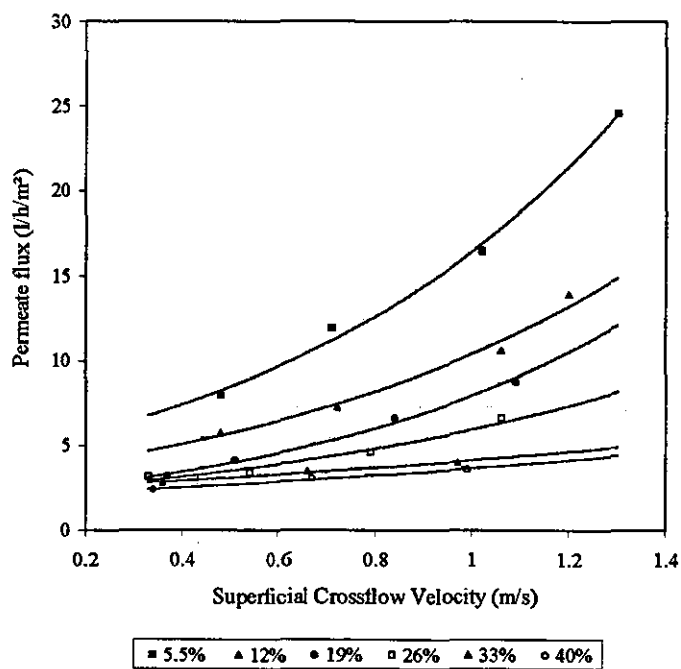
Figure IV.1 Raw steady state flux data collected at 0.5 bar
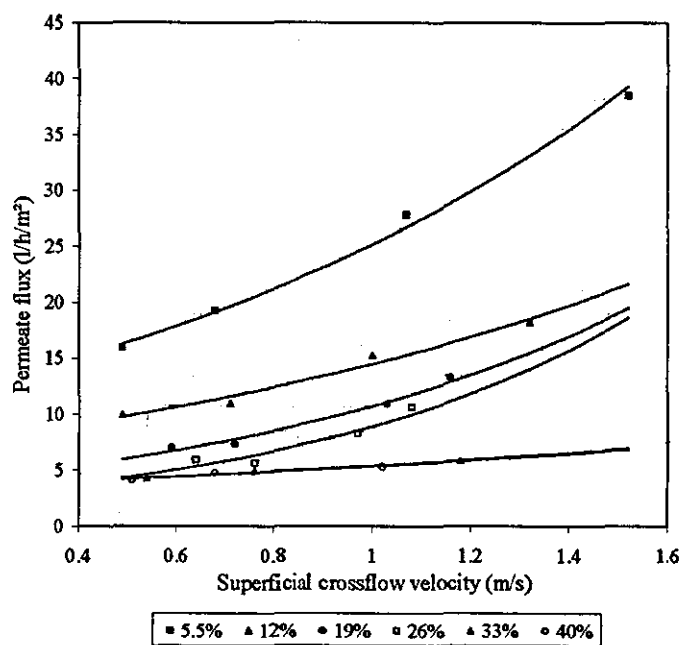
Figure IV.2 Raw steady state flux data collected at 1 bar
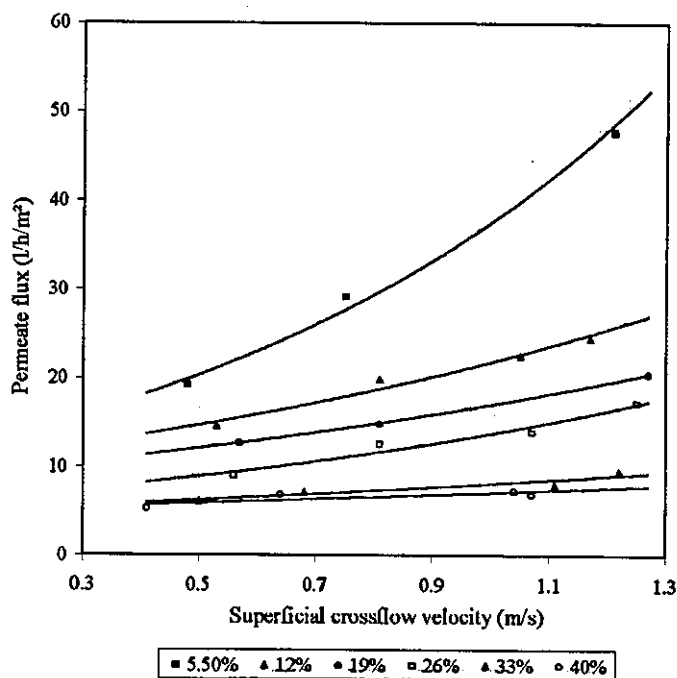
Figure IV.3 Raw steady state flux data collected at 2 bar

The curves fitted to Figures IV.1 to IV.3, were used to interpolate steady state fluxes for each feed solids concentration and transmembrane pressure at specific superficial crossflow velocities of 0.4, 0.8 and 1.2ms^{-1}. This data is plotted in Figures IV.4 to IV.9, which show the trends in steady state permeate flux with varying process parameters.
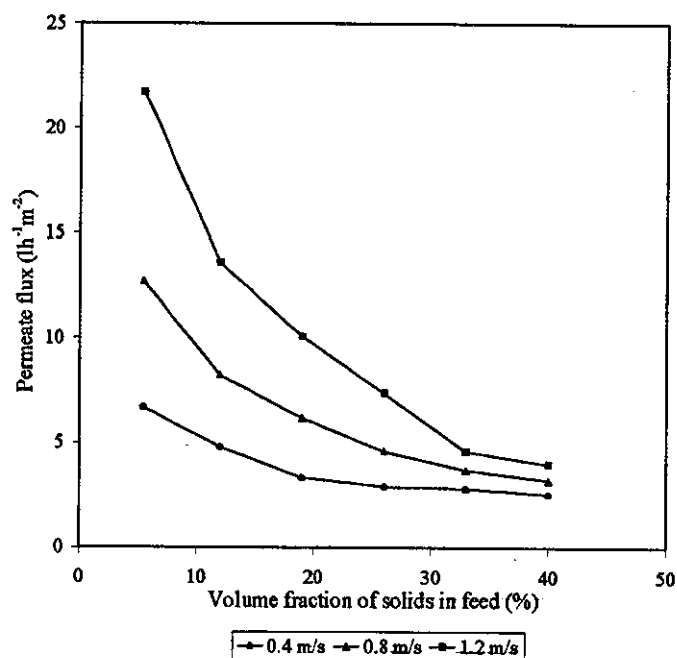
Figure IV.4 Steady state permeate flux vs. feed suspension volume solids at 0.5 bar
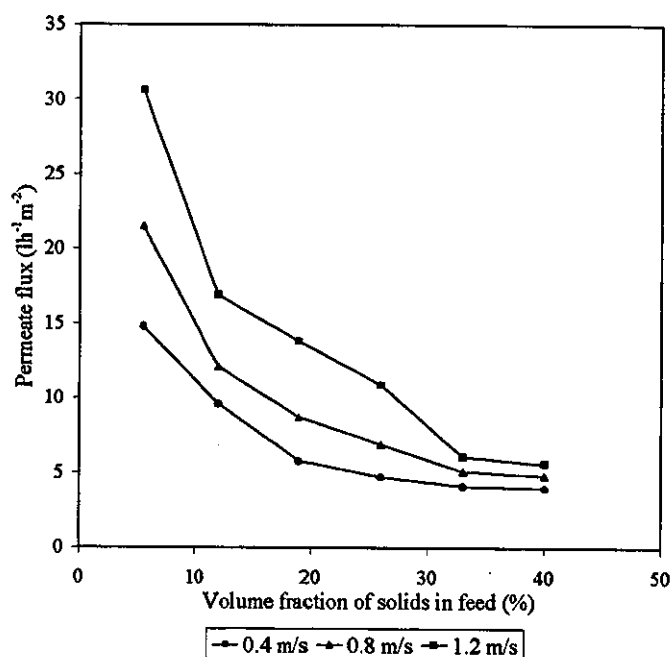
Figure IV.5 Steady state permeate flux vs. feed suspension volume solids at 1 bar

202
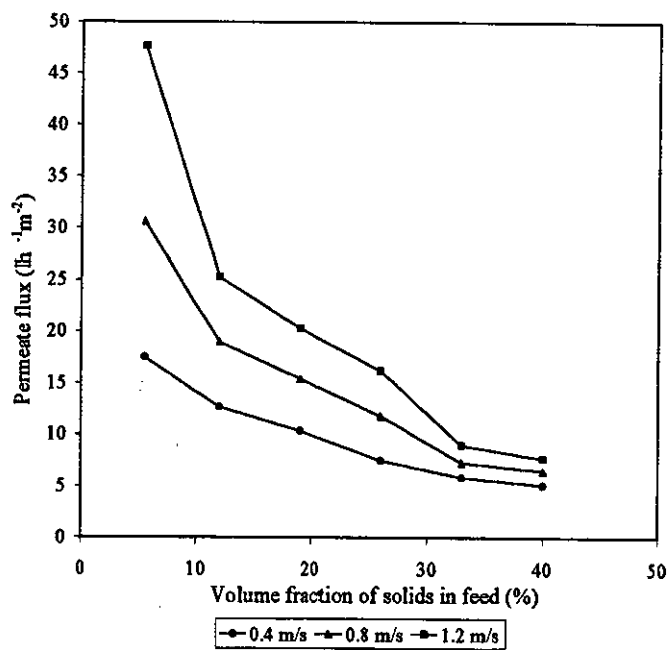
Figure IV.6 Steady state permeate flux vs. suspension volume solids at 2 bar
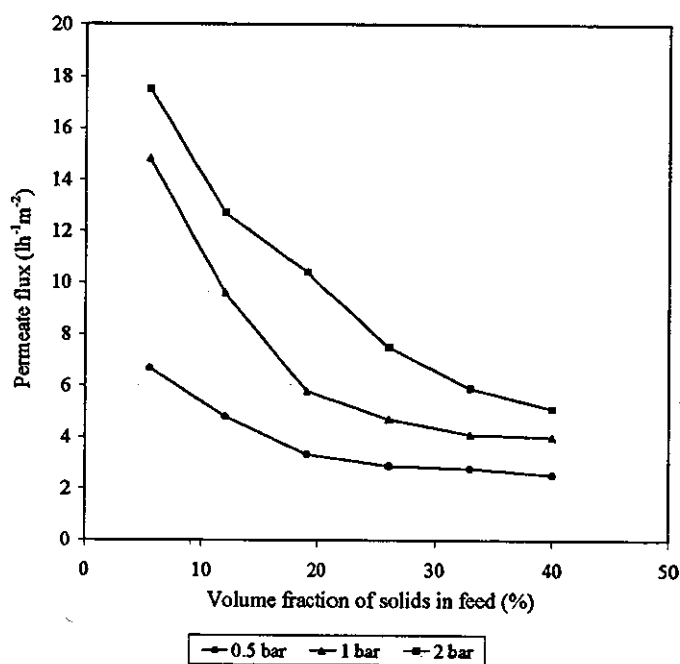
Figure IV.7 Steady state permeate flux vs. suspension volume solids at 0.4ms^{-1}
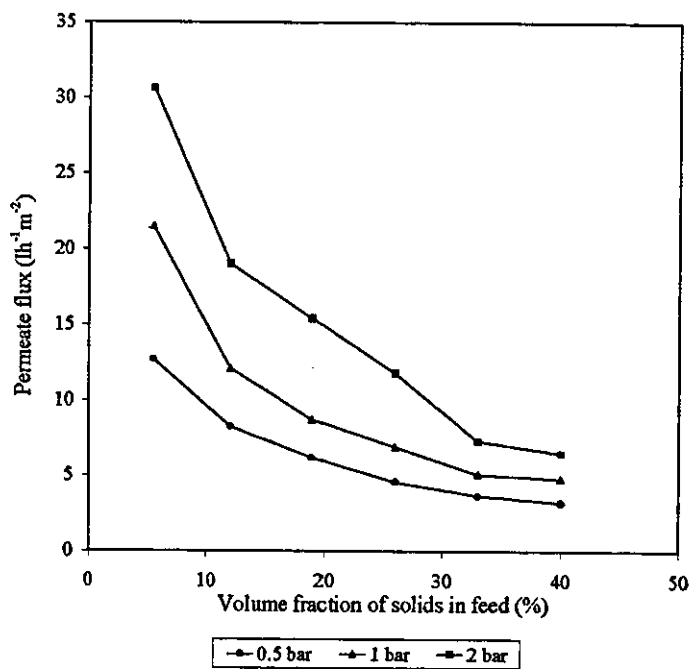
Figure IV.8 Steady state permeate flux vs. feed suspension volume solids at 0.8ms^{-1}
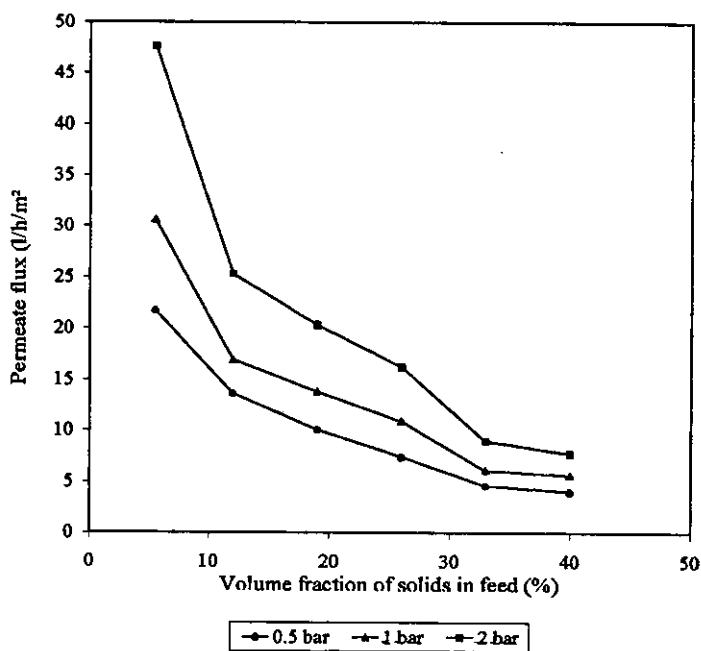
Figure IV.9 Steady state permeate flux vs. feed suspension volume solids at 1.2ms^{-1}

204

IV.2 Calculation of filter cake thickness from steady state permeate flux data

Dead end filtration theory can be used to calculate a crossflow filter cake thickness at steady state using permeate flux data.

Using the modified Darcys law equation (equation 1.14), values are required for the membrane resistance (R_m, from equation 1.12), filter cake resistance (R_c, from equation 1.13), permeate viscosity (μ_p), transmembrane pressure (ΔP_{TM}), and filter tube radius (H_o), where δ_{css} is the steady state cake thickness and J_{ss} is the steady state permeate flux (based on the clean tube diameter).

$$J_{ss} = \frac{\Delta P_{TM}}{\mu_p \left(R_m + R_c H_o \ln\left[\dfrac{H_o}{H_o - \delta_{css}} \right] \right)} \qquad (1.14)$$

Using the data in Figure 3.23 at a superficial velocity of 0.8ms^{-1} as an example, the values of cake thickness calculated were related back to the suspension feed solids concentration as follows.

Steady state permeate flux data was read off for feed volume solids compositions of 5, 12, 19, 26, 33 and 40% at 0.8ms^{-1} (Table IV.1). These values were substituted into equation 1.14 and rearranged to yield a steady state cake thickness, using a transmembrane pressure of 1x10^5 Pa, permeate viscosity of 1x10^{-3} Pas, filter tube radius 0.008m, the membrane resistance was estimated at 4x10^{11}m^{-1}, and the specific cake resistance was calculated for a cake volume solids fraction of 0.595 using equation 1.13 (giving R_c = 7.807x10^{15}m^{-2}).

The values of cake thickness were then used to calculate the open flow diameter (d_f) and the steady state crossflow velocity (CF_{Vel}) for each system (Table IV.1).

Table IV.1 Data extracted from, and calculated using data from Figure 3.24

Feed vol. fraction (%)	J_{ss} ($lm^{-2}h^{-1}$)	δ_{css} (mm)	d_f (mm)	CF_{Vel} (ms^{-1})
5	21.6	1.8	12.4	1.3
12	12.1	3.0	10.0	2.1
19	8.82	3.8	8.4	2.9
26	7.06	4.4	7.2	4.0
33	5.10	5.4	5.2	7.6
40	4.9	5.5	5.0	8.2

IV.3 Effect of solids concentration on shear stress (Figure 3.27)

Casson constants for yield stress and consistency coefficient (from Appendix VII, Tables VII.2 to VII.7) were used to calculate shear stresses for suspensions across a range of feed solids concentrations and at shear rates of between 500 and $2500s^{-1}$. This data shows the effect of feed solids concentration on wall shear stress at constant shear rate.

APPENDIX V

THEORETICAL CURVES FOR DEAD-END FLUX DECLINE

The flux decline curves from crossflow filtration experiments were compared with theoretical flux decline curves, calculated using dead-end filtration theory (Section **4.1**, equations 4.1 to 4.4).

The values used for clean water flux (J_o), transmembrane pressure (ΔP_{TM}) and feed solids fraction (ϕ_b) were those measured for the equivalent crossflow experiment (Table V.1). A value of $0.16\mu m$ was used for the mean particle radius (a), and 1mPas was used for the permeate viscosity (μ_p). The fraction of solids in the cake (ϕ_c) was measured experimentally at 0.595 (by removing a sample of cake from the filter), and this was corroborated in work by Datta and Gaddis[38], who obtained titania cakes from crossflow filtration experiments with average volume solids concentrations of 0.58-0.6.

Table V.1 Data for theoretical flux decline calculations using dead-end theory

Experiment	J_o (m^{3}s^{-1}m^{-2})	ΔP_{TM} (Pa)	ϕ_b (fraction)
ExptC71	1.92x10^{-4}	1x10^5	0.055
ExptC74	3.25x10^{-4}	2x10^5	0.19
ExptC80	1.57x10^{-4}	1x10^5	0.19
ExptC81	1.43x10^{-4}	1x10^5	0.40
ExptC82	1.23x10^{-4}	1x10^5	0.33
ExptC83	1.53x10^{-4}	1x10^5	0.055
ExptC84	1.53x10^{-4}	1x10^5	0.12
ExptC89	2.02x10^{-4}	1x10^5	0.26

The theoretical curves are plotted along with the experimental flux decline curves for each experiment in Figures V.1 to V.8.
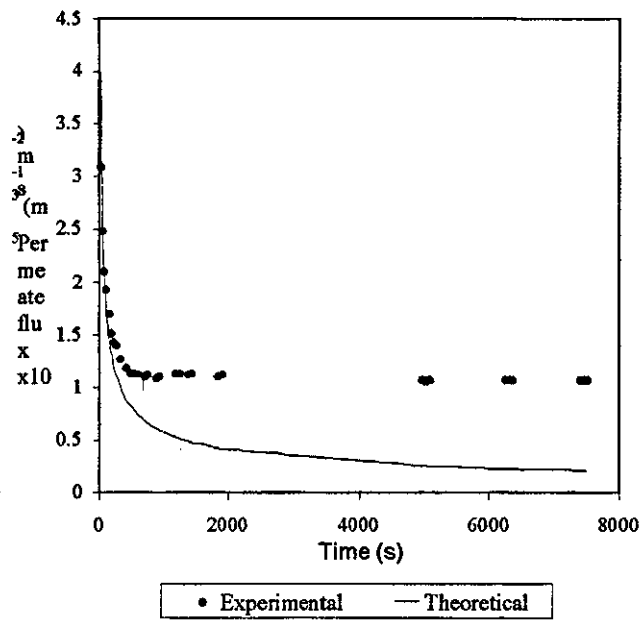
Figure V.1 Theoretical and actual flux decline curves for experiment C71
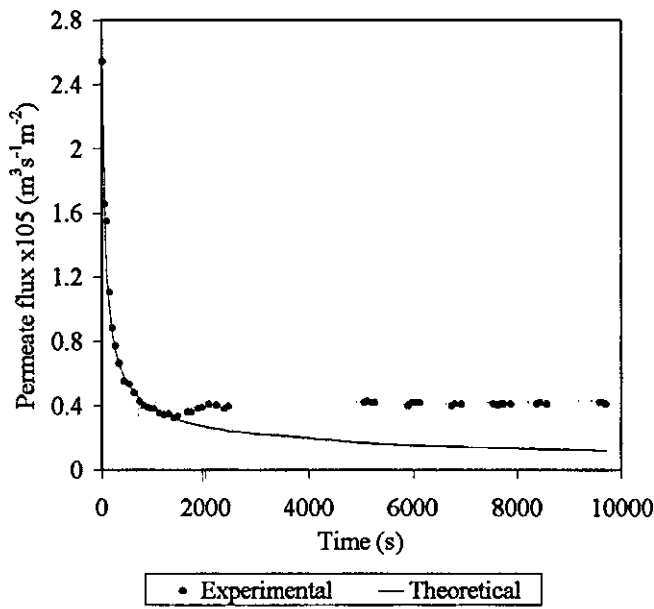
Figure V.2 Theoretical and actual flux decline curves for experiment C74

208
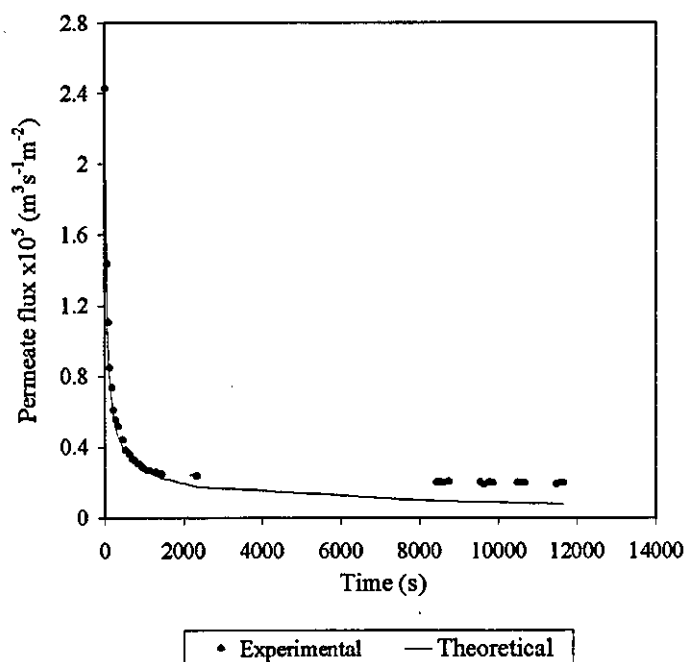
Figure V.3 Theoretical and actual flux decline curves for experiment C80
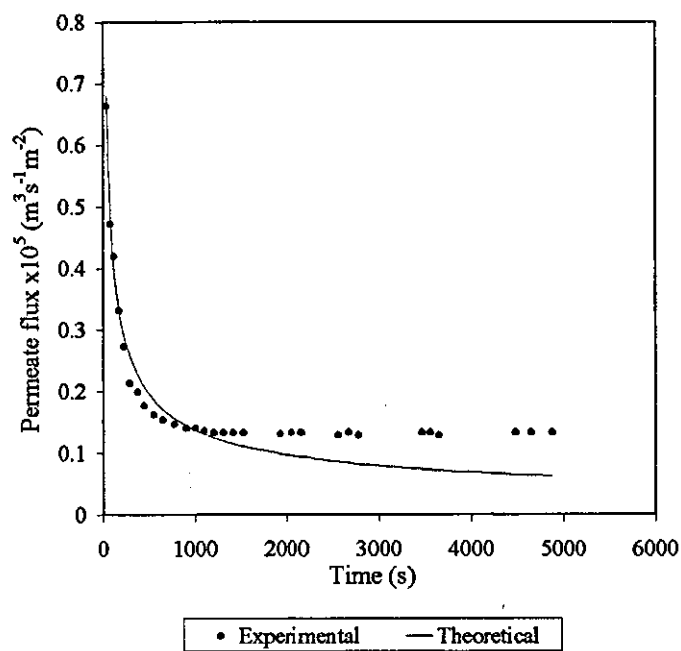
Figure V.4 Theoretical and actual flux decline curves for experiment C81
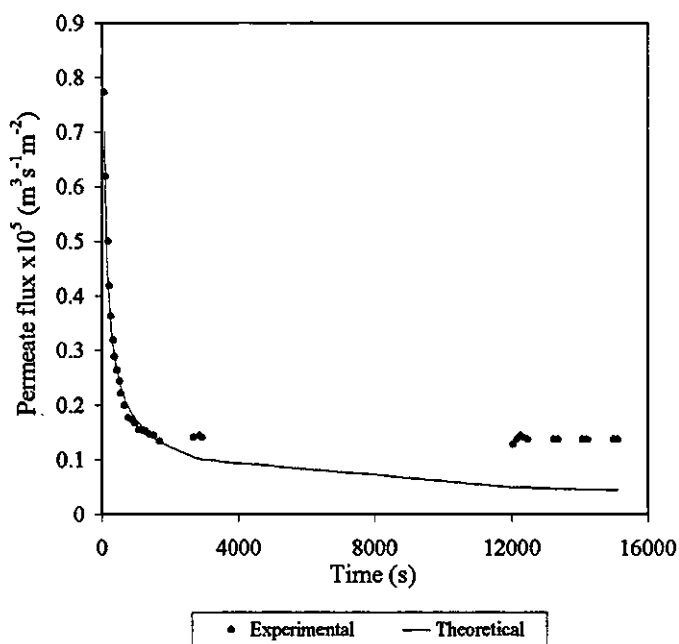
Figure V.5 Theoretical and actual flux decline curves for experiment C82
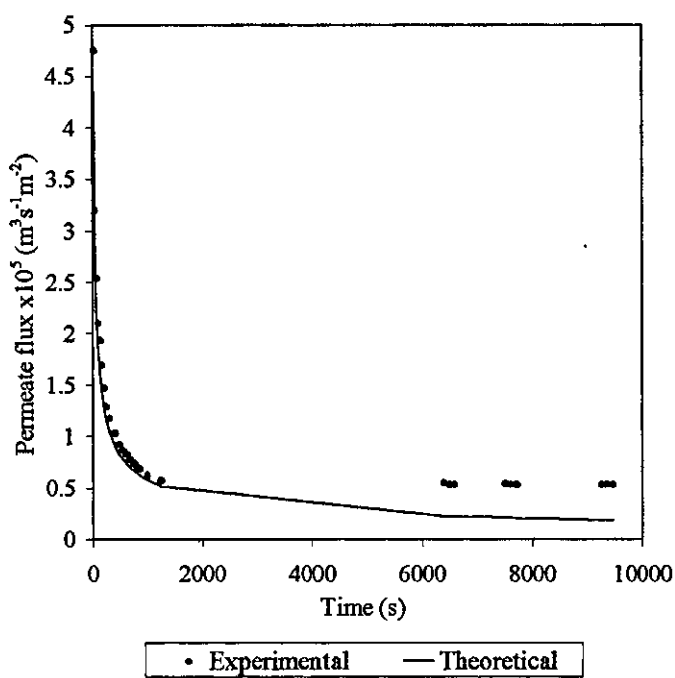
Figure V.6 Theoretical and actual flux decline curves for experiment C83

210
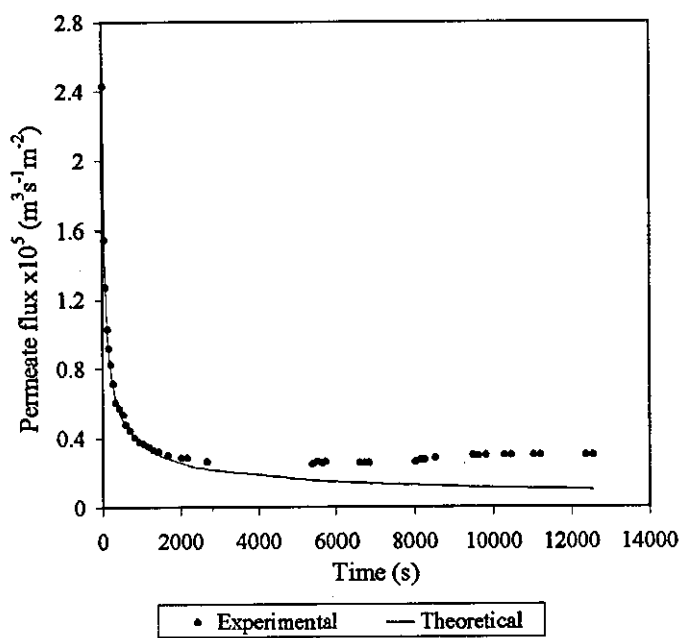
Figure V.7 Theoretical and actual flux decline curves for experiment C84
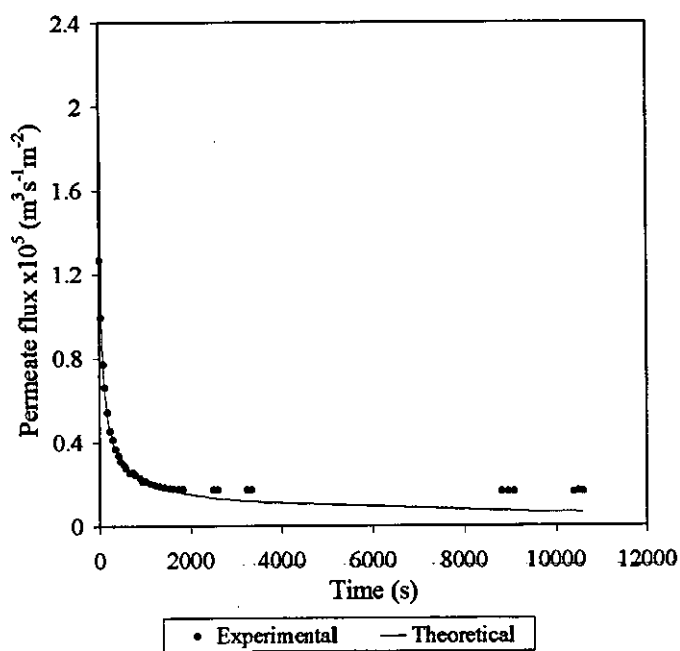
Figure V.8 Theoretical and actual flux decline curves for experiment C89

211

APPENDIX VI

CALCULATIONS ASSOCIATED WITH THE MODEL OF HOLDICH et al.[84,85] AND ISMAIL[86]

The model presented in equation 4.7, aims to determine the steady state cake thickness for a specific system, under any operating conditions, once the empirical constant (k_1x) has been determined for that system.

$$d_f^3 = \frac{k_1 x f \rho_m 4 Q^2 \mu_p}{\pi^2 \Delta P_{TM}} \left[\frac{\ln\left(d_o / d_f\right)}{K_c} + \frac{2R_m}{d_o} \right] \qquad (4.7)$$

Estimating an initial value of the steady state diameter open to flow (d_f) and substituting it into the right hand side of the equation, yields a calculated value of d_f (from d_f^3). Through successive iterations, the correct value of d_f can be arrived at, this having been achieved when the value resulting from the resolution of equation 4.7 is the same as the initial value estimated.

VI.1 Data, constants and calculations for use in equation 4.7

A value of 1mPa s was used for the permeate viscosity (μ_p), the clean tube diameter (d_o) was 0.016m, and the feed volumetric flow rates (Q) and transmembrane pressures (ΔP_{TM}) were measured during the crossflow experiments (Table VI.2).

VI.1.1 Calculation of suspension density (ρ_m)

The suspension density (ρ_m) was calculated using equation VI.1:

$$\rho_m = \left(\rho_{TiO_2} \times frac_{TiO_2}\right) + \left(\rho_{H_2O} \times frac_{H_2O}\right) \qquad \text{(VI.1)}$$

where 4260 kg m^{-3} was used as the density of rutile (ρ_{TiO_2}), 1000 kg m^{-3} for the density of water (ρ_{H_2O}), and $frac_{TiO_2}$ and $frac_{H_2O}$ were the volume fractions of titania and water in suspension respectively. The calculated densities are given in Table VI.1.

VI.1.2 Calculation of membrane resistance (R_m)

The membrane resistance (m^{-1}) was calculated using equation 4.3 and the clean water flux (J_o), measured at the start of each experiment.

$$R_m = \frac{\Delta P_{TM}}{\mu_p J_o} \qquad \text{(4.3)}$$

Values for clean water permeate flux (J_o) can be found in the statement of experiments (Appendix VIII).

VI.1.3 Calculation of filter cake permeability (K)

The filter deposit permeability was calculated using the Kozeny-Carman equation (equation VI.2).

$$K_c = \frac{(2a)^2 (1 - \phi_c)^3}{180(\phi_c)^2} \qquad \text{(VI.2)}$$

where a is the mean particle radius (0.16μm) and ϕ_c is the solids fraction of the filter cake. Assuming that the solids fraction in the filter cake was constant for all experiments, and equal to 0.595 (Section **3.3.1**), then:

$$K_c = \frac{(3.2 \times 10^{-7})^2 \, 0.405^3}{180(0.595)^2} = 1.067 \times 10^{-16} \, m^2$$

VI.1.4 Calculation of fanning friction factor (f)

The fanning friction factor was calculated using the Dodge-Metzner correlation[86] (equation VI.3), using a spreadsheet to iterate through values of f until the equation was balanced.

$$\frac{1}{\sqrt{f}} = \frac{4}{n^{0.75}} \log\left(Re^* \, f^{1 - n/2} \right) - \frac{0.4}{n^{1.2}}$$ (VI.3)

n is the flow behaviour index and Re^* is the modified Reynolds number[86] for power law fluids (equation VI.4).

$$Re^* = \frac{8\rho_m \left(\frac{4Q}{\pi d_f^2} \right)^{2-n} d_f^n}{\eta_1 \left(6n + \frac{2}{n} \right)^n}$$ (VI.4)

Equation VI.4 contains an expression for d_f, and thus required re-calculating (as therefore did equation VI.3) for successive iterations of equation 4.7.

The flow behaviour index (n) and consistency coefficients (η_1) for the different concentration suspensions were obtained by fitting rheological data to a power law model (equation VI.5)

$$\tau = \eta_1 \dot{\gamma}^n$$ (VI.5)

214

This was done using software supplied with the Carrimed constant stress rheometer (Appendix VII), and the values of n and η_l for the different concentration feed suspensions are given in Table VI.1.

Table VI.1 Suspension density and rheological constants for Dodge-Metzner correlation

Solids fraction (%)	ρ_m (kg m^{-3})	n	η_l (N s m^{-2})
5.5	1179.3	0.8493	4.547e^{-3}
12	1391.2	0.8666	4.970e^{-3}
19	1619.4	0.7424	0.02278
26	1847.6	0.6064	0.19655
33	2075.8	0.8774	0.4796
40	2304	0.3958	2.1958

VI.1.5 Calculation of the empirical constant k_1x

In the absence of data correlating tube length pressure drop and tube diameter (as used by Holdich[83]), the constant, k_1x, was determined using equation 4.10, with the wall shear stress (τ_w) having been resolved using equation 4.9.

$$\tau_w = \frac{d_f \Delta P_L}{4L} \tag{4.9}$$

$$k_1 x = \frac{J_{ss}}{\tau_w} \tag{4.10}$$

Equation 4.9 uses the estimated value of d_f, with an experimentally determined tube length pressure drop (Appendix VI.1.5.1), and the filter tube length (L) of 0.9m. The steady state permeate flux (J_{ss}) was calculated using an experimentally determined permeate volumetric flow rate and the estimated open flow diameter d_f.

As in the case of the fanning friction factor, τ_w, J_{ss} and therefore k_1x are all functions of d_f, and must therefore be re-calculated with each successive iteration through equation 4.7.

VI.1.5.1 Calculation of tube length pressure drop (ΔP_L)

The pressure drop along the length of the filter was calculated as a proportional fraction of the experimentally measured trans-module pressure drop at steady state. Pressures transducers 1 and 2 were positioned at either end of the crossflow module (1.3m apart), and pressures from each were recorded automatically, throughout experiments, using the computer logging system. Pressures for the steady state system were read from the logged data (see Appendix IX) and used to calculate a steady state trans-module pressure drop. A first approximation to the pressure drop over the filter was thus calculated as 0.9/1.3 of the trans-module pressure drop.

The procedure used to determine k_1x (via correct determination of d_f) is shown in a flowchart (Figure VI.1).
This procedure was followed using data from 11 of the series C crossflow filtration experiments to determine d_f and the constant k_1x. The data used and produced in this procedure is shown in Table VI.2. The fouled diameters were used to calculate values of wall shear stress using equation 4.9 (τ_{w2}), and these were then plotted against steady state permeate flux in (Section **4.2.2**, Figure 4.3). As all these filtration experiments were conducted using the same system, the resulting data points should all lie on a single line with gradient k_1x.
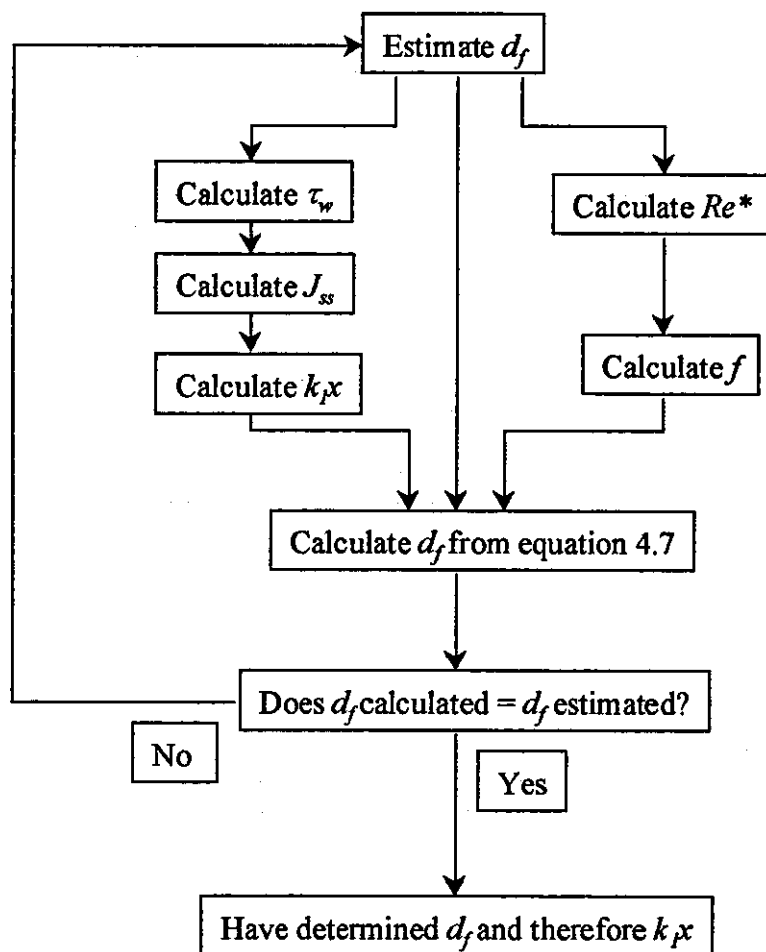
Figure VI.1 Flowchart of the procedure for calculation of $k_l x$

VI.1.6 Shear rates calculated for Section 4.2.3.1, Figure 4.4

Values of wall shear stress were also calculated, for the same 11 experiments, using equation 4.14 (τ_{wl}). The data required for these calculations can be obtained from Tables VI.1 and VI.2, and Table VI.2 also gives the resulting values. The two shear stresses (τ_{wl} and τ_{w2}) were plotted against each other in Figure 4.4.

Experiment	C50	C52	C51	C54	C53	C59	C60	C56	C55	C58	C57
Solids (%)	12	19	26	33	40	5.5	12	19	26	33	40
ΔP_{TM} (bar)	1	1	1	1	1	2	2	2	2	2	2
Q (m^{3}s^{-1})	$9.806e^{-5}$	$1.180e^{-4}$	$1.148e^{-4}$	$1.08e^{-4}$	$1.018e^{-4}$	$9.65e^{-5}$	$1.065e^{-4}$	$1.146e^{-4}$	$1.126e^{-4}$	$1e^{-4}$	$8.24e^{-5}$
J_{ss} (m^{3}s^{-1}m^{-2})	$6.08e^{-6}$	$4.61e^{-6}$	$2.77e^{-6}$	$2.38e^{-6}$	$3.29e^{-6}$	$12.77e^{-6}$	$9.69e^{-6}$	$8.73e^{-6}$	$6.4e^{-6}$	$4.0e^{-6}$	$5.45e^{-6}$
ΔP_L (Pa)	20210	27894	32239	39942	63398	25346	27570	34653	40047	62882	101402
d_f (mm)	7.27	7.04	6.39	7.94	5.56	6.69	6.69	6.48	6.25	6.77	4.33
δ_c (mm)	4.37	4.48	4.81	4.03	5.22	4.66	4.66	4.76	4.88	4.62	5.84
CF_{Vel} (ms^{-1})	2.36	3.03	3.58	2.18	4.19	2.75	3.03	3.47	3.67	2.78	5.6
τ_{w2} (Pa)	40.8	54.5	57.2	88.1	97.9	47.1	51.2	62.4	69.5	118.3	122.0
k_1x	$1.49e^{-7}$	$8.44e^{-8}$	$4.84e^{-8}$	$2.70e^{-8}$	$3.36e^{-8}$	$2.71e^{-7}$	$1.89e^{-7}$	$1.40e^{-7}$	$9.21e^{-8}$	$3.39e^{-8}$	$4.47e^{-8}$
f	0.0064	0.0059	0.0064	0.029	0.0054	0.0061	0.0061	0.0053	0.0064	0.027	0.0047
τ_{w1} (Pa)	24.84	43.87	75.63	143.20	109.45	27.11	38.95	51.82	79.64	216.26	169.54

Table VI.2 Data used and produced in calculation of k_{1x}, τ_w vs J_{ss} plotted in Figure 4.3

APPENDIX VII

ANNULUS MODEL CALCULATIONS

The model presented in Section **4.4.1** was evaluated using empirical data from filtration experiments covering a range of feed solids concentrations, crossflow velocities, and transmembrane pressures. A computer program (procedure outlined in Figure 4.8) was used to predict a steady state cake thickness, and predict a corresponding permeate flux.

The input values common to each experiment were the filter length (0.9m), filter tube internal diameter (0.016m), the volume fraction of solids in the filter cake (0.595), and the number of annuli considered in each case (10). The input values specific to each experiment are given in Table VII.1, along with the resulting model-calculated steady state cake thickness (δ_c model) and permeate flux (J_{ss} model). Values of 'experimental' steady state permeate flux (J_{ss} expt.) have also been calculated, using experimental permeate flow rates, but based on a model predicted open area (calculated using the relevant model predicted cake thickness).

The predicted and experimental steady state permeate fluxes (both based on the open area at the surface of the model predicted cake, not the filter tube internal diameter) are compared in Figure 4.11.

VII.1 Calculation of filter cake resistance (R_c)

The specific cake resistance of filter cakes formed during the filtration of titania suspensions was calculated using the Blake-Kozeny equation (4.4)

$$R_c = \frac{150\phi_c^2}{(2a)^2(1-\phi_c)^3} \qquad (4.4)$$

219

Where 0.595 was used for the cake solids fraction (ϕ_c) (from Section **3.3.1**), and 0.16e^{-6}m for the mean particle radius (a). Thus R_c=7.81e^{15} m^{-2}.

VII.2 Calculation of cake thickness based on experimental permeate flux

Assuming a cake solids content of 59.5% by volume, equation 4.6 was used with the data in Table VII.1 to determine a value of cake thickness (δ_c expt.) based on experimental permeate flow rates. These values have been plotted against the model calculated cake thicknesses in figure 4.12.

VII.3 Calculation of cake solids fraction based on experimental permeate flux

Using values of cake thickness predicted by the annulus model, cake solids fractions were determined, which would enable the model to correctly predict permeate flux.

Equation 4.6 was rearranged to calculate R_c for each experiment in Table VII.1, using the model predicted cake thickness and experimental steady state permeate flow rate. By process of iteration, values of cake solids fraction were then substituted into equation 4.4 until the desired value of R_c was obtained. The values of cake solids fraction (ϕ_c expt) are given in table VII.1, and plotted against feed solids fraction in figure 4.13.

VII.4 Determination of rheological constants

Data collected in the rheological study was fitted to both Herschel-Bulkley and Casson rheological models using the Carrimed software. This gave values for the yield stress (τ_y), consistency coefficient (K), and the constants η_l and n.

The constants from experiments either side of pH 9.5 were averaged and interpolated linearly to give values at pH 9.5 and feed concentrations of 2, 5, 10, 20, 30 and 40%. This data is given in Tables VII.2 to VII.7.

Table VII.1 Values associated with annulus model calculations

Expt	ΔP_{TM}	Feed solids	Q	ΔP_L	R_m	δ_c model	J_{ss} model	J_{ss} Expt.	δ_c expt.	ϕ_c expt.
	Bar	vol %	m^3s^{-1}	Pa	m^{-1}	mm	$m^3s^{-1}m^{-2}$	$m^3s^{-1}m^{-2}$	mm	vol%
C71	1	5.5	$3.137e^{-4}$	36563	$4.88e^{11}$	5.65	$1.298e^{-6}$	$3.637e^{-5}$	0.95	25.5
C49	1	5.5	$9.89e^{-5}$	17506	$3.40e^{11}$	5.9	$1.192e^{-6}$	$1.684e^{-5}$	1.9	32.9
C50	1	12	$9.81e^{-5}$	20210	$3.40e^{11}$	5.85	$1.213e^{-6}$	$1.027e^{-5}$	2.6	38.1
C52	1	19	$1.18e^{-4}$	27894	$3.02e^{11}$	5.75	$1.257e^{-6}$	$7.218e^{-6}$	3.05	42.1
C51	1	26	$1.15e^{-4}$	32239	$3.07e^{11}$	5.55	$1.347e^{-6}$	$3.621e^{-6}$	4.05	49.8
C54	1	33	$1.08e^{-4}$	39942	$3.07e^{11}$	5.3	$1.467e^{-6}$	$3.493e^{-6}$	3.95	51.1
C53	1	40	$1.02e^{-4}$	63398	$3.40e^{11}$	5.3	$1.466e^{-6}$	$3.384e^{-6}$	4.0	51.4
C59	2	5.5	$9.749e^{-5}$	25346	$3.48e^{11}$	6.1	$2.219e^{-6}$	$2.248e^{-5}$	2.6	36.3
C65	2	5.5	$2.44e^{-4}$	27389	$5.22e^{11}$	5.65	$2.596e^{-6}$	$4.528e^{-5}$	1.4	30.3
C60	2	12	$1.06e^{-4}$	27570	$3.48e^{11}$	5.9	$2.384e^{-6}$	$1.544e^{-5}$	3.05	40.8
C66	2	12	$2.17e^{-4}$	25833	$5.22e^{11}$	5.6	$2.641e^{-6}$	$2.272e^{-5}$	2.25	37.7
C56	2	19	$1.14e^{-4}$	34654	$4.13e^{11}$	5.9	$2.382e^{-6}$	$1.349e^{-5}$	3.3	42.2
C62	2	19	$2.55e^{-4}$	25422	$5.36e^{11}$	5.3	$2.925e^{-6}$	$1.692e^{-5}$	2.5	41.8
C55	2	26	$1.13e^{-4}$	40047	$4.13e^{11}$	5.65	$2.600e^{-6}$	$8.541e^{-6}$	3.85	47.7
C61	2	26	$2.52e^{-4}$	49002	$3.74e^{11}$	5.45	$2.786e^{-6}$	$1.503e^{-5}$	2.8	42.7
C58	2	33	$1.01e^{-4}$	62882	$3.36e^{11}$	5.7	$2.568e^{-6}$	$5.882e^{-6}$	4.5	51.4
C64	2	33	$1.92e^{-4}$	47675	$5.22e^{11}$	5.3	$2.925e^{-6}$	$6.550e^{-6}$	4.05	51.6
C57	2	40	$8.27e^{-5}$	101402	$4.84e^{11}$	5.7	$2.553e^{-6}$	$5.126e^{-6}$	4.7	52.7
C63	2	40	$2.09e^{-4}$	96992	$7.35e^{11}$	5.2	$3.016e^{-6}$	$5.789e^{-6}$	4.2	53.1

J_{ss} expt. is calculated using experimental permeate flow rate and δ_c model.

δ_c expt. is calculated using the procedure in VII.2.

ϕ_c expt. is calculated using the procedure in VII.3.

The annulus model (equation 4.22) contains expressions for the Casson model, rheological constants of yield stress (τ_y) and consistency coefficient (K). These constants are a function of the feed solids concentration (as seen in Tables VII.2 to

VII.7), and to be incorporated into the computer program, this relationship had to be quantified. The interpolated yield stresses and consistency coefficients for pH 9.5 were thus plotted against solids concentration, and curves fitted to the resulting points. These are shown in Figures 3.11 and 3.12.

Table VII.2 Viscosity model coefficients for a 2% volume solids suspension at pH9.5

2% solids		Herschel-Bulkley constants			Casson constants	
	Expt	τ_y (Pa)	η_l (Pas)	n	τ_y (Pa)	K (Pas)
pH 8.8	Nuvisc_25	0.04642	$4.669e^{-3}$	0.8390	0.02356	$1.19e^{-3}$
	Nuvisc_26	0.05271	$3.7e^{-3}$	0.8685	0.01950	$1.199e^{-3}$
	Nuvisc_27	0.05222	$3.652e^{-3}$	0.8712	0.1891	$1.21e^{-3}$
	Average	0.05045	$4.007e^{-3}$	0.8596	0.02066	$1.1997e^{-3}$
pH 9.6	Nuvisc_19	0.06439	$5.716e^{-3}$	0.8155	0.04370	$1.139e^{-3}$
	Nuvisc_20	0.03432	$5.014e^{-3}$	0.8298	0.02408	$1.184e^{-3}$
	Nuvisc_21	0.05066	$3.937e^{-3}$	0.8647	0.02363	$1.215e^{-3}$
	Average	0.04979	$4.889e^{-3}$	0.8367	0.03047	$1.179e^{-3}$
	Interpolated	**0.04987**	**$4.779e^{-3}$**	**0.8396**	**0.02924**	**$1.182e^{-3}$**

Table VII.3 Viscosity model coefficients for a 5% volume solids suspension at pH9.5

5% solids		Herschel-Bulkley constants			Casson constants	
	Expt	τ_y (Pa)	η_l (Pas)	n	τ_y (Pa)	K (Pas)
pH 9.16	Nuvisc5_4	0.003855	$5.88e^{-3}$	0.8081	0.02844	$1.164e^{-3}$
	Nuvisc5_5	0.05300	$3.848e^{-3}$	0.868	0.02143	$1.231e^{-3}$
	Nuvisc5_6	0.04540	$4.406e^{-3}$	0.8511	0.02273	$1.236e^{-3}$
	Average	0.04565	$4.711e^{-3}$	0.8424	0.02420	$1.210e^{-3}$
pH 9.72	Nuvisc5_7	0.05183	$4.237e^{-3}$	0.8603	0.02309	$1.273e^{-3}$
	Nuvisc5_8	0.04074	$4.690e^{-3}$	0.8456	0.01990	$1.284e^{-3}$
	Nuvisc5_9	0.04599	$4.397e^{-3}$	0.8556	0.02087	$1.289e^{-3}$
	Average	0.04619	$4.441e^{-3}$	0.8538	0.02129	$1.282e^{-3}$
	Interpolated	**0.04598**	**$4.547e^{-3}$**	**0.8493**	**0.02243**	**$1.254e^{-3}$**

Table VII.4 Viscosity model coefficients for a 10% volume solids suspension at pH9.5

10% solids	Herschel-Bulkley constants			Casson constants	
Expt	τ_y (Pa)	η_l (Pas)	n	τ_y (Pa)	K (Pas)
pH 9.43 Nuvisc10_7	0.06781	$4.607e^{-3}$	0.8687	0.02926	$1.461e^{-3}$
Nuvisc10_8	0.04781	$5.169e^{-3}$	0.8539	0.02504	$1.489e^{-3}$
Nuvisc10_9	0.06221	$4.393e^{-3}$	0.8764	0.02566	$1.494e^{-3}$
Average	0.05928	$4.723e^{-3}$	0.8663	0.02645	$1.481e^{-3}$
pH 9.96 Nuvisc10_10	0.1180	$6.45e^{-3}$	0.8695	0.05509	$1.994e^{-3}$
Nuvisc10_11	0.1105	$6.746e^{-3}$	0.8651	0.05453	$2.022e^{-3}$
Nuvisc10_12	0.1177	$6.581e^{-3}$	0.8711	0.05588	$2.064e^{-3}$
Average	0.1154	$6.592e^{-3}$	0.8686	0.05517	$2.027e^{-3}$
Interpolated	**0.0667**	$4.970e^{-3}$	**0.8666**	**0.03024**	$1.553e^{-3}$

Table VII.5 Viscosity model coefficients for a 20% volume solids suspension at pH9.5

20% solids	Herschel-Bulkley constants			Casson constants	
Expt	τ_y (Pa)	η_l (Pas)	n	τ_y (Pa)	K (Pas)
pH 9.05 Nuvisc20_7	0.2501	0.01947	0.7569	0.2267	$2.167e^{-3}$
Nuvisc20_8	0.2352	0.02016	0.7571	0.2238	$2.266e^{-3}$
Nuvisc20_9	0.2405	0.02025	0.7580	0.2266	$2.294e^{-3}$
Average	0.2419	0.01996	0.7573	0.2257	$2.242e^{-3}$
pH 9.58 Nuvisc20_10	0.2557	0.02333	0.7378	0.2555	$2.212e^{-3}$
Nuvisc20_11	0.2440	0.02288	0.7422	0.2478	$2.261e^{-3}$
Nuvisc20_12	0.2462	0.02362	0.7404	-	-
Average	0.2486	0.02328	0.7401	0.2517	$2.237e^{-3}$
Interpolated	**0.2476**	**0.02278**	**0.7427**	**0.2478**	$2.238e^{-3}$

Table VII.6 Viscosity model coefficients for a 30% volume solids suspension at pH9.5

30% solids		Herschel-Bulkley constants			Casson constants	
	Expt	τ_y (Pa)	η_l (Pas)	n	τ_y (Pa)	K (Pas)
pH 9.20	Nuvisc30_10	0.6632	0.2781	0.5235	1.524	$4.022e^{-3}$
	Nuvisc30_11	0.8350	0.2710	0.5288	1.593	$4.129e^{-3}$
	Nuvisc30_12	0.6468	0.2947	0.5187	1.553	$4.134e^{-3}$
	Average	0.7150	0.2813	0.5237	1.557	$4.095e^{-3}$
pH 9.73	Nuvisc30_13	0.6985	0.3262	0.5137	1.654	$4.404e^{-3}$
	Nuvisc30_14	0.6518	0.3560	0.5013	1.665	$4.382e^{-3}$
	Nuvisc30_15	0.8084	0.3263	0.5125	1.753	$4.298e^{-3}$
	Average	0.7196	0.3362	0.5092	1.691	$4.361e^{-3}$
	Interpolated	0.7176	0.3124	0.5155	1.6328	$4.246e^{-3}$

Table VII.7 Viscosity model coefficients for a 40% volume solids suspension at pH9.5

40% solids		Herschel-Bulkley constants			Casson constants	
	Expt	τ_y (Pa)	η_l (Pas)	n	τ_y (Pa)	K (Pas)
pH 9.01	Nuvisc40_7	1.460	1.744	0.4227	5.660	$10.73e^{-3}$
	Nuvisc40_8	1.151	1.800	0.4198	5.482	$11.07e^{-3}$
	Nuvisc40_9	2.751	1.639	0.4285	6.448	$10.31e^{-3}$
	Average	1.787	1.728	0.4237	5.863	$10.70e^{-3}$
pH 9.54	Nuvisc40_10	1.130	3.081	0.3495	7.685	$9.249e^{-3}$
	Nuvisc40_11	1.139	2.064	0.4001	6.078	$10.27e^{-3}$
	Nuvisc40_12	3.261	1.557	0.4309	6.829	$9.53e^{-3}$
	Average	1.843	2.234	0.3935	6.864	$9.683e^{-3}$
	Interpolated	1.839	2.196	0.3958	6.788	$9.760e^{-3}$

APPENDIX VIII

STATEMENT OF EXPERIMENTS

This chapter provides a basic summary of the process parameters used in each of the filtration experiments.

Process temperature: All the experiments were performed with the feed suspension at 50°C.

Suspension pH: Series A and C were conducted at pH 9.5, and series B was conducted at pH 4.0.

Clean water flux: The permeability of the filter tube was determined as a percentage of the new tube clean water flux prior to each experiment (values given in the fluxdata directory files). Using this value with equation II.7 or II.8 (depending on the filter) at the relevant experimental transmembrane pressure allowed calculation of the experimental clean water flux.

EXPERIMENTAL SERIES A

Concentrating experiments

ExptA1   Failed

ExptA1r

Initial feed solids concentration (volume %):	6
Final feed solids concentration (volume %):	18
Transmembrane pressure (bar):	1
Superficial crossflow velocity (ms^{-1}):	2
Pre-experiment clean water flux ($lm^{-2}h^{-1}$):	595

ExptA2

Initial feed solids concentration (volume %):	18
Final feed solids concentration (volume %):	50
Transmembrane pressure (bar):	1
Superficial crossflow velocity (ms^{-1}):	2
Pre-experiment clean water flux ($lm^{-2}h^{-1}$):	508

ExptA6

Initial feed solids concentration (volume %):	2
Final feed solids concentration (volume %):	6
Transmembrane pressure (bar):	1
Superficial crossflow velocity (ms^{-1}):	2
Pre-experiment clean water flux ($lm^{-2}h^{-1}$):	496

ExptA6r

Initial feed solids concentration (volume %):	2
Final feed solids concentration (volume %):	6
Transmembrane pressure (bar):	1
Superficial crossflow velocity (ms^{-1}):	2
Pre-experiment clean water flux ($lm^{-2}h^{-1}$):	499

Experiments at constant concentration

ExptA3

Feed solids concentration (volume %):	15
Transmembrane pressure (bar):	1
Superficial crossflow velocity (ms^{-1}):	2
Pre-experiment clean water flux ($lm^{-2}h^{-1}$):	644
Steady state permeate flux ($lm^{-2}h^{-1}$):	18.9

ExptA4

Feed solids concentration (volume %):	25
Transmembrane pressure (bar):	1
Superficial crossflow velocity (ms^{-1}):	2
Pre-experiment clean water flux ($lm^{-2}h^{-1}$):	595
Steady state permeate flux ($lm^{-2}h^{-1}$):	8.1

ExptA5

Feed solids concentration (volume %):	35
Transmembrane pressure (bar):	1
Superficial crossflow velocity (ms^{-1}):	2
Pre-experiment clean water flux ($lm^{-2}h^{-1}$):	451
Steady state permeate flux ($lm^{-2}h^{-1}$):	4.5

EXPERIMENTAL SERIES B

ExptB1

Initial feed solids concentration (volume %):	20
Final feed solids concentration (volume %):	22
Transmembrane pressure (bar):	1
Superficial crossflow velocity (ms^{-1}):	2
Pre-experiment clean water flux ($lm^{-2}h^{-1}$):	520

ExptB2

Initial feed solids concentration (volume %):	2
Final feed solids concentration (volume %):	6
Transmembrane pressure (bar):	1
Superficial crossflow velocity (ms^{-1}):	2
Pre-experiment clean water flux ($lm^{-2}h^{-1}$):	423

ExptB2r

Initial feed solids concentration (volume %):	2
Final feed solids concentration (volume %):	6
Transmembrane pressure (bar):	1
Superficial crossflow velocity (ms^{-1}):	2
Pre-experiment clean water flux ($lm^{-2}h^{-1}$):	588

ExptB3

Initial feed solids concentration (volume %):	6
Final feed solids concentration (volume %):	13
Transmembrane pressure (bar):	1
Superficial crossflow velocity (ms^{-1}):	2
Pre-experiment clean water flux ($lm^{-2}h^{-1}$):	456

EXPERIMENTAL SERIES C

ExptC1

Feed solids concentration (volume %):	5.5
Transmembrane pressure (bar):	1
Superficial crossflow velocity (ms^{-1}):	0.38
Pre-experiment clean water flux (lm^{-2}h^{-1}):	545
Steady state permeate flux (lm^{-2}h^{-1}):	17.9

ExptC2

Feed solids concentration (volume %):	12
Transmembrane pressure (bar):	1
Superficial crossflow velocity (ms^{-1}):	0.38
Pre-experiment clean water flux (lm^{-2}h^{-1}):	545
Steady state permeate flux (lm^{-2}h^{-1}):	11.27

ExptC3

Feed solids concentration (volume %):	26
Transmembrane pressure (bar):	1
Superficial crossflow velocity (ms^{-1}):	0.38
Pre-experiment clean water flux (lm^{-2}h^{-1}):	466
Steady state permeate flux (lm^{-2}h^{-1}):	7.16

ExptC4

Feed solids concentration (volume %):	19
Transmembrane pressure (bar):	1
Superficial crossflow velocity (ms^{-1}):	1.18
Pre-experiment clean water flux (lm^{-2}h^{-1}):	406
Steady state permeate flux (lm^{-2}h^{-1}):	8.49

ExptC5

Feed solids concentration (volume %):	40
Transmembrane pressure (bar):	1
Superficial crossflow velocity (ms^{-1}):	0.94
Pre-experiment clean water flux ($lm^{-2}h^{-1}$):	287
Steady state permeate flux ($lm^{-2}h^{-1}$):	4.38

ExptC6

Feed solids concentration (volume %):	33
Transmembrane pressure (bar):	1
Superficial crossflow velocity (ms^{-1}):	0.99
Pre-experiment clean water flux ($lm^{-2}h^{-1}$):	337
Steady state permeate flux ($lm^{-2}h^{-1}$):	4.38

ExptC7

Feed solids concentration (volume %):	5.5
Transmembrane pressure (bar):	2
Superficial crossflow velocity (ms^{-1}):	0.75
Pre-experiment clean water flux ($lm^{-2}h^{-1}$):	788
Steady state permeate flux ($lm^{-2}h^{-1}$):	35.8

ExptC8

Feed solids concentration (volume %):	12
Transmembrane pressure (bar):	2
Superficial crossflow velocity (ms^{-1}):	1.05
Pre-experiment clean water flux ($lm^{-2}h^{-1}$):	788
Steady state permeate flux ($lm^{-2}h^{-1}$):	22.55

ExptC9

Feed solids concentration (volume %):	26
Transmembrane pressure (bar):	2
Superficial crossflow velocity (ms^{-1}):	1.09
Pre-experiment clean water flux (lm^{-2}h^{-1}):	730
Steady state permeate flux (lm^{-2}h^{-1}):	13.93

ExptC10

Failed

ExptC11

Feed solids concentration (volume %):	40
Transmembrane pressure (bar):	2
Superficial crossflow velocity (ms^{-1}):	1.07
Pre-experiment clean water flux (lm^{-2}h^{-1}):	653
Steady state permeate flux (lm^{-2}h^{-1}):	6.9

ExptC12

Feed solids concentration (volume %):	33
Transmembrane pressure (bar):	2
Superficial crossflow velocity (ms^{-1}):	1.22
Pre-experiment clean water flux (lm^{-2}h^{-1}):	557
Steady state permeate flux (lm^{-2}h^{-1}):	9.55

ExptC13-18

All failed

ExptC19

Feed solids concentration (volume %):	5.5
Transmembrane pressure (bar):	2
Superficial crossflow velocity (ms^{-1}):	1
Pre-experiment clean water flux (lm^{-2}h^{-1}):	519
Steady state permeate flux (lm^{-2}h^{-1}):	33.2

ExptC20

Feed solids concentration (volume %):	12
Transmembrane pressure (bar):	2
Superficial crossflow velocity (ms^{-1}):	1
Pre-experiment clean water flux (lm^{-2}h^{-1}):	519
Steady state permeate flux (lm^{-2}h^{-1}):	25.2

ExptC21

Feed solids concentration (volume %):	26
Transmembrane pressure (bar):	2
Superficial crossflow velocity (ms^{-1}):	1
Pre-experiment clean water flux (lm^{-2}h^{-1}):	538
Steady state permeate flux (lm^{-2}h^{-1}):	13.93

ExptC22

Feed solids concentration (volume %):	19
Transmembrane pressure (bar):	2
Superficial crossflow velocity (ms^{-1}):	1.17
Pre-experiment clean water flux (lm^{-2}h^{-1}):	461
Steady state permeate flux (lm^{-2}h^{-1}):	15.25

ExptC23

Feed solids concentration (volume %):	40
Transmembrane pressure (bar):	2
Superficial crossflow velocity (ms^{-1}):	1.1
Pre-experiment clean water flux (lm^{-2}h^{-1}):	269
Steady state permeate flux (lm^{-2}h^{-1}):	6.37

ExptC24

Feed solids concentration (volume %):	33
Transmembrane pressure (bar):	2
Superficial crossflow velocity (ms^{-1}):	1
Pre-experiment clean water flux (lm^{-2}h^{-1}):	327
Steady state permeate flux (lm^{-2}h^{-1}):	6.3

ExptC25

Feed solids concentration (volume %):	5.5
Transmembrane pressure (bar):	0.5
Superficial crossflow velocity (ms^{-1}):	1.3
Pre-experiment clean water flux (lm^{-2}h^{-1}):	105
Steady state permeate flux (lm^{-2}h^{-1}):	24.54

ExptC26

Feed solids concentration (volume %):	12
Transmembrane pressure (bar):	0.5
Superficial crossflow velocity (ms^{-1}):	1.2
Pre-experiment clean water flux (lm^{-2}h^{-1}):	105
Steady state permeate flux (lm^{-2}h^{-1}):	13.93

ExptC27

Feed solids concentration (volume %):	26
Transmembrane pressure (bar):	0.5
Superficial crossflow velocity (ms^{-1}):	1.06
Pre-experiment clean water flux (lm^{-2}h^{-1}):	158
Steady state permeate flux (lm^{-2}h^{-1}):	6.63

ExptC28

Feed solids concentration (volume %):	19
Transmembrane pressure (bar):	0.5
Superficial crossflow velocity (ms^{-1}):	1.09
Pre-experiment clean water flux (lm^{-2}h^{-1}):	147
Steady state permeate flux (lm^{-2}h^{-1}):	8.75

ExptC29

Feed solids concentration (volume %):	40
Transmembrane pressure (bar):	0.5
Superficial crossflow velocity (ms^{-1}):	0.99
Pre-experiment clean water flux (lm^{-2}h^{-1}):	174
Steady state permeate flux (lm^{-2}h^{-1}):	3.58

ExptC30

Feed solids concentration (volume %):	33
Transmembrane pressure (bar):	0.5
Superficial crossflow velocity (ms^{-1}):	1.14
Pre-experiment clean water flux (lm^{-2}h^{-1}):	179
Steady state permeate flux (lm^{-2}h^{-1}):	3.98

ExptC31

Feed solids concentration (volume %):	5.5
Transmembrane pressure (bar):	1
Superficial crossflow velocity (ms^{-1}):	1.07
Pre-experiment clean water flux (lm^{-2}h^{-1}):	397
Steady state permeate flux (lm^{-2}h^{-1}):	27.85

ExptC32

Feed solids concentration (volume %):	12
Transmembrane pressure (bar):	1
Superficial crossflow velocity (ms^{-1}):	1
Pre-experiment clean water flux (lm^{-2}h^{-1}):	397
Steady state permeate flux (lm^{-2}h^{-1}):	15.25

ExptC33

Feed solids concentration (volume %):	26
Transmembrane pressure (bar):	1
Superficial crossflow velocity (ms^{-1}):	0.97
Pre-experiment clean water flux (lm^{-2}h^{-1}):	337
Steady state permeate flux (lm^{-2}h^{-1}):	8.22

ExptC34

Feed solids concentration (volume %):	19
Transmembrane pressure (bar):	1
Superficial crossflow velocity (ms^{-1}):	0.97
Pre-experiment clean water flux (lm^{-2}h^{-1}):	327
Steady state permeate flux (lm^{-2}h^{-1}):	7.96

ExptC35

Failed

ExptC36

Failed

ExptC37

Feed solids concentration (volume %):	5.5
Transmembrane pressure (bar):	0.5
Superficial crossflow velocity (ms^{-1}):	0.71
Pre-experiment clean water flux (lm^{-2}h^{-1}):	1025
Steady state permeate flux (lm^{-2}h^{-1}):	11.94

ExptC38

Feed solids concentration (volume %):	12
Transmembrane pressure (bar):	0.5
Superficial crossflow velocity (ms^{-1}):	0.72
Pre-experiment clean water flux (lm^{-2}h^{-1}):	1025
Steady state permeate flux (lm^{-2}h^{-1}):	7.29

ExptC39

Feed solids concentration (volume %):	26
Transmembrane pressure (bar):	0.5
Superficial crossflow velocity (ms^{-1}):	0.81
Pre-experiment clean water flux (lm^{-2}h^{-1}):	789
Steady state permeate flux (lm^{-2}h^{-1}):	4.59

ExptC40

Feed solids concentration (volume %):	26
Transmembrane pressure (bar):	0.5
Superficial crossflow velocity (ms^{-1}):	0.84
Pre-experiment clean water flux ($lm^{-2}h^{-1}$):	769
Steady state permeate flux ($lm^{-2}h^{-1}$):	6.63

ExptC41

Feed solids concentration (volume %):	40
Transmembrane pressure (bar):	0.5
Superficial crossflow velocity (ms^{-1}):	0.7
Pre-experiment clean water flux ($lm^{-2}h^{-1}$):	461
Steady state permeate flux ($lm^{-2}h^{-1}$):	3.05

ExptC42

Feed solids concentration (volume %):	33
Transmembrane pressure (bar):	0.5
Superficial crossflow velocity (ms^{-1}):	0.7
Pre-experiment clean water flux ($lm^{-2}h^{-1}$):	758
Steady state permeate flux ($lm^{-2}h^{-1}$):	3.51

ExptC43

Feed solids concentration (volume %):	5.5
Transmembrane pressure (bar):	0.5
Superficial crossflow velocity (ms^{-1}):	0.48
Pre-experiment clean water flux ($lm^{-2}h^{-1}$):	635
Steady state permeate flux ($lm^{-2}h^{-1}$):	7.96

ExptC44

Feed solids concentration (volume %):	12
Transmembrane pressure (bar):	0.5
Superficial crossflow velocity (ms^{-1}):	0.48
Pre-experiment clean water flux ($lm^{-2}h^{-1}$):	635
Steady state permeate flux ($lm^{-2}h^{-1}$):	5.73

ExptC45

Feed solids concentration (volume %):	26
Transmembrane pressure (bar):	0.5
Superficial crossflow velocity (ms^{-1}):	0.33
Pre-experiment clean water flux ($lm^{-2}h^{-1}$):	584
Steady state permeate flux ($lm^{-2}h^{-1}$):	3.12

ExptC46

Feed solids concentration (volume %):	19
Transmembrane pressure (bar):	0.5
Superficial crossflow velocity (ms^{-1}):	0.37
Pre-experiment clean water flux ($lm^{-2}h^{-1}$):	615
Steady state permeate flux ($lm^{-2}h^{-1}$):	3.18

ExptC47

Feed solids concentration (volume %):	40
Transmembrane pressure (bar):	0.5
Superficial crossflow velocity (ms^{-1}):	0.34
Pre-experiment clean water flux ($lm^{-2}h^{-1}$):	654
Steady state permeate flux ($lm^{-2}h^{-1}$):	2.39

ExptC48

Feed solids concentration (volume %):	33
Transmembrane pressure (bar):	0.5
Superficial crossflow velocity (ms^{-1}):	0.36
Pre-experiment clean water flux ($lm^{-2}h^{-1}$):	666
Steady state permeate flux ($lm^{-2}h^{-1}$):	2.79

ExptC49

Feed solids concentration (volume %):	5.5
Transmembrane pressure (bar):	1
Superficial crossflow velocity (ms^{-1}):	0.49
Pre-experiment clean water flux ($lm^{-2}h^{-1}$):	1060
Steady state permeate flux ($lm^{-2}h^{-1}$):	15.92

ExptC50

Feed solids concentration (volume %):	12
Transmembrane pressure (bar):	1
Superficial crossflow velocity (ms^{-1}):	0.49
Pre-experiment clean water flux ($lm^{-2}h^{-1}$):	1060
Steady state permeate flux ($lm^{-2}h^{-1}$):	9.95

ExptC51

Feed solids concentration (volume %):	26
Transmembrane pressure (bar):	1
Superficial crossflow velocity (ms^{-1}):	0.57
Pre-experiment clean water flux ($lm^{-2}h^{-1}$):	1173
Steady state permeate flux ($lm^{-2}h^{-1}$):	3.98

ExptC52

Feed solids concentration (volume %):	19
Transmembrane pressure (bar):	1
Superficial crossflow velocity (ms^{-1}):	0.59
Pre-experiment clean water flux ($lm^{-2}h^{-1}$):	1192
Steady state permeate flux ($lm^{-2}h^{-1}$):	7.29

ExptC53

Feed solids concentration (volume %):	40
Transmembrane pressure (bar):	1
Superficial crossflow velocity (ms^{-1}):	0.51
Pre-experiment clean water flux ($lm^{-2}h^{-1}$):	1060
Steady state permeate flux ($lm^{-2}h^{-1}$):	4.11

ExptC54

Feed solids concentration (volume %):	33
Transmembrane pressure (bar):	1
Superficial crossflow velocity (ms^{-1}):	0.54
Pre-experiment clean water flux ($lm^{-2}h^{-1}$):	1173
Steady state permeate flux ($lm^{-2}h^{-1}$):	4.24

ExptC55

Feed solids concentration (volume %):	26
Transmembrane pressure (bar):	2
Superficial crossflow velocity (ms^{-1}):	0.56
Pre-experiment clean water flux ($lm^{-2}h^{-1}$):	1741
Steady state permeate flux ($lm^{-2}h^{-1}$):	9.02

ExptC56

Feed solids concentration (volume %):	19
Transmembrane pressure (bar):	2
Superficial crossflow velocity (ms^{-1}):	0.57
Pre-experiment clean water flux (lm^{-2}h^{-1}):	1741
Steady state permeate flux (lm^{-2}h^{-1}):	12.73

ExptC57

Feed solids concentration (volume %):	40
Transmembrane pressure (bar):	2
Superficial crossflow velocity (ms^{-1}):	0.41
Pre-experiment clean water flux (lm^{-2}h^{-1}):	1487
Steady state permeate flux (lm^{-2}h^{-1}):	5.31

ExptC58

Feed solids concentration (volume %):	33
Transmembrane pressure (bar):	2
Superficial crossflow velocity (ms^{-1}):	0.50
Pre-experiment clean water flux (lm^{-2}h^{-1}):	2140
Steady state permeate flux (lm^{-2}h^{-1}):	6.10

ExptC59

Feed solids concentration (volume %):	5.5
Transmembrane pressure (bar):	2
Superficial crossflow velocity (ms^{-1}):	0.48
Pre-experiment clean water flux (lm^{-2}h^{-1}):	2068
Steady state permeate flux (lm^{-2}h^{-1}):	19.23

ExptC60

Feed solids concentration (volume %):	12
Transmembrane pressure (bar):	2
Superficial crossflow velocity (ms^{-1}):	0.53
Pre-experiment clean water flux ($lm^{-2}h^{-1}$):	2068
Steady state permeate flux ($lm^{-2}h^{-1}$):	14.59

ExptC61

Feed solids concentration (volume %):	26
Transmembrane pressure (bar):	2
Superficial crossflow velocity (ms^{-1}):	1.18
Pre-experiment clean water flux ($lm^{-2}h^{-1}$):	1923
Steady state permeate flux ($lm^{-2}h^{-1}$):	17.24

ExptC62

Feed solids concentration (volume %):	19
Transmembrane pressure (bar):	2
Superficial crossflow velocity (ms^{-1}):	1.1
Pre-experiment clean water flux ($lm^{-2}h^{-1}$):	1342
Steady state permeate flux ($lm^{-2}h^{-1}$):	20.56

ExptC63

Feed solids concentration (volume %):	40
Transmembrane pressure (bar):	2
Superficial crossflow velocity (ms^{-1}):	1.00
Pre-experiment clean water flux ($lm^{-2}h^{-1}$):	979
Steady state permeate flux ($lm^{-2}h^{-1}$):	7.29

ExptC64

Feed solids concentration (volume %):	33
Transmembrane pressure (bar):	2
Superficial crossflow velocity (ms^{-1}):	0.8
Pre-experiment clean water flux (lm^{-2}h^{-1}):	1379
Steady state permeate flux (lm^{-2}h^{-1}):	7.96

ExptC65

Feed solids concentration (volume %):	5.5
Transmembrane pressure (bar):	2
Superficial crossflow velocity (ms^{-1}):	1.21
Pre-experiment clean water flux (lm^{-2}h^{-1}):	1379
Steady state permeate flux (lm^{-2}h^{-1}):	47.76

ExptC66

Feed solids concentration (volume %):	12
Transmembrane pressure (bar):	2
Superficial crossflow velocity (ms^{-1}):	0.99
Pre-experiment clean water flux (lm^{-2}h^{-1}):	1379
Steady state permeate flux (lm^{-2}h^{-1}):	24.51

ExptC67

Feed solids concentration (volume %):	26
Transmembrane pressure (bar):	1
Superficial crossflow velocity (ms^{-1}):	1.08
Pre-experiment clean water flux (lm^{-2}h^{-1}):	587
Steady state permeate flux (lm^{-2}h^{-1}):	10.66

ExptC68

Feed solids concentration (volume %):	19
Transmembrane pressure (bar):	1
Superficial crossflow velocity (ms^{-1}):	1.16
Pre-experiment clean water flux (lm^{-2}h^{-1}):	606
Steady state permeate flux (lm^{-2}h^{-1}):	13.26

ExptC69

Feed solids concentration (volume %):	40
Transmembrane pressure (bar):	1
Superficial crossflow velocity (ms^{-1}):	1.02
Pre-experiment clean water flux (lm^{-2}h^{-1}):	757
Steady state permeate flux (lm^{-2}h^{-1}):	5.31

ExptC70

Feed solids concentration (volume %):	33
Transmembrane pressure (bar):	1
Superficial crossflow velocity (ms^{-1}):	1.18
Pre-experiment clean water flux (lm^{-2}h^{-1}):	814
Steady state permeate flux (lm^{-2}h^{-1}):	5.84

ExptC71

Feed solids concentration (volume %):	5.5
Transmembrane pressure (bar):	1
Superficial crossflow velocity (ms^{-1}):	1.52
Pre-experiment clean water flux (lm^{-2}h^{-1}):	738
Steady state permeate flux (lm^{-2}h^{-1}):	38.46

ExptC72

Feed solids concentration (volume %):	12
Transmembrane pressure (bar):	1
Superficial crossflow velocity (ms^{-1}):	1.32
Pre-experiment clean water flux (lm^{-2}h^{-1}):	738
Steady state permeate flux (lm^{-2}h^{-1}):	18.24

ExptC73

Feed solids concentration (volume %):	26
Transmembrane pressure (bar):	2
Superficial crossflow velocity (ms^{-1}):	0.81
Pre-experiment clean water flux (lm^{-2}h^{-1}):	1379
Steady state permeate flux (lm^{-2}h^{-1}):	12.60

ExptC74

Feed solids concentration (volume %):	19
Transmembrane pressure (bar):	2
Superficial crossflow velocity (ms^{-1}):	0.81
Pre-experiment clean water flux (lm^{-2}h^{-1}):	1197
Steady state permeate flux (lm^{-2}h^{-1}):	14.85

ExptC75

Feed solids concentration (volume %):	40
Transmembrane pressure (bar):	2
Superficial crossflow velocity (ms^{-1}):	0.64
Pre-experiment clean water flux (lm^{-2}h^{-1}):	0342
Steady state permeate flux (lm^{-2}h^{-1}):	6.90

ExptC76

Feed solids concentration (volume %):	33
Transmembrane pressure (bar):	2
Superficial crossflow velocity (ms^{-1}):	0.68
Pre-experiment clean water flux (lm^{-2}h^{-1}):	1415
Steady state permeate flux (lm^{-2}h^{-1}):	7.16

ExptC77

Feed solids concentration (volume %):	5.5
Transmembrane pressure (bar):	2
Superficial crossflow velocity (ms^{-1}):	0.75
Pre-experiment clean water flux (lm^{-2}h^{-1}):	1088
Steady state permeate flux (lm^{-2}h^{-1}):	29.18

ExptC78

Feed solids concentration (volume %):	12
Transmembrane pressure (bar):	2
Superficial crossflow velocity (ms^{-1}):	0.81
Pre-experiment clean water flux (lm^{-2}h^{-1}):	1088
Steady state permeate flux (lm^{-2}h^{-1}):	19.89

ExptC79

Feed solids concentration (volume %):	26
Transmembrane pressure (bar):	1
Superficial crossflow velocity (ms^{-1}):	0.76
Pre-experiment clean water flux (lm^{-2}h^{-1}):	662
Steady state permeate flux (lm^{-2}h^{-1}):	5.57

ExptC80

Feed solids concentration (volume %):	19
Transmembrane pressure (bar):	1
Superficial crossflow velocity (ms^{-1}):	0.72
Pre-experiment clean water flux (lm^{-2}h^{-1}):	606
Steady state permeate flux (lm^{-2}h^{-1}):	7.03

ExptC81

Feed solids concentration (volume %):	40
Transmembrane pressure (bar):	1
Superficial crossflow velocity (ms^{-1}):	0.68
Pre-experiment clean water flux (lm^{-2}h^{-1}):	549
Steady state permeate flux (lm^{-2}h^{-1}):	4.77

ExptC82

Feed solids concentration (volume %):	33
Transmembrane pressure (bar):	1
Superficial crossflow velocity (ms^{-1}):	0.70
Pre-experiment clean water flux (lm^{-2}h^{-1}):	473
Steady state permeate flux (lm^{-2}h^{-1}):	4.91

ExptC83

Feed solids concentration (volume %):	5.5
Transmembrane pressure (bar):	1
Superficial crossflow velocity (ms^{-1}):	0.68
Pre-experiment clean water flux (lm^{-2}h^{-1}):	587
Steady state permeate flux (lm^{-2}h^{-1}):	19.23

ExptC84

Feed solids concentration (volume %):	12
Transmembrane pressure (bar):	1
Superficial crossflow velocity (ms^{-1}):	0.71
Pre-experiment clean water flux (lm^{-2}h^{-1}):	587
Steady state permeate flux (lm^{-2}h^{-1}):	10.94

ExptC85

Feed solids concentration (volume %):	26
Transmembrane pressure (bar):	0.5
Superficial crossflow velocity (ms^{-1}):	0.54
Pre-experiment clean water flux (lm^{-2}h^{-1}):	379
Steady state permeate flux (lm^{-2}h^{-1}):	3.38

ExptC86

Feed solids concentration (volume %):	19
Transmembrane pressure (bar):	0.5
Superficial crossflow velocity (ms^{-1}):	0.51
Pre-experiment clean water flux (lm^{-2}h^{-1}):	359
Steady state permeate flux (lm^{-2}h^{-1}):	4.11

ExptC87

Feed solids concentration (volume %):	5.5
Transmembrane pressure (bar):	0.5
Superficial crossflow velocity (ms^{-1}):	1.02
Pre-experiment clean water flux (lm^{-2}h^{-1}):	369
Steady state permeate flux (lm^{-2}h^{-1}):	16.44

ExptC88

Feed solids concentration (volume %):	12
Transmembrane pressure (bar):	0.5
Superficial crossflow velocity (ms^{-1}):	1.06
Pre-experiment clean water flux ($lm^{-2}h^{-1}$):	369
Steady state permeate flux ($lm^{-2}h^{-1}$):	10.64

ExptC89

Feed solids concentration (volume %):	26
Transmembrane pressure (bar):	1
Superficial crossflow velocity (ms^{-1}):	0.64
Pre-experiment clean water flux ($lm^{-2}h^{-1}$):	776
Steady state permeate flux ($lm^{-2}h^{-1}$):	5.90

ExptC90

Feed solids concentration (volume %):	19
Transmembrane pressure (bar):	1
Superficial crossflow velocity (ms^{-1}):	1.03
Pre-experiment clean water flux ($lm^{-2}h^{-1}$):	643
Steady state permeate flux ($lm^{-2}h^{-1}$):	10.88

APPENDIX IX

EXPERIMENTAL DATA RECORDED ON FLOPPY DISK

Raw data and manipulated data from both the rheological and filtration experiments have been stored on 3½" floppy disks. Microsoft Excel files have been created using Office 97. The directories/ filenames and their contents are as follows.

IX.1 RHEOLOGICAL DATA
Stored in the 'Rheodata\' directory

The files in this directory contain the experimental stress-strain data recorded by the PC attached to the Carrimed constant stress rheometer. The files have been sorted into sub directories according to volume solids concentration. The Carrimed software can be used to plot the rheological data or fit a model to the data from any selected experiment.

Data from these files can also be read by opening them in the DOS editor, Windows notepad, or a suitable spreadsheet package. The title lines clearly state the solids concentration and pH for each experiment, along with the configuration used and a number of other set-up parameters. The shear rate-shear stress data commences after the line reading F400***, where the last two digits of *** represent the filename extension.

IX.2 VISCOSITY DATA
Stored in the 'Viscdata\' directory

Measurements of apparent viscosity were extracted from the **Rheodata** files, across a range of solids concentrations (2, 5, 10, 20, 30, 40% by volume), shear rates (500, 1000, 1500, 2000 and 2500s^{-1}) and the pH range. This data is tabulated in **viscdat.xls** along with corresponding measurements of particle size, sampled

before each rheological experiment. This data is also plotted within the file, and the relevant graphs can be found in Section **3.2.2**.

IX.3 PERMEATE FLUX DATA
Stored in the 'Fluxdata\' directory

This directory contains permeate flux data as a function of filtration time for all the filtration experiments in experimental sets A, B, and C. The titles for each experiment establish the feed solids concentration, pH, process parameters, and the percentage of clean water flux. This can be used to calculate the actual clean water permeate flux using equation II.7 and II.8 (Appendix II). The permeate flux decline data has also been plotted and can be viewed within the relevant file.

IX.4 STEADY STATE PERMEATE FLUX DATA
Stored in the 'Ssdata\' directory

The steady state permeate flux data, for all series C experiments, has been plotted and manipulated to show trends in steady state flux with varying process parameters (**statdat.xls**). The results of this work can be seen in appendix IV and Section **3.3.3**.

IX.5 DATA LOGGED BY THE FILTRATION RIG
Stored in the 'Logdata\' directory

This directory contains the data logged by the filtration rig computer for all series A, B, and C filtration experiments. The **rawdata** sub-directory contains the files directly from the PC, and their contents can be viewed by loading them into the filtration rig software. The same data has been re-configured for use in Microsoft excel worksheets, and these can be found in the **xlsdata** sub-directory. The filenames are self explanatory in both cases however, where the experiment number

is followed by a 'b', this indicates that the original data log for that experiment ceased temporarily, and was recommenced under this new filename.

Where unspecified, the unit of time used in these worksheets is seconds.

APPENDIX X

ANNULUS MODEL PASCAL COMPUTER PROGRAM

This is a copy of the computer program used to determine values of cake thickness via the annulus model.

```
{A programme to determine filter cake thickness using the annulus
model. This assumes that there is a 'transitionary, mobile cake
layer' between the stationary cake at the filter surface (cake
concentration) and the bulk flow of suspension through the filter
core (feed concentration). A parabolic concentration profile has
been superimposed on this transition region enabling 'boundary
diameters' to be calculated for annuli of given concentrations.
This data is used to calculate volumetric flow rates and solids
flow rates through the annuli, and a permeate flow rate through the
fixed cake. These are then compared to the experimentally
determined values (flow rate and mass balances performed).
Concentration and velocity profiles may also be generated
potentially.
Required input data is the feed solids concentration, feed flow
rate, transmembrane pressure, tube length pressure drop and
membrane resistance. The cake concentration is assumed to be 59.5%
solids in all cases, thus specific cake resistance is also
constant.}




PROGRAM ProfileCalc;
        USES Crt;


    VAR
            n:real;
            {A:real; A is the selected number of annuli}
            X:real; {estimation of cake thickness (mm)}
            T:real; {estimation of limit of transition region (mm)}
            P:real; {Pressure drop along the filter length (Pa)}
            {Cc,}Cf,Cn,Cm:real;
                    {Cc is cake concentration}
                    {Cf is feed concentration}
                    {Cn is concentration at diameter dn}
                    {Cm is concentration at diameter dn-1}
            dc,df,dn,dm:real;
                    {dc is estimated open diameter of caked tube}
                    {df is estimated diameter of transition region
                    boundary}
                    {dn is diameter of annulus n}
                    {dm is diameter dn-1}
            Kn,Tyn:real;
                    {Kn is the consistency coefficient for suspn at
                    dn}
```

```
                                    {Tyn is the yield stress for suspn at dn}
              Qt,Qa,Qb,Qsum,Qsol,Qn:real;
                                    {Qsum is the model-calculated sum of volumetric
                                    flow rates
                                    through the annuli}
                                    {Qsol is the model-calculated sum of solids
                                    flowing through
                                    the annuli}
                                    {Qn is the volumetric flow rate through an
                                    annulus n}
                                    {Qt is the process feed flow rate}
              Rm{,Rc}:real;
                                    {Rm is the membrane resistance}
                                    {Rc is the specific cake resistance}
              Vw,Jss,DP:real;
                                    {Jss is the calculated permeate flux based on
                                    estimated cake thickness}
                                    {Vw is the corresponding permeate flow rate}
                                    {DP is the transmembrane pressure}


        CONST
              Fd=0.016;          {Filter diameter (m)}
              L=0.9;             {Filter length (m)}
              Cc=59.5;
              Rc=7.806568309e15;   {assumes Cc is 59.5%}
              j=0.0001;
              A=10;                 {No. of annuli is set to 10}

PROCEDURE Calqdn;
{Calculates the outer diameter of each annulus}
         BEGIN
               dn:=df+((n-1)*((dc-df)/(A-1)));
         END;{Calqdn}


PROCEDURE CalqCn;
{Calculates the suspension concentration at diameter dn}
         BEGIN
               Cn:=Cf+((Cc-Cf)*sqr((dn-df)/(dc-df)));
         END;{CalqCn}


PROCEDURE CalqKn;
{Calculates the Casson consistency coefficient at concentration
Cn}
         BEGIN
               Kn:=(5E-9*Cn*Cn*Cn*Cn)-(2E-7*Cn*Cn*Cn)+(3E-
6*Cn*Cn)+(3E-5*Cn)+0.0011;
         END;{CalqKn}


PROCEDURE CalqTyn;
{Calculates the yield stress at concentration Cn}
         BEGIN
               Tyn:=(7E-8*Cn*Cn*Cn*Cn*Cn)+(2E-7*Cn*Cn*Cn*Cn)-(2E-
5*Cn*Cn*Cn)+(0.0007*Cn*Cn)-(0.0062*Cn)+0.0391;
         END;{CalqTyn}
```

```
PROCEDURE CalqQn;
{Calculates the volumetric flow rate through annulus n}
          BEGIN
                Qn:=((pi*dn*(sqr(dn)-sqr(dm)))/(32*Kn))*
                (sqr((sqrt((P*dn)/(4*L)))-(sqrt(Tyn))));
          END;{CalqQn}


PROCEDURE SumQ;
{Sums the volumetric flow rate through all the annuli}
          BEGIN
                Qsum:=Qsum+Qn;
                Qsol:=Qsol+(Qn*((Cn+Cm)/2));
          END;{SumQ}


PROCEDURE FindOne;
{Prints the results of calculated diameters when balances approach
unity}
      BEGIN
            If Qa<1.03 then
            if Qa>0.97 then
            if Qb<1.03 then
            if Qb>0.97 then

            begin
            writeln;
            writeln('         dc           df         Flow balance
Solids balance');
            writeln('            ',(dc*1000):2:2,'mm
',(df*1000):2:2,'mm        ',Qa:3:8,'            .',Qb:3:8);
            writeln;
            writeln('      Cake thickness       Permeate flow
Permeate flux');
            writeln('               ',(((Fd*1000)-(dc*1000))/2):2:2,'mm
',(Vw*60000000):2:1,'ml/min          ',
            (Jss*1000000):2:3,'e-6 m/s');
            end;
      End;{FindOne}


PROCEDURE FindQz;
{Performs calculations in order}
      BEGIN
      Cm:=Cf;
       dm:=0;
       Qsum:=0;
       Qsol:=0;
       n:=0;
       While n<A
          do begin
             n:=n+1;
             Calqdn;
             CalqCn;
             CalqTyn;
             CalqKn;
             CalqQn;
             SumQ;
             dm:=dn;
```

```
            Cm:=Cn;
            {writeln('        n=',n:1:0,' C=',Cn:2:1,'
d=',(dn*1000):4:2,
            ' Ty=',Tyn:4:4,' K=',Kn:4:4,' Tw=',((P*dn)/(4*L)):4:4,'
U=',
            ((dn/(8*Kn))*(sqr((sqrt((P*dn)/(4*L)))-
(sqrt(Tyn)))))):1:1,' Qn=',Qn:4:8);}
            end;
              Qa:=(QSum/(Qt-Vw));
              Qb:=(Qsol/(Qt*Cf));
            FindOne;
         END;{FindQz}


   PROCEDURE Loop2;
  {Sets diameters open to flow and performs calculation}
     BEGIN
     df:=dc;
     WHILE df>j
     do begin df:=df-j;
            FindQz;
     end;
     END;{Loop2}


  PROCEDURE CalcVw;
  {Calculates steady state permeate flux and permeate flow rate
based on dc)
     BEGIN
     Jss:=(DP*1e5)/(0.001*(Rm+(Rc*(Fd/2)*(ln(Fd/dc)))));
     Vw:=(pi*dc*L)*Jss;
     END;{CalcVw}




  PROCEDURE Loop1;
  {Progressively sets values of tube diameter-cake thickness}
     BEGIN
     dc:=Fd+j;
     WHILE dc>j
     do begin dc:=dc-j;
            CalcVw;
            Loop2;
     end;
     END;{Loop1}



  BEGIN
       Clrscr;
       writeln;
       writeln('      ***** Annuli model for determination of filter
cake depth *****');
       writeln;
       writeln('          Please type in values for the
following:');writeln;
       {writeln(' Filter length (m):');}
       {readln(L);}
       {writeln('   Filter diameter (mm):');}
       {readln(Fd);}
```

256

```pascal
        write('           Volume fraction of solids in feed (%): ');
        readln(Cf);
        {write('           Volume fraction of solids in cake (%): ');}
        {readln(Cc);}
        write('           Pressure drop along filter length (Pa): ');
        readln(P);
        write('           Volumetric flowrate of suspension (m3/s):
');
        readln(Qt);
        write('           Membrane resistance (m-1): ');
        readln(Rm);
        {write('           Specific cake resistance (m-2): ');}
        {readln(Rc);}
        write('           Transmembrane Pressure (bar): ');
        readln(DP);

        {window(1,5,80,25);}
        writeln('     Please wait');
        Loop1;
        writeln('     FINISHED');
        repeat until keypressed;
         END.
```

APPENDIX XI

PUBLISHED WORK AND PRESENTATIONS

Work produced in the course of this project has also been used in a number of papers, presentations, and poster presentations.

The two papers produced for the Chemical Engineering Journal[2,3], and the admission to the proceedings of the 1997, IChemE Jubilee Research Event[90], are reprinted within this Appendix.

Poster presentations have been made to;

The ICI Colloid and Surface Science Symposium, 16th April 1996 at University College, Stockton-on-Tees.

The EPSRC Processing of Soft Solids and Particle Technology meeting, 18th April 1996 at The University of Birmingham.

The EPSRC Processing of Soft Solids and Particle Technology meeting, 15th April 1997 at Loughborough University.

And presentations have been made to;

The IChemE Particle Technology Subject group at their 1997 annual general meeting, Loughborough University.

Tioxide Group Ltd., 24th September 1997.

The influence of pH and temperature on the rheology and stability of aqueous titanium dioxide dispersions

P. Mikulášek [b,*], R.J. Wakeman [a], J.Q. Marchant [a]

[a] *Department of Chemical Engineering, Loughborough University, Loughborough, Leicester LE11 3TU, UK*
[b] *Department of Chemical Engineering, University of Pardubice, nám. Čs. legií 565, CZ-532 10 Pardubice, Czech Republic*

Abstract

The effects of pH and temperature on the rheology and stability of aqueous dispersions of rutile (titanium dioxide) were investigated systematically. The dispersions exhibit shear-thinning behaviour, conforming to the Herschel–Bulkley or the Casson-type models in the shear rate range investigated. Extreme sensitivity with pH was observed, whereby the dispersion viscosity can be changed by as much as an order of magnitude with pH variation at constant volume fraction. The temperature effect study indicates that the relative contribution of Brownian motion and shear flow to the viscosity is dependent on the flocculation state of the dispersion. The rheological behaviour of the dispersions in this study has been explained in terms of hydrodynamic interactions between particles as well as non-hydrodynamic interactions. These observations have important implications in crossflow microfiltration of these dispersions. © 1997 Elsevier Science S.A.

Keywords: Rheology; Titanium dioxide; Concentrated dispersions; pH; Thermal effects

1. List of symbols

a	radius of particle/m
k	Boltzmann constant/$J\,K^{-1}$
K	consistency parameter/Pas^n
n	flow index
$Pé_r$	rotational Péclet number
T	absolute temperature/K

Greek letters

γ	shear rate/s^{-1}
η	apparent viscosity/Pas
η_r	relative viscosity
μ_o	dynamic viscosity of water/Pas
η_∞	constant viscosity at the infinite shear limit/Pas
τ	shear stress/Pa
τ_C	yield stress in the Casson model/Pa
τ_{HB}	yield stress in the Herschel–Bulkley model/Pa
τ_r	relative shear stress

2. Introduction

The motivation for this study was to understand some aspects of the crossflow microfiltration of dispersions. Cross-

* Corresponding author. Tel: +420 40 582 147; fax: +420 40 514 530; e-mail: mikulase@hlb.upce.cz

flow microfiltration of dispersions is encountered in a wide variety of engineering applications, such a solid–liquid separation, water purification, and drilling operations. The primary focus of our study is the crossflow microfiltration of concentrated dispersions of titanium dioxide in water. These concentrated dispersions arise in various industrial applications such as paints, coatings, and joint treatment compounds. These systems typically exhibit complex rheological behaviour [1,2].

Models based on the theory of fouling phenomena and concentration polarization and hydrodynamic models have been developed to predict the steady state permeate flux of crossflow microfiltration (see, for example, Davis [3] and Belfort et al. [4]). These models can be loosely categorized as being based either on a film theory, following a development based on convection of matter towards the membrane and diffusion of the retained species back into the crossflow, possibly incorporating lift forces, or on a cake theory which applies Darcy's law to relate the filtration rate to the average pressure difference between inside the filter and the permeate line. However, the applicability of these models over a wide range of operating conditions, including temperature, crossflow velocity, pressure drop, particle size, particle concentration in the dispersion, pH, and electrolyte concentration, is in doubt because they do not consider the influence of all of the significant terms and their outcomes. For any model to be

realistic it must be able to show the effects of the dispersion viscosity and particle–particle interactions, which may have hydrodynamic or non-hydrodynamic origins. The qualitative difference in the crossflow microfiltration behaviour of non-Newtonian dispersions under constant tangential feed and constant inlet pressure conditions, shown, for example, by Vassilieff et al. [5], are not consistent with the predictions of these models.

The rheological properties of dispersions are governed by the microstructure of the system. In these systems, the solid particles are relatively small and the interparticle forces are significantly pronounced so as to influence the microstructure, the state of aggregation of the dispersion and, consequently, the mechanical and rheological properties of the system. Thus, it is of interest to study the rheological behaviour of these systems in order to understand and control the flow behaviour and stability of these materials.

Studies of the rheological behaviour of dispersions of titanium dioxide have been conducted by previous researches [6–10]. The effect of pH, flocculation, polyacrylic acid adsorption, processing, and particle concentration on viscosity has been studied at the ambient temperature. They found that for titanium dioxide dispersions a change in the particle size leads to totally different rheological behaviour, that is, the effects of moving from an electrostatically stabilized to a sterically stabilized dispersion were observed. The addition of surfactant into the solution and increasing the pH level caused an increase in ionic strength of the system. However, the reason for the change in the rheological properties with temperature is poorly understood. To understand this behaviour, it is the objective of this paper to study the effects of temperature and pH on the rheology of titanium dioxide dispersions by analysing the relative contribution of the interaction forces and their relationship with the microstructure of the dispersion.

3. Experimental

3.1. Materials

The titanium dioxide used was rutile supplied by Tioxide Group Ltd., England. Rutile (density 4260 kg m^{-3}) has a higher refractive index, higher density and greater chemical stability than anatase. The crystal size for rutile TiO$_2$ pigments, which is distinct from particle size (0.25–0.40 μm), is 0.17–0.24 μm. Transmission electron microscopy was used to estimate the shape and aspect ratio of the rutile crystals, which were found to be approximately elliptic and 2 to 3, respectively. The particle size distributions were measured using a MasterSizer MS20 (Malvern Instruments Ltd., UK).

The dispersions were prepared by mixing the appropriate amounts of millipore-filtered water and titanium dioxide in a high-shear, Ultra-Turrax T25, mixer (Janke and Kunkel, IKA-Labortechnik, Germany), with the help of the dispersant CALGON (sodium hexametaphosphate). The samples were prepared containing 0.15% by weight of dispersant. Even as the volume percent of solids was varied, the mass of dispersant per unit mass of solids was kept unchanged. This was to ensure that there was always an adequate amount of dispersant available for steric stabilization.

Zeta potential measurements to obtain information on the state of charge at the solid–liquid interface were carried out by means of a microelectrophoresis device (Zetasizer 3, Malvern Instruments Ltd., UK).

The pH level of the system was adjusted by adding various amounts of HCl or NaOH to deionised water, which was used as the suspending medium employed. All soluble acid and alkali reagents used were analytical grade. The pH was measured with a pH meter Model 80 (Griffin and George Ltd., UK). The dispersion was stirred until a steady pH reading was obtained.

3.2. Rheological measurements

A Carri-Med Model CS 100 controlled stress rheometer, with either a double concentric or cone and plate system, was used for the steady shear measurements. However, the cone and plate system was used for the highest volumetric concentrations of solids in the samples (50 vol%) only. The temperature of the samples was controlled by a Peltier system. All measurements except those of the temperature effect study were conducted under ambient conditions ($T = 20\,°C$). Measurements of the effect of temperature were conducted for temperatures ranging from ambient to 50 °C. The temperature was maintained to within ±0.1 °C of the desired preset value. Water evaporation was potentially a serious problem when the experiment was performed above 30 °C. Therefore, the interface exposed to the atmosphere was coated with a thin layer of silicone oil to minimize evaporation. The rheological measurements suggested the use of a model of the Herschel–Bulkley type

$$\tau = \tau_{HB} + K\gamma^n \qquad (1)$$

or of the Casson type

$$\tau^{1/2} = \tau_C^{1/2} + (\eta_\infty \gamma)^{1/2} \qquad (2)$$

to characterize the rheological behaviour of these dispersions [11]. The existence of a yield stress has been observed, especially at the highest volumetric concentrations of solids. This value has been obtained by taking the first 5% of the shear stress/shear rate pairs and fitting a straight line which is then extrapolated to zero shear rate. It is hoped that this will correlate with the yield stress obtained from controlled shear rate instruments which are unable to measure the yield value directly and therefore normally some form of extrapolation is used. In addition, it should be noted that a positive value for the hysteresis loop area was obtained and this indicates that the samples with the highest concentrations of the solids had some thixotropy. In order to match results taken by controlled shear rate instruments, it is occasionally necessary to test material under controlled shear rate conditions

and in the shortest time, consistent with the rheology of the sample. It is possible to do this in flow mode by using a firmware control loop in the instrument to simulate shear rate conditions. This has the effect of eliminating the history of the system (energy input, time, temperature, etc.) and the particle migration across or along the gap in the concentric system [12].

4. Results and discussions

4.1. Effect of pH

The effect of pH on the rheological properties of 30 vol% titanium dioxide/water dispersions is shown in Fig. 1. The results in Fig. 1 show that the dispersions are shear-thinning and are characterized by non-linear flow curves that converge at low shear rate to the yield stress of the dispersion. The position of the shear-thinning flow curves is pH-dependent. This is due to the different degrees of flocculation in the dispersion at different pH. The high shear stress behaviour at extremely high pH (pH 13), as observed in Fig. 1, may be explained by the fact that the high ionic strength of the system (due to NaOH addition) can lead to a reduction of the electrical double layer thickness, and flocculation reoccurs due to van der Waals forces.

Fig. 2 shows the effect of pH on the apparent viscosity of 1, 10, 30, and 50 vol% titanium dioxide dispersions. The viscosity was evaluated at the shear rate of 500 s^{-1}. On the basic side (pH 7–14), the viscosity first decreases with pH, reaching a minimum near pH 9, and then increases as the pH becomes higher. The low apparent viscosity behaviour is a strong indication that the dispersions are dispersed. On the acidic side (pH 7–0), the same trend is observed. As the pH decreases (i.e. through the addition of more HCl), the ionic strength is raised. This can lead to a decrease of the electrical double layer repulsion and flocculations occur due to van der Waals attractions. The high viscosity behaviour at pH 4, as observed in Fig. 2, may be explained by this ionic strength effect. The pH at maximum viscosity should correspond to the isoelectric point of the titanium dioxide. The isoelectric
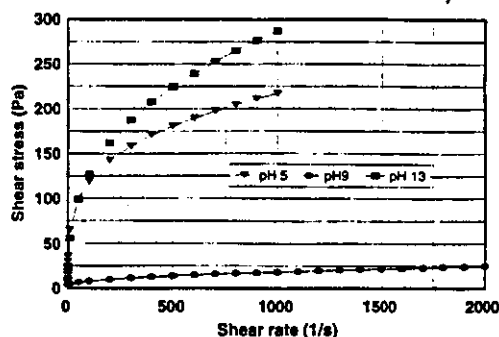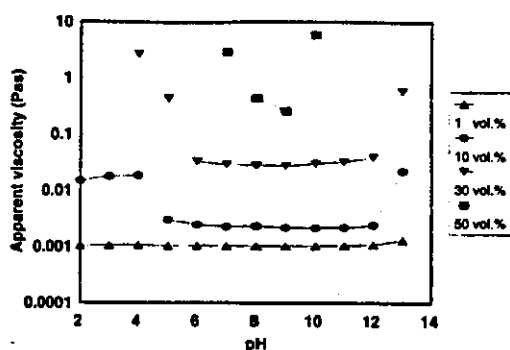

Fig. 2. Effect of pH on the apparent viscosity (evaluated at 500 s^{-1}) of 1, 10, 30, and 50 vol% titanium dioxide dispersions.
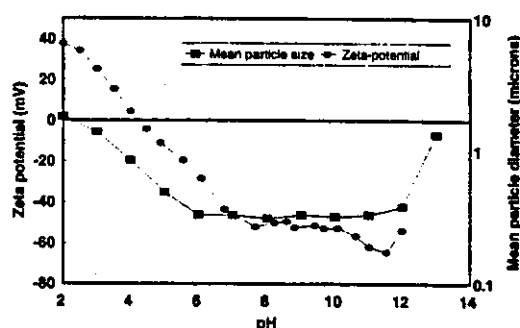

Fig. 3. The variation of zeta-potential and mean particle diameter with pH for rutile (titanium dioxide) used in the experiments.

point is the pH at which the electrophoretic mobility is zero, which occurs when there is no net surface charge on the colloidal particle. At a pH below the isoelectric point, the surface charge for most metallic oxides such as alumina, titania, zirconia, is positive which is attributed to the protonation of the surface hydroxyl group [13].

In order to verify the effect of pH on the system behaviour, the zeta (ζ) potential vs. pH relationship was measured and is shown in Fig. 3. At pH 4.0, the ζ-potential was 4.4 mV, at pH 6.8 (the natural approximate pH of the dispersion) it was −43.6 mV, and at pH 9.4 it was −51.4 mV. The isoelectric point, or the point of zero electrophoretic mobility, is at pH 4.2. This value agrees well with a value of between 4 from the viscosity measurements and a value of about 5 obtained from particle size measurements (see Fig. 3). The electrophoretic mobility parameter, which is a measure of the velocity of a charged particle in an electric field, is dependent on the ionic strength, the presence of the dispersant, and the presence of an inorganic coating on the titanium dioxide particles. Since impurities are difficult to eliminate completely it is common to find a range in the isoelectric point quoted for the same material in the literature. A literature survey reveals that the isoelectric point reported for titanium dioxide varies from pH 4.0 to 6.1 [8,14,15].

A plot of the variation of the apparent viscosity (evaluated at 500 s^{-1}) as a function of the volumetric concentration of

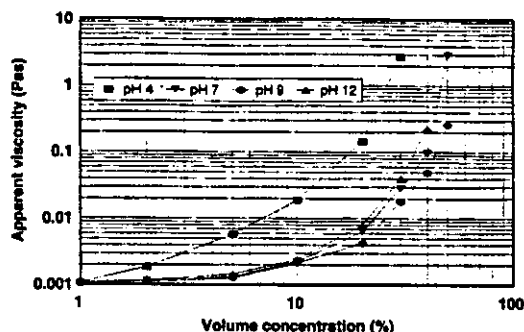Fig. 1. Effect of pH on the flow properties of 30 vol% titanium dioxide dispersions at temperature 20 °C.

Fig. 4. Variation of apparent viscosity (evaluated at 500 s^{-1}) with the concentration of titanium dioxide dispersions used.

solids and pH (Fig. 4) shows that the viscosity increases strongly above the concentration of 10 vol% and depends on the pH of the dispersions. The results in Fig. 4 also show that the difference in viscosity between the different states of flocculation or dispersion can be very large. For example, one order of magnitude difference in viscosity is observed between the flocculated 10 vol% dispersion at pH 4 and the dispersed state dispersion at pH 9. The apparent viscosity is about 2.2 mPa s for the dispersed 10 vol% dispersion and 19 mPa s for the flocculated dispersion at pH 4.

4.2. Effect of temperature

The rheological behaviour of 10 and 30 vol% titanium dioxide dispersions at different temperatures and also at different pH values are shown in Figs. 5 and 6. The results in Figs. 5 and 6 show that the dispersions are shear-thinning and are characterized again by a non-linear flow curve for all temperatures studied. The mechanism of shear-thinning of a dispersion of fine particles is a result of a reduction in the effective volume of the disperse phase caused by deflocculation of the particles upon shearing [16]. In the case of sterically stabilized systems, partial compression of the steric barrier due to shear, and therefore a reduction in the hydrodynamic volume fraction, could be the cause of shear-thinning [17]. Figs. 5 and 6 also show low and intermediate shear regions in certain conditions. In the low shear limit, Brownian motion of the particles is expected to be in control, whereas in the high shear limit the shear-induced motion (hydrodynamic effects) dominates over the Brownian contribution to the particle interactions. The location of the intermediate shear-thinning region will depend upon the relative strength of Brownian and shear-induced contributions. This balance will be affected by several parameters such as particle size, temperature, and concentration. Temperature has a strong effect on the apparent viscosity of the dispersions. In all cases, the apparent viscosity η of the dispersions decreased with temperature.

A discussion of the theoretical aspects of Brownian motion has been given by several authors including Brenner [18]. Brownian motion can be conveniently decomposed as a rota-
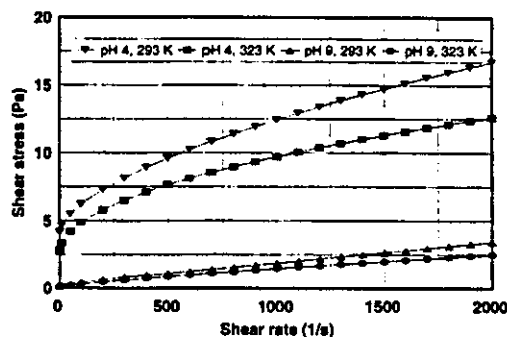

Fig. 5. Effect of temperature on the flow properties of 10 vol% titanium dioxide dispersions at pH 4 and pH 9.
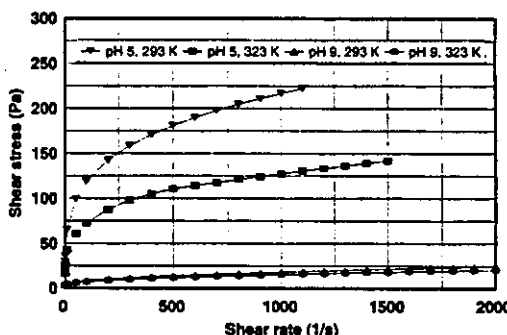

Fig. 6. Effect of temperature on the flow properties of 30 vol% titanium dioxide dispersions at pH 5 and pH 9.

tional Brownian motion and a translational Brownian motion. For systems subjected to simple shear flow, the effects of Brownian motion and shear are superimposed and their relative importance is governed by the magnitude of the rotational and translational Péclet number. For spherical particles, the rotational Péclet number is defined as

$$Pé_r = 8\pi\mu_0\gamma a^3/kT \tag{3}$$

where μ_0 is the viscosity of the medium (water), γ is the shear rate, a is the radius of a particle, k is the Boltzmann constant, and T is the absolute temperature. According to Eq. (3), increasing Pé$_r$ corresponds to increasing shear rate γ. Thus, the dispersion displays shear-thinning behaviour. This shear-thinning behaviour for dispersions of non-spherical particles can be explained as follows. The shear flow tends to promote alignment of the particles in such a manner as to alleviate the viscous stress and, hence, to reduce the viscosity. The rotational Brownian motion, on the other hand, tends to randomize the particle orientations, thereby destroying the alignment and increasing the viscosity. This corresponds to high viscosity at low Pé$_r$. Therefore, shear and Brownian motion have opposite effects on the dispersion viscosity, and both effects can be correlated to a single dimensionless variable, Pé$_r$ (Brenner [18]).

In order to verify whether or not Brownian interactions are the dominant mechanism in these dispersions, temperature

depend on the balance between Brownian motion forces on the one hand and electrostatic, steric and van der Waals forces on the other. The effect of shear flow is always to align particles and consequently to lower the viscosity.

5. Conclusions

The rheological measurements for titanium dioxide dispersions of different concentrations have indicated that their rheological behaviour is of the shear-thinning type. This behaviour can be modelled by the Herschel–Bulkley or Casson rheological relationships. The results also show that the apparent viscosity increases sharply with increasing volumetric concentration of solids when the latter exceeds 10 vol%.

The results of the pH effect study indicate that it is possible to control the flocculation state and, consequently, the rheological behaviour of titanium dioxide dispersions by adjusting the pH level of the system. The mechanism by which pH affects the system behaviour is by influencing the surface charge of the titanium dioxide particles and, consequently, the electrostatic attraction between these particles.

The temperature effect study indicates that the relative contribution of Brownian motion and shear flow to the viscosity is dependent on the concentration of the dispersion. For concentrated dispersions, Brownian motion promotes particle–particle interactions. However, the effect of Brownian motion on the 10 vol% dispersion was found to be much less significant than for concentrated dispersions. Our work shows that for such concentrated aqueous dispersions of the titanium dioxide, temperature-independent curves can be obtained if one plots the relative viscosity against the relative shear stress in dimensionless form.

Acknowledgements

References

[1] Th.F. Tadros, Physical stability of suspension concentrates, Adv. Colloid Interface Sci. 12 (1980) 141–261.

[2] D.A.R. Jones, B. Leary, D.V. Boger, The rheology of concentrated colloidal suspension of hard spheres, J. Colloid Interface Sci. 147 (1991) 479–495.

[3] R.H. Davis, Modeling of fouling of crossflow microfiltration membranes, Sep. Purif. Methods 21 (1992) 75–126.

[4] G. Belfort, R.H. Davis, A.L. Zydney, The behaviour of suspensions and macromolecular solutions in crossflow microfiltration, J. Membr. Sci. 96 (1994) 1–58.

[5] C.S. Vassilieff, I.G. Momtchilova, R.A. Krustev, Cross-flow microfiltration of kaolinite-in-water dispersions, Colloids Surf. A 92 (1994) 231–247.

[6] K. Umeya, T. Kanno, Effect of flocculation on the dilatant flow for aqueous suspensions of titanium dioxides, J. Rheol. 23 (1979) 123–140.

[7] A.S. Rao, Rheology of aqueous dispersions of alumina, titania and a mixture of alumina and titania powders, J. Dispersion Sci. Technol. 8 (1987) 457–465.

[8] H. Strauss, H. Heegn, I. Strienitz, Effect of PAA adsorption on stability and rheology of TiO$_2$ dispersions, Chem. Eng. Sci. 48 (1993) 323–332.

[9] P.V. Liddell, D.V. Boger, Influence of processing on the rheology of titanium dioxide pigment suspensions, Ind. Eng. Chem. Res. 33 (1994) 2437–2442.

[10] T. Sato, Effect of particle concentration on physical properties of titanium dioxide suspensions, J. Dispersion Sci. Technol. 17 (1996) 83–96.

[11] Q.D. Nguyen, D.V. Boger, Measuring the flow properties of yield stress fluid, Annual Rev. Fluid Mech. 24 (1992) 47–88.

[12] D. Leighton, A. Acrivos, The shear-induced migration of particles in concentrated suspensions, J. Fluid Mech. 181 (1987) 415–439.

[13] Y.K. Leong, D.V. Boger, D. Parris, Surface and rheological properties of zirconia suspensions, Trans IChemE, Part A 69 (1991) 381–384.

[14] W.R. Bowen, X. Goenaga, Properties of microfiltration membranes. Part 3. Effect of physicochemical conditions on crossflow microfiltration at aluminium oxide membranes, I. Chem. E. Symp. Ser. 118 (1990) 107.

[15] R. Hunter, Foundations of Colloid Science, Vol. I, Oxford Science Publications, Oxford, 1987, p.386.

[16] J. Mewis, A.J.B. Spaull, Rheology of concentrated dispersions, Adv. Colloid Interface Sci. 6 (1976) 173–200.

[17] C.E. Chaffey, I. Wagstaff, Shear thinning and thickening rheology. II. Volume fraction and size of dispersed particles, J. Colloid Interface Sci. 59 (1977) 63–75.

[18] H. Brenner, Suspension rheology, in: W. Schowalter (Ed.), Progress in heat and mass transfer. Vol. 5, Pergamon, Oxford, 1972, pp.89–129.

[19] I.M. Krieger, T.J. Dougherty, A mechanism for non-Newtonian flow in suspension of rigid spheres, Trans. Soc. Rheol. 3 (1959) 137–152.

[20] I.M. Krieger, A dimensional approach to colloid rheology, Trans. Soc. Rheol. 7 (1963) 101–109.

1

Crossflow microfiltration of shear-thinning aqueous titanium dioxide dispersions

P. Mikulášek [a,*], R.J. Wakeman [b], J.Q. Marchant [b]

[a] Department of Chemical Engineering, University of Pardubice, nám. Čs. legií 565, 532 10 Pardubice, Czech Republic
[b] Department of Chemical Engineering, Loughborough University, Loughborough, Leicestershire, LE11 3TU, UK

Abstract

Crossflow microfiltration experiments were performed on aqueous dispersions of rutile (titanium dioxide) through a 0.1 μm pore size ceramic membrane at various operating parameters. The initial transient flux decline follows deadend filtration theory, with the membrane resistance determined from the initial flux and the cake resistance determined from the rate of flux decline due to cake build-up. For a long time, the observed fluxes reached steady or nearly steady-state values, presumably as a result of the cake growth being arrested by the shear exerted at its surface. The steady-state fluxes increase with increasing inlet crossflow velocity and decreasing feed concentration. The steady-state permeate flux values were determined from the steady-state model based on the Kozeny–Carman equation for cake resistance and Darcy's law applied over the filter area to relate filtration rate to average pressure difference between the feed and permeate sides of the filter. The model includes a cake resistance of the cake layer, which was determined for the titanium dioxide dispersions by fitting the experimental flux data to the model. The apparent viscosity of the dispersion, which is an input parameter in the flux model, is also adjusted to account for a model of the Herschel–Bulkley type. The resulting fluxes obtained from the model using simple values for the membrane resistance, cake resistance, and rheological parameters for each data set are in good agreement with the measured fluxes. © 1998 Elsevier Science S.A.

Keywords: Crossflow microfiltration; Titanium dioxide dispersion; Ceramic membrane

1. Introduction

Crossflow membrane microfiltration is a separation process for the removal of dispersed matters in sizes ranging from 0.05 to 10 μm from a liquid stream by forcing the liquid through a porous membrane. As opposed to deadend microfiltration, where the dispersion flow is normal to the membrane, the dispersion flows in crossflow filtration tangentially to the membrane surface. The tangential flow generates forces which tend to remove the deposited layers from the membrane surface thus, helping to keep the membrane relatively clean. The main applications of this process are in the production of ultrapure water, the processing of food and dairy products, the recovery of electrodeposition paints, the treatment of oil and latex emulsions and in biotechnology, oriented applications such as fractionation of fermentation broths and high performance reactors for enzymatic and fermentation processes. As well as solid–liquid separation processes, crossflow microfiltration of dispersions is encountered

in a variety of other engineering applications such as wellbore drilling operations. The primary focus of our study is the crossflow microfiltration of concentrated dispersions of titanium dioxide in water. These concentrated dispersions arise in various industrial applications such as paints, coatings, and joint treatment compounds. These systems typically exhibit complex rheological behaviour [1,2].

Crossflow microfiltration can be operated on a continuous basis because the flow on the retentate side of the filter exerts a shear at the membrane surface. This shear prevents the continued build-up of a fouling or cake layer on the membrane surface, and a steady or quasi-steady permeate flux which often increases with the shear rate is observed. The mechanisms responsible for the steady-state reached in crossflow filtration processes are not clearly understood. Brownian diffusion is one likely mechanism for particles less than 0.1 μm diameter [3]. For larger particles, several possible mechanisms may be responsible for the steady-state. These include back-transport mechanisms such as inertial lift [4,5] and shear-induced diffusion [6–11] which carry particles away from the membrane, and surface-transport mechanisms [12] by which the shear forces and torques on a

* Corresponding author. Tel.: +420-40-582147; fax: +420-40-514530; e-mail: Petr.Mikulasek@upce.cz

particle at the cake surface overcome contact and adhesive forces. There are several reviews to which the interested reader may wish to refer [13–15].

In the present article, crossflow filtration experiments have been performed on aqueous dispersions of titanium dioxide through a tubular ceramic membrane. The feed concentration, flow rate and transmembrane pressure were varied. The focus is on determining the transient flux decline due to formation of a cake layer of rejected titania particles and the steady-state flux due to shear forces arresting the growth of the particle cake. The approximate procedure to predict the total behaviour of the permeate flux, from time zero to steady-state, is to use the deadend filtration theory until the time the steady-state is reached and then use the steady-state flux value from the steady-state model based on cake theory which applies Darcy's law to relate filtration rate to the average pressure difference between the feed and permeate sides of the filter. The goal is to obtain a better qualitative and quantitative understanding of the factors affecting titania dispersion filtration under crossflow conditions.

2. Experimental

2.1. Materials

The titanium dioxide used was rutile supplied by Tioxide Group, England. Rutile (density: 4260 kg m^{-3}) has a higher refractive index, higher density and greater chemical stability than anatase. The crystal size for rutile TiO$_2$ pigments, which is distinct from particle size (0.25–0.40 μm), is 0.17–0.24 μm. Transmission electron microscopy was used to estimate the shape and aspect ratio of the rutile crystals, which were found to be approximately elliptic and 2–3, respectively. The particle size distributions were measured using a MasterSizer MS20 (Malvern Instruments, England).

The dispersions were prepared by mixing the appropriate amount of 'Millipore-filtered' water and titanium dioxide in a high shear Ultra-Turrax T25 mixer (Janke & Kunkel, IKA-Labortechnik, Germany) using CALGON (sodium hexametaphosphate) as a dispersant. The samples were prepared containing 0.15% by weight of dispersant. Even as the volume percent of solids was varied, the mass of dispersant per unit mass of solids was kept unchanged. This was to ensure that there was always an adequate amount of dispersant available for steric stabilisation.

Zeta potential measurements to get information on the state of the charge at the solid–liquid interface were carried using a microelectrophoresis device (Zetasizer 3, Malvern Instruments, England).

The pH level of the system was adjusted to pH 9 with 0.05 M analytical grade NaOH in deionised water, which was used as the suspending medium. The pH was measured with a Model 80 (Griffin & George, England) pH meter. The dispersion was stirred until a steady pH reading was obtained.

At pH 9 the zeta potential was about −50 mV enabling a stable, well dispersed suspension to produced.

2.2. Rheological measurements

A Carri-Med Model CS 100 controlled stress rheometer, with either a double concentric or a cone and plate system, was used for the steady shear measurements. The cone and plate system was used only for the highest volumetric concentrations of solids in the samples (50 vol.%). The temperature of the samples was controlled by a Peltier system. All measurements except those of the temperature effect study were conducted under ambient conditions ($T = 20°$C). Measurements of the effect of temperature were conducted for temperatures ranging from ambient to 50°C. The temperature was maintained to within ±0.1°C of the desired preset value. Water evaporation was potentially a serious problem when the experiment was performed above 30°C. Therefore, the interface exposed to the atmosphere was coated with a thin layer of silicone oil to minimise evaporation. The rheological measurements suggested the use of a model of the Herschel–Bulkley type

$$\tau = \tau_{HB} + K\gamma^n \tag{1}$$

or of the Casson type

$$\tau^{1/2} = \tau_C^{1/2} + (\eta_\infty \gamma)^{1/2} \tag{2}$$

to characterise the rheological behaviour of these dispersions [16]. The existence of a yield stress has been observed, especially at the highest volumetric concentrations of solids. In addition, it should be noted that a positive value for the hysteresis loop area has been obtained and this indicates that the samples with the highest concentrations of the solids had some thixotropy.

2.3. Filtration experiments

2.3.1. Membranes

The ceramic membranes studied in this work were asymmetric, double-layered, silicon carbide (SiC) membranes (Atech Innovations, Germany). They were configured as single cylindrical tubes 0.9 m long, 16 mm ID and 25 mm OD, consisting of a thin SiC layer deposited on the internal surface of the tubular support. In our experiments, the microfiltration membranes were used with the mean pore diameter of 0.1 μm.

2.3.2. Equipment

A schematic diagram of the experimental apparatus is shown in Fig. 1. The dispersion is fed to the filter by a variable speed Mono pump, thus allowing a range of crossflow velocities to be examined. Pressure transducers at either end of the filter module measure the transmembrane pressure, which is controlled using full flow ball valves. Temperatures are monitored by thermocouples, computer controlled, and maintained by a hot water jacket around the feed tank. An auto-
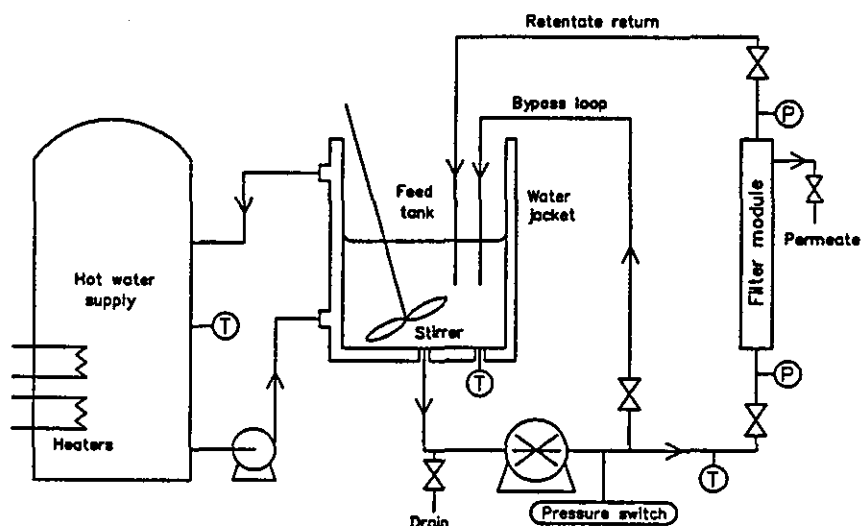
Fig. 1. Schematic diagram of crossflow microfiltration rig.

matic data logging system records transmembrane pressure, temperature and pump speed while permeate flux measurements are taken manually.

Once the dispersion is circulating through the bypass loop at the required volumetric flow rate, concentration, pH, and temperature, the valve to the filter module is opened and the bypass loop closed. The filter module exit valve is then adjusted to achieve the desired transmembrane pressure, following which permeate flux readings are taken and the flux decline monitored until a steady-state is reached.

Experiments were carried out at 50°C. The permeate flux, J, for various inlet crossflow velocities in the range 0.3–2 m s^{-1} and various transmembrane pressures in the range 50–200 kPa, was evaluated. The same membrane was used in each experiment, and before the run, the pure water flux through the membrane was measured. The flux through the membrane was measured by collecting the permeate from the outer stainless steel tube surrounding the membrane into a graduated cylinder and timing the collection period. Both the permeate and the retentate were recycled to the storage tank. Therefore, the concentration in the container remained effectively constant. The unit allowed studies in which the transmembrane pressure and the crossflow velocity were independently varied. By systematically adjusting one process variable while maintaining all others constant, steady-state permeate flux values were obtained as a function of each variable.

3. Results and discussion

3.1. Viscosity measurements

The results of the viscosity measurements are presented in Fig. 2 showing a pronounced non-Newtonian behaviour of
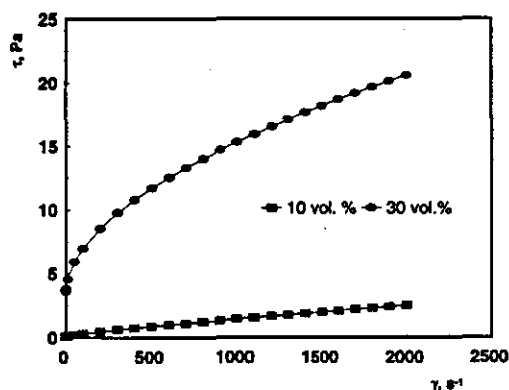

Fig. 2. Rheogram of the shear stress against the shear rate for 10 and 30 vol.% titanium dioxide dispersions at pH 9 and temperature 50°C.

Table 1
Parameters of the Herschel–Bulkley model as a function of the solids volume fraction of aqueous titania dispersions ($T = 50°C$)

ϕ	τ_{HB} [Pa]	K [Pa s^n]	n
0	0	5.494×10^{-4}	1
0.05	0.0106	1.519×10^{-3}	0.919
0.10	0.1592	4.468×10^{-3}	0.834
0.20	1.459	0.1041	0.676
0.30	3.517	0.2982	0.529
0.40	10.99	0.6232	0.487
0.50	25.52	1.108	0.448

the aqueous titania dispersions (in agreement with data presented in Ref. [2]). The pronounced shear-thinning rheological behaviour can be approximated with a model of the Herschel–Bulkley type or of the Casson type. For the former, Table 1 gives the values obtained for the various parameters as functions of the solids volume fraction.
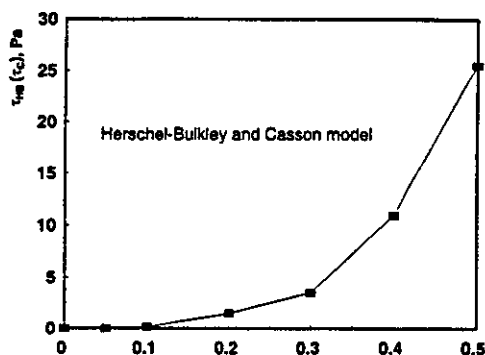
Fig. 3. Variation of the yield stress as a function of the solids volume fraction.
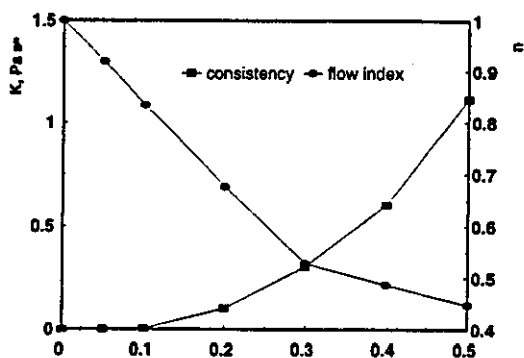

Fig. 4. Variation of the consistency and the flow index as a function of the solids volume fraction (Herschel–Bulkley model).

A plot of the variation of the yield stress as a function of the solids volume fraction (see Fig. 3) shows that neither τ_{HB} or τ_C increases strongly above concentration of 10%. The values of the yield stresses, calculated on the basis of the two rheological models, are very close to one another for the volume fractions above 10% (the differences between the two values fall between 2 and 5%). The percentile difference is considerably larger for lower concentration.

The consistency, K, of the Herschel–Bulkley model (see Fig. 4) also increases strongly above this critical volume fraction of 10%. In addition, in this same figure, the curve for the variation of the flow index, n, of the dispersion shows clearly that there is a change in the rheological behaviour of the titania dispersions when the solids volume fraction exceeds 30%. For the Herschel–Bulkley model, the variation of the yield stress, consistency, and of the flow index, can be represented by the relationships

$$\tau_{HB} = 235\phi^{3.275} \tag{3}$$

$$K = 5.494 \times 10^{-4}(1-\phi)^{-19.93} \text{ for } \phi \leq 0.1 \tag{4a}$$

$$K = 6.564\phi^{2.573} \text{ for } \phi > 0.1 \tag{4b}$$

$$n = 1 - 1.574\phi \text{ for } \phi < 0.3 \tag{5a}$$

$$n = 0.65 - 0.405\phi \text{ for } \phi > 0.3 \tag{5b}$$

The empirical relationships presented in Eqs. (3), (4) and (5) are based on experimental measurements over a concentration range $0 < \phi < 0.5$, and are expected to be valid during crossflow microfiltration of these dispersions.

3.2. Typical flux decline curves

Analysis of the permeate composition showed complete retention of the titania particles in the feed. Note that no long term flux decline was observed, which is not surprising since the particles were bigger than the membrane pores.

The expected dependence of crossflow microfiltration behaviour on dispersion stability (or pH) in the case of titania-in-water dispersions has been shown experimentally [17]. In contrast to the case studied in this paper, the unstable dispersion (pH 4) shows different filtration characteristics. The different qualitative behaviour could be explained by the formation of very large flocs in the case of the unstable dispersion [2].

The effect of inlet crossflow velocity, u, and bulk dispersion solids volume fraction, ϕ, on the permeate flux-time curve are depicted in Figs. 5 and 6. As a general rule, the steady-state flux during crossflow microfiltration was sub-.
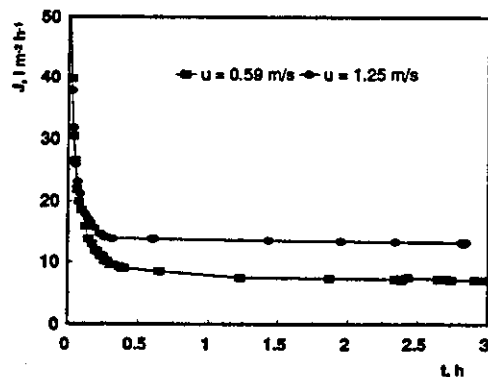
Fig. 5. Effect of inlet velocity on flux-time curve ($\phi = 0.19$, $\Delta P = 100$ kPa).
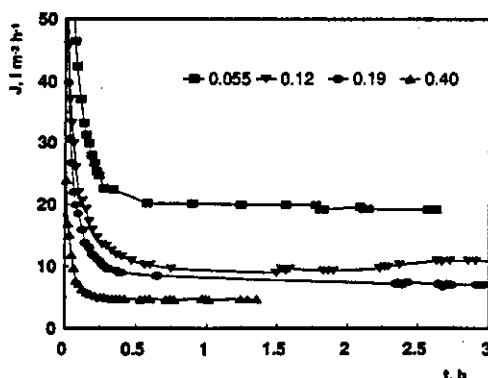
Fig. 6. Effect of bulk solids volume fraction on flux-time curve ($u = 0.7$ m s^{-1}, $\Delta P = 100$ kPa).

stantially lower than the pure water flux ranging from 1% to 10% of the pure water values. Besides the fact that low levels of permeate flux were achieved (for comparison see Refs. [18,19]), the most noticeable feature in Figs. 5 and 6 is the strong dependence of the flux on the operating variables. The following trends are evident: (a) a significant flux decay was observed mainly in the initial periods of the process, and (b) the flux decline shows significant dependence on operating conditions such as inlet velocity and bulk dispersion solids volume fraction.

The flux decay in the initial periods of the process could be explained by build-up of a cake layer on the membrane surface which offers the controlling hydraulic resistance to permeation. Steady-state conditions are reached when the convective transport of particles to the membrane is equal to the sum of the permeate flow plus the diffusive back transport of the particles. In addition, the filter cake continues to grow until it reaches a state where further growth is curtailed by the applied axial fluid shear upon the cake layer. At this point, a steady-state flux should be reached.

The effects of the operating variables on the steady-state flux are shown in Fig. 7. The steady-state flux is a strong function of the operating variables investigated. It is evident from Fig. 7 that the steady-state flux increases (the thickness of the cake layer and its hydraulic resistance decreases) with the superficial velocity. Similar trends were observed before [18,20–22]. Increasing the crossflow velocity of the dispersion increases the shear effect on the filter cake surface. This helps to limit the thickness of filter cake formed, but may also serve to agitate particles in the cake surface layer, resulting in cake consolidation and therefore, an increased resistance to permeate flow [23].

The effects of increasing dispersion concentration on permeate flux can be seen in Fig. 7. At higher concentrations, the relatively high initial flux of particles to the filter surface results in the rapid deposition of a cake layer, minimising the tendencies of particle penetration into the membrane pores and resulting in a more immediate decline in permeate flux. At steady-state, the higher concentration results in a thicker filter cake and consequently a lower permeate flux. Additionally, the effects of pH, crossflow velocity and transmembrane pressure on permeate flux are all more pronounced at low concentrations and have reduced effect at higher concentrations [17]. At pH 4, close to the isoelectric point, the permeate flux is much higher than at other pH values. For example, the steady-state flux when filtering a 4% by volume feed is about 380 $l\,m^{-2}\,h^{-1}$ at pH 4 and 30 $l\,m^{-2}\,h^{-1}$ at pH 9.5. With a 12% feed the corresponding fluxes are 130 and 20 $l\,m^{-2}\,h^{-1}$ (these fluxes were all measured at a transmembrane pressure of 100 kPa, crossflow velocity of 1.3 m s^{-1} and temperature of 50°C). Increasing the transmembrane pressure increased the steady-state permeate flux; for example, filtering 33% feed (using a crossflow velocity of 0.8 m s^{-1}, pH 9.5, 50°C) produced fluxes of 3.3, 4.7 and 6.5 $l\,m^{-2}\,h^{-1}$ at transmembrane pressure of 50, 100 and 200 kPa. The

highest concentration reached during filtration was 48% solids by volume (pH 9.5, 50°C, 100 kPa, 1.3 m s^{-1}).

Of interest is the semi-log relationship exhibited between steady-state permeate flux and log volume solids fraction (Fig. 8), a trend also observed by Fane [24]. Such linear relationships have been found when filtering other dispersed systems: by extrapolating the permeate flux (J_{ss}) vs. log[feed concentration (ϕ)] to obtain a concentration that corresponds to $J_{ss}=0$, a so-called gel concentration (ϕ_g) can be defined—more correctly referred to as a cake concentration in this work. Fig. 8 indicates that ϕ_g is independent of the filter operating conditions; this has also been found from the crossflow filtration of surfactant [25–27] and latex [28] dispersions, water soluble polymers [29] and for filtering some proteins under certain conditions [30]. However, ϕ_g does depend on the solute (particle)-membrane interactions [31].

Clearly, the effects that operating variables have on flux differ from system to system. The only general conclusion that may be drawn is that the permeate flux increases with operating velocity and decreases with increasing dispersion concentration. This probably explains why models developed for a particular system may often contradict experimental
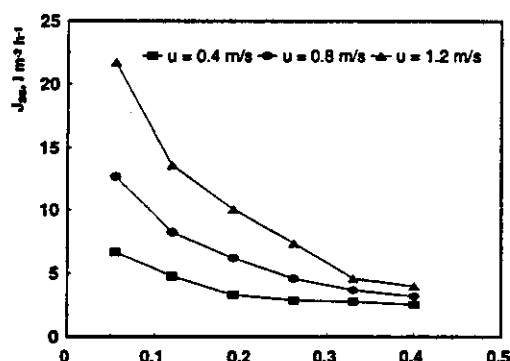

Fig. 7. Effect of crossflow velocity and bulk solids volume fraction on the steady state flux.
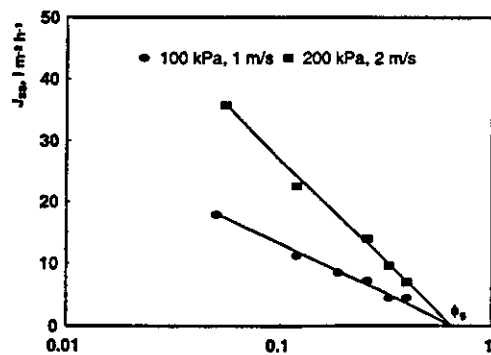

Fig. 8. Semi-log relationship between the steady state flux and bulk solids volume fraction.

observations obtained on different systems (see, for example. Refs. [13–15]).

3.3. Comparison of experiments with theory

The general trends predicted by the theory presented in the previously published papers [13–15]—such as an increasing permeation flux with increasing transmembrane pressure difference and shear rate, and a decreasing permeation flux with increasing feed volume fraction—have been verified experimentally.

Crossflow filtration limits the build-up of rejected particles on the membrane. and at steady-state the particle layer formed on the walls is assumed to attain a thickness that is invariant with time but increases with axial distance from the filter entrance. The resistance produced by the cake and flowing (polarised) particle layers along with the intrinsic resistance of the membrane are considered to act in series. and the permeate flux is then described by Darcy's law. The resistance due to the flowing layer is usually much less than the membrane resistance and is inconsequential in all cases of practical interest [9]. Thus

$$J_{ss} = \Delta P / \mu_o (R_m + r\delta) = J_o R_m / (R_m + r\delta) \qquad (6)$$

where J_{ss} is the steady-state permeate flux, μ_o is the solvent (in this case, water) viscosity, R_m is the membrane resistance, r is the cake resistance, and δ is the cake thickness. The second equality in Eq. (6) expresses J_{ss} as a function of the permeate flux of the clean membrane: $J_o = \Delta P / \mu_o R_m$. The resistance of the cake layer. r, is estimated using the Blake–Kozeny correlation [32]

$$r = 37.5 \phi_{max}^2 / a^2 (1 - \phi_{max})^3 \qquad (7)$$

where ϕ_{max} = volume fraction of the maximally packed particles in the cake layer.

3.3.1. Analysis method for time-dependent permeate flux

The effect of time-dependent decreases in permeate flux on the average permeate flux over an operating time, t, can be approximated using a procedure in which the steady-state model for crossflow filtration is combined with a transient model for deadend batch filtration. This procedure has been shown [13,14] to yield a good approximation to the exact solution [11] for the time varying permeate flux $J(t)$. A mathematical analysis of the classic constant pressure blocking filtration laws, with due allowance for a crossflow removal mechanism, has been completed by Field et al. [33]. However. this work demonstrates that provided certain terms take finite values. fluxes should exist at which there is no decline of flux with time.

An explicit solution for $J(t)$ is derived from a mass balance at the edge of a growing cake layer in a deadend filtration operation [13]:

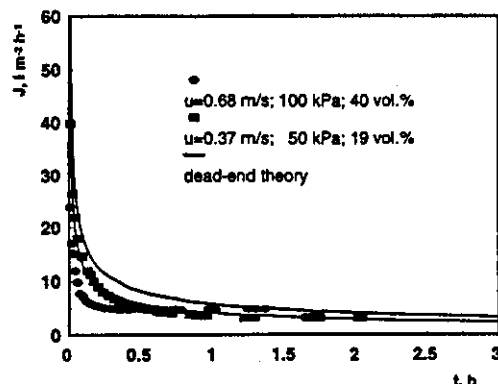$$(J + d\delta/dt)\phi = \phi_{max} d\delta/dt \qquad (8)$$

Fig. 9. Comparison between predicted and experimentally observed flux-time curves.

Eq. (8) is combined with Eq. (6) and integrated to give the following expression for the time-dependent permeate flux [14]:

$$J(t) = J_o / (1 + 2t/\tau_{cr})^{1/2} \qquad (9)$$

where $\tau_{cr} = R_m (\phi_{max} - \phi) / (J_o r\phi)$ is the time constant associated with the flux decline.

The approximate procedure to predict the total behaviour of the permeate flux. from time zero to steady-state, is to use Eq. (9) from deadend batch filtration until the time the steady-state is reached and then use the steady-state flux value from the steady-state model [14]. The underlying reason behind this combined solution is that while the cake is initially developing, the effect of the shear rate is small and can be neglected over short times so that crossflow filtration theory can be effectively approximated by deadend filtration theory. Nearing the steady-state, however, the shear rate begins to arrest the cake growth in crossflow filtration while deadend flux profile continues to decline with time. The approximate time to steady-state. t_{ss}, is determined by substituting the steady-state flux, J_{ss}, in Eq. (9)

$$t_{ss} = [(J_o/J_{ss})^2 - 1] \tau_{cr}/2 \qquad (10)$$

The characteristics of permeate flux decline, and the associated operating time required to achieve the steady-state flux, vary as a function of the concentration of dispersions and operating parameters.

The results for the permeate flux as a function of the time are shown in Fig. 9. The solid lines are the theoretical predictions for the conditions corresponding to those of the experiments. The quantitative agreement between theory and experiment is good. although the theory overpredicts the permeate flux observed in some of the experiments (see Fig. 9). This may indicate that the cake layer resistance determined from Eq. (7) was less than its value during microfiltration. Note that the transient flux decline follows the deadend theory given by Eq. (9) for short times and then levels off for long times.

269

3.3.2. Analysis method for steady-state flux

The steady-state thickness is found from a balance between the convective transport of particles toward the cake and the shear-induced transport or diffusion of particles away from or along the top of the cake. For an initially clean membrane, and unless the shear rate at the membrane surface exceeds a critical value, particles are convected to the membrane with the permeate flux more rapidly than they are removed. As a result, the stagnant cake layer forms and grows. The permeate flux is reduced as the cake thickness increases (due to increased cake resistance), and the shear at the cake surface increases as the cake thickness increases (due to reduced cross-sectional area for axial flow, and assuming that the feed pump is able to deliver a constant flow rate as the channel becomes constricted).

The model of Datta and Gaddis [34], using the Kozeny–Carman equation for cake resistance and Darcy's law applied over the filter area to calculate steady-state cake thickness or permeate flux was used. Mathematically, the limiting cake thickness may be obtained from the simultaneous solutions of the pressure drop due to Kozeny–Carman drag due to flow through a packed bed having uniform volume concentration of the cake, which is equal to the maximum packing density for the solids, ϕ_{max}. Therefore, at steady-state the cake thickness can be predicted from Datta and Gaddis [34] as

$$(R_m\delta^2 + r\delta^3)\tau/\eta_c = [2\Delta P\phi/\mu_o(\phi_{max} - \phi)]x \tag{11}$$

where τ is the shear stress, x is coordinate denoting longitudinal direction of feed (dispersion) flow, and η_c is the cake apparent viscosity, which can be determined from Mooney's equation [35]

$$\eta_c/\mu_o = \exp[2.5\phi_{max}\phi^*/(\phi^* - \phi_{max})] \tag{12}$$

Here ϕ^* ($=0.74$) is the maximal value of the packing density (volume concentration) of rigid spheres [35].

It should be noted that the theoretical model requires values for volume fraction in the cake layer and apparent shear viscosity of bulk dispersion. The volume fraction of the maximally packed particles in the cake layer, ϕ_{max}, was not measured directly, but a reasonable estimate is given by $\phi_g = \phi_{max} = 0.65$, from Fig. 8. Alternatively, it has been suggested that ϕ_{max} up to 0.65 can be used [28]. The apparent shear viscosity for the dispersion at different concentrations was determined from the data of Mikulášek et al. [2] by

$$\eta = \tau_{HB}/\gamma + K\gamma^{n-1} \tag{13}$$

Corresponding values of yield stress, τ_{HB}, consistency, K, and flow index, n, Eqs. (3), (4) and (5) respectively, were used in Eq. (13).

From Eq. (11) the cake layer thickness distribution $\delta(x)$, (i.e., variation of the cake thickness with longitudinal distance, x) can be calculated. Model parameters required for the solution of the steady-state equation, i.e., the maximum solids volume fraction, ϕ_{max}, the shear stress, τ, and the cake layer resistance, r, were subsequently quantified on experimental data. A solution procedure was used (see Refs.
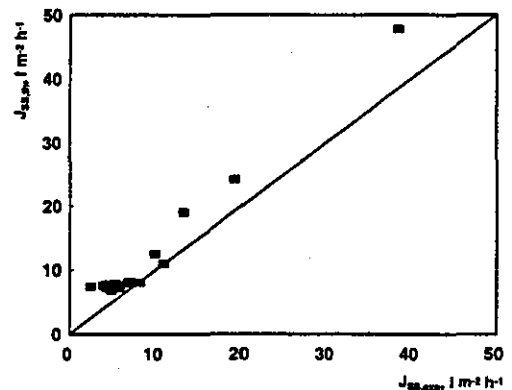

Fig. 10. Comparison between predicted and experimentally observed steady state fluxes ($\Delta P = 100$ kPa).

[34,36]), enabling prediction of the steady-state cake thickness. This thickness (Eq. (11)) yields a distribution $J(x)$ whose average value is the observed mean steady-state, length-averaged permeate flux for specified operating variables. The cake thicknesses in the range from 1×10^{-3} to 7.5×10^{-3} m were estimated, which were in agreement with visual observation of the filter cake after microfiltration. At high feed concentration, the filter tube was almost blocked by cake.

The overall model performance is shown in Fig. 10, where predicted steady-state fluxes are compared to experimental values. The quantitative agreement between theory and experiment is good, although the theory overpredicts the steady-state permeate flux observed in our experiments (Fig. 10). This may indicate that a flowing sublayer was present over the stagnant cake layer or that the apparent viscosity of the cake was somewhat lower than the value used in making the theoretical predictions and/or the cake layer resistance determined from Eq. (7) was less than its value during microfiltration. The apparent viscosity of the cake layer estimate is quite sensitive to the viscosity model used to correlate concentration with viscosity. Though Mooney's model (Eq. (12)) [35] may be adequate for high shear stresses it may underpredict the apparent viscosity values at smaller shear stresses. This inference can be drawn easily based on the experimental apparent viscosity values for titania dispersions [34].

Crossflow experiments were conducted to investigate the effects of module hydrodynamics and dispersions parameters on permeate flux. However, even though an increased shear decreased the mass of particles deposited, thinner cakes did not necessarily result in higher permeate fluxes in experiments using the more widely distributed particles and low initial permeation rates. Thus, the benefits of a decrease in the cake mass at higher shear rates (or shear stress) may be counteracted by an increase in the cake resistance. In other words, the cake resistance during the microfiltration of a polydisperse dispersion is dependent on operating conditions. This may be attributed to two phenomena:

1. higher shear stresses selected for smaller particles in the cake in these experiments, and
2. higher shear stresses may favour more dense packing geometries.

Hydrodynamic selection of smaller particles and cake reorganisation result in cakes with a higher resistance during the crossflow microfiltration of polydisperse dispersions [22]. Thus, increasing the wall shear stress beyond a critical value is expected to have a limited value in increasing permeate flux. Similar observations have also been made during the turbulent crossflow filtration of mineral suspensions that formed compressible cakes [37].

As the shear rate increases progressively, smaller particles in the feed are expected to be selectively deposited [38]. Cakes formed at higher shear rates are also expected to be more compact. Therefore, for a given composition of the feed (i.e., solids volume fraction, ϕ) the cake resistance should increase with shear rate. Also, because initially deposited particles are less likely to be rearranged at higher permeation rates, cake resistance should be inversely related to J_0 for any given inlet crossflow velocity of bulk dispersion. Experimental data from the experiments are consistent with these expectations.

One way to estimate the cake resistance is to parameter fit the model prediction to the measured time dependent permeate flux. The graphs of $[(J_0/J)^2 - 1]$ vs. t was plotted for the titania dispersions flux decline data. These graphs yield a straight lines for short times. This confirms that the transient flux decline occurs due to formation of a cake layer of the rejected particles, similar to deadend filtration. For longer times, the data deviate from the straight line. This is because the arrest of cake growth due to shear causes the flux for crossflow microfiltration to be greater than for the deadend filtration after the same time interval; hence, the value of $[(J_0/J)^2 - 1]$ becomes less for the crossflow mode as compared to deadend filtration at longer time intervals. A linear regression of the data was performed to give an equation for the best-fit line. From the slope of the line the cake resistance has been calculated. The cake resistances for the titania dispersions were determined on the order of $(2-4) \times 10^{16}$ m^{-2}.

Fig. 11 illustrates the effect of taking the experimentally determined specific cake resistance into account in the calculation of permeate flux. In all these theoretical predictions, the respective values of the membrane resistance and the cake resistance cited above were used. The symbols are the measured fluxes, and the solid lines are the fluxes predicted by the deadend theory and by the steady-state model based on the Kozeny–Carman equation for cake resistance and Darcy's law applied over the filter area to relate filtration rate to average pressure difference between the feed and permeate sides of the filter. Tube constriction due to formation of thick cake layers is accounted for in the theoretical predictions.

Predicted fluxes show a notably good correspondence with experimental values. This is remarkable in view of the fact that correlations employed in the model were developed for systems vastly different from the crossflow microfiltration
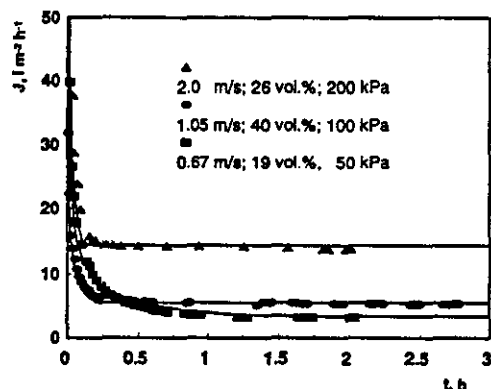

Fig. 11. Comparison between predicted and experimentally observed flux-time curves at different operating variables.

system used in this work. The filtration flux correlates well with wall shear stress, reducing to a unique relation in the absence of pore plugging, i.e., when the filter resistance is dominated by the properties of the deposit and flow conditions. Thus, the filter tube diameter and rheological properties of the dispersions will influence the wall shear stress and have a consequent effect on the flux.

4. Conclusions

The characteristic permeate flux-time behaviour and effects of operating variables on flux data have been presented for aqueous titanium dioxide dispersions that were crossflow microfiltered in a ceramic membrane tube.

The flux-time curve, and the steady-state permeate flux, are functions of all the operating variables studied, i.e., inlet crossflow velocity of bulk dispersion, bulk solids volume fraction and transmembrane pressure difference.

The transient flux decline under crossflow conditions was observed to follow deadend filtration theory, independent of the shear rate, for short times. For long times, however, the measured fluxes were observed to level out and reach a near steady-state value. This results from the hydrodynamic shear imposed by the crossflow arresting the cake growth. The initial flux and the rate of flux decline for short times were used to determine the membrane resistance and the cake resistance, respectively. The cake resistances for the titania dispersions are considerably higher than those predicted by the Blake–Kozeny equation for laminar flow through incompressible packed beds of monodispersed, rigid spheres. It is likely, that cakes formed under crossflow conditions are more compact that those formed deadend or stagnant conditions. Predicted fluxes show a notable correspondence with experimentally measured values. The model thus gives a basis for estimating the optimal parameters for the design of crossflow microfiltration systems operating on concentrated dispersions.

Appendix A. Nomenclature

a	Particle radius (m)
J	Permeate flux ($l\,m^{-2}\,h^{-1}$)
$J(t)$	Permeate flux at time t ($l\,m^{-2}\,h^{-1}$)
J_o	Pure water flux ($l\,m^{-2}\,h^{-1}$)
J_{ss}	Steady-state permeate flux ($l\,m^{-2}\,h^{-1}$)
K	Consistency parameter (Pa s^n)
n	Flow index
ΔP	Transmembrane pressure (Pa)
r	Cake layer resistance (m^{-2})
R_m	Membrane resistance (m^{-1})
t	Time (s)
t_{ss}	Time predicted to achieve steady-state (s)
u	Inlet crossflow velocity of bulk dispersion (m s^{-1})
x	Coordinate denoting longitudinal direction of dispersion flow (m)

Greek letters

δ	Cake layer thickness (m)
γ	Shear rate (s^{-1})
η	Apparent viscosity (Pa s)
η_C	Apparent viscosity of the cake layer (Pa s)
η_∞	Constant viscosity at the infinite shear limit (Pa s)
μ_o	Dynamic viscosity of pure fluid (Pa s)
τ	Shear stress (Pa)
τ_C	Yield stress in the Casson model (Pa)
τ_{cr}	Time constant (s)
τ_{HB}	Yield stress in the Herschel–Bulkley model (Pa)
ϕ	Solids volume fraction
ϕ_g	Gel concentration
ϕ_{max}	Maximum solids volume fraction in the cake layer
ϕ^*	Maximum packing density of particles, Eq. (12)

References

[1] D.A.R. Jones, B. Leary, D.V. Boger, J. Coll. Interface Sci. 147 (1991) 479–495.

[2] P. Mikulášek, R.J. Wakeman, J.Q. Marchant, Chem. Eng. J. 67 (1997) 97–102.

[3] W.F. Blatt, A. Dravid, A.S. Michaels, L. Nelson, Solute polarization and cake formation in membrane ultrafiltration: causes, consequences and control techniques, in: J.E. Flinn (Ed.), Membrane Science and Technology, Plenum, New York, 1970, pp. 47–97.

[4] F.W. Altena, G. Belfort, Chem. Eng. Sci. 39 (1984) 343–355.

[5] D.A. Drew, J.A. Schonberg, G. Belfort, Chem. Eng. Sci. 46 (1991) 3219–3224.

[6] A.L. Zydney, C.K.A. Colton, Chem. Eng. Commun. 47 (1986) 1–7.

[7] R.H. Davis, D.T. Leighton, Chem. Eng. Sci. 42 (1987) 275–281.

[8] D. Leighton, A. Acrivos, J. Fluid Mech. 181 (1987) 415–430.

[9] C.A. Romero, R.H. Davis, J. Membr. Sci. 39 (1988) 157–185.

[10] R.H. Davis, J.D. Sherwood, Chem. Eng. Sci. 45 (1990) 3203–3209.

[11] C.A. Romero, R.H. Davis, Chem. Eng. Sci. 45 (1990) 13–25.

[12] W.M. Lu, S.C. Ju, Sep. Sci. Technol. 24 (1989) 517–540.

[13] R.H. Davis, Sep. Purif. Meth. 21 (1992) 75–126.

[14] R.H. Davis, Theory for crossflow microfiltration, in: W.S. Winston Ho, K.K. Sirkar (Eds.), Membrane Handbook, Van Nostrand Reinhold, New York, 1992, pp. 480–505.

[15] G. Belfort, R.H. Davis, A.L. Zydney, J. Membr. Sci. 96 (1994) 1–58.

[16] Q.D. Nguyen, D.V. Boger, Annu. Rev. Fluid Mech. 24 (1992) 47–88.

[17] J.Q. Marchant, R.J. Wakeman, Crossflow microfiltration of concentrated titania suspensions, Proc. IChemE Jubilee Research Event, Vol. 2, Nottingham, 1997, p. 1061.

[18] M. Asaadi, D.A. White, Chem. Eng. J. 48 (1992) 11–16.

[19] R.G. Holdich, I.W. Cumming, B. Ismail, Trans. IChemE 73A (1995) 20–26.

[20] R. Rautenbach, G. Schock, J. Membr. Sci. 30 (1988) 231–242.

[21] G. Schulz, S. Ripperger, J. Membr. Sci. 40 (1989) 173–187.

[22] R.J. Wakeman, Trans. IChemE, 72A (1994) 530–540.

[23] E.S. Tarleton, R.J. Wakeman, Trans. IChemE 72A (1994) 431–440.

[24] A.G. Fane, J. Membr. Sci. 20 (1984) 249–259.

[25] G. Akay, R.J. Wakeman, Chem. Eng. Sci. 49 (1994) 271–283.

[26] G. Akay, R.J. Wakeman, J. Membr. Sci. 88 (1994) 177–195.

[27] G. Akay, Z.G. Bhumgara, R.J. Wakeman, Trans. IChemE 73A (1995) 783–796.

[28] R.J. Wakeman, G. Akay, J. Membr. Sci. 106 (1995) 57–65.

[29] R.J. Wakeman, G. Akay, J. Membr. Sci. 91 (1994) 145–152.

[30] R.J. Wakeman, Electrically enhanced microfiltration of albumin suspensions, Trans IChemE (submitted).

[31] R.J. Wakeman, G. Akay, Filtr. Sep. 34 (1997) 511–519.

[32] R.B. Bird, W.E. Steward, E.N. Lightfoot, Transport Phenomena, Wiley, New York, 1960.

[33] R.W. Field, D. Wu, J.A. Howell, B.B. Gupta, J. Membr. Sci. 100 (1995) 259–272.

[34] S. Datta, J.L. Gaddis, Sep. Sci. Technol. 32 (1997) 327–353.

[35] M. Mooney, J. Coll. Sci. 6 (1951) 162–170.

[36] G. Green, G. Belfort, Desalination 35 (1980) 129–147.

[37] R.J. Baker, A.G. Fane, C.J.D. Fell, B.H. Yoo, Desalination 53 (1985) 81–93.

[38] E.S. Tarleton, R.J. Wakeman, Trans. IChemE 71A (1993) 399–410.

CROSSFLOW MICROFILTRATION OF CONCENTRATED TITANIA SUSPENSIONS

J.Q.Marchant and R.J.Wakeman
Department of Chemical Engineering, Loughborough University, Loughborough, Leics, LE11 3TU.

The effect of process variables on permeate flux during the crossflow microfiltration of concentrated titania suspensions has been investigated. Filtration experiments carried out on ceramic, tubular, crossflow modules have shown that increases in transmembrane pressure, crossflow velocity and the degree of suspension flocculation all result in an improved permeate flux. Rheological work has shown that the titania suspension is shear thinning and that the viscosity is pH dependent. The effects of both shear rate and pH are enhanced as the suspension concentration is increased and the iso-electric point approached.

INTRODUCTION

Crossflow microfiltration was developed as an alternative to deadend filtration for concentrating suspensions. It differs from conventional filtration in that the retentate flows parallel to and across the filter surface rather than perpendicular to and toward it. The shearing effect of the crossflowing suspension serves to limit the thickness of the filter cake formed by removing deposited particles from its surface. A pseudo steady state is eventually reached where the rate of particle deposition equals the rate of particle removal and the permeate flux is constant.

This work has investigated the effects of process variables on permeate flux during the crossflow microfiltration of concentrated titania slurries (up to 50% solids by volume). These include the transmembrane pressure (0.5 to 2 bar), crossflow velocity (1 to 4ms⁻¹), suspension concentration (2 to 50% volume solids) and suspension pH (4 to 11). The suspension temperature is maintained at 50°C. Additional work on the characterisation of titania suspensions has also been carried out with a view to developing a mathematical model for the crossflow microfiltration process.

CHARACTERISATION

Titania suspensions have been characterised by their concentration, particle size distribution and viscosity; the viscosity is dependent on concentration, pH and shear rate. A Malvern Mastersizer was used to provide values of mean particle size, and a Carrimed CS100 controlled stress rheometer with a concentric cylinder measuring cell was used to determine suspension viscosity as a function of pH, concentration and shear rate.

Increasing the suspension concentration results in a corresponding rise in viscosity (Figure 1), which is also shown to be dependent on shear rate. The drop in viscosity as shear rate is increased indicates that the titania suspension is pseudoplastic (shear thinning). The suspension pH is altered using sodium hydroxide solution or hydrochloric acid. This induces a change in the surface charge of the particles in suspension, causing them to disperse or agglomerate. The effect of pH on viscosity (Figure 2) can be explained using the zeta potential curve (Figure 3) which shows the iso-electric point of the suspension to lie around pH 4, while between pH 6 and 11 the surface charge is relatively high. At pH 4, the particles tend to agglomerate, resulting in increased suspension viscosity, while the range of low viscosities correspond to a well dispersed suspension.
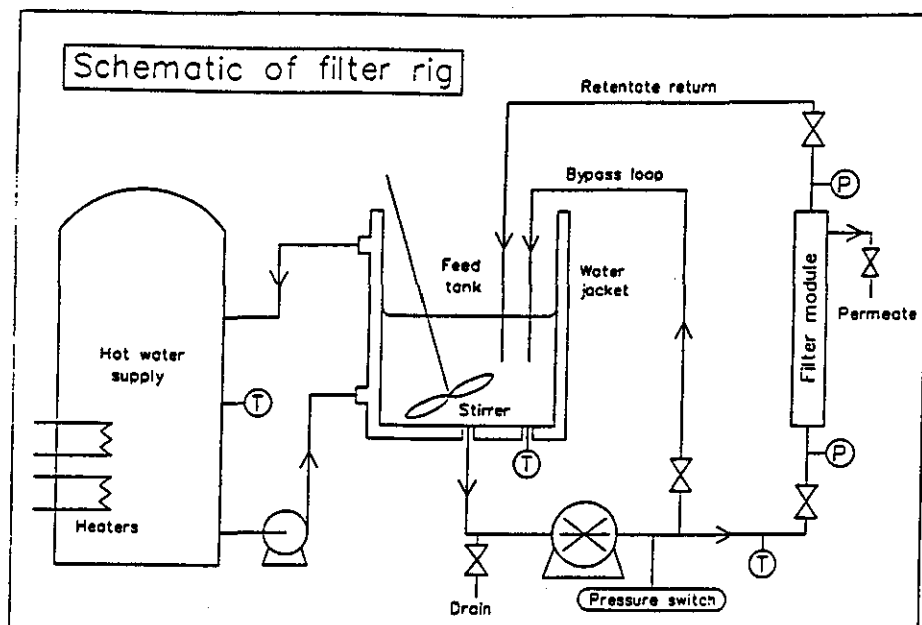
273

Figure 4

EXPERIMENTAL

The apparatus used for the filtration experiments is shown as a schematic in Figure 4. The suspension is fed to the filter by a variable speed monopump, thus allowing a range of crossflow velocities to be examined. The filter is a silicon carbide tube (0.9m long, 16mm internal diameter, mean pore size 0.1μm) housed in a stainless steel module. Permeate is removed from the filter module while the retentate is returned to the feed tank. Pressure transducers at either end of the filter module measure the transmembrane pressure, which is controlled using full flow ball valves. Temperatures are monitored by thermocouples, computer controlled, and maintained by a hot water jacket around the feed tank. An automatic data logging system records transmembrane pressure, temperatures and pump speed while permeate flux measurements are taken manually.

Once the suspension is circulating through the bypass loop at the required volumetric flow rate, concentration, pH and temperature, the valve to the filter module is opened and the bypass loop closed. The filter module exit valve is then adjusted to achieve the desired transmembrane pressure, following which, permeate flux readings are taken and the flux decline monitored until a steady state is reached.

RESULTS

By systematically adjusting one process variable whilst maintaining all others constant, steady state permeate flux values can be obtained as a function of each variable. Plotting this data allows the effects of each variable to be assessed individually. Figures 5 to 7 demonstrate the effects of pH, crossflow velocity, transmembrane pressure and concentration on the steady state permeate flux.

Figure 5 shows that the permeate flux achieved by filtering a suspension at pH 4 is much greater than that obtained at pH 9.5. This can be explained by the degree of agglomeration at pH 4 (Figure 3) compared to the well dispersed suspension at pH 9.5. A filter cake composed of larger aggregates will have a much higher porosity than one of smaller particles, thus providing less resistance to the permeate flow.

Increasing the crossflow velocity of the suspension increases the shear effect on the filter cake surface. This helps to limit the thickness of filter cake formed, but may also serve to agitate particles in the cake surface layer, resulting in cake consolidation and therefore an increased resistance to permeate flow[1]. Figure 6 shows a significant increase in permeate flux with crossflow velocity, suggesting also that the shear effect is limiting the thickness of cake formed.

The permeate flux through an unfouled membrane is proportional to the transmembrane pressure and depends little on crossflow velocity. A compressible cake, however, may yield to increased pressure, thus reducing permeate flux. Figure 7 shows an increase in permeate flux with pressure, but a doubling of the flux does not occur when the transmembrane pressure is doubled. This may be due to partial blocking of entrances to the pores in the membrane, as the cake formed is considered to be incompressible[1].

The effects of increasing suspension concentration on permeate flux can be seen in Figures 5, 6 and 7. At higher concentrations, the relatively high initial flux of particles to the filter surface results in the rapid deposition of a cake layer, minimising the tendencies of particle penetration into the membrane pores and resulting in a more immediate decline in permeate flux. At steady state, the higher concentration results in a thicker filter cake and consequently a lower permeate flux. Additionally, the effects of pH, crossflow velocity and transmembrane pressure on permeate flux are all more pronounced at low concentrations and have a reduced effect at higher concentrations. The highest concentration reached during filtration was 48% solids by volume (pH9.5, 50°C, 1bar, 1.3ms^{-1}).

CONCLUSIONS

The characterisation has revealed that the titania suspension has a peak viscosity around the iso-electric point (pH4.0), at which point the effective mean particle size is also at a maximum. The suspension is pseudoplastic and thus becomes less viscous as shear rate is increased, also becoming more viscous with increasing solids fraction. Results of crossflow experiments have revealed a decrease in flux with an increased solids concentration, a lower crossflow velocity and a smaller transmembrane pressure. The cake appears to be incompressible and tends not to consolidate further with increasing crossflow velocity. There is also a significant increase in permeate flux when the pH is close to the iso-electric point.
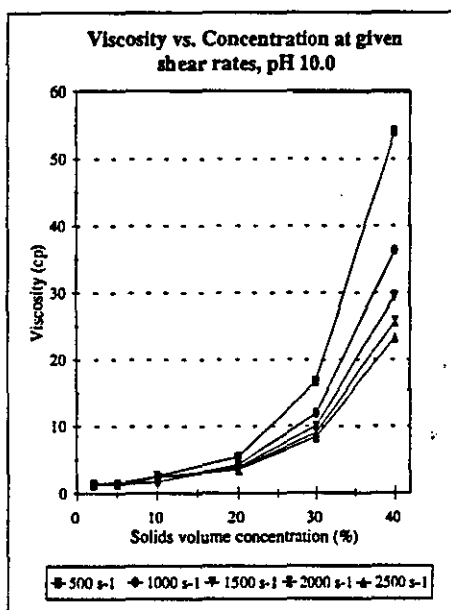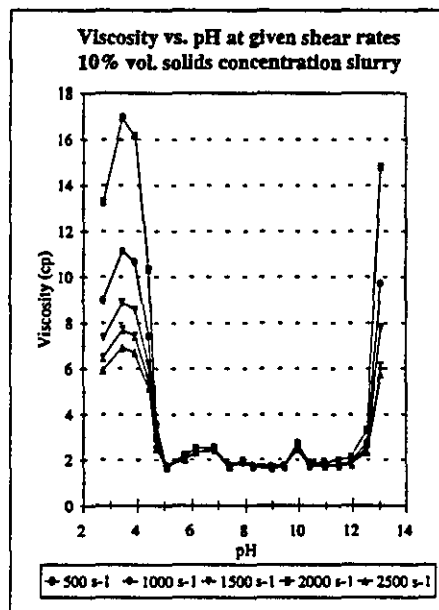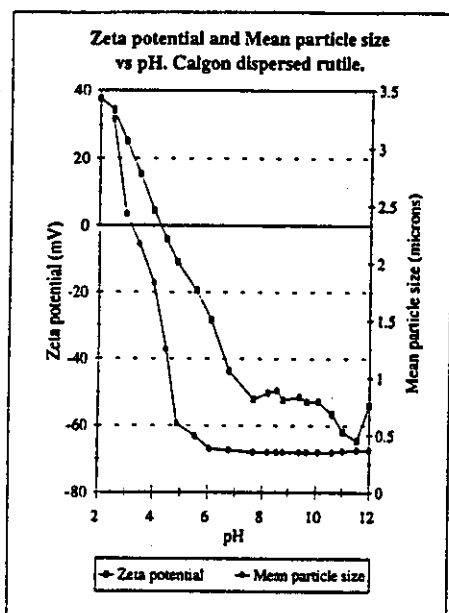

Figure 1

Figure 2

275

Figure 3
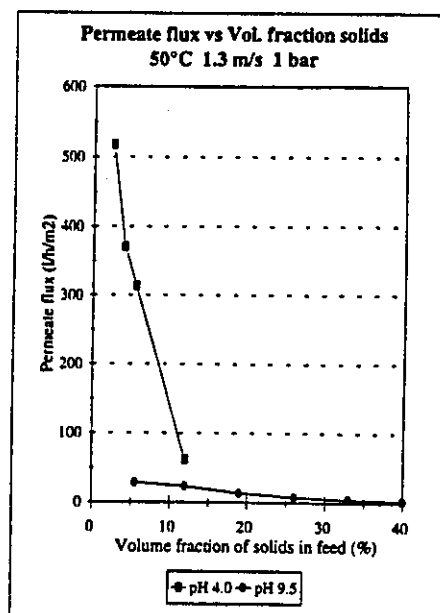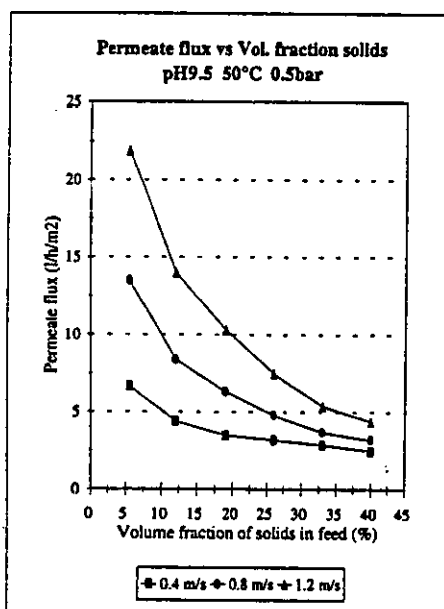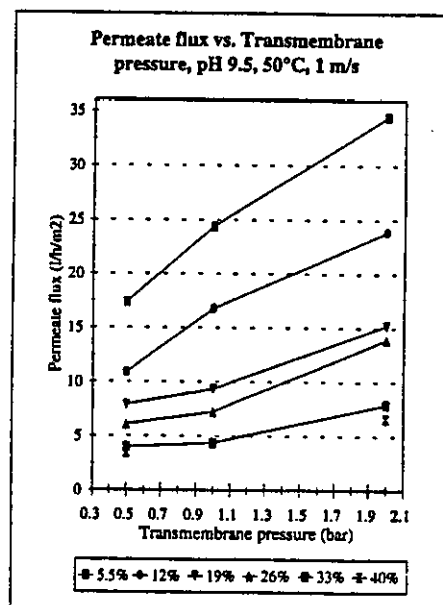

Figure 5

Figure 6

Figure 7

REFERENCES
1. Wakeman, R.J., 1994, Visualisation of Cake Formation in Crossflow Microfiltration, Trans. IChemE, 72A: 530-540.

276

ACCOMPANYING DISK HELD AT ISSUE DESK